

A STUDY ON THE EFFECTS OF HISTORICAL METEOROLOGICAL DATA SET ON
SIMULATED RADIOACTIVE DISPERSION FROM A NUCLEAR POWER PLANT
ACCIDENT BY NACAC CODE



A Dissertation Submitted in Partial Fulfillment of the Requirements
for the Degree of Doctor of Philosophy in Nuclear Engineering
Department of Nuclear Engineering
Faculty Of Engineering
Chulalongkorn University
Academic Year 2023

การศึกษามลกระทบของชุดข้อมูลสภาพภูมิอากาศย้อนหลังที่มีต่อการจำลองการกระจายตัวของ
สารกัมมันตรังสีจากอุบัติเหตุของโรงไฟฟ้านิวเคลียร์โดยใช้โปรแกรม NACAC



วิทยานิพนธ์นี้เป็นส่วนหนึ่งของการศึกษาตามหลักสูตรปริญญาวิศวกรรมศาสตรดุษฎีบัณฑิต
สาขาวิชาวิศวกรรมนิวเคลียร์ ภาควิชาวิศวกรรมนิวเคลียร์
คณะวิศวกรรมศาสตร์ จุฬาลงกรณ์มหาวิทยาลัย
ปีการศึกษา 2566

นราภานต์ คุณศรีเมฆ : การศึกษาผลกระทบของชุดข้อมูลสภาพภูมิอากาศย้อนหลังที่มีต่อการจำลองการกระจายตัวของสารกัมมันตรังสีจากอุบัติเหตุของโรงไฟฟ้านิวเคลียร์โดยใช้โปรแกรม NACAC. (A STUDY ON THE EFFECTS OF HISTORICAL METEOROLOGICAL DATA SET ON SIMULATED RADIOACTIVE DISPERSION FROM A NUCLEAR POWER PLANT ACCIDENT BY NACAC CODE) อ.ที่ปรึกษาหลัก : รศ. ดร.สมบุญ รัศมี, อ.ที่ปรึกษาร่วม : ดร.กัมปนาท ชิลวา

ความแปรปรวนในการทำนายผลของโปรแกรมจำลองการกระจายตัวของสารกัมมันตรังสี จากอิทธิพลการเปลี่ยนแปลงข้อมูลภูมิอากาศถูกตรวจสอบในการศึกษานี้ ข้อมูลภูมิอากาศย้อนหลังในช่วง พ.ศ.2559 ถึง 2563 จาก National Centers for Environmental Prediction (NCEP) และอุบัติเหตุสมมุติที่เกิดการช้อนทับกันระหว่าง Loss Of Offsite Power (LOOP) และ Large-Break Loss Of Coolant Accident (LBLOCA) ถูกใช้เป็นเงื่อนไขเริ่มต้นและขอบเขตในการศึกษา โรงไฟฟ้านิวเคลียร์ Fangchenggang ในประเทศจีนซึ่งตั้งอยู่ใกล้กับประเทศไทยถูกพิจารณาเป็นพื้นที่ศึกษา โปรแกรม Nuclear Accident Consequence Assessment Code (NACAC) ถูกใช้เป็นเครื่องมือสำหรับจำลองผล ประสิทธิภาพการทำนายผลของโปรแกรม NACAC ถูกตรวจสอบโดยการเปรียบเทียบผลการจำลองกับโปรแกรม Java-based Realtime Online DecisiOn Support system (JRODOS) ผลการตรวจสอบพบว่ากระบวนการคำนวณที่ต่างกันของทั้งสองโปรแกรมส่งผลให้ระยะการกระจายตัวของสารกัมมันตรังสีต่างกันประมาณ 200 กิโลเมตร และ ค่าความเข้มข้นของสารกัมมันตรังสีต่างกันประมาณ 1 ลำดับขนาด การตรวจสอบอิทธิพลของข้อมูลลม ฝน และความเสถียรบรรยากาศ ต่อการคำนวณความพร่องของสารกัมมันตรังสี ระยะการกระจายตัวของสารกัมมันตรังสี และขอบเขตการกระจายตัวของสารกัมมันตรังสี ในโปรแกรม NACAC ได้ถูกดำเนินการ ผลการตรวจสอบพบว่า ชุดข้อมูลนำเข้าที่มีปริมาณฝนต่ำ ความเร็วลมต่ำ และความเสถียรบรรยากาศสูง (ระดับ F) ส่งผลให้ค่าความเข้มข้นเฉลี่ยของสารกัมมันตรังสีมีค่าสูงที่สุด อิทธิพลของความแปรปรวนในข้อมูลภูมิอากาศต่อการทำนายผลของโปรแกรม NACAC ถูกตรวจสอบ ผลการตรวจสอบพบว่าข้อมูลภูมิอากาศแต่ละชนิดมีความแปรปรวนสูงในช่วงกลางปีซึ่งส่งผลให้ลักษณะการกระจายตัว และความเข้มข้นของสารกัมมันตรังสีจากการทำนายผลในแต่ละปีมีความต่างจากการจำลองผลโดยใช้ข้อมูลภูมิอากาศห้าปีก่อนให้เกิดผลการจำลองที่ครอบคลุมมากกว่าการจำลองผลโดยใช้ข้อมูลภูมิอากาศหนึ่งปี โดยผลการจำลองที่ 50 เปอร์เซ็นต์เป็นช่วงที่มีความต่างมากที่สุดของการจำลองผลทั้งสองวิธี โดยค่าสัมประสิทธิ์สหสัมพันธ์ของปริมาณรังสีสมมูลยังผลโดยเฉลี่ยตลอดทั้งปี ในช่วงระยะสั้น กลาง และ ยาว ของผลการจำลองที่ 50 เปอร์เซ็นต์ได้ถูกพบที่ 0.79 0.81 และ 0.66 ตามลำดับ

| | | |
|------------|--------------------|----------------------------------|
| สาขาวิชา | วิศวกรรมนิวเคลียร์ | ลายมือชื่อนิสิต |
| ปีการศึกษา | 2566 | ลายมือชื่อ อ.ที่ปรึกษาหลัก |
| | | ลายมือชื่อ อ.ที่ปรึกษาร่วม |

6171454721 : MAJOR NUCLEAR ENGINEERING

KEYWORD: Atmospheric dispersion, Radiation consequence evaluation, Climate Change,
Meteorological data selection, Verification, Severe accident

Narakhan Khunsrimek : A STUDY ON THE EFFECTS OF HISTORICAL METEOROLOGICAL
DATA SET ON SIMULATED RADIOACTIVE DISPERSION FROM A NUCLEAR POWER PLANT
ACCIDENT BY NACAC CODE. Advisor: Assoc. Prof. SOMBOON RASSAME, Ph.D. Co-advisor:
Kampanart Silva, Ph.D.

Quantifying the variability in the prediction of atmospheric dispersion code from the Influences of variations in meteorological data is investigated in this study. Historical meteorological data from 2016 to 2020 by the National Centers for Environmental Prediction (NCEP) and the overlap hypothetical accident Loss Of Offsite Power (LOOP) and Large-Break Loss Of Coolant Accident (LBLOCA) are used as initial and boundary conditions. The Fangchenggang nuclear power plant in China, close to Thailand, is considered a study location. The Nuclear Accident Consequence Assessment Code (NACAC) is used as a simulation tool for the investigation process. The NACAC prediction performance is verified by comparing the predicted result with the Java-based Realtime Online DecisiOn Support system (JRODOS). It found that different computational schemes cause variations in dispersion distances of about 200 km and activity concentration of about one order of magnitude. A sensitivity test with various meteorological input data is performed in NACAC to demonstrate the Influences of meteorological characteristic changes on the predicted results. Variations in rain, wind, and atmospheric stability class data affected radionuclides' depletion, dispersion range, and dispersion boundary. The scenario with low rain intensity, low wind speed, and stable atmospheric stability class (F class) causes the highest average radionuclide concentration. The influences of variations in meteorological data on NACAC predicted results are investigated. The high variants of each meteorological data are found in the middle of the year. This variability causes differences in dispersion characteristics and activity concentration for each year. Utilizing five years of meteorological data for simulation yields more comprehensive predicted results than a single year. The high disparity in both predicted results is found at the 50th percentile. The average correlation coefficient of the total effective dose equivalent value over a year in the short, medium, and long dispersion distances of predicted results at the 50th percentile are found at 0.79, 0.81, and 0.66, respectively.

Field of Study: Nuclear Engineering

Student's Signature

Academic Year: 2023

Advisor's Signature

Co-advisor's Signature

ACKNOWLEDGEMENTS

I would like to express my sincere appreciation to the Royal Golden Jubilee Ph.D. Scholarship (funding number PHD/0010/2561), Thailand Institute of Nuclear Technology (Public Organization), Office of Atoms for Peace and Department of Nuclear Engineering, Chulalongkorn University for supporting the study.

The achievement of completing this project would not have been possible without the unwavering support, encouragement, assistance, and invaluable guidance from my advisor, Associate Professor Dr. Somboon Rassame, and my co-advisor, Dr. Kampanart Silva.

I would like to express my gratitude to all committees for their valuable suggestions that have contributed to enhancing the quality of this dissertation.

Finally, I express my profound gratitude to my family for their support throughout the duration of this research.

Narakhan Khunsrimek

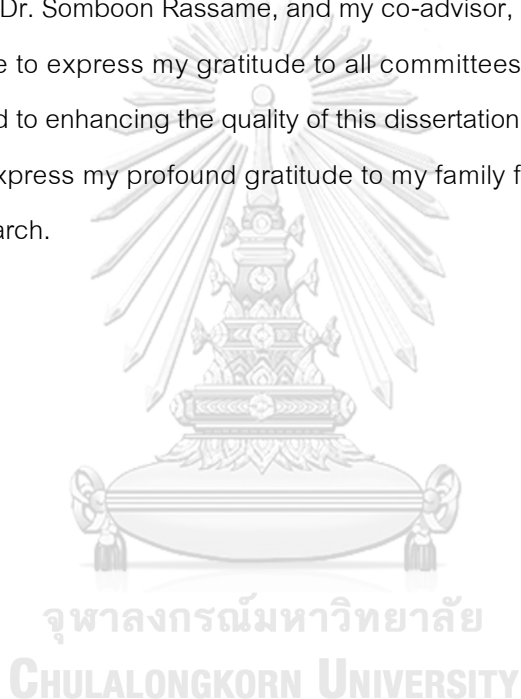


TABLE OF CONTENTS

| | Page |
|--|------|
| | iii |
| ABSTRACT (THAI)..... | iii |
| | iv |
| ABSTRACT (ENGLISH)..... | iv |
| ACKNOWLEDGEMENTS..... | v |
| TABLE OF CONTENTS..... | vi |
| LIST OF TABLES..... | xiii |
| LIST OF FIGURES..... | xv |
| DISCLAIMER..... | 1 |
| CHAPTER 1 INTRODUCTION..... | 2 |
| 1.1 Background and statement of the problem..... | 2 |
| 1.2 Objective..... | 4 |
| 1.3 Scope of study..... | 4 |
| 1.4 Expectation..... | 5 |
| CHAPTER 2 THEORY AND LITERATURE REVIEW..... | 6 |
| 2.1 Nuclear power plant..... | 6 |
| 2.1.1 Fission reaction in nuclear power plant..... | 6 |
| 2.1.2 Past nuclear severe accident..... | 7 |
| 2.1.3 General characteristics of severe accidents..... | 8 |
| 2.1.4 Station blackout..... | 9 |

| | |
|--|----|
| 2.1.5 Loss Of Offsite Power (LOOP) and Large-Break Loss Of coolant Accident (LBLOCA) | 10 |
| 2.2 Meteorological conditions involved in the calculation of atmospheric dispersion. 12 | |
| 2.2.1 Atmospheric layer | 12 |
| 2.2.2 Atmospheric circulation..... | 13 |
| 2.2.3 Lanina and Elnino phenomena..... | 14 |
| 2.2.4 Monsoon | 15 |
| 2.2.5 Air stability | 15 |
| 2.2.6 Atmospheric stability class classification | 17 |
| 2.3 Atmospheric dispersion..... | 18 |
| 2.3.1 Mixing height..... | 18 |
| 2.3.2 Plume rise | 18 |
| 2.3.3 Air concentration..... | 18 |
| 2.3.4 Deposition and depletion | 20 |
| 2.3.5 Resuspension..... | 20 |
| 2.4 Dose estimation and emergency planning | 21 |
| 2.4.1 Dose limit | 21 |
| 2.4.2 Emergency planning..... | 22 |
| 2.5 Radiological consequence evaluations..... | 26 |
| 2.5.1 Evaluation by measured data..... | 26 |
| 2.5.2 Evaluation by predicted results | 26 |
| 2.6 Atmospheric dispersion code | 27 |
| 2.6.1 Nuclear accident consequence analysis code (NACAC)..... | 29 |
| 2.6.2 Java-based Realtime Online DecisiOn Support system (JRODOS) | 34 |

| | |
|--|----|
| 2.6.3 Differences between the NACAC and JRODOS | 38 |
| 2.7 Meteorological data selections | 40 |
| 2.7.1 Sequential data selection | 40 |
| 2.7.2 Extreme data selection | 40 |
| 2.7.3 Representative data selection | 41 |
| 2.8 Demonstration of predicted results by percentile levels..... | 45 |
| 2.9 Literature review | 45 |
| 2.9.1 Potential dangers of nuclear power plants in China | 45 |
| 2.9.2 Climate changes..... | 46 |
| 2.9.3 Influences of variations in meteorological data on air pollution behavior..... | 47 |
| 2.9.4 Calculation processes in the atmospheric dispersion code and comparing prediction results by different atmospheric dispersion code..... | 49 |
| 2.9.5 Effects of using different meteorological data sources and defining simulation period | 50 |
| CHAPTER 3 METHODOLOGY | 55 |
| 3.1 NACAC computational process..... | 56 |
| 3.2 Boundary and initial conditions | 57 |
| 3.2.1 Study location..... | 57 |
| 3.2.2 Source terms | 58 |
| 3.2.3 Meteorological data | 59 |
| 3.3 Verification of calculation performance in NACAC..... | 59 |
| 3.3.1 Verification conditions..... | 59 |
| 3.3.2 Comparison processes | 62 |
| 3.3.3 Comparison patterns | 63 |

| | |
|--|-----|
| 3.4 Investigation of appropriate meteorological data selection | 63 |
| 3.4.1 Modification of representative data selection | 65 |
| 3.4.2 Comparisons of sequential and representative data selection | 67 |
| 3.5 Influences of each meteorological parameter on NACAC calculations | 69 |
| 3.6 Influences of variations in meteorological data on predicted results | 71 |
| CHAPTER 4 RESULT AND DISCUSSION..... | 74 |
| 4.1 NACAC verification results | 74 |
| 4.1.1 Comparisons of radionuclide transportation patterns | 74 |
| 4.1.2 Comparisons of calculated results | 79 |
| 4.2 Effects of different computational methods on the predicted results of atmospheric dispersion code..... | 82 |
| 4.2.1 Effects of input data preparation..... | 82 |
| 4.2.2 Effects of advection calculation | 87 |
| 4.3 Results of modifying representative data selection..... | 93 |
| 4.3.1 Effects of optional weather parameters and area boundaries | 94 |
| 4.3.2 Effects of sampling rates..... | 97 |
| 4.4 Results of investigating appropriate meteorological data selection | 100 |
| 4.4.1 Total Effective Dose Equivalence (TEDE)..... | 100 |
| 4.4.2 Dispersion characteristics..... | 101 |
| 4.5 Results of investigating influences of meteorological data on NACAC computational..... | 106 |
| 4.6 Results of investigating the influences of variations in meteorological data on the predicted results..... | 113 |

| | |
|---|-----|
| 4.6.1 Influences of variations in meteorological data on predicted results for a year..... | 113 |
| 4.6.1.1. Change in meteorological data over one year..... | 113 |
| 4.6.1.2 Change in projected results over one year..... | 117 |
| Dispersion characteristics | 117 |
| Activity concentrations | 122 |
| 4.6.2 Influences of variations in meteorological data on predicted results for five years..... | 124 |
| 4.6.2.1 Change in meteorological data over five years..... | 124 |
| 4.6.2.2 <i>Change in predicted results over five years</i> | 130 |
| Dispersion characteristics | 130 |
| Activity concentrations | 134 |
| 4.6.3 Variability of the predicted results | 139 |
| 4.6.3.1 Variation of predicted results for each year and average | 139 |
| 4.6.3.2 Variation of predicted results for each year and five years..... | 146 |
| CHAPTER 5 CONCLUSIONS AND SUGGESTIONS..... | 159 |
| REFERENCES | 167 |
| APPENDIX A EXTENDED RESULTS..... | 178 |
| A1. Average values for 24 hours of each meteorological parameter in the NACAC calculation process..... | 179 |
| A2. Dispersion characteristics from sensitivity test of varying meteorological input data in 12 cases | 182 |
| A3.Frequency distribution of wind direction of ten layers in each month..... | 185 |
| A4. Monthly average activity concentration of Cs-137 | 186 |

| | |
|---|-----|
| A5. Dispersion characteristics of TEDE after the accident for 24 hours..... | 187 |
| A6. Frequency distribution of wind direction and average wind speed of ten layers between 2016-2020 | 199 |
| A7. Activity concentrations in dominant dispersion direction of annual average dispersion characteristic..... | 205 |
| Air concentration values of Cs-137 | 205 |
| Air concentration values of I-131 | 207 |
| Ground concentration values of Cs-137..... | 209 |
| Ground concentration values of I-131 | 211 |
| Total effective dose equivalence (TEDE) | 213 |
| A8. Statistical values of AMBE, RMBE, and CC to investigate the difference in predicted results between a single year and an average over five years. | 215 |
| AMBE 1 year VS Average | 215 |
| RMSE 1 year VS Average | 218 |
| CC 1 year VS Average..... | 221 |
| A9. Statistical values of AMBE, RMBE, and CC to investigate the difference in predicted results between a single year and five years. | 224 |
| AMBE 1 year VS 5 years | 224 |
| RMSE 1 year VS 5 years | 227 |
| CC 1 year VS 5 years..... | 230 |
| APPENDIX B NACAC COMPUTATIONAL PROCESSES..... | 233 |
| B1. Preparing meteorological data | 234 |
| B2. Computational processes in NACAC | 237 |
| B2.1 Input data..... | 238 |

| | |
|---|-----|
| B2.2 Preprocessing process module | 240 |
| Import input data | 240 |
| B2.3 Meteorological data selection module..... | 242 |
| B2.4. Atmospheric dispersion calculation module | 243 |
| B2.4.1 Depletion | 243 |
| B2.4.2 Dispersion..... | 243 |
| B2.4.3 Concentration..... | 244 |
| B2.5 Result display | 245 |
| VITA..... | 247 |



LIST OF TABLES

| | Page |
|---|------|
| Table 1. Main Radioactive Fission Products[18]..... | 6 |
| Table 2. Released source term of loss of offsite power accidents (LOOP) and large-break loss of coolant (LBLOCA) [GBq][25] | 11 |
| Table 3 Conditions for evaluation of solar quantity[32]..... | 17 |
| Table 4 Conditions for atmospheric stability classification[31]..... | 17 |
| Table 5 Conditions for mixing height evaluation [33]..... | 18 |
| Table 6 Recommended dose limits in planned exposure situations[35] | 23 |
| Table 7 Deterministic effects [37]..... | 24 |
| Table 8 Responded actions in emergency situations to reduce risks [36]..... | 25 |
| Table 9 Differences between the NACAC and JRODOS[2]..... | 39 |
| Table 10 Literature reviews..... | 52 |
| Table 11 Boundary and initial conditions | 60 |
| Table 12 Metrological data classification[1]..... | 66 |
| Table 13 Computational cases to identify effects of optional weather parameters and area boundaries[1]..... | 69 |
| Table 14 Meteorological input data cases..... | 71 |
| Table 15 Statistical parameters values at 500 km in the dominant dispersion direction of four cases[2] | 80 |
| Table 16 Representative positions for the meteorological data collection from the different data preparation system evaluations[2]..... | 83 |
| Table 17 Summary of research results | 153 |

Table 18 Average over a year of statistical values demonstrating variation between predicted results by each year and the average predicted results over five years. 158

Table 19 Average over a year of statistical values demonstrating variation between predicted results by each year and the predicted by five years. 158



LIST OF FIGURES

| | Page |
|--|------|
| Figure 1. Atmospheric temperature characteristics [26] | 13 |
| Figure 2. Atmosphere circulation of the Earth [27] | 14 |
| Figure 3. Behavior of Lanina and Elnino phenomena [28] | 15 |
| Figure 4. Plume pattern under various conditions of atmospheric stability [30] | 16 |
| Figure 5 Plume rise characteristic. | 18 |
| Figure 6 General calculation process in the atmospheric dispersion code[1]. | 29 |
| Figure 7 Calculation flow chart in atmospheric dispersion calculation part | 30 |
| Figure 8 Advection calculation pattern of the NACAC [59]..... | 31 |
| Figure 9 Receptor selection in NACAC | 32 |
| Figure 10 Trajectory characteristics in the NACAC [60]..... | 33 |
| Figure 11 Advection calculation pattern of the JRODOS [66] | 37 |
| Figure 12 Sequential data selection[1] | 43 |
| Figure 13 Representative data selection[1] | 44 |
| Figure 14 Methodology flow chart | 55 |
| Figure 15 Calculation flow chart in NACAC | 57 |
| Figure 16 Fangchenggang power plant location[1] | 58 |
| Figure 17 Flow chart of the verification process[2]..... | 61 |
| Figure 18 Wind fluctuation at the release point for 96 hours from (a) January 18, 2018, 7:00 UTC, (b) March 20, 2018, 3:00 UTC. (c) August 10, 2018, 5:00 UTC, and (d) September 19, 2018, 3:00 UTC[2]. | 61 |
| Figure 19 Modified result after swapping from a cartesian grid to a polar grid[2]. | 63 |

| | |
|---|----|
| Figure 20 Predicted air concentration of I-131 every 24 h from the NACAC and JRODOS at (a) 24 h, (b) 48 h, (c) 72 h, and (d) 96 h in the case of January 18, 2018, 7:00 UTC[2]. | 77 |
| Figure 21 Air concentration of I-131 for 96 hours predicted by the NACAC and JRODOS of (a) March 20, 2018, 3:00 UTC (b) August 10, 2018, 5:00 UTC, and (c) September 19, 2018, 3:00 UTC[2]. | 78 |
| Figure 22 Comparison of the predicted air concentration, ground concentration, and effective dose rate from the NACAC and JRODOS in the dominant dispersion direction in the case of January 18, 2018, 7:00 UTC[2]. | 81 |
| Figure 23 Comparison of the different (a) rain, (b) wind speeds, and (c) wind direction obtained from the NACAC and JRODOS data preparation systems in the case of January 18, 2018, 7:00 UTC[2]. | 84 |
| Figure 24 Atmospheric stability class data on January 18, 2018, 23 UTC derived from the (a) NACAC and (b) JRODOS[2]. | 86 |
| Figure 25 Wind proportion for the trajectory calculation in NACAC in the case of January 18, 2018, 7:00 UTC[2]. | 87 |
| Figure 26 The wind (a) direction and (b) speed obtained from the NACAC using the vector summation at a latitude of 21° to 25° and longitude of 105° to 109° in case of January 18, 2018, 7:00 UTC[2]. | 88 |
| Figure 27 Example of the trajectory characteristic in the first and second groups generated in the NACAC simulation in the case of January 18, 2018, 7:00 UTC[2]. | 89 |
| Figure 28 Comparison between the JRODOS predicted I-131 air concentration transportation patterns and wind data at 10 m after (a) 24 h, (b) 48 h, (c) 72 h, and (d) 96 h in the case of January 18, 2018, 7:00 UTC[2]. | 92 |
| Figure 29 Total dose rate of I-131 and Cs-137 at Fangchenggang NPP after 96 h derived from the (a) NACAC and (b) JRODOS predictions after 96 h in the case of March 20, 2018, 3:00 UTC[2]. | 93 |

| | |
|--|-----|
| Figure 30 Data consistency investigation of TEDE values after 24 hours at 50 th , 90 th , and 99.5 th percentile between simulation using sequential data selection and representative data selection by case no. 2 to 8 based on statistical values[1]..... | 96 |
| Figure 31 Comparing TEDE value predicted by simulation using sequential and representative data selection at a radius of 9 km in the NE direction | 97 |
| Figure 32 CC values of case no. 5 with five-sampling rate conditions at (a) 50 th , (b) 90 th , and (c) 99.5 th percentile[1]. | 99 |
| Figure 33 Comparing TEDE values after 24 hours at the 50 th percentile within a radial of 900 km in 16 directions predicted by simulation using representative and sequential data sections..... | 103 |
| Figure 34 Comparing TEDE values after 24 hours at the 90 th percentile within a radial of 900 km in 16 directions predicted by simulation using representative and sequential data sections..... | 104 |
| Figure 35 Comparing TEDE values after 24 hours at the 99.5 th percentile within a radial of 900 km in 16 directions predicted by simulation using representative and sequential data sections..... | 105 |
| Figure 36 Comparing dispersion characteristics at the 50 th , 90 th , and 99.5 th percentile by simulation using sequential and representative data selection | 106 |
| Figure 37 Depletion parameters | 108 |
| Figure 38 Dispersion parameters | 109 |
| Figure 39 Concentration parameters | 110 |
| Figure 40 Prediction results of 12 meteorological input data sorted in ascending order concentration parameters where Avg AC, Avg GC, and Avg TEDE are average total for 24 hours of air concentration [Bq/m ³], ground concentration [Bq/m ²], and total effective dose equivalent [mSv]..... | 111 |

| | |
|---|-----|
| Figure 41 Combinations of meteorological parameters causing the highest value of each calculation parameter in NACAC..... | 113 |
| Figure 42 Wind pathway in the first seven and last three layers in each month in 2016 | 114 |
| Figure 43 Monthly average wind speed value of each layer in 2016 | 116 |
| Figure 44 Monthly average (a) atmospheric stability class and (b) rain intensity in 2016 | 117 |
| Figure 45 TEDE in 2016 at 99.5 th percentile..... | 118 |
| Figure 46 TEDE in 2016 at 90 th percentile..... | 119 |
| Figure 47 TEDE in 2016 at 50 th percentile..... | 120 |
| Figure 48 Monthly average activity concentration in each radius location at 50 th , 90 th , and 99.5 th percentile in 2016..... | 124 |
| Figure 49 Average hourly meteorological parameter in each year within a radius of 900 km from Fangchenggang NPP..... | 126 |
| Figure 50 Frequency of wind direction at 10 m of each year within a radius of 900 km from Fangchenggang NPP | 127 |
| Figure 51 Monthly statistical values of AMBE, RMSE, and CC, demonstrating differences in each meteorological parameter in each year from the average value over five years..... | 129 |
| Figure 52 TEDE values at 99.5 th percentile comparison in dominant dispersion direction of the yearly average dispersion characteristic | 137 |
| Figure 53 TEDE values at 90 th percentile comparison in dominant dispersion direction of the yearly average dispersion characteristic..... | 138 |
| Figure 54 TEDE values at 50 th percentile comparison in dominant dispersion direction of the yearly average dispersion characteristic..... | 139 |

| | |
|--|-----|
| Figure 55 AMBE values in each single year of TEDE at 50 th ,90 th , and 99.5 th percentiles compared with an average value over five years in short, medium, and long distances. | 143 |
| Figure 56 RMSE values in each single year of TEDE at 50 th ,90 th , and 99.5 th percentiles compared with an average value over five years in short, medium, and long distances. | 144 |
| Figure 57 CC values in each single year of TEDE at 50 th ,90 th , and 99.5 th percentiles compared with an average value over five years in short, medium, and long distances. | 145 |
| Figure 58 Yearly average TEDE values at the 90 th percentile in short, medium, and long in the 1 st month..... | 146 |
| Figure 59 AMBE values in each single year of TEDE at 50 th ,90 th , and 99.5 th percentiles compared with five years in short, medium, and long distances. | 149 |
| Figure 60 RMSE values in each single year of TEDE at 50 th ,90 th , and 99.5 th percentiles compared with five years in short, medium, and long distances. | 150 |
| Figure 61 CC values in each single year of TEDE at 50 th ,90 th , and 99.5 th percentiles compared with five years in short, medium, and long distances. | 151 |
| Figure 62 Variation of TEDE values at the 99.5 th percentile in short, medium, and long distances on the 11 th month of each year | 152 |

DISCLAIMER

This research used released source terms from the environmental impact report of the Fangchenggang power plant (site selection for units 3 and 4) published information. The radiation effect evaluation processes in this research are performed by hypothetical severe accidents, leading to results being consistent or inconsistent with actual events.



CHAPTER 1

INTRODUCTION

1.1 Background and statement of the problem

The Fukushima Nuclear Accident demonstrated that the radionuclides from a severe nuclear power plant (NPP) accident could affect other regions worldwide once released into the environment. According to Marzo's study [3], the radionuclides from the Fukushima nuclear accident could be transported through the atmosphere over the northern hemisphere and Europe. Povinec et al.[4] and Nakano et al. [5] showed that they could disperse all over the Pacific and Indian Oceans. In addition, the radiation detection measurements in Vietnam also demonstrated that the radionuclides could disperse to neighboring countries [6].

The facts mentioned above cause several countries to be concerned and interested in evaluating the radiation effect from neighboring countries. For example, Leung [7] showed that the radionuclides from a hypothetical accident in Guangdong NPP and Lingao NPP in China directly affected Hong Kong from April to May. This situation caused some parts of the northeastern region to have a thyroid equivalent dose higher than 50 mSv in the first week. Min and Kim's demonstrated that the worst-case scenario at Haiyang NPP in China caused an effective dose higher than 100 mSv over the Korean Peninsula [8]. Klein et al. investigated the radionuclide consequence in Norway from the Sellafield reprocessing plant in England. They found that the radionuclide significantly affected the western part of Norway with ground concentration higher than 10 Bq/m² [9].

Thailand is a country in the Indochinese Peninsula with a seasonal monsoon from the high-pressure areas in the northern hemisphere of Mongolia and China blowing past [10]. Many nuclear power plants in western China are located under this monsoon pathway and may cause radiation effects on Thailand. Among them, the Fangchenggang NPP, Yangjian NPP, and Changjiang NPP are located within a radius of 1,500 km from Thailand's capital. Therefore, these nuclear power plants are a good

starting point for Thailand to study the transboundary radiation effect of a hypothetical accidental release.

The Nuclear Accident Consequence Analysis Code (NACAC) is an atmospheric dispersion code designed to evaluate the radiation effect from these nuclear power plants. The NACAC is developed by the Thailand Institute of Nuclear Technology (TINT). The calculation algorithms in the code are referred to the Offsite Consequence Analysis Code for Atmospheric Release in reactor accidents (OSCAAR), developed by the Japan Atomic Energy Research Institute [9]. The NACAC is performed in three main calculation parts. The one year of meteorological data from NCEP is formatted in the cartesian coordinate grid with a resolution of 0.5 degrees in the meteorological data preparation part. The formatted data is then sent to the atmospheric dispersion calculation part to predict plume advection, activity concentration, and the Total Effective Dose Equivalence (TEDE). Prediction results are presented in polar coordinates, providing convenience in defining the dispersion of radionuclides in the result display part. This program is used to evaluate the transboundary radiation effect from the neighboring countries.

However, the climate change effect may cause changing air pollution patterns. It modifies meteorological parameters, significantly affecting pollutant transportation [11]. Mickley et al. demonstrated that the weakening of air circulation in the period of 1950 to 2052 led to a decrease in the number of cyclones and increased air pollution in the Northeastern and Midwestern United States [12]. Jacob and Winner evaluated changing meteorological data within the 21st century by simulation and found that weakening global circulation caused increasing ozone gas in the summertime of North America, Europe, and Asia [13]. Liu et al. simulated the concentration of PM_{2.5} produced by wildfires in North America between 2041 to 2051. They showed that the climate change effect caused the concentration of PM_{2.5} by wildfire to increase 160% on average [14].

These facts show that changing climate data each year leads to changing air pollution character. One year of meteorological data in the prediction of the NACAC may not be enough to provide comprehensive prediction results, especially the impact

assessment from neighboring countries. Thus, the meteorological data selection and climate change effect on the prediction of the NACAC for the transboundary radiation effect is investigated. The hypothetical severe accident Loss Of Offsite Power (LOOP) and the Large-Break Loss Of Coolant Accident (LBLOCA) at the Fangchenggang nuclear power plant [15] are used as the initial condition.

The NACAC is used as a representative code in the investigation process. It is verified with the JRODOS code that has been validated with the Fukushima nuclear accident [7,16,17]. The verification process is conducted by result comparison. The activity concentration, TEDE, and dispersion characteristic map from both codes are compared to investigate prediction performance for long-range dispersion in the NACAC. Then, the optimum data preparation process is investigated to prepare meteorological input data for transboundary radiation effect evaluation. The prediction result produced by the representative and sequential data selection is compared. One of them providing comprehensive prediction results is demonstrated. The historical meteorological data for five years are then used to analyze variations in meteorological data in a year. The meteorological data for each year is prepared as input data for simulation in the NACAC. The difference in prediction results by each meteorological input dataset is investigated by statistical methods to demonstrate the effect of variations in meteorological data on the prediction result.

1.2 Objective

To study the effects of historical meteorological data set on simulated radioactive dispersion from a nuclear power plant accident by NACAC code

1.3 Scope of study

- Historical meteorological data for five years and hypothetical severe accident Loss Of Offsite Power and Large-Break Loss Of Coolant Accident are the initial conditions for the study.
- Fangchenggang nuclear power plant is a study location.

- Conduct atmospheric dispersion simulation and total effective dose equivalence calculation using Nuclear Accident Consequence Assessment Code (NACAC).
- Verify the Nuclear Accident Consequence Assessment Code (NACAC) calculation using Realtime Online DecisiOn Support system (JRODOS).
- Investigation of Influence of meteorological characteristic changes such as wind pattern rain pattern and atmospheric stability class pattern on simulation result of atmospheric dispersion code such as dispersion characteristic, activity concentration, and total effective dose equivalence.
- Compare dispersion characteristic, activity concentration, and total effective dose equivalence from simulation using meteorological data of a single year and five years.

1.4 Expectation

It can point out the effect of meteorological data set selection on the prediction result of atmospheric dispersion code and demonstrate the effect of variations in meteorological data for five years on atmospheric dispersion code prediction results.

CHAPTER 2

THEORY AND LITERATURE REVIEW

2.1 Nuclear power plant

2.1.1 Fission reaction in nuclear power plant

The fission reaction is the heat source used to generate electricity in nuclear power plants. It is an interaction between thermal neutrons and uranium fuel. The uranium isotope absorbing neutron becomes an unstable nucleus or compound nucleus. Then, the nucleus dissociates into two or three parts called fission products. Meanwhile, this reaction also provides a free neutron and energy of around 200 MeV. Some fission products decay or capture neutrons, causing a new isotope. All isotopes from these phenomena have a mass number from 72 to 161. The main isotopes produced from these phenomena are shown in Table 1[18].

Table 1. Main Radioactive Fission Products[18]

| Active in the short term | | Active in the medium-term | | Active in the long term | |
|--------------------------|---------------|---------------------------|--------------|-------------------------|-----------|
| Fission product | Half-life | Fission product | Half-life | Fission product | Half-life |
| Kr-88 | 2.8 h | Zr-95/Nb-95 | 64 d/35 d | Kr-85 | 10.7 y |
| Sr-91/Y-91m | 9.5 h/0.8 h | Mo-99 | 2.8 d | Sr-90 | 28.6 y |
| Sr-92/Y-92 | 2.7 h/3.7 h | Ru-103 | 39 d | Ru-106 | 1.0 y |
| Y-93 | 10.5 h | Sb-127 | 3.8 d | Ag-110m | 0.7 y |
| Zr-97/Nb-97 | 17 h/1.2 h | I-131 | 8.0 d | Sb-125 | 28 y |
| Ru-105/Rh-105 | 4.4 h/ 35.5 h | Te-131m | 1.2 d | Cs-134 | 2.1 y |
| I-133 | 20.8 h | Te-132/I-132 | 3.2 d/ 2.3 h | Cs-137 | 30.1 y |
| I-134 | 0.9 h | Xe-133 | 5.2 d | Ce-144 | 284 d |
| I-135 | 6.6 h | Xe-133m | 2.2 d | Eu-144 | 8.6 y |
| Xe-135 | 9.1 h | Ba-140/La-140 | 12.8 d/1.7 d | | |

Continuous Table 1.

| Active in the short term | | Active in the medium-term | | Active in the long term | |
|--------------------------|-----------|---------------------------|-----------|-------------------------|-----------|
| Fission product | Half-life | Fission product | Half-life | Fission product | Half-life |
| Ce-143 | 1.4 d | Ce-141 | 32 d | | |
| | | Ce-143 | 1.4 d | | |
| | | Nd-147 | 11.1 d | | |
| | | Np-239 | 2.43 d | | |

2.1.2 Past nuclear severe accident

The nuclear power plant is a thermal power plant that uses a fission reaction of uranium fuel and thermal neutron in the thermal generation process. This reaction provides a lot of heat energy, leading to high electricity production. However, It causes fission products, which are harmful to organisms. Previously, three severe accidents caused leakage of these fission products into the environment.

First is the Three-Mile Island accident. The accident began with the failure of the coolant pump in the secondary coolant loop of the pressurized water reactor. This loss caused the steam generator and the turbine system to lack water and steam, respectively. This abnormality caused the turbine and the reactor trip. Besides, the pump loss increased pressure in the primary loop. Thus, the release valve was opened to decrease the pressure in the system. However, the control valve failure prevented the closing of the valve. This leads to leakage of the coolant in the primary loop, causing a water pump malfunction. The staff decided to stop the pump operation and emergency coolant system. However, this process caused reactor core melt and radionuclide leakage into the environment on March 28, 1979 [19].

The Chernobyl nuclear power plant accident is the second incident that caused leakage of the radionuclide into the environment. On April 26, 1986, operational testing

of the turbine system with the main power supply lost was conducted in the NPP. However, operators with insufficient knowledge ignored to consider the xenon poison effect in the setting experiment. They constantly decreased the power in the NPP until it was too low power. They increased the power by closing the emergency system and withdrawing most control rods. This caused instability in the power system and led to a sharp increase in the fission reaction. They decided to decrease the power by quickly inserting the control rod into the reactor. However, the control rod was designed to have a moderate neutron at the end. This caused a rapidly increased fission reaction. The temperature and pressure in the system subsequently increased. Then, an explosion of pressure vessels and leakage of radionuclides were found [20].

The Fukushima nuclear accident is the third incident that caused leakage of radionuclides into the environment. The 9.0 magnitude earthquake in the Pacific Ocean on March 11, 2011, caused a tsunami wave. The wave hit the NPP, damaging the external power source and electrical generator within the NPP. The lack of electricity stopped the coolant system from working and caused the core to melt in units 1, 2, and 3. The interaction of zirconium in cladding and the hot water caused hydrogen gas. The gas interaction with oxygen led to the exploding and release of the radionuclide into the environment at unit 1, unit 3, and unit 4 of the NPP [21].

2.1.3 General characteristics of severe accidents [22]

A severe accident is an accident that leads to a melting of the reactor core due to the loss of coolant. After a severe accident, the incident can be separated into two phases: in-vessel and ex-vessel. For the in-vessel, the lack of coolant results in the cladding heat and meal subsequently. The gas in the gap between the cladding and the fuel is released into the pressure vessel and contaminates the coolant. The contaminated coolant leaks into the containment and the environment through leaks in the pipeline. For the ex-vessel, the lack of coolant for a long period leads to melting fuel

rods. The core melt destroys the pressure vessel and relocates to the cavity, which is hole concrete for supporting the melted core. However, the reaction between molten corium and concrete can cause the concrete to break in some parts. It results in radionuclides being released into the environment.

2.1.4 Station blackout [23]

The station blackout is an accident that disasters damage the power supply outside the power plant. This situation causes a loss of alternating current in the nuclear power plant, stopping the systems depending on the alternating current and the failure of the reactor subsequently.

The risk assessment analysis in NUREG-1150 [24] showed that the station blackout accident has a frequency of core damage greater than Anticipated Transients Without Scram (ATWS) and Loss Of Coolant Accident (LOCA). Besides, it is also the cause of the Fukushima nuclear accident, leading to the release of radionuclides into the environment.

Many types of disasters cause the station blackout. One of them is an earthquake incident causing two types of station blackouts. First is a short-term station blackout caused by an earthquake of 0.5–1.0 g peak ground acceleration (PGA). This incident results in a sudden loss of the power plant's external power supply and reserve. This causes the coolant system to be lost, leading to core melt at the 3rd hour after the accident. The pressure vessel is then the brake, and the radionuclide is released to containment at the 8th hour. Finally, radionuclides are leaked into the environment at the 25th hour after the accident. This accident has a core damage frequency of 3×10^{-7} per reactor year.

The second type is the long-term station blackout accident. This accident occurs when affected by an earthquake of 0.3 to 0.5 g(PGA). This accident has a higher frequency of occurring than the short-term station blackout, with a core damage

frequency of 3×10^{-6} per reactor year. The long-term station blackout causes the power plant to lose power supply from outside, but the power reserve system still operates. This situation causes the reactor core to melt in the 9th hour after the accident. The radionuclides are released to containment through the release valve of the pressurizer at the 16th hour. Then, they are released into the environment at the 45th hour after the accident.

2.1.5 Loss Of Offsite Power (LOOP) and Large-Break Loss Of coolant Accident (LBLOCA) [25]

An overlay of Loss Of Offsite Power (LOOP) and Large-Break Loss Of coolant Accident (LBLOCA) is an accident designed as more serious accident conditions than expected operational events. This scenario evaluated the radiation effect in the site location selection phase of the Fangchenggang NPP in 2014. The LBLOCA causes a decrease in the cooling water level in the primary coolant loop. Then, the temperature in the reactor core increases, and the reactor core melts. The melted core ruptures the pressure vessels, causing radionuclides to leak into the reactor containment. Meanwhile, the LOOP will cause the safety systems to become unavailable. The loss of safety mitigation results in an increased temperature and pressure in the containment facility, driving radionuclide release into the environment through the ventilation system. The released source term of radionuclide by this scenario with units 1 and 2 core inventories of Fangchenggang NPP is shown in Table 2.

Table 2. Released source term of loss of offsite power accidents (LOOP) and large-break loss of coolant (LBLOCA) [GBq][25]

| Isotopes | 2 hours | 8 hours | 24 hours | 4 days | 30 days |
|----------|----------|----------|----------|----------|-----------|
| Kr-83m | 6.71E+04 | 1.84E+05 | 2.12E+04 | 5.01E+01 | 7.52E-11 |
| Kr-85m | 1.52E+05 | 6.21E+05 | 3.71E+05 | 3.40E+04 | 4.86E-01 |
| Kr-85 | 5.19E+03 | 3.04E+04 | 8.10E+04 | 3.62E+05 | 3.00E+06 |
| Kr-87 | 3.10E+05 | 6.83E+05 | 2.72E+04 | 4.54E+00 | 4.52E-17 |
| Kr-88 | 4.41E+05 | 1.51E+06 | 4.42E+05 | 8.97E+03 | 1.97E-04 |
| Xe-131m | 5.87E+03 | 3.41E+04 | 8.86E+04 | 3.57E+05 | 1.41E+06 |
| Xe-133m | 2.61E+04 | 1.48E+05 | 3.42E+05 | 8.88E+05 | 5.53E+05 |
| Xe-133 | 8.48E+05 | 4.90E+06 | 1.23E+07 | 4.34E+07 | 8.43E+07 |
| Xe-135m | 1.69E+05 | 1.74E+05 | 1.41E-02 | 1.73E-21 | 1.35E-106 |
| Xe-135 | 2.75E+05 | 1.34E+06 | 1.63E+06 | 6.82E+05 | 2.86E+03 |
| Xe-138 | 7.78E+05 | 7.91E+05 | 1.61E-02 | 4.93E-23 | 2.41E-115 |
| I-131 | 8.83E+02 | 1.06E+04 | 3.00E+04 | 1.15E+05 | 3.38E+05 |
| I-132 | 1.27E+03 | 8.48E+03 | 4.55E+03 | 6.85E+01 | 2.57E-08 |
| I-133 | 1.88E+03 | 2.10E+04 | 4.51E+04 | 5.84E+04 | 5.77E+03 |
| I-134 | 2.09E+03 | 8.47E+03 | 3.90E+03 | 3.20E-01 | 5.45E-26 |
| I-135 | 1.76E+03 | 1.68E+04 | 2.07E+04 | 5.00E+03 | 2.63E+00 |
| Cs-134 | 1.90E+02 | 3.23E+03 | 9.54E+03 | 4.26E+04 | 3.50E+05 |
| Cs-136 | 5.47E+01 | 9.25E+02 | 2.68E+03 | 1.09E+04 | 4.57E+04 |
| Cs-137 | 1.11E+02 | 1.89E+03 | 5.58E+03 | 2.50E+04 | 2.07E+05 |
| Cs-138 | 1.34E+03 | 7.06E+03 | 3.05E+03 | 1.38E-03 | 5.30E-44 |
| Rb-88 | 6.98E+02 | 3.22E+03 | 1.57E+03 | 1.74E-08 | 1.51E-81 |
| Rb-89 | 9.21E+02 | 4.18E+03 | 2.08E+03 | 5.89E-10 | 2.10E-94 |

2.2 Meteorological conditions involved in the calculation of atmospheric dispersion.

2.2.1 Atmospheric layer

The air is a mixture of gas consisting of 78.084% nitrogen, 20.948% oxygen, 0.934% argon, and approximately 1% other gases. These gases are attracted by gravity and become a layer of air surrounding the Earth. This air layer is called the atmosphere. The Earth's atmosphere can be classified into four layers according to temperature conversion: the troposphere, stratosphere, mesosphere, and thermosphere [26]. The troposphere is the first layer of the atmosphere, which has a height above the ground layer of around 10 to 18 km. Due to it being located near the ground surface, the density of air in this layer is more than others. The components in this layer consist of carbon dioxide and dust, which can absorb the radiation from the sun in the range of 0.28 to 0.32 microns. The density of these components is inverse with height, resulting in the temperature characteristic in this layer decreasing with height.

The stratosphere is the second layer, with a height above the ground of around 18 to 50 km. The radiation from the sun in the range of 0.2 to 0.3 microns is absorbed in this layer. This layer has three types of temperature characteristics: stable temperature in the range of altitudes 18 to 20 km, slow rise temperature in the range of altitudes 20 to 32 km, and rapid temperature in the range of altitudes 32 to 50 km. The third layer is the mesosphere layer, high from the ground surface in the range of 50 to 80 km. The photodissociation reaction produces ozone gas with a reaction between radiation waves in the range of 0.1 to 0.2 microns and the oxygen in this layer. The temperature characteristic in this layer decreases with high. The last layer is the thermosphere, which is over 80 km above the earth's surface. The sun's radiation, with a wavelength lower than 0.1 microns, interacts with the nitrogen and oxygen atoms by the photoionization reaction, causing ion and free electrons in this layer. The temperature profile in this layer increases with height.

However, the troposphere, which is the atmosphere closest to the ground, has the most significant plume dispersion. This is because the temperature difference between the ground surface and the top of the layer results in the movement of the air both vertically and horizontally, which is a dispersion carrier. The temperature profile of each atmosphere layer is presented in Figure 1.

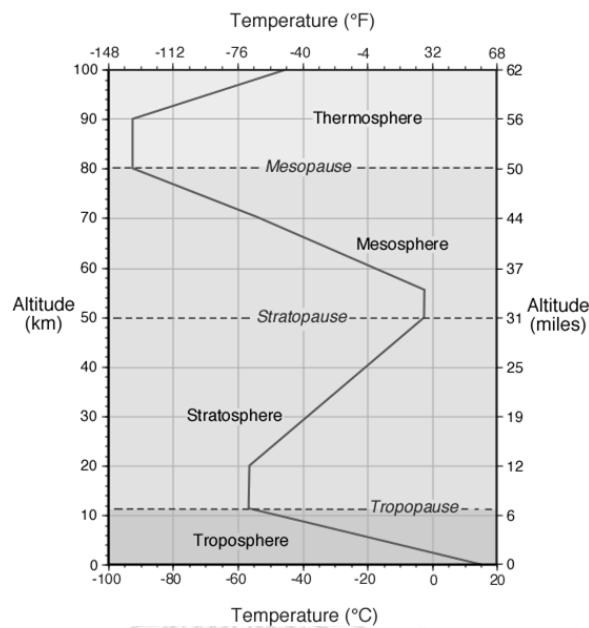


Figure 1. Atmospheric temperature characteristics [26]

2.2.2 Atmospheric circulation

The wind is a natural phenomenon caused by the air masses movement, which transports from the low-temperature area to the high-temperature area [27]. The solar radiation hits the Earth's surface, causing the ground temperature to increase. However, the temperature in each area is not the same. It depends on the density of sunlight. The equator, which is perpendicular to the sun, receives more energy than the north and south poles. This situation causes the equator area to have a temperature higher than the pole area. Air masses with high temperatures in the equatorial region float and move to the polar regions. Meanwhile, low-temperature air masses in the pole sink and move to the equator. However, the Earth's rotation force resulting in this air circulation is divided into three parts: Hadley cell, Ferrel cell, and Polar cell, as shown in Figure 2.

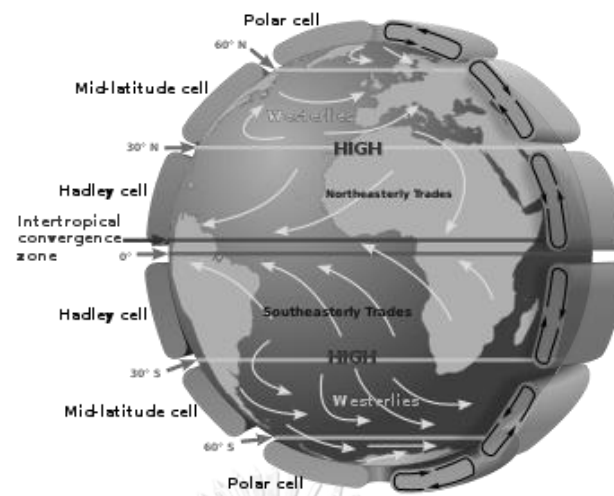


Figure 2. Atmosphere circulation of the Earth [27]

2.2.3 Lanina and Elnino phenomena

Anomalies in atmospheric circulation cause the Elnino and Lanina phenomena, which occur every five years [28]. These phenomena occur from abnormal trade winds, causing unusual rainfall in Southeast Asia. Generally, the trade wind blows from South America's coast to the west of the Pacific Ocean. It carries moisture over the ocean around Indonesia to the atmosphere, causing rainfall in Southeast Asia and northern Australia. The Lanina is a phenomenon in which the trade wind blows too strong. The warm seawater in the Pacific Ocean moves from east to west. When the air rises, it produces many rain clouds, leading to heavy rain in southeast Asia. The Elnino phenomenon is the opposite of the Lanina phenomenon. The wind around Indonesia country blows to the east of the Pacific Ocean and floats around South America's coast. This causes heavy rainfall in South America, and the drought occurs in Southeast Asia. The behavior of these phenomena is shown in Figure 3.

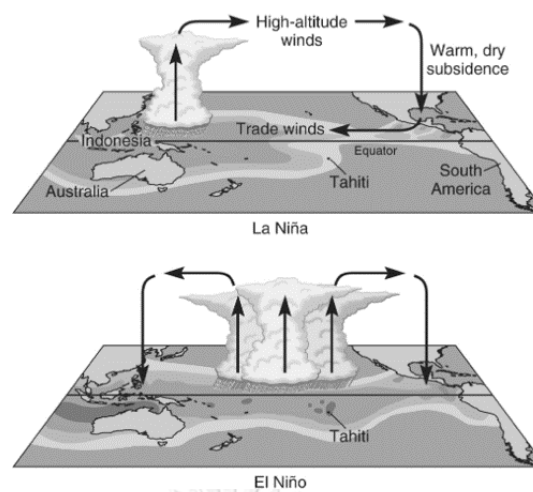


Figure 3. Behavior of Lanina and Elnino phenomena [28]

2.2.4 Monsoon

Monsoon wind is the air mass circulation from the low-temperature area to the high-temperature area between land and ocean [10]. Two types of monsoons affect Thailand. First is the northeast monsoon that occurs from November to April. The solar radiation hits the ocean more than land. The air temperature on the ocean surface increases and floats, while the air on land with low temperature moves to replace. This circulation results in the cold air from Siberia blowing through China into the northeast region of Thailand. Second is the southwest monsoon that occurs from May to October. The air circulation is inverse to the northeast monsoon, in which the air on the ocean with high humidity moves to replace the air on land. This circulation causes rainfall in Thailand.

2.2.5 Air stability

The heat energy accumulated in the ground transfers to the air by convection. This phenomenon increases the air temperature and causes an imbalance between the air and the environment temperature. The temperature difference leads to vertical air movement. The air rises when the air temperature is higher than the ambient temperature, while the air sinks when the air temperature is lower than the ambient temperature. This movement results in temperature inside the air changes in adiabatic

form, classified into two types. The first type is the dry adiabatic lapse rate, which occurs in the air without moisture. When the air rises, the pressure surrounding the air decreases. The energy carried from the ground is used to expand the air volume to balance the pressure. The expansion causes a temperature decrease of 10 Celsius per 1 km. Another type is the saturated adiabatic lapse rate, considering the air with moisture. The water is condensed in the air volume, causing a loss of energy and decreasing temperature to around 5 Celsius per 1 km [29].

Generally, the pattern of air stability can be classified into three patterns according to the adiabatic process evaluated by comparing the environmental lapse rate and the adiabatic lapse rate. The first pattern is unstable. The temperature lapse rate of the environment and air change by altitude. With increasing altitude, the environmental lapse rate is greater than, equal to, and less than the dry adiabatic lapse rate. This causes an unbalanced temperature of air and environment. The plume in this state fluctuates as a looping pattern. The second pattern is stable, contrary to the first pattern. The environment lapse rate is lower than, equal to, and higher than the dry adiabatic lapse rate, causing air to move upwards with equilibrium temperature as the fanning pattern. The third pattern is natural, with an equal environment lapse rate and adiabatic lapse rate. The air in this pattern does not float or sink since the temperature between the air and the environment is balanced. This causes the plume to move along the altitude line as the coning pattern [30]. The plume patterns described before are shown in Figure 4.

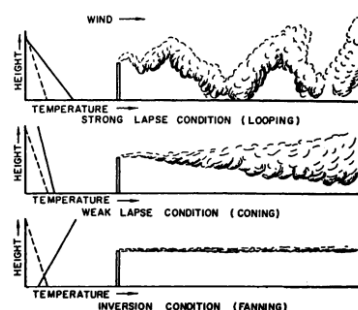


Figure 4. Plume pattern under various conditions of atmospheric stability [30]

2.2.6 Atmospheric stability class classification

The abovementioned demonstrates that the air transportation depends on various factors. The temperature difference between air mass and the environment is the most influence on air movement. Pasquill has classified the atmosphere stability state by considering the relationship between wind speed and solar quantity, which has conditions according to Table 3 and Table 4. The turbulence patterns from classification in this method are separated into seven classes consisting of extremely unstable (A), moderately (B), slightly unstable (C), natural (D), slightly stable (E), moderately stable (F), and strongly stable (G) [31].

Table 3 Conditions for evaluation of solar quantity[32].

| Sky Cover (Opaque or Total) | Solar Elevation Angle > 60° | Solar Elevation Angle < 60° but, > 35° | Solar Elevation Angle < 35° but, > 15° |
|---|--------------------------------|--|--|
| 4/8 or less or, Any amount of High Thin Clouds | Strong | Moderate | Slight |
| 5/8 to 7/8 Middle Clouds | Moderate | Slight | Slight |
| 5/8 to 7/8 Low Clouds | Slight | Slight | Slight |

Table 4 Conditions for atmospheric stability classification[31]

| Surface Wind Measured at 10 m (m / sec) | Day Incoming Solar Radiation | | | Night | |
|---|---------------------------------|----------|--------|-----------------|-----------------|
| | Strong | Moderate | Slight | > 4/8 low cloud | ≤ 4/8 low cloud |
| < 2 | A | A-B | B | F | F |
| 2 - 3 | A-B | B | C | E | F |
| 3 - 5 | B | B-C | C | D | E |
| 5 - 6 | C | C-D | D | D | D |
| 6 | C | D | D | D | D |

Note A: extremely unstable, B: moderately, C: slightly unstable, D: natural, E: slightly stable, F: moderately stable, and G: strongly stable.

2.3 Atmospheric dispersion

2.3.1 Mixing height

An explanation of the atmosphere layer in section 2.2.1 shows that the temperature in the troposphere decreases with height, causing vertical and horizontal radioactive transport. The limited height of changing temperature in this layer is called mixing height. Thus, the mixing height is the maximum height of the radionuclide transport layer [33]. Generally, it can be indicated with the atmospheric stability class, as shown in Table 5.

Table 5 Conditions for mixing height evaluation [33]

| Atmospheric stability class | A | B | C | D | E | F |
|-----------------------------|--------|--------|-------|-------|-------|-------|
| Mixing layer height | 1600 m | 1100 m | 800 m | 560 m | 320 m | 200 m |

2.3.2 Plume rise

The plume released into the environment is influenced by heat within containment. It causes the plume to rise in a vertical direction for Δh . Then, the plume disperse along with the wind in the horizontal direction [33]. The simulation code assumes that the initial position of plume dispersion is effective height, which is the summation of stack height (H) and range of plume rise (Δh), as shown in Figure 5.

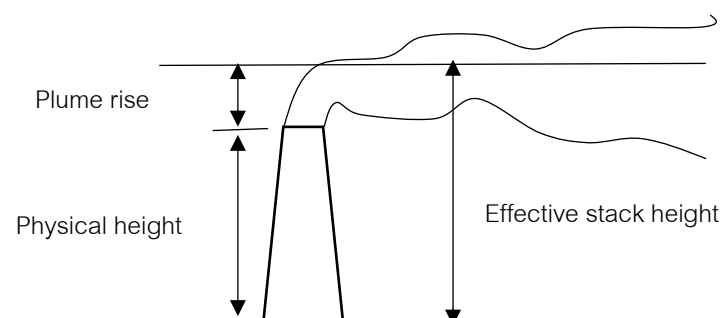


Figure 5 Plume rise characteristic.

2.3.3 Air concentration

Presently, there are many models developed to calculate the concentration of pollution in the atmosphere. One of them is the Gaussian model, which describes a

concentration field from a point source. The model assumes that the dispersion of radionuclides is a normal distribution that occurs both vertically and horizontally at the same time. The air concentration is calculated along with the receptor point located on a horizontal plane. The Gaussian model is rather suitable for a simple distribution situation, which is non-complex terrain. It can provide effective prediction results in short-range transport with constant meteorological conditions. The Gaussian model is developed to be the Gaussian puff model to increase prediction efficiency. The calculations in the puff model are conducted step by step, and each step consists of two parts. The first part is the plume advection calculation, which provides the direction and distance of the plume movement. Another part is the air concentration calculation, carried out with the Gaussian equation, as Equation 1 [34].

$$C_{Ai}(x_r, y_r, z_r) = \frac{Q(i)}{2\pi^{\frac{3}{2}}\sigma(i)_x\sigma(i)_y\sigma(i)_z} \exp \left[-\frac{1}{2} \left[\left[\frac{x(i)_c - x_r}{\sigma(i)_x} \right]^2 + \left[\frac{y(i)_c - y_r}{\sigma(i)_y} \right]^2 + \left[\frac{H - z_r}{\sigma(i)_z} \right]^2 \right] \right] \quad (1)$$

Where $C_{Ai}(x_r, y_r, z_r)$, $x(i)_c$, $y(i)_c$, $\sigma(i)_x$, $\sigma(i)_y$, $\sigma(i)_z$, $Q(i)$, and H represent the air concentration of puff number i at the receptor coordinate x_r, y_r, z_r [Bq/m^3]. The puff center in x and y axis [-], the diffusion coefficient in x, y , and z direction [m], the concentration emission rate in each isotope [Bq/s], and the puff height [m], respectively. The distribution of each step is a puffed pattern that had size according to the dispersion coefficient. This coefficient can be calculated from many methods. One method widely used is the formula from Pasquill's experiment [33], as presented in Equation 2.

$$\sigma_i = p_{i,c} \cdot x^{q_{i,c}} \quad (2)$$

Where x , i , and c represent a distance from the source [m], an index for direction x or y and an index for diffusion category, respectively. Meanwhile, $p_{i,c}$ and $q_{i,c}$ are empirical constants.

2.3.4 Deposition and depletion

Two main phenomena reduce the radionuclides in the atmosphere. The first phenomenon is decay. The unstable radionuclides emit radiation and go back to a steady state. The activity of these radionuclides is decreased as an exponential form according to the half-life of each isotope. The second phenomenon is the deposition consisting of dry deposition and wet deposition [34]. As for dry deposition, the gravity force, wind turbulence, and particle sedimentation process lead to radionuclide deposition to the ground. The dry deposition rate is called deposition velocity, which is the ratio between the time-integrated air concentration and ground concentration. The deposition velocity of noble gasses, particles, and reactive vapors has values around 0, 1×10^{-3} , and 1×10^{-2} , respectively. The wet deposition is the leaching of radioactive material from the atmosphere to the ground by precipitation. The radionuclide accumulated on the ground is calculated ground concentration by Equation 3.

$$C_{Gi}(x_r, y_r, z_r) = \frac{C_{Ai}(x_r, y_r, z_r) \cdot (V_d + V_w) \cdot (1 - e^{-\lambda_E \cdot T_b})}{\lambda_E} \quad (3)$$

Where $C_{Gi}(x_r, y_r, z_r)$ represents the ground concentration of isotope i at receptor coordinate x_r, y_r, z_r [Bq/m^2], V_d and V_w are dry and wet deposition coefficient [m/s], λ_E is the effective decay constant, which is the summation of the decay constant of isotope and natural decay in soil [s^{-1}]. T_b is the duration of the radionuclide discharge [s].

2.3.5 Resuspension

The radionuclide deposition from the atmosphere to the ground can disperse to the air again by wind, traffic, or agricultural activities. This process is called resuspension. The dose is calculated from this phenomenon, considering inhalation. However, the dose from this phenomenon is relatively low compared to other groups [33]. Thus, this research does not consider the resuspension effect.

2.4 Dose estimation and emergency planning

The radionuclides contaminated in the environment are calculated with a two-part dose [33]. The first is the external dose, which considers cloud shine and ground shine radiation. The calculation in this method does not consider the effect of alpha radiation because it has a low penetrating ability. Meanwhile, the effect of beta radiation is considered only skin. The formula for the external calculation method is presented as Equation 4. Another part is the internal dose, which takes into account the effects of internal radioactivity from ingestion and inhalation. However, the dose calculation from ingestion required various information that is difficult to prepare, such as the consumption rate in each age and each food type. Thus, this research considers only the internal dose with inhalation, calculated by Equation 5. The total effective dose is the summation value of Equations 4 and 5 [34].

$$E_{ex} = ((C_{Ai} \cdot DF_{cl}) + (C_{Gi} \cdot DF_{gr})) \cdot O_f \quad (4)$$

$$E_{in} = C_{Ai} \cdot R_{ih} \cdot DF_{ih} \quad (5)$$

Where E_{in} is the internal dose from inhalation [Sv], R_{ih} is inhalation rate [m^3/s], DF_{ih} is inhalation dose coefficient [Sv/Bq], E_{ex} is the summation of external dose from cloud shine and ground effect [Sv]. DF_{cl} and DF_{gr} are dose conversion factor of cloud shine [$Sv \text{ per } Bq^3/m$] and ground shine [$Sv \text{ per } Bq^2/m$]. O_f is the factor of the group member who receives the radionuclide effect.

2.4.1 Dose limit

The International Commission on Radiological Protection (ICRP) is an independent and international organization. They recommend the radiation exposure limit for occupational workers and public people to ensure that no person is exposed to excessive radiation in normal, as shown in Table 6.

The effect of receiving a radiation dose can be separated into two parts: deterministic and stochastic. The deterministic effect causes malfunction of the system

of internal organs when radiation exposure exceeds the limit of individual organs. The body anomalies according to radiation exposure levels are shown in Table 7. The stochastic effect is a health effect from receiving low exposure over a long period. This situation leads to cancer and genetic disorders [35].

2.4.2 Emergency planning

The above-mentioned demonstrates that severe accidents at nuclear power plants can lead to the release of radionuclides into the atmosphere. They can transport along with the wind and deposit to the ground by wet and dry deposition. The contamination of these radionuclides in the environment can affect humans, both internal and external exposure. Radiation exposure causes deterministic and stochastic effects. The emergency plan is a necessary thing that helps manage and decrease this risk. The main strategies used in a nuclear accident consist of nine strategies.

The first is evacuation. It is the evacuation of people from the area expected to be a high risk before the risk arrives. The second is sheltering, which uses a suitable barrier to protect or decrease the radiation effect. The third is respiratory protection, which uses significant material to protect radiation effects by inhalation, such as facemasks, towels, or cloth. Remove the contaminated material from people, such as washing or removing any contaminated clothing. Relocation is moving people to new areas with low radiation concentrations. The potassium iodide (KI) blockage or taking stable iodine is one of the strategies for decreasing radiation of unstable iodine in the thyroid gland. Decontamination of the city and protecting the food chain decreases the radionuclide effect over a long period. Finally, medical treatment reduces the risk to the sufferer [33]. The International Atomic Energy Agency (IAEA) has recommended protective action to reduce the stochastic effect risk [36], as shown in Table 8.

Meanwhile, ICRP has recommended the framework to decrease the risk of radiation exposure in an emergency [35]. The risk level or the reference level is defined into three parts according to radiation exposure. The first part is that the incident causes

the individual to be exposed to radiation less than or equal to 1 mSv. The sufferer should receive general information about the exposure level, and the occupational worker should investigate the exposure pathway. The second part is that the incident causes the individual to be exposed to more than 1 mSv to 20 mSv radiation. Radiation assessment and dose reduction are performed on the patient. The constraints for the occupational worker are defined in the emergency plant. The last part is the incident leading to radiation exposure of more than 20 mSv to 100 mSv in individuals. The radiation dose reduction in the environment is conducted. The risk information should be presented to the public. Radiation assessment and dose reduction are performed on the patient.

Table 6 Recommended dose limits in planned exposure situations[35]

| Application | Recommended dose limits | |
|------------------------|--|-----------------|
| | Occupational | Public |
| Effective dose | 20 mSv per year averaged over 5 years. | 1 mSv in a year |
| Annual equivalent dose | | |
| - The lens of the eye | 150 mSv | 15 mSv |
| - The skin | 500 mSv | 50 mSv |
| - The hand and feet | 500 mSv | 50 mSv |

Table 7 Deterministic effects [37]

| List | Exposure dose | | | | |
|---------------------------|-------------------------|---|---------------------|--|---|
| | 1 – 2 Sv | 2 – 6 Sv | 6 – 10 Sv | 10 – 50 Sv | More than 50 Sv |
| vomit | 1 Sv : 5% 2 Sv : 50% | 3 Sv : 100% | 100% | 100% | 100% |
| Damaged organ system | Hematopoietic system | | | Digestive system | Central nervous system |
| symptom | Low white blood cells | Bleeding will not stop, easily contracted, and hair loss. | | Diarrhea, fever, loss of electrolyte balance | Convulsions, tremors, uncontrollable muscles, unconsciousness |
| Time for symptoms | - | 4 to 6 weeks | 5 to 14 weeks | 1 to 48 hours | |
| Period returned to normal | Several weeks | 1 to 12 months | More than 12 months | - | - |
| Cause of death | - | Bleeding does not stop | Infectious diseases | The circulatory system stops working. | The respiratory system does not work, water retention in the brain. |

Table 8 Responed actions in emergency situations to reduce risks [36].

| Generic criteria | | Examples of protective actions |
|--|---|---|
| The criteria for urgent protective actions | | |
| - H (thyroid) | 50 mSv in the first 7 days | Iodine thyroid blocking |
| - E | 100 mSv in the first 7 days | Sheltering; evacuation; contamination control; public reassurance; decontamination; restriction |
| - H (Fetus) | 100 mSv in the first 7 days | of the consumption of food, milk, and water |
| The criteria for taking protective actions and other response actions early in the response | | |
| - E | 100 mSv per annum | Temporary relocation; public reassurance; decontamination; replacement of food, milk, and |
| - H (Fetus) | 100 mSv for the full period of in utero development | water |
| The criteria for taking medical actions to detect and treat radiation-induced health effects | | |
| - E | 100 mSv in a month | Screening, according to doses equivalent to specific radiation-sensitive organs. |
| - H (Fetus) | 100 mSv for the full period of in utero development | Counseling to allow informed decisions to be made in individual circumstances |

Equivalent dose in an organ (HT) or tissue (T); Effective dose (E).

2.5 Radiological consequence evaluations

The examination of all factors impacted by an accident or environmental radioactive material release is known as the radiological consequence evaluation. It can usually be divided into two types: the consequence evaluation by measured data and predicted results.

2.5.1 Evaluation by measured data

Beta and gamma radiation detected by on-site radiation detectors are used to assess radiation doses, determine population hazards, and take appropriate precautions [38]. Generally, results from this kind of evaluation are relatively accurate. However, It is limited in determining the radiation impact in an area where measurement data cannot be accessed. In addition, this process cannot be used to assess radiation effects by a hypothetical accident.

2.5.2 Evaluation by predicted results

This process evaluated the radiation effects by considering the prediction results of a simulation code performed with the chemical and physical transformation. The boundary and initial conditions used in the prediction process are based on actual events in the past, such as the release period, release source term, and meteorological data. Generally, this process is performed with measurement data to evaluate the radiation effects in regions where measurements cannot be accessed. In addition, it is used in examining the potential radiation effects of hypothetical nuclear accidents. Generally, the evaluation by prediction results can be categorized into two types by considering the assessment boundary. The first type is inside boundary evaluation monitoring radiation effects around power plant location [39-41]. Adverse meteorological conditions and worst-case scenarios are generally considered in this method to provide

conservative prediction results [42]. The second type is outside boundary evaluation monitoring transboundary radiation effects from neighboring countries [7,8,43]. However, It has no clear requirements or recommendations in the assessment process. It is generally conducted with worst-case scenarios and considers the release characteristics. This is because the release characteristics are related to meteorological data that significantly impact concentration calculations [44-46].

2.6 Atmospheric dispersion code

The atmospheric dispersion code is a computational code designed to investigate radionuclide transportation and health effects. Most atmospheric dispersion codes have a similar calculation process consisting of three main parts: pre-processing process, atmospheric dispersion calculation process, and report data process, as presented in Figure 6.

The pre-processing process is input data preparation before being sent to the dispersion calculation process. The input data commonly applies in the code consisting of meteorological data and release source term data [47]. The release source term data is the activity concentration of a radionuclide released from the nuclear power plant system into the environment. Two patterns of release source term data are commonly used in radiation consequence assessment. First is the actual release data measured from real incidents in the past, such as the Chernobyl nuclear accident [48], the Fukushima nuclear accident [49], and the wildland fires in Chernobyl [50]. Second is the predicted release data evaluated from the simulation code. The radionuclide behavior within the containment building is initially predicted. The amount of radionuclides leaking into the environment is then calculated. [39,51].

Meteorological data is weather data from observation or evaluation by a meteorological provider. It is applied in the atmospheric dispersion code to evaluate the

transportation behavior of radionuclides in the atmosphere. The meteorological parameters imported in each code depend on the calculation design. Generally, the code performs with atmospheric stability class, wind, and rain data defining atmospheric suitability, speed and direction of dispersion, and deposition, respectively.

The release source term and meteorological data are used in the atmospheric dispersion calculation process to predict the radionuclide dispersion by the dispersion model. The dispersion model in the codes is commonly one of the following three models. Firstly, the Gaussian plume model calculates radionuclide dispersion under a single release point with constant meteorological data conditions [52]. Secondly, the Puff model calculates dispersion, assuming that the plume dispersed from the trajectory line changed according to weather conditions [53,54]. Thirdly, the Lagrangian dispersion model calculates distribution by assuming that a radionuclide is a particle pattern that diffuses through an atmospheric flow [55].

These models use mathematical equations to predict radionuclide transportation in the atmosphere, considering downwind and atmospheric turbulence. Removing radionuclide phenomena, such as radioactive decay and wet and dry deposition, are considered in calculating air and ground concentration at an interesting location. All radiation effects from the contaminated environment are then used to calculate internal and external doses [56]. The calculated results from the atmospheric dispersion calculation process are sent to the reporting process to demonstrate the consequent evaluation results. A display pattern commonly applied in the codes consists of the statistics graphs, the tabulated results, and the graphical results.

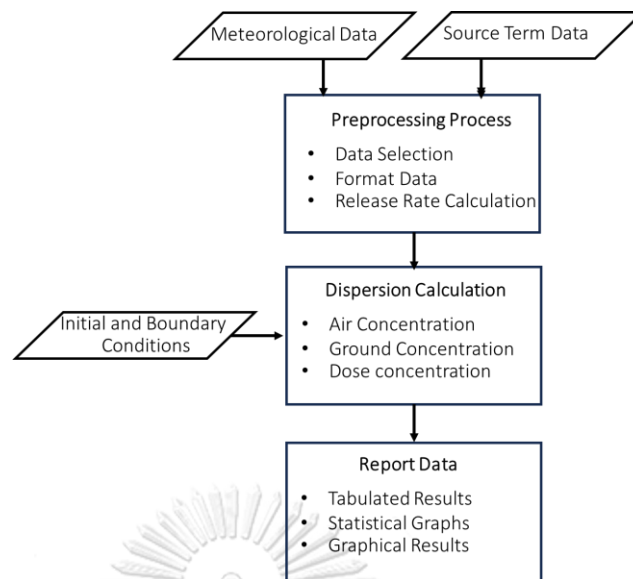


Figure 6 General calculation process in the atmospheric dispersion code[1].

2.6.1 Nuclear accident consequence analysis code (NACAC)

NACAC is a program that has been used in this research. It is the atmospheric dispersion model developed by the Thailand Institute of Nuclear Technology (TINT). The program referred to the OSCAAR code algorithm developed by the Japan atomic energy agency (JAEA) and verified with JAEA projects [57,58]. The algorithms in the NACAC are designed to allow evaluation of the radiation covering the Asian region. There are two layers of the computational grid in NACAC. The first is the meteorological data grid designed as a cartesian coordinate according to the National Center for Environmental Protection data (NCEP) format. The second is the concentration calculation grid designed as a polar coordinate with 400 calculation receptors located at 25 radii and 16 directions. The calculation process in the NACAC consists of three parts: the data preparation, atmospheric dispersion calculation, and the result display.

As for data preparation, the source term data is used to calculate the release rate, defined as a step according to the puff form as Equation 6. Meanwhile, the meteorological data from the NCEP is prepared in the meteorological data grid with a $55.5 \times 55.5 \text{ km}^2$ resolution. There are three main meteorological parameters used in the

NACAC. Firstly, the atmospheric stability class data is used to define atmospheric turbulence. Secondly, the wind data is used for the radionuclide transportation evaluation. Thirdly, the rain data is used for radionuclide depletion evaluation. The atmospheric stability class and rain data are prepared at the surface layer (10 m). Meanwhile, the wind data is prepared with ten layers consisting of surface wind (10 m), 1,000, 975, 950, 925, 900, 850, 800, 750, and 700 hPa, respectively.

$$QR = \frac{QT}{TS \cdot PF_i} \quad (6)$$

Where QR is the activity release in each step of the isotope i [Bq/h], QT is the total release activity [Bq], TS is the total simulation time [h], and PF_i is the size particle fraction of the isotope i .

As for atmospheric dispersion calculation, the meteorological and source term data from the previous section are used in the Gaussian puff model to calculate dispersion, depletion, and concentration with 16 parameters, as shown in Figure 7. In the dispersion calculation part, the atmospheric stability class is used to evaluate the diffusion coefficient in horizontal (σ_y) and vertical (σ_z) directions by the Pasquill-Grifford method.

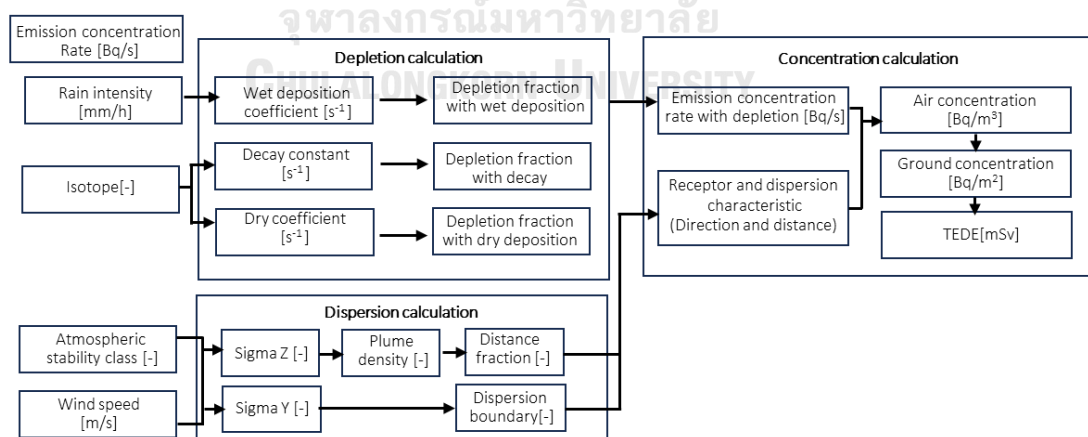


Figure 7 Calculation flow chart in atmospheric dispersion calculation part

The dispersion coefficient in vertical directions is used to calculate the plume density fraction in each wind layer. The wind data in each layer is then weighed by the

plume density and averaged to calculate the average wind component in X and Y directions, as shown in Equation 7. The effective vector of the averaged wind component is multiplied with advection time to determine the plume dispersion distance and direction in each calculation step on the meteorological data grid. Then, the dispersion coefficient in the horizontal direction is used to calculate the dispersion boundary fraction in each advection step to select the calculation receptor, as in Equation 8.

$$W_{AV} = \frac{\sum_{i=1}^{10} h_i \cdot w \cdot e^{-0.5\left(\frac{h_i-h_E}{\sigma_z}\right)^2}}{\sum_{i=1}^{10} h_i \cdot e^{-0.5\left(\frac{h_i-h_E}{\sigma_z}\right)^2}} \quad (7)$$

$$Db = 5 \cdot \sigma_y \quad (8)$$

Where W_{AV} , w , h_i , h_E , Db , σ_z , and σ_y are the average wind component [m/s], wind components in the x or y directions [m/s], geographical heights at layer i [m], effective release height [m], dispersion boundary fraction [-], the diffusion coefficient in z and y direction [-], respectively.

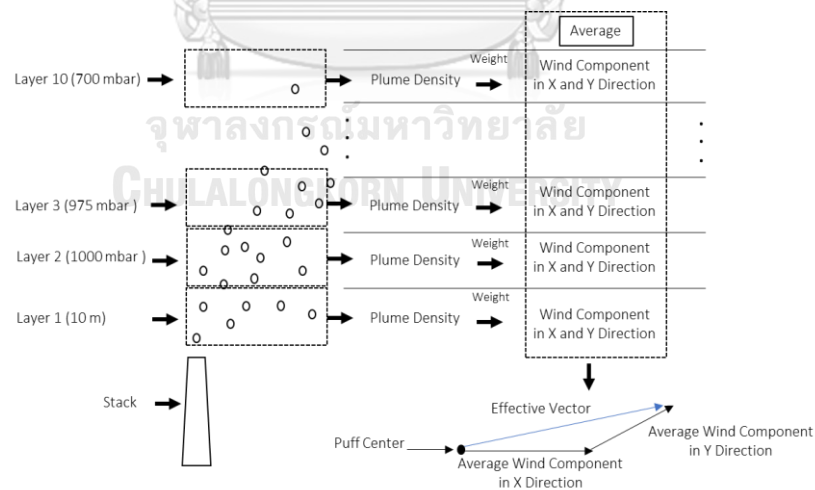


Figure 8 Advection calculation pattern of the NACAC [59]

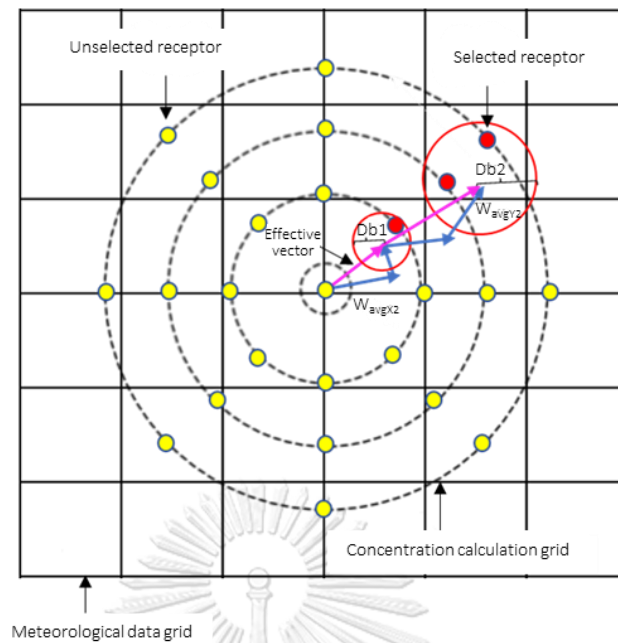


Figure 9 Receptor selection in NACAC

In the depletion calculation part, the decay, wet, and dry deposition phenomena are taken into account in this part. All phenomena cause decreasing the emission concentration in exponential form as Equation 9. The decay depends on the half-life of radionuclides. The dry deposition depends on the dry depletion coefficient and considering radionuclide distribution from puff center to ground as Equation 10. The wet deposition depends on the wet depletion coefficient evaluated by a wash coefficient and average rain within the dispersion boundary, as Equation 11. Depletion of all phenomena is considered according to advection time in each calculation step.

$$Q_d(i) = Q(i) \cdot e^{-(\lambda_i + Wd + Dd) \cdot t} \quad (9)$$

$$Dd = \frac{Dv}{\sigma_z \cdot \sqrt{2\pi}} \cdot e^{-\frac{(H-h_g)^2}{2 \cdot \sigma_z^2}} \quad (10)$$

$$Wd = W_{c1} \cdot \bar{R}^{W_{c2}} \quad (11)$$

$$t = \frac{T \cdot \sigma_y}{S} \quad (12)$$

Where i , $Q_d(i)$, $Q(i)$, λ_i , Wd , Dd , t , T , Dv , σ_y , σ_z , H , h_g , \bar{R} , S , $e^{-(\lambda_i+Wd+Dd)t}$ and W_{c1} or W_{c2} present radionuclide isotope i [-], emission concentration rate with depletion [Bq/s], emission concentration rate [Bq/s], decay constant [s^{-1}], wet depletion coefficient [s^{-1}], dry depletion coefficient [s^{-1}], sub advection time [s], advection time [s], dry deposition velocity [m/s], diffusion coefficient in horizontal and vertical direction [-], the puff height [m], ground height [m], average rain [mm/h], advection distance fraction [-], sum depletion faction [-], and wash coefficient [-], respectively.

In the concentration calculation part, the emission concentration rate with depletion is used to calculate the air concentration at the selected receptors by Equation 1 in section 2.3.3. These calculation patterns continue until the end of the simulation time, causing the plume trajectory, as shown in Fig. 10. Meanwhile, the ground concentration is calculated by multiplying the air concentration in each receptor with the deposition coefficient considered wet and dry deposition phenomena as Equation 3 in section 2.3.4.

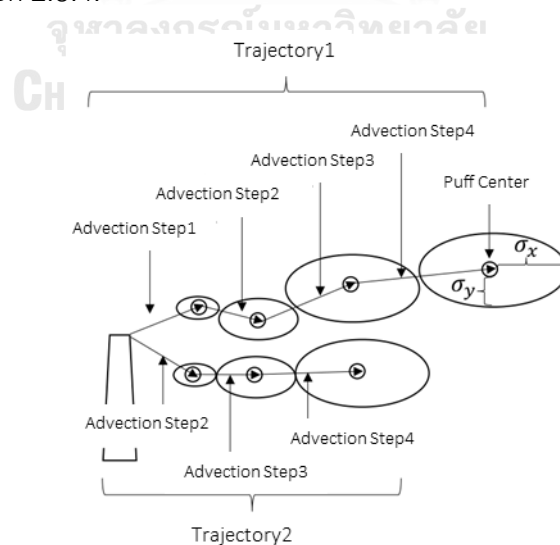


Figure 10 Trajectory characteristics in the NACAC [60].

The external and internal dose calculation processes in the NACAC are determined as in NUREG/CR-0494 and NUREG/CR-4214, respectively [61,62]. The internal dose considers the effect of the radionuclide brought into the body by breathing. Thus, the inhalation rate and the air concentration are used in the calculation process by multiplying the inhalation dose coefficient, as shown in Equation. 4 in section 2.4. Meanwhile, the external dose considers the effect of gamma and beta rays from ground and cloud shine phenomena, calculated as Equation 5 in section 2.4.

As for the result display, the calculated results are shown in polar coordinates according to the concentration calculation grid, providing convenience in defining the dispersion of radioactive materials.

2.6.2 Java-based Realtime Online DecisiOn Support system (JRODOS)

The JRODOS code is the program for offsite emergency management evaluation covering both local, regional, and national levels. The code is developed by the Karlsruhe Institute of Technology in Germany [63]. It is a well-known code widely used for radiological emergency response [64]. Previously, the prediction performance of JRODOS was investigated by comparing predicted results with measurement data from the Fukushima nuclear accident in several studies.

Leung, Ma [7] investigated the capability of the JRODOS code by estimating the radiation effect from the Fukushima nuclear accident. The release source conditions of Cs-137 in the period from March 12 to April 5, 2011, were considered. The JRODOS calculates the dispersion and deposition of the radionuclide with forecast meteorological data from the German Weather Service (DWD). Measurement data from the United States Department of Energy (DOE) and the Ministry of Education, Culture, Sports, Science and Technology (MEXT) of Japan are used as reference values for the verification process. It noted that the predicted result from JRODOS agrees well with measurement data. The same order of magnitude of ground concentration is found.

However, slight differences in dispersion characteristics are noted by the effect of the forecast meteorological data.

Dvorzhak, Puras [16] estimated the radiation effect from the Fukushima nuclear accident in the period March 12 to 24, 2011 by the JRODOS code. The released source term data is evaluated by RASCAL code according to the status and accident information of the Fukushima nuclear accident. The forecast meteorological data from the European Centre for Medium-Range Weather Forecasts (ECMWF) is considered. Comparing predicted results with measurement data of Cs-137 from Tokyo Electric Power Company (TEPCO) at Ibaraki, Yamagata, and Tochigi provinces are performed. It was found that JRODOS can provide a ground concentration of Cs-137 lower than measurement data in all locations by effect discrepancies in the released source term. However, the predicted result and measurement are in the same order of magnitude in almost all positions.

Landman, Päsler-Sauer [17] recalculated the dispersion of Cs-137 from the Fukushima nuclear accident in the period March 12 to 26, 2011 by the JRODOS code. The calculation is performed with source terms from the German Gesellschaft für ReaktorsicherheitFootnote5 (GRS) installed in JRODOS and has released concentration close to measurement data. Meteorological data from Weather Research & Forecasting Model (WRF) is used. A Predicted result is compared with measurement data from published information by United States and Japanese institutions. It noted that JRODOS can provide dispersion characteristics correlated with the published information. The maximum concentration of ground concentration agrees well with measurement data. However, the overestimate with the extension of the impact area is found by the effect of variation in forecast meteorological data.

Generally, the JRODOS provides reasonably agreed predicted results with measurement data with similar dispersion characteristics. However, there are limitations

in observing actual data throughout the accident period. These limitations cause released source terms and meteorological data by estimation to be used in the evaluation process, leading to some variation in the JRODOS predicted result and measurement data.

The JRODOS code is a program used in the NACAC verification process. The code uses three data sets for atmospheric dispersion calculation: source term data, meteorological data, and terrain data. In the beginning, the source term data is used to calculate the release rate, while the meteorological data is sent to the meteorological preprocess to prepare data for the atmospheric dispersion calculation. In this process, all meteorological data are taken to the computational grids with various resolutions in five domains consisting of 2 x 2, 4 x 4, 8 x 8, 16 x 16, and 32 x 32 km² recommended in the JRODOS [65]. Wind data and terrain data are used to analyze wind turbulence. This results in the wind characteristic changes according to the topography. The high roughness area has complex wind directions and low wind speed, while the low roughness area has strong wind and single directions. The atmospheric stability class is evaluated by one of the following methods depending on data available at each grid position. Wind surface and net radiation data are first used for the evaluation if available. If the net radiation data is not available, the stability class will be evaluated from the temperature lapse rate and surface wind. Finally, if the temperature lapse rate is not available, the Pasquill-Gifford method will be used to evaluate the atmospheric stability class [66]. Then, the processed data are sent to the atmospheric dispersion module to calculate dispersion characteristics and activity concentrations. There are three different dispersion models in JRODOS: the puff model, the particle model, and the long-range model. The puff model called RIMPUFF, mostly similar to NACAC, is used in the verification process.

The RIMPUFF model considers the 3D wind data in calculating plume advection [67], as shown in Figure 11. The wind data is imported from the meteorological data file and instated at the reference heights designed in the JRODOS code. Meanwhile, the wind data in the gaps between the reference heights are calculated by three interpolation processes. The logarithmic interpolation is performed when the plume is located inside the surface layer. The power-law interpolation is conducted when the plume is located between the surface layer and the mixing height. Finally, linear interpolation is used when the plume is above the mixing height [66]. The effective vector at the puff position is calculated to define the dispersion distance and direction in each calculation step. The Gaussian equation is used to calculate air concentration in the atmosphere. Meanwhile, ground concentration is calculated based on the deposition coefficient varying with the type of isotopes. The JRODOS calculates dose values by the dose model and terrestrial food chain considering four radiation effects: ingestion effect, inhalation effect, cloud effect, and ground shine effect. The dose conversion coefficient used in the dose calculation process refers to the internal dosimetry program PLEIADES, the National Radiation Protection Board (NRPB), and GSF-12/90 report. All prediction results in the JRODOS is calculated and displayed on cartesian coordinate with five-domain grid resolution.

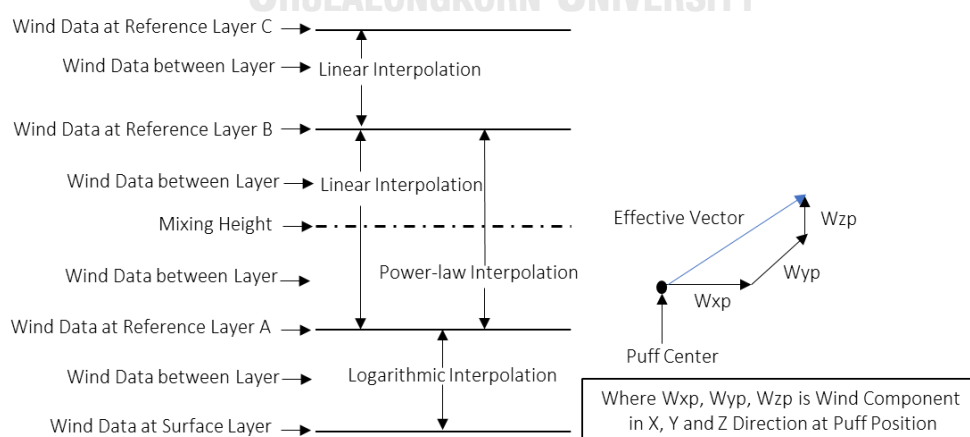


Figure 11 Advection calculation pattern of the JRODOS [66]

2.6.3 Differences between the NACAC and JRODOS

As mentioned above, it is noted that the NACAC and JRODOS codes have different and similar parts. They have the same calculation pattern. Firstly, the meteorological data is prepared in the pre-processing process. Then, the processed data are sent to the atmospheric dispersion model to calculate activity concentration and dose. Finally, all results are sent to the display part to demonstrate the predicted results. However, both codes also have different calculation details in each process.

As for the pre-preparation process, NACAC used the Pasquill-Grofford method [31] and ignored terrain data to evaluate the atmospheric stability class and generate wind field, respectively. In addition, all meteorological data in NACAC are prepared in a single domain resolution grid of $55.5 \times 55.5 \text{ km}^2$. In comparison, the JRODOS used three methods to evaluate atmospheric stability class and generate wind field by considering the terrain data. Preparing meteorological data in the JRODOS is performed with five domains resolution grid of $2 \times 2 \text{ km}^2$, $4 \times 4 \text{ km}^2$, $8 \times 8 \text{ km}^2$, $16 \times 16 \text{ km}^2$, and $32 \times 32 \text{ km}^2$, respectively.

As for the atmospheric dispersion calculation, the two codes use different advection calculation models. The NACAC determines plume advection by a 2D effective vector. The average wind data according to plume density in each wind layer are used in the calculation process. In comparison, the JRODOS defines plume advection by considering a 3D vector of wind data at the puff center. In addition, both codes also have different schemes for calculating activity concentration and dose. Although both codes calculate air concentration by the Gaussian equation, JRODOS calculates ground concentration by wet deposition coefficient higher than NACAC, around 1.25-fold. Besides, the information used in the dose calculation of both codes is different. The NACAC refers to information on NUREG/CR-4214 and NUREG/CR-0494, while JRODOS refers to information on the NRPB internal dosimetry program PLEIADES and GSF-12/90 report.

As for the result display, the NACAC shows all predicted results on a polar coordinate map, while the JRODOS shows them on a Cartesian coordinate map. Details of differences between NACAC and JRODOS are summarized in Table 9.

Table 9 Differences between the NACAC and JRODOS[2].

| List | NACAC | JRODOS |
|---|---|---|
| Data preparation system | | |
| Wind field evaluation | Ignore terrain effect | Consider terrain effect |
| Atmospheric stability class evaluation | Pasquill-Gifford method | Evaluate by one of three methods: - Wind surface and net radiation - Temperature lapse rate and surface wind - Pasquill-Gifford method |
| Meteorological data preparation grid resolution | Single domain with a resolution of 55.5 x 55.5 km ² | Five domains with different resolutions: 2 x 2 km ² , 4 x 4 km ² , 8 x 8 km ² , 16 x 16 km ² , and 32 x 32 km ² |
| Atmospheric dispersion model | | |
| Advection calculation | Use a 2D effective vector of averaged wind data proportional to the plume density. | Use 3D effective vector of wind data at plume position. |
| Concentration calculation | Calculated on a polar grid | Calculated on a Cartesian grid |
| Deposition coefficient | | |
| - Aerosol (I is precipitation rate) | Dry deposition 0.001 [m/s] Wet deposition $1 \times 10^{-4} I^{0.8}$ [s ⁻¹] | Dry deposition 0.001 [m/s] Wet deposition $8 \times 10^{-5} I^{0.8}$ [s ⁻¹] |
| - Iodine organic (I is precipitation rate) | Dry deposition 0.0005 [m/s] Wet deposition $1 \times 10^{-6} I^{0.8}$ [s ⁻¹] | Dry deposition 0.001 [m/s] Wet deposition $8 \times 10^{-8} I^{0.8}$ [s ⁻¹] |
| Information for dose calculation | NUREG/CR-0494 NUREG/CR-4214 | The NRPB internal dosimetry program PLEIADES Report GSF-12/90 |
| Result display | | |
| Concentration map | Polar coordinate map | Cartesian coordinate map |

2.7 Meteorological data selections

Evaluating radiation consequences requires carefully selecting meteorological data because meteorological data vary with time, causing various computed results. Thus, defining simulation time relating to meteorological data is important. The meteorological data selection is a process designed to prepare meteorological data before being sent to a consequence evaluation process. It is generally used to define a format and time for simulation. Three types of meteorological selection processes are widely applied, consisting of sequential, extreme, and representative data selection [68].

2.7.1 Sequential data selection

Sequential data selection or cyclic sampling is the selection of meteorological data in sequence with the same interval, as shown in Figure 12. Each sequence includes the meteorological parameters required for evaluating the consequences according to the evaluation period. This process typically applies with a year of meteorological data to provide comprehensive assessment results [69-71]. The 8,760 meteorological sequences are prepared as input data for a simulation process. Then, a percentile or average of all prediction results is used as a representative value for evaluating radiation consequences. This process provides a comprehensive prediction result. However, it requires a large computational resource.

2.7.2 Extreme data selection

Extreme data selection is the selection of meteorological data with extreme or adverse situations. In general, the extreme situation is considered with the highest severity of meteorological parameters or weather characteristics that greatly affect the area of interest. For example, Kaviani, Memarian [72] select a high rainfall period to evaluate domestic radiation consequences from Bushehr NPP in Iran with the

hypothetical severe accident. Extreme data selection is generally used to produce a conservative result in the evaluation process. However, some overestimated predicted results may be found with a low occurrence rate of extreme conditions [73].

2.7.3 Representative data selection

Representative data selection or stratified meteorological sampling is designed to improve efficiency in evaluating the radiation effect with low computational resource situations [74]. This process generates an input dataset covering all meteorological conditions by selecting representatives of all meteorological characteristics. As a result, the simulation is performed with a low simulation case. However, it also provides quite comprehensive prediction results for all phenomena.

Previously, this process was frequently utilized to assess the radiation effects surrounding NPPs [75-77]. Generally, this process is performed by grouping time with similar weather characteristics and then selecting the representative time of each group to generate a new dataset, as shown in Figure 13 [74,78]. There are three steps performed in the representative data selection: data preparation, data classification, and representative selection.

The data preparation step is a process for collecting meteorological parameters. There are four parameters widely used in this step. Firstly, rain intensity plays an important role in defining the deposition potential of radionuclides. Secondly, the atmospheric stability class demonstrates the atmospheric conditions for dispersion. Thirdly, wind direction indicates the pathway or direction of plume movement. Fourthly, the wind speed or the travel time shows the speed of plume movement. These hourly meteorological parameters are collected by average or summation in an area covering a study site to confirm that the collected meteorological data influence prediction results in the area of interest.

The data classification step categorizes the corrected meteorological data into several groups by considering the characteristics and severity level of the meteorological data. Generally, the collected data is separated into a wet and dry group or a high and low rain level group [77-79]. The low rain group data is classified by the parameters influencing a plume movement, such as wind speed, travel time, and atmospheric stability class [77,80]. However, travel time and wind speed have the same property in the dispersion investigation. Thus, one of them is performed in the classification process. As for the high rain group, most of the data in this group cause radionuclide deposition by wet deposition phenomena. Hence, the classification in this group ignores the parameters influencing a plume movement. Finally, wind direction is used in the classification of all subgroups to categorize meteorological characteristics at each time.

The representative selection step selects representative data in each subgroup by a random function with the appropriate selection rate. All selected data are generated as input data for simulations.

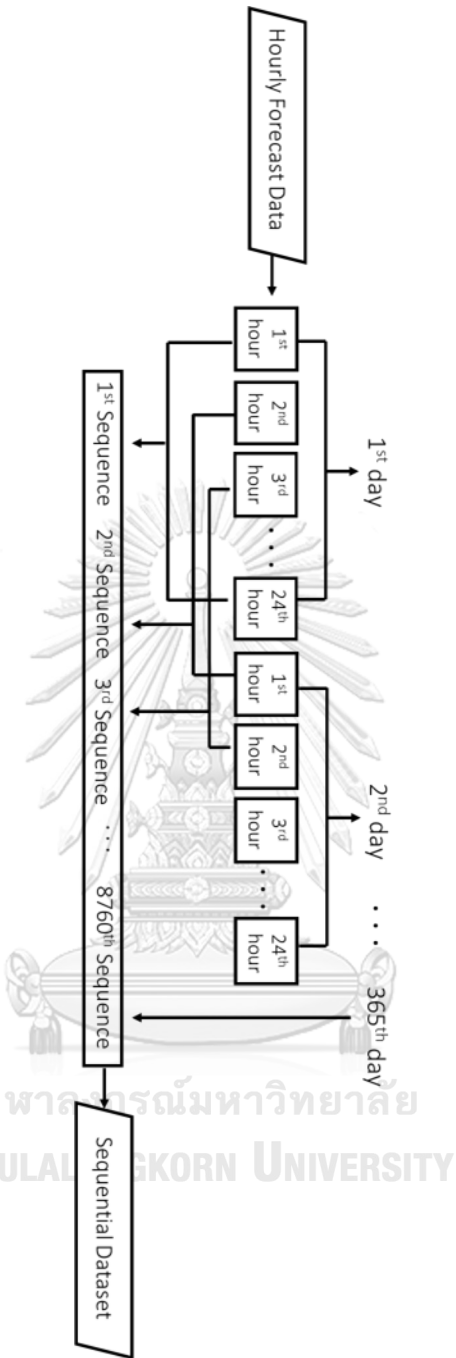


Figure 12 Sequential data selection[1]

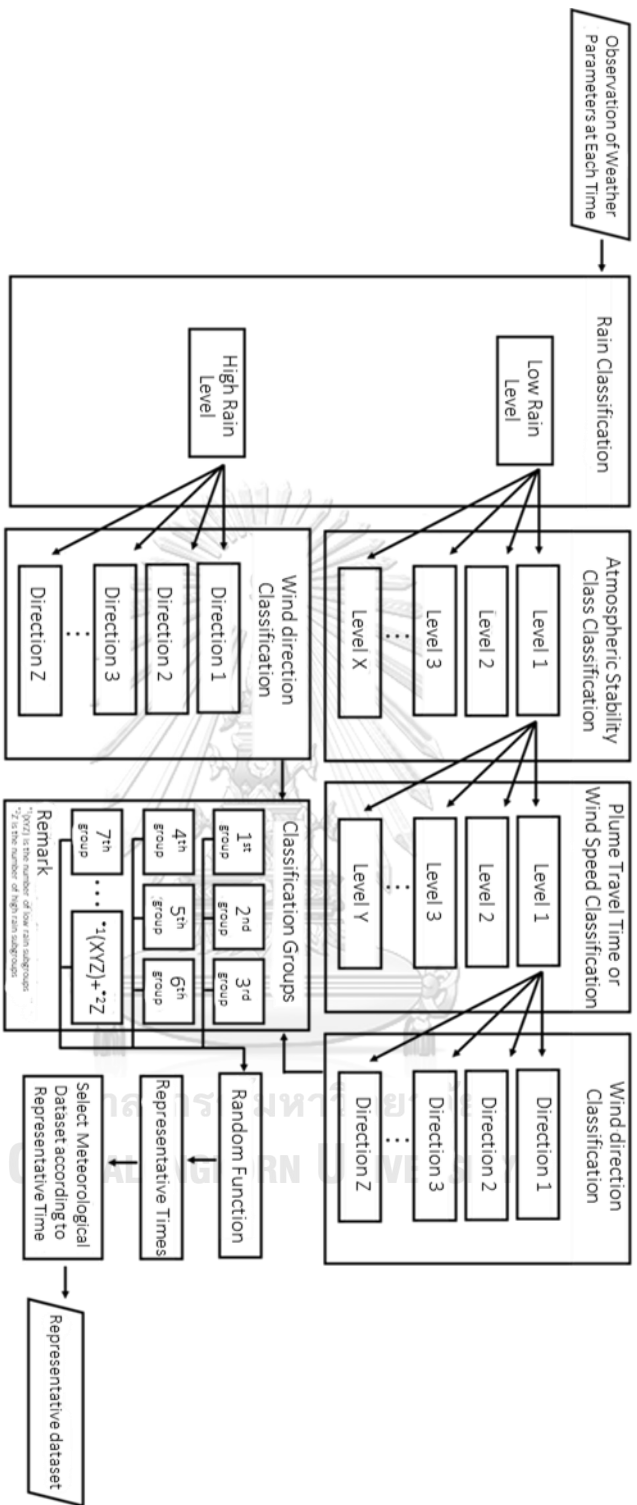


Figure 13 Representative data selection[1]

2.8 Demonstration of predicted results by percentile levels

Demonstration of predicted results by percentile levels is widely used in Probabilistic Safety Assessment (PSA) [59,75,81,82]. This process is performed to select representative predicted results according to consequence levels. Assessing radiation consequences from a hypothetical accident is conducted with meteorological conditions. Predicted results by each meteorological condition are sorted from low consequence to high consequence according to concentration levels. The representative results are selected according to percentile for radiation consequence evaluation. The predicted result at the 100th percentile represents the highest concentration from all simulation cases, leading to the highest consequence.

2.9 Literature review

2.9.1 Potential dangers of nuclear power plants in China

Qiang wang [83] studied the nuclear power strategy in China and found that the industrial growth in China caused higher electricity demand. However, this problem was not solved by coal plants because air pollution remains a concern in China. China was one of the countries that emit the most carbon dioxide, producing acid rain and sulfur dioxide. Thus, the nuclear power plant was the best option for increasing electricity generation capacity in China. China planned to increase nuclear generation up to 70 GWe. Most of these power plants were built along with the coastal areas from Guanxi to Jilin province. Some parts of nuclear power plants were built in central China, such as Anhui, Henan, and Jiangxi province. Some of these provinces were located under the northeast monsoon blowing to Thailand.

Chritoudias et al. [84] studied global risk using ECHAM/MEESY and EMAC codes. The research studies the radionuclide effect by assuming that all the nuclear power plants in the world had an accident leading to the release of I-131 and Cs-137 to an environment of 1 PBq per station. The result showed that the USA was most affected

by radioactive contamination, followed by India, France, Germany, Japan, and China for the current station. Meanwhile, if the power plant under construction was operated, China would be the highest-risk country, followed by India and the USA. Besides, this research also defined that the radionuclide effect could occur in countries without a nuclear power plant from the Influence of wind circulation and rain. These researchers point out that China is a country with high radiation risk. Thus, the evaluated effect of radionuclides from China's nuclear power plants is necessary for Thailand, located near China.

2.9.2 Climate changes

Several studies have examined changing monsoon characteristics and found that the northern East Asian summer monsoon (EASM) circulation had been weak since the late 1970s. The cause of the monsoon weakening was investigated. Yu et al. [85] suggested that decreasing temperature in the troposphere was the main cause. Meanwhile, Yang and Lau [86] demonstrated that the sea surface temperature warming over the central and eastern Pacific was another cause. Besides, Zhu et al., [87] found that greenhouse gases could produce the warming trend of the surface air temperature around Lake Baikal, causing weak circulation of the East Asian summer monsoon.

Mickley et al. [12] studied the changing air quality from 1950 to 2052. The research analyzed carbon dioxide behavior each year, assuming that carbon dioxide emissions from industrial plants in the United States were constant. The result showed that global warming caused the air circulation pattern to gradually change. This led to the wind blowing through the northeast and midwestern United States to decrease. It caused high concentrations of carbon dioxide in these areas. Besides, Daniel and Darrell [13] also confirmed that the Earth's air circulation was weak by studying the behavior of air quality for the twenty-first century. This research supports the hypothesis

that a single year of meteorological data may not be sufficient to study atmospheric radionuclide dispersion.

2.9.3 Influences of variations in meteorological data on air pollution behavior

Chen et al. [88] studied the relationship between meteorological variation and concentration of $PM_{2.5}$ and O_3 in the North China Plain (NCP), Yangtze River Delta (YRD), and Fen-wei Plain (FWP) in the period of 2014 to 2018. Hourly observation data of $PM_{2.5}$ and O_3 was used together with meteorological data from the European Centre for Medium-Range Weather Forecasts Reanalysis Interim (ERA-Interim) in the Multiple linear regression (MLR) models. The research evaluated the meteorological impact of changing air quality trends. The investigation result demonstrated that the meteorological variation significantly changed the air quality in each area. The increased planetary boundary layer caused the concentration of $PM_{2.5}$ at the surface layer to decrease. Meanwhile, increased temperature caused the concentration of O_3 to increase.

Hu et al. [89] investigated the impact of meteorology on ozone gas in China. The daily meteorological data from the China Meteorological Data Network from 2015 to 2017 and O_3 measurement data from 334 cities were used. The investigation results showed that yearly meteorological data caused a significant change in O_3 concentration. These results correspond to Chen et al. study [88]. Increasing temperature and decreasing humidity were a productivity accelerator of O_3 . It was noted that the summer season caused the highest concentration of O_3 , followed by spring, autumn, and winter, respectively.

Xu et al. (2020) [90] have studied the consequence of meteorological variation to $PM_{2.5}$ pollution in China. The Community Multiscale Air Quality (CMAQ) model was used in the simulation to study the characteristics of $PM_{2.5}$ pollution covering 31 provinces in China. Meteorological data from 2000 to 2017 from the Weather Research and

Forecasting (WRF) model was used in the simulation process. Each year, the simulation was conducted with varying meteorological data. The $PM_{2.5}$ concentration from the different scenarios was compared with the $PM_{2.5}$ mean concentration to evaluate the impact of meteorological variation on air quality. The result showed that the meteorological data in each year shows a significant change in the concentration of $PM_{2.5}$ in each area.

Rudas and Pazmandi [73] investigated the consequences of selecting different subsets of meteorological data to utilize in the deterministic safety analysis. The research is conducted under the hypothesis that evaluating radiation effects using one meteorological dataset makes it hard to provide representative results covering all potential consequences. Thus, radiation effect investigations using various meteorological data sets were performed. The Calculating Atmospheric Release Criteria software (CARC) was used together with source term data from the REM case study and the meteorological measurement data for five years from 2014 to 2018.

For the first case, they evaluated the effective dose for seven days at 1 km from the release point at one receptor point using the worst-case meteorological condition each year. The dose comparison demonstrated that the conservative results in each year were significantly different. The meteorological condition in 2014 caused the highest effective dose, followed by the meteorological condition in 2017, 2015, 2016, and 2018, respectively.

For the second case, they calculated the effective dose for seven days at one position of 30 km from the release point using meteorological data every three months in 2014. The result showed that meteorological data in each season caused different dose concentration values. The dose values from meteorological data in the period of April to June were the highest, followed by the dose values from meteorological data from July to September, January to March, and October to September, respectively.

For the last case, they calculated the effective dose for seven days at 1 km, 3 km, 10 km, and 30 km from the release point using annual meteorological data. They found that the meteorological data each year provided a significantly different result. The meteorological data for one year could not provide an effective prediction result.

2.9.4 Calculation processes in the atmospheric dispersion code and comparing prediction results by different atmospheric dispersion code

Ádám Leelossy et al. [47] reviewed the atmospheric dispersion model construction, with detail as follows. Several models were used in the study of atmospheric dispersion, such as the Gaussian, Eulerian, Computational fluid dynamics (CFD) simulations, and Lagrangian models. Most models used source term and meteorological data as input data to calculate radionuclide movement. The meteorological data was the main parameter to define dispersion pathways. The common calculation function in the atmospheric dispersion model consisted of air concentration, ground concentration, and total effective dose calculation. As for the ground concentration, the program considers the radionuclide deposition by two processes. The first was dry deposition by gravitational force characterized by the deposition velocity. The second was wet deposition by precipitation. Atmospheric dispersion codes generally were verified by comparing the predicted results with the measurement data. There were various aspects of comparisons, such as plume dispersion characteristics, peak concentration values, arrival time at specific locations, or the integrated concentration throughout the pollution period. The measurement values from the actual accidents and measured from the experiments were widely used in the comparison process. The radionuclides with low background concentrations, such as Cs-137 and I-131, were considered in the verification process. This research points out the general construction of the atmospheric dispersion model and demonstrates the common verification method.

Rakesh et al. [91] investigated the performance of FLEXPART and SPEEDI codes. Both codes were used to evaluate radiation effects from the Durance Valley in France. The meteorological data from the WRF model, which evaluated turbulence from terrain data, was used in the process. The hypothetical release of Ar-41 from the Mediterranean Sea coast (5.74 E, 43.69 N) was used as a source term. The comparison results showed that the different calculation schemes resulted in different dispersion characteristics. The FLEXPART code provided a wider dispersion than the SPEEDI code. The different methods for evaluation of the atmospheric stability class also resulted in the dose from the FLEXPART code being higher than the SPEEDI code. This research shows that the calculation scheme is significant to simulation results. Although both codes were verified, the different calculation schemes caused different simulation results.

2.9.5 Effects of using different meteorological data sources and defining simulation period

The meteorological data is the main parameter that influences the accuracy of atmospheric dispersion models. Many organizations have developed numerical weather prediction and provide meteorological data for various fields. However, each model may have a different calculation scheme that leads to different results in the atmospheric distribution model. D. Arnold et al. [92] studied the influence of meteorological data on the atmospheric dispersion model and provided the assumption that different meteorological data sources might cause different prediction results of atmospheric dispersion code. The FLEXPART model was used to simulate the dispersion of radionuclides in the case of the Fukushima nuclear accident using meteorological data from different sources. This research focused on the difference in the precipitation data, which was taken from ECMWF, NCEP, Mesoscale (precipitation) analysis of JMA, and Radar/rain gauge precipitation analysis of JMA. The other necessary parameters for the calculation were bought from the same source. The simulation result showed that rain

data from different sources led to different ground concentration patterns. This points out that the meteorological data significantly influences the simulation results. All the contents of these research studies are summarized in Table 10.

The content related to this research can be described as follows. The studies of Qiang wang and Chritoudias et al. demonstrated that China had a high electricity demand but environmental problems. Thus, they planned to build many nuclear power plants in a short period. These studies pointed out that China will be a country with high radiation risk if a severe accident occurs. Thus, this supports this research's objective that evaluating the radionuclide effect from China's nuclear power plants is necessary. The studies of Mickley et al., Yu et al., Yang, and Lau, Zhu et al. showed that climate change caused air circulation changes. In addition, the studies of Chen et al., Hu et al. Xu et al., Rudas, and Pazmandi demonstrate that yearly meteorological data caused variations in air pollution concentration. These studies support the hypothesis that a single year of meteorological data is insufficient for radiation evaluation. However, It does not demonstrate a quantitative variation of radiation consequence evaluation in atmospheric dispersion codes. Thus, quantifying the variability of the predicted results of atmospheric dispersion codes from the influence of the climate change effect is investigated in this research.

As simulation in atmospheric dispersion code, Ádám Leelossy points out the pattern of the atmospheric dispersion calculation model, making it clear to understand the sequence of steps in the calculation. Arnold shows that the meteorological data from different sources caused different simulation results. Therefore, using meteorological data from the same source is necessary in the verification process. Rakesh compared the prediction results of FLEXPART and SPEEDI. The different calculation schemes were found to be significant to both codes' different results. These studies are useful for using the atmospheric dispersion code in this study.

Table 10 Literature reviews

| Title | Author | Content |
|---|--------------------|--|
| Potential dangers of nuclear power plants in China | | |
| China needing a cautious approach to nuclear power strategy | Qiang wang | China had plans to increase nuclear generation up to 70 GWe along the coastal areas from Guanxi to Jilin province. Some of these provinces were located under the northeast monsoon blowing to Thailand. |
| Global risk from the atmospheric dispersion of radionuclides by nuclear power plant accidents in the coming decades | Chritoudias et al. | Radiation effect evaluation with a hypothetical accident showed that China will be the highest-risk country if the power plant under construction operates. |
| Climate changes | | |
| Tropospheric cooling and summer monsoon weakening trend over East Asia | Yu et al. | The decreasing temperature in the troposphere weakened the monsoon wind. |
| Trend and variability of China precipitation in spring and summer: linkage to sea-surface temperatures | Yang and Lau | The sea surface temperature warming over the central and eastern Pacific weakened the monsoon wind. |
| Recent weakening of northern East Asian summer monsoon: A possible response to global warming | Zhu et al. | Greenhouse gases could produce a warming trend in the surface air temperature, leading to the weak circulation of the East Asian summer monsoon. |
| Particulate air pollution from wildfires in the Western US under climate change | Mickley et al. | Global warming caused changes in air circulation and air pollution patterns. |
| Influence of climate change on air pollution behavior | | |
| Meteorological influences on PM _{2.5} and O ₃ trends and associated health burden since China's clean air actions | Chen et al. | Observation data of PM _{2.5} and O ₃ in China from 2014 to 2018 indicated that meteorological variations significantly changed air quality concentration. |

Continue Table 10

| Title | Author | Content |
|---|----------------------|--|
| Understanding the impact of meteorology on ozone in 334 cities of China | Hu et al. | Observation data of meteorological data and O ₃ in China from 2015 to 2017 was performed. It was noted that meteorological data each year showed a significant change in O ₃ concentration. |
| Spatiotemporal variation in the impact of meteorological conditions on PM _{2.5} pollution in China from 2000 to 2017 | Xu et al. | The consequence of meteorological variation to PM _{2.5} pollution in China was performed with a simulation code. The meteorological data from 2000 to 2017 showed a significant change in the concentration of PM _{2.5} in each area of China. |
| Consequences of selecting different subsets of meteorological data to utilize in deterministic safety analysis | Rudas and Pazmandi | influence of meteorological data on the prediction of atmospheric dispersion code was investigated. It was found that meteorological data each season and each year caused significant differences in predicted results. |
| Calculation process in the atmospheric dispersion code and comparing prediction results by different atmospheric dispersion code | | |
| A review of numerical models to predict the atmospheric dispersion of radionuclides | Ádám Leelossy et al. | Reviewed computational process in an atmospheric dispersion code |
| Simulation of radioactive plume gamma dose over a complex terrain using Lagrangian particle dispersion model | Rakesh et al. | A comparison of the computational process and predicted results of FLEXPART and SPEEDI was performed. It found that the different calculation schemes led to different simulation results. |

Continue Table 10

| Title | Author | Content |
|---|------------------|--|
| Effect of using different meteorological data sources and defining simulation period | | |
| Influence of the meteorological input on the atmospheric transport modelling with FLEXPART of radionuclides from the Fukushima Daiichi nuclear accident | D. Arnold et al. | A comparison of predicted results of the FLEXPART model with meteorological data from different sources was performed. It was shown that different sources caused different variations in predicted results. |



CHAPTER 3

METHODOLOGY

This research aimed to understand the effects of variations in meteorological data on the prediction results of an atmospheric dispersion code. Figure 14 shows the methodology flow chart in this research. The NACAC was used as a simulation tool to investigate the effects of variations in meteorological data. The calculation processes in NACAC were described in 3.1. The boundary and initial conditions used in the investigation were described in section 3.2. Verification of calculation performance in NACAC was conducted, as described in section 3.3. The appropriate meteorological data preparation for investigating the influence of variations in meteorological data on predicted results was examined, as detailed in section 3.4. The influences of each meteorological parameter on NACAC calculations were investigated, as detailed in section 3.5. The influences of variations in meteorological data on NACAC predicted results were investigated, as detailed in section 3.6.

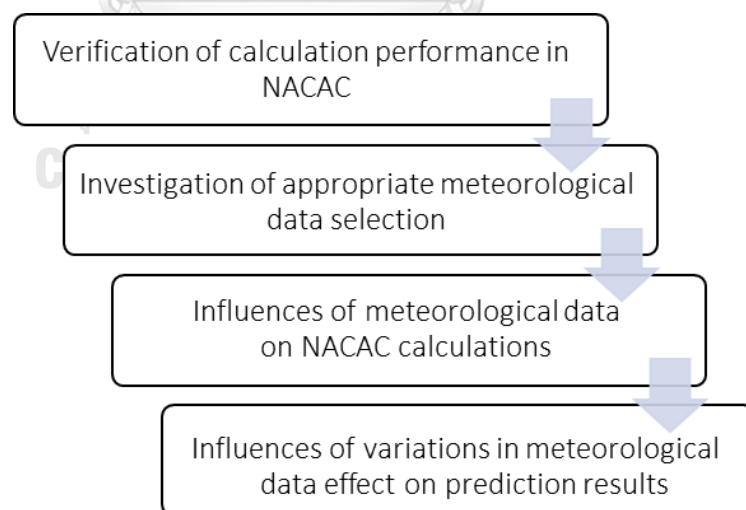


Figure 14 Methodology flow chart

3.1 NACAC computational process

The NACAC was a program developed by the Thailand Institute of nuclear technology. The program was written in the Fortran language. The simulation was performed through Compaq Visual Fortran. The calculation algorithms in the code were referred from OSCAAR, developed by the Japan Atomic Energy Research Institute [9]. Figure 15 shows the calculation flow in NACAC. The NACAC was performed with two input data: source term and meteorological data. As for the source term data, total emission concentrations of I-131 and Cs-137 demonstrating short and long-radiation effects were used in this investigation. As for meteorological data, five parameters of meteorological data with a resolution of $55.5 \times 55.5 \text{ km}^2$ were prepared. The wind components in Y and X directions, rain intensity (total precipitation), total cloud cover, geopotential high, and solar elevation were downloaded from NCEP.

Wind components at 10 m, total cloud cover, and solar radiation were used to evaluate atmospheric stability class by the Pasquill Gifford method, as detailed in section 2.26. Then, source term data, wind components in X and Y directions, rain intensity, atmospheric stability class, and geopotential high were sent to the preprocessing process module. It calculated the emission concentration rate according to Equation 6 in section 2.6.1 and formatted meteorological data into meteorological data grids with a resolution of $55.5 \times 55.5 \text{ km}^2$. The meteorological data selection module defined the simulation dates to select meteorological data for simulation. There were three meteorological data selections in this module: sequential, representative, and extreme data selection. Each scheme had calculation details, as described in section 2.7. Meteorological data according to simulation dates and emission concentration rate were sent to the atmospheric dispersion calculation module. This module calculated the depletion, dispersion, and activity concentration of radionuclides, as detailed in section 2.6.1. A polar coordinate presented the calculation results from the atmospheric

dispersion calculation module. Details of computational processes, as mentioned above, were demonstrated in Appendix B.

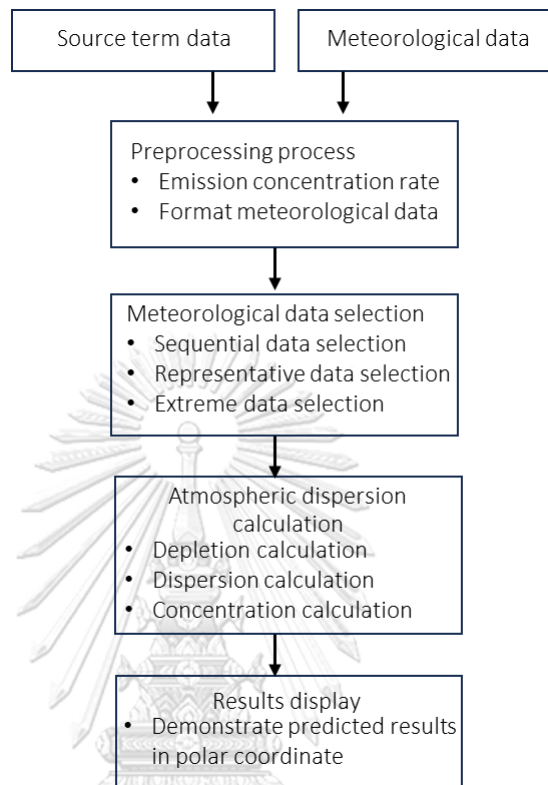


Figure 15 Calculation flow chart in NACAC

3.2 Boundary and initial conditions

3.2.1 Study location

Fangchenggang NPP in China was used as the study location because its release source term information was accessible. This power plant was located with a latitude and longitude of 21.67 and 108.55 degrees and was surrounded by five countries within a 900 km radius, as shown in Figure 16: Vietnam, Laos, Thailand, Cambodia, and Myanmar. Silva, Krisanungkura [93] suggested that the release of radionuclides from this NPP had a high possibility of affecting these neighboring countries during the monsoon period. Therefore, this study examined radiation effects within a 900 km radius, which was the shortest distance that radioactivity can spread to all five countries.

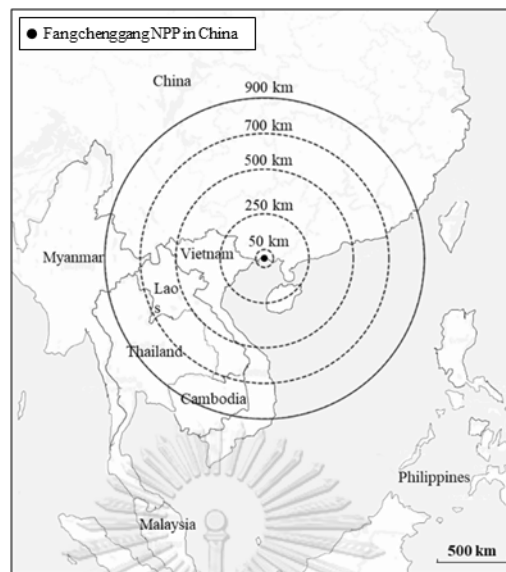


Figure 16 Fangchenggang power plant location[1]

3.2.2 Source terms

This research was performed with the release data reported by the radiation impact report of Fangchengnag NPP in China. This release data was evaluated with serious accidents before constructing units 3 and 4 [15]. The overlap of LBLOCA and LOOP scenarios designed for more severe accident conditions than ordinarily accidental events was considered. The I-131 and Cs-137 represented short-term and long-term radiation effects according to their half-life were taken into account. The total release data of Cs-137 with aerosol form 100% and I-131 with aerosol form 97 % and organic form 3% of the accident were used. The NACAC verification process was performed with a total release of 96 hours to demonstrate prediction performance over a long period, while the investigation of appropriate meteorological data selection and the effects of variations in meteorological data on prediction results were performed with a total release of 24 hours to define the effect in a day.

3.2.3 Meteorological data

Several meteorological parameters, namely geopotential high, wind component, total cloud cover, and rain intensity, with a $55.5 \times 55.5 \text{ km}^2$ resolution, were processed to generate the wind, rain intensity, geopotential high, and atmospheric stability class data for the calculation in NACAC. In the NACAC verification section, the meteorological data from the JRODOS database connected with the National Oceanic and Atmospheric Administration (NOAA) [94] were used to control the same meteorological input data for comparing predicted results between NACAC and JRODOS. However, this section started in 2019. Thus, meteorological data from 2018 was used, the most updated historical climate data. Meanwhile, the other sections were carried out with meteorological data from the CFSv2 model of NCEP [95], which was convenient to access. The investigations of appropriate meteorological data selection and the influence of variation in meteorological data effect on prediction results were investigated with meteorological data in 2020 and from 2016 to 2020, respectively. The boundary and initial conditions of all sections were summarized in Table 10

3.3 Verification of calculation performance in NACAC

This section described details verifying the NACAC performance in predicting radionuclides' transportation and radiation effects by comparing them with the JRODOS prediction results. Figure 17 shows the verification process flow chart with details of input data, calculation model, and comparison results of the JRODOS and NACAC codes. The details of the verification process were described as follows:

3.3.1 Verification conditions

Initially, the NACAC was designed to monitor the radiation effects of nuclear power plants near Thailand. The code cannot access areas where past accidents occurred, such as Chernobyl, Fukushima, and Three Mile Island NPPs. This limitation causes difficulty in comparing the predicted results and the actual incident.

Consequently, comparing the predicted results of a hypothetical severe accident by the JRODOS and NACAC was performed in the performance verification process. The extreme cases with the potential to affect neighboring countries were used as a condition for defining the simulation dates. The representative extreme cases from four seasons with high fluctuation wind direction, as shown in Figure 18, were selected: Winter (January 18, 2018, 7:00 UTC), Spring (March 20, 2018, 3:00 UTC), Summer (August 10, 2018, 5:00UTC),

Table 11 Boundary and initial conditions

| Section | Study location | Source term | Meteorological data |
|---|------------------------------------|---|--------------------------------|
| Verification of calculation performance in NACAC | Fangchenggang NPP units 3 and 4 | LBLOCA and LOOP for 96 hours - Cs-137: 2.50×10^{13} Bq - I-131: 1.15×10^{14} Bq | Data in 2018 by NOAA |
| Investigation of appropriate meteorological data selection | Fangchenggang NPP units 3 and 4 | LBLOCA and LOOP for 24 hours - Cs-137: 5.58×10^{12} Bq - I-131: 3.00×10^{13} Bq | Data in 2020 by NCEP |
| Influence of meteorological data on NACAC computational | Fangchenggang NPP units 3 and 4 | LBLOCA and LOOP for 24 hours - Cs-137: 5.58×10^{12} Bq - I-131: 3.00×10^{13} Bq | Data designed in Table 14 |
| Influence of variation in meteorological dataeffect on prediction results | Fangchenggang NPP units 3 and 4 | LBLOCA and LOOP for 24 hours - Cs-137: 5.58×10^{12} Bq - I-131: 3.00×10^{13} Bq | Data from 2016 to 2020 by NCEP |

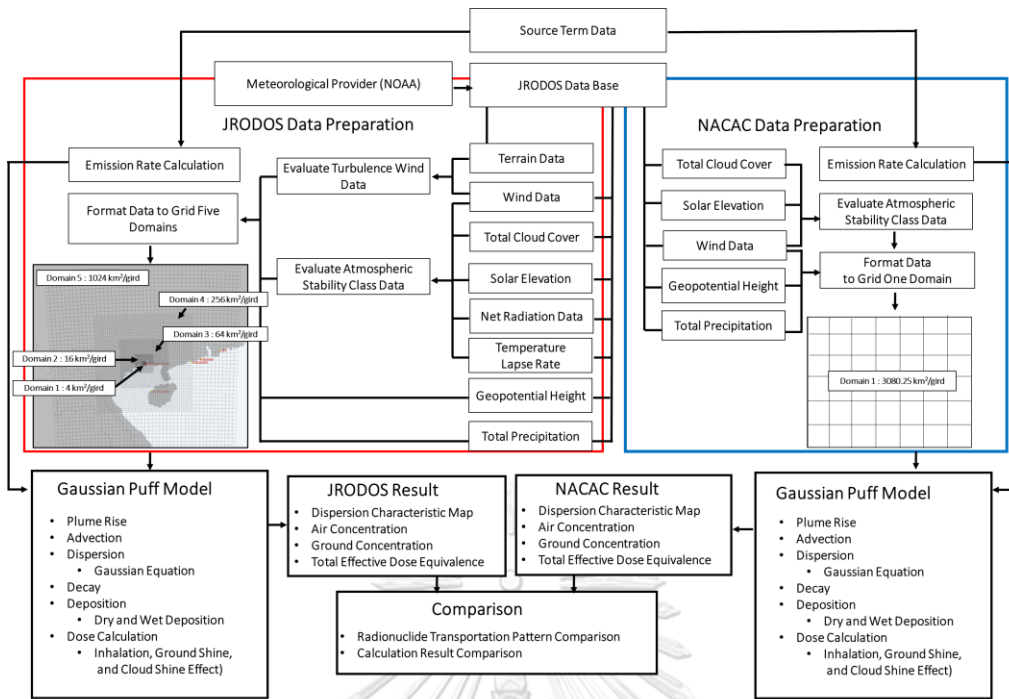


Figure 17 Flow chart of the verification process[2].

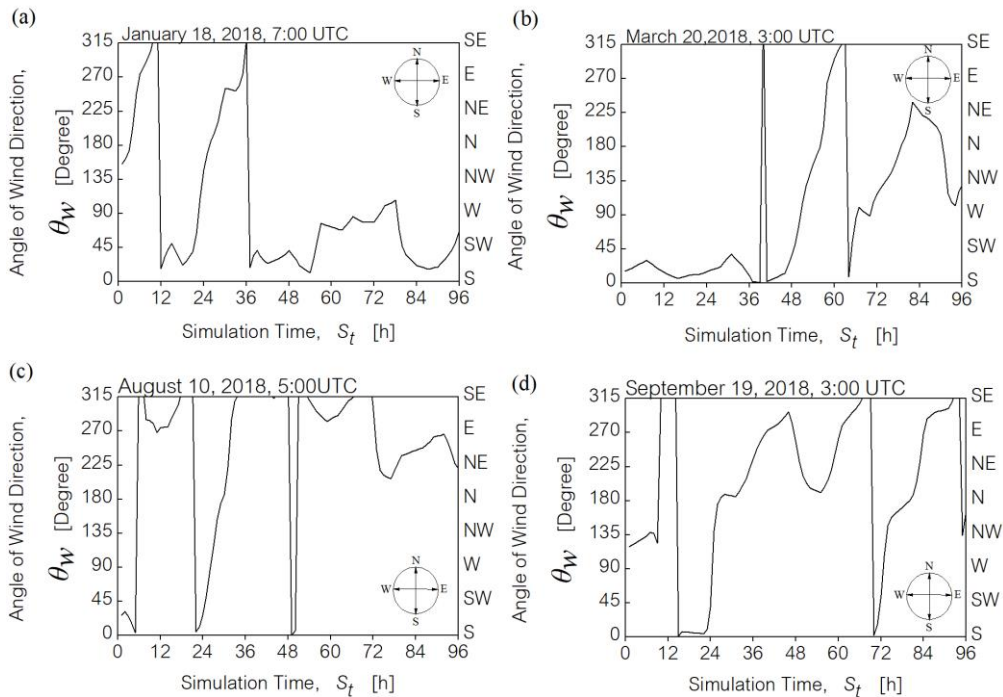


Figure 18 Wind fluctuation at the release point for 96 hours from (a) January 18, 2018, 7:00 UTC, (b) March 20, 2018, 3:00 UTC. (c) August 10, 2018, 5:00 UTC, and (d) September 19, 2018, 3:00 UTC[2].

3.3.2 Comparison processes

The simulation in NACAC and JRODOS were carried out to determine the daily radiation consequence over a 96 hours post-accident period. The source term and meteorological data of the four extreme cases were used in the simulation. The concentration calculation of both codes was conducted every 24 hours throughout the 96 hours of simulation. Simultaneously, the total effective dose rate for 96 hours was calculated by considering the effects of ground shine, cloud shine, and inhalation.

The verification process compared the predicted results obtained from both codes in two parts. Firstly, the air concentration maps of each 24 hours over 96 hours were compared to point out differences in the daily distribution changes and estimate NACAC performance in predicting the radionuclide's dispersion pattern, as detailed in section 4.1.1. Secondly, ground concentration, air concentration, and effective dose rate in the dominant dispersion direction were compared point by point to demonstrate NACAC performance in predicting radiation consequences, as detailed in section 4.1.2. In addition, to investigate the NACAC performance in evaluating the transboundary radiation effects, consistent prediction results between NACAC and JRODOS at a distance between the Fangchenggang NPP and Thailand border (500 km) were performed by three statistical parameters. The three statistical parameters are Absolute Mean Bias Error (AMBE), Root Mean Square Error (RMSE), and Correlation coefficient (CC) as follows:

$$AMBE = \frac{1}{N} \sum |P_i - O_i| \quad (13)$$

$$RMSE = \sqrt{\frac{1}{N} (P_i - O_i)^2} \quad (14)$$

$$CC = \frac{\sum[(P_i - \bar{P}) \cdot (O_i - \bar{O})]}{\sqrt{\sum(P_i - \bar{P})^2 \cdot \sum(O_i - \bar{O})^2}} \quad (15)$$

where O_i and P_i represented the JRODOS and NACAC results at the time i by site, while N and overbars signify the number of results and mean over time, respectively.

3.3.3 Comparison patterns

The JRODOS and NACAC had different calculation processes and display patterns, as mentioned in section 2.6.3. The NACAC was designed for a radial emergency response to facilitate the determination of the dispersion direction and distance, so the result display and calculation process were polar coordinates. In contrast, the JRODOS calculated results in cartesian coordinates with the five domains' grid resolution. These differences caused a limitation in comparing the radionuclides dispersion pattern between the two codes. Changing the visual style to be the same in both programs made it easier to compare. The polar coordinate was selected with better identification of the dispersion distance and direction. The JRODOS predicted results were modified to the NACAC polar grid form by moving the plume pattern, as shown in Figure 19.

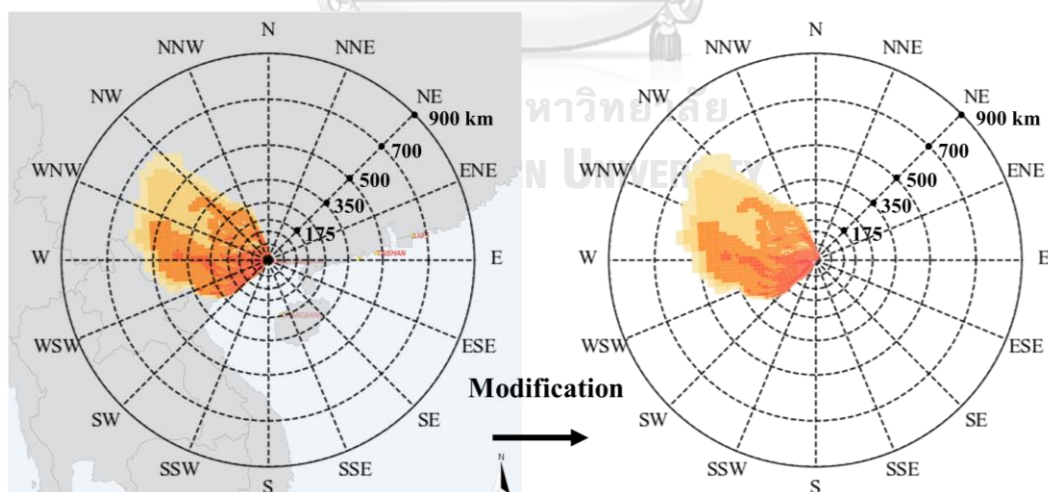


Figure 19 Modified result after swapping from a cartesian grid to a polar grid[2].

3.4 Investigation of appropriate meteorological data selection

Generally, meteorological data selection is preparing input data for simulation by

selecting meteorological data in each time period. Hence, it is significant in defining the dates for the simulation. Previously, there were several meteorological data selection methods performed in evaluating radiation consequence effects. Different selection methods produced different input characteristics. However, it lacked the selection method to investigate the effects of variations in meteorological data on radiation consequence evaluation. Thus, the Investigation of appropriate meteorological data selection to define simulation dates for investigating the effects of variations in meteorological data on the prediction results of an atmospheric dispersion code was performed.

Investigating the effects of variations in meteorological data on the prediction result required a meteorological dataset that could define changing climate behavior. The meteorological dataset, including incomprehensive climate behavior, cannot demonstrate all aspects of the effects of variations in meteorological data on prediction results. Previously, three data selection methods were performed in meteorological data selection, as mentioned in section 2.7. The extreme data selection was preparing a meteorological dataset by considering cases with a maximum severity level of the meteorological parameters. This process required less computational resources but might provide incomprehensive prediction results with a low occurrence rate [96]. Thus, the extreme data selection, which cannot represent all climatic data conditions, was ignored for this investigation. The sequential data selection was preparing a meteorological dataset by considering all cases of meteorological data. It provided a comprehensive prediction result but required large computational resources. The representative data selection was one of the preferable schemes, requiring less computational resources than the sequential data selection and providing more comprehensive prediction results than the extreme data selection. This process was generally designed for domestic radiation consequence evaluation. However, this study aimed to evaluate the radiation effect from neighboring countries. Thus, the representative data selection was modified to be able to assess the transboundary

radiation effect, as detailed in section 3.4.1. Then, the Investigation of appropriate meteorological data selection to demonstrate the variation in meteorological data effect on the prediction result between sequential and representative data selection was performed as detailed in section 3.4.2.

3.4.1 Modification of representative data selection

Representative data selection was a sampling process to select representative data that reflected individual climate characteristics, as mentioned in section 2.7.3. It significantly reduced computational resources in radiation consequence evaluation. This method was previously used to evaluate the effects of radiation in a country. The evaluation was performed with protective action criteria, suggesting awareness of radiation effects within a radius of 100 km [97]. Thus, only meteorological data surrounding NPP was required in the evaluation. In addition, the criteria for classifying meteorological data was generally performed with determined values requiring experience and understanding of the climate behavior surrounding the study site [98].

However, the classification criteria by the pre-determined values might not cause a distributed classification of meteorological data for transboundary radiological effect problems. Moreover, excessive meteorological data might be required to predict a long-range dispersion of radionuclides. Thus, investigating and modifying the existing algorithm of meteorological data classification in representative data selection of the COSYMA code [79] and the OSCAAR code [59] were conducted in this study. The percentile level was used to identify subgroups of meteorological data instead of using a specific range of weather parameters in the classification process. This scheme equally classified data and prevented excessive data in each classification group.

Table 12 shows a pattern of the meteorological data classification used in this study. The rain level and atmospheric stability class were the main weather parameters. Meanwhile, plume travel time or wind speed level was defined as the optional weather parameter. All meteorological parameters were classified into low, medium, and high severity levels. The low rain level was defined with the percentile of rain data at 2.5

mm/h, showing light rain characteristics [99]. The medium and high rain level was determined by percentile levels of rain, indicating half of the remaining data. The three severity levels of the other parameters were classified with a 33.3 percentile interval. The upper boundary of classification criteria for a low, medium, and high level is a value of 33.3, 66.6, and 100 percentiles of all collected data in each parameter, respectively. Consequently, the 11 subgroups of metrological data are produced. Then, the wind directions demonstrating the plume pathway classified the metrological data in the last step with 45-degree intervals.

Table 12 Metrological data classification[1]

| Group ^{*1} | Main Parameter | Main Parameter | Optional Parameter | | |
|---------------------|--------------------------|---|---------------------------------------|--------------------------------------|---|
| | Rain Level ^{*2} | Atmospheric Stability Class ^{*3} | Plume Travel Time, (PT) ^{*3} | Wind Speed Level, (WS) ^{*3} | |
| Low rainfall | Low | Low | Low | Low | |
| | | | Medium | Medium | |
| | | | High | High | |
| | | Medium | Low | Low | |
| | | | Medium | Medium | |
| | | | High | High | |
| | High | Low | Low | | |
| | | Medium | Medium | | |
| | | High | High | | |
| | High rainfall | Medium | - | - | - |
| | | High | - | - | - |

Remark

^{*1} Low rainfall and high rainfall groups were classified by eight wind directions with 45 degrees intervals to produce 88 subgroups of metrological data

^{*2} Rain levels were separated into low, medium, and high levels defined with data at percentile $\leq P_R(2.5mm/h)$, $\leq \frac{P_R(\max) - P_R(2.5mm/h)}{2} + P_R(2.5mm/h)$, and $>$, respectively.

^{*3} Atmospheric stability class, plume travel time, and wind speed level were separated into three severity levels defined with data at percentile ≤ 33.3 , ≤ 66.6 , and ≤ 100 .

3.4.2 Comparisons of sequential and representative data selection

In fact, the sequential data selection provides the most comprehensive predicted result by preparing all cases of meteorological data in simulation. Therefore, it is rather appropriate to investigate the effects of variations in meteorological data on a prediction result. However, using a large computational resource in this method obstructs the investigation, requiring several years of meteorological data. Representative data selection modified for transboundary radiation effect evaluation is another option that solves this problem.

However, there are several ambiguous selection schemes in the representative data selection. Previously, an area boundary for meteorological data collection (area boundary) was defined at the released point [100] or a short radius surrounding the NPP [59,77] for radiation effect evaluation within a country. The transboundary radiation effect evaluation may need an extension of the area boundaries. Besides, two optional weather parameters for meteorological data classification (optional parameters) are proposed with plume travel time [80] and wind speed level [77].

Thus, the computational cases were designed, as shown in Table 13, to identify the effect of selected optional parameters and area boundaries. Case nos. 1 up to 4 used the plume travel time as the optional parameter and used the area boundaries at the release point, 100 km, 200 km, and 300 km radius around the power plant, respectively. However, case no.1 was ignored because the plume travel time at a released point could not be calculated. Case nos. 5 up to 8 used the wind speed level as the optional parameter and used the area boundaries at the release point, 100 km, 200 km, and 300 km radius around the power plant, respectively. All cases were performed with the rate of selecting representative data (sampling rate) 1:100, as suggested by Homma [80].

Then, the off-site consequence for 24 hours was calculated using the NACAC and meteorological data prepared by sequential and each case of representative data selection. The TEDE values at the 50th, 90th, and 99.5th percentile in several locations within 900 km from the release point were compared. Performance in providing

comprehensive assessment results in each case of representative data selection was investigated by Absolute Mean Bias Error (AMBE), Root Mean Square Error (RMSE), and Correlation Coefficient (CC) as Equations 16 to 18. The details of the investigation were shown in section 4.3. Then, comparisons of transboundary radiation effects by sequential data selection and representative data selection with the optimum case were performed to investigate the appropriate simulation method for predicting dispersion characteristics and TEDE in a long-range dispersion, as detailed in section 4.4.

$$AMBE_i = \frac{1}{N} \sum_{j=1}^{16} |R_{ij} - S_{ij}| \quad (16)$$

$$RMSE_i = \sqrt{\frac{1}{N} \sum_{j=1}^{16} (R_{ij} - S_{ij})^2} \quad (17)$$

$$CC = \frac{\sum_{j=1}^{16} [(R_{ij} - \bar{R}_i) \cdot (S_{ij} - \bar{S}_i)]}{\sqrt{\sum_{j=1}^{16} (R_{ij} - \bar{R}_i)^2 \cdot \sum_{j=1}^{16} (S_{ij} - \bar{S}_i)^2}} \quad (18)$$

Where R_{ij} and S_{ij} were TEDE values predicted by simulation using representative and sequential data selection at distance i , and j direction. N and overbars were the numbers of data in the distance i and averages over 16 directions.

Table 13 Computational cases to identify effects of optional weather parameters and area boundaries[1].

| Cases | Optional Weather Parameter | Area Boundary of Metrological data |
|-----------------|----------------------------|------------------------------------|
| 1 ^{**} | | At Release Point |
| 2 | Plume Travel Time | 100 km Radius |
| 3 | | 200 km Radius |
| 4 | | 300 km Radius |
| 5 | | At Release Point |
| 6 | Wind Speed Level | 100 km Radius |
| 7 | | 200 km Radius |
| 8 | | 300 km Radius |

Remark ^{**} Case no. 1 was ignored in the analysis process since plume travel time collection at a single point cannot be computed.

3.5 Influences of each meteorological parameter on NACAC calculations

Understanding the influences of each meteorological parameter on each calculation process in NACAC was important for investigating the effects of variations in meteorological data. As mentioned in section 2.6.1, it was noted that each meteorological parameter significantly affected several calculation parameters in NACAC. The wind speed and atmospheric stability class data affected the diffusion coefficient in the horizontal and vertical directions. The diffusion coefficient in the vertical direction affected the dry coefficient, plume density, and distance faction, respectively. The diffusion coefficient in the horizontal direction affected the dispersion boundary. The distance faction and dispersion boundary affected the receptor and dispersion characteristic. Meanwhile, the rain intensity data affected the wet deposition coefficient

and subsequently affected the depletion fraction with wet deposition. In addition, the type of isotope affected the decay constant and dry coefficient, causing an effect on depletion fraction with decay and dry deposition, respectively. The depletion fractions with decay, dry deposition, and wet deposition affected the emission concentration rate. Finally, the emission concentration rate and dispersion characteristics affected the air concentration, ground concentration, and TEDE values.

To understand the influences of each meteorological parameter on these calculation parameters in NACAC, 13 cases of meteorological input data were designed, as shown in Table 14. All cases were defined by wind direction in the northeast direction. Case Nos. 1 up to 3 were meteorological input data designed to study the influences of changing atmospheric stability class with low wind speed and no rainfall on predicted results. These cases defined rain intensity at 0 mm/h and wind speed at 0.3 m/s, demonstrating light wind characteristics. Meanwhile, the atmospheric stability class was varied as unstable (A), natural (D), and stable (F) conditions. Case Nos. 4 up to 6 were meteorological input data designed to study the influences of changing atmospheric stability class with low wind speed and heavy rainfall on predicted results. The meteorological conditions in these cases differed from the first three cases only rain intensity defined by heavy rainfall with 7.6 mm/h

Case Nos. 7 up to 9 were meteorological input data designed to study the influence of changing atmospheric stability class with high wind speed and low rainfall on predicted results. The meteorological conditions in these cases differed from the first three cases in wind speed defined by strong breeze rainfall with 10.8 m/s. Case Nos. 10 up to 12 were meteorological input data designed to study the influences of changing atmospheric stability class with high wind speed and heavy rainfall on predicted results. The meteorological conditions in these cases differed from the first three cases, with rain intensity defined by the heavy rainfall and wind speed defined by the strong breeze.

Each case of meteorological input data was used in NACAC to evaluate the radiation effect for 24 hours. The calculation parameters of each calculation process in NACAC were compared to demonstrate the influences of each meteorological parameter in NACAC.

Table 14 Meteorological input data cases.

| Cases | Wind direction, [-] | Wind speed, [m/s] | Rain intensity, [mm/h] | Atmospheric stability class, [-] |
|-------|------------------------|----------------------|---------------------------|-------------------------------------|
| 1 | Northeast | 0.3: Light air | 0.0: No rain | A: Unstable |
| 2 | Northeast | 0.3: Light air | 0.0: No rain | D: Natural |
| 3 | Northeast | 0.3: Light air | 0.0: No rain | F: Stable |
| 4 | Northeast | 0.3: Light air | 7.6: Heavy rain | A: Unstable |
| 5 | Northeast | 0.3: Light air | 7.6: Heavy rain | D: Natural |
| 6 | Northeast | 0.3: Light air | 7.6: Heavy rain | F: Stable |
| 7 | Northeast | 10.8: Strong breeze | 0.0: No rain | A: Unstable |
| 8 | Northeast | 10.8: Strong breeze | 0.0: No rain | D: Natural |
| 9 | Northeast | 10.8: Strong breeze | 0.0: No rain | F: Stable |
| 10 | Northeast | 10.8: Strong breeze | 7.6: Heavy rain | A: Unstable |
| 11 | Northeast | 10.8: Strong breeze | 7.6: Heavy rain | D: Natural |
| 12 | Northeast | 10.8: Strong breeze | 7.6: Heavy rain | F: Stable |

3.6 Influences of variations in meteorological data on predicted results

This section quantified the variability of the predicted results from the influences of variations in meteorological data performed in two parts. The first part investigates the Influences of variations in meteorological data on predicted results in a year. Hourly meteorological data in 2016 within a radius of 900 km from Fangchenggang NPP was used as a sample in the investigation. A monthly meteorological behavior indicating seasonal changes was examined by the frequency distribution of wind direction and average wind speed, atmospheric stability class, and rain intensity. Changing monthly meteorological behavior within a year was studied. Monthly meteorological input data was then prepared. Simulation by sequential data selection to investigate radiation

effect for 24 hours throughout each month was performed. A correlation between monthly changes in meteorological behavior and predicted results was examined.

The second part investigated the Influences of variations in meteorological data on predicted results each year and between a year and five years. Hourly meteorological data from 2016 to 2020 within a radius of 900 km from Fangchenggang NPP were used to investigate changes in meteorological behavior each year. The statistical parameters of Absolute Mean Bias Error (AMBE), Root Mean Square Error (RMSE), and Correlation Coefficient (CC) evaluated the monthly difference in all data within the radius of 900 km of the wind speed, rain intensity, and atmospheric stability class data in each year by comparing average values of five years. Since wind direction is a vector quantity, all data within the radius of 900 km of each year was calculated as frequency distribution first. Then, they were compared by the average frequency distribution of five years with the three statistical methods as Equations 19 to 21.

$$AMBE_{ik} = \frac{1}{N} \sum_{j=1}^N |P_{jk} - O_{jk}| \quad (19)$$

$$RMSE_{ik} = \sqrt{\frac{1}{N} \sum_{j=1}^N (P_{jk} - O_{jk})^2} \quad (20)$$

$$CC_{ik} = \frac{\sum_{j=1}^N [(P_{jk} - \bar{P}_i) \cdot (O_{jk} - \bar{O}_i)]}{\sqrt{\sum_{j=1}^N (P_{jk} - \bar{P}_i)^2 \cdot \sum_{j=1}^N (O_{jk} - \bar{O}_i)^2}} \quad (21)$$

Where k, i, and j presented the year, month, and data in a month sequence, respectively. O_i was the average wind speed, rain intensity, and atmospheric stability class in each latitude and longitude within the radius of 900 km of every year or the average frequency distribution of wind direction of every year. S_{ik} was each

meteorological parameter in year k. N and overbars were the numbers of data in a month and an average value over N data.

The radiation consequence evaluation for 24 hours by NACAC was performed with monthly meteorological data for each year and monthly meteorological data for five years. The air concentration, ground concentration, and TEDE were critical parameters in investigating the influence of variation in meteorological data on prediction results by AMBE, RMSE, and CC methods, as in Equations 22 to 24. The investigation was performed with three distances: short (0-10km), medium (10-100km), and long (100-1000 km). The average monthly predicted results of every single year and monthly prediction results for five years were used as a reference value in the examination of the different predicted results of each year and different predicted results between a single year and five years, respectively.

$$AMBE_{ik} = \frac{1}{N} \sum_{j=1}^N |P_{jk} - O_j| \quad (22)$$

$$RMSE_{ik} = \sqrt{\frac{1}{N} \sum_{j=1}^N (P_{jk} - O_j)^2} \quad (23)$$

$$CC_{ik} = \frac{\sum_{j=1}^N [(P_{jk} - \bar{P}_i) \cdot (O_{jk} - \bar{O}_i)]}{\sqrt{\sum_{j=1}^N (P_{jk} - \bar{P}_i)^2 \cdot \sum_{j=1}^N (O_{jk} - \bar{O}_i)^2}} \quad (24)$$

Where k , i , and j presented the year, month, and data in a month sequence, respectively. O_j was the average predicted results of every single year or prediction results for five years. S_{ik} was the concentration of predicted results in year k. N and overbars were the numbers of data in a month and an average value over N data.

CHAPTER 4

RESULT AND DISCUSSION

This section showed the results according to the investigation process described in section 3. The NACAC verification results were demonstrated in section 4.1. Meanwhile, the effects of different computational methods on the predicted results of atmospheric dispersion code were investigated in section 4.2. The verification of the modified representative data selection for the assessment of the transboundary radiation effect was presented in Section 4.3. The results of investigating appropriate meteorological data selection for demonstrating the influence of variation in meteorological data on prediction results were shown in section 4.4. The results of investigating meteorological parameters on the calculation process in NACAC were demonstrated in section 4.5. The results of investigating the effects of variations in meteorological data on NACAC prediction results were shown in section 4.6.

4.1 NACAC verification results

The activity concentrations and radionuclide transportation patterns by the NACAC were compared with those by the JRODOS in this section. Advection calculation and input data preparation effects on calculated results were investigated.

4.1.1 Comparisons of radionuclide transportation patterns

The daily transportation patterns of radionuclides were compared based on the air concentration maps obtained from both codes every 24 hours throughout the 96 hours of simulation time. This study indicated Cs-137 as aerosol form, while I-131 was defined as organic form 3% and aerosol form 97% according to a recommendation of the Environmental impact report of Fangchenggang NPP [15]. However, the dispersion patterns of I-131 were more apparent than Cs-137. Hence, the comparisons were conducted using the air concentration maps of I-131. It was found that the different resolutions of displayed results between the JRODOS and NACAC occurred from two

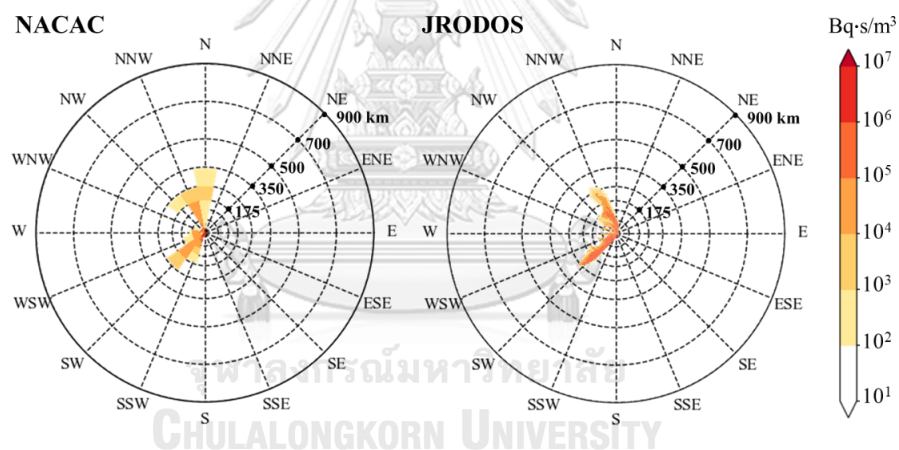
issues. First was the number of computational positions (receptor points) of the JRODOS higher than the NACAC, resulting in the JRODOS results getting more natural than the NACAC results. Second was the NACAC display results in the polar coordinate grid by original design, leading to the NACAC results being sharper than the JRODOS results, which were modified from cartesian to polar grid display for comparison purposes.

Figures 20(a), 20(b), 20(c), and 20(d) compared the air concentration maps after the accident occurred 24 hours, 48 hours, 72 hours, and 96 hours from the NACAC and JRODOS prediction in the case of January 18, 2018, 7:00 UTC (Winter season). Figure 20(a) showed that the NACAC and JRODOS provided consistent simulated results throughout the first 24 hours. Most plumes were separated into the NNW and SW directions with a maximum distance of around 250 km. However, a slight difference was found in the SSW and N directions. The NACAC provided plumes more dispersed than the JRODOS. Figure 20(b) showed that most plumes from both codes dispersed to the WSW region at 48 hours. The plume from the NACAC also dispersed further than the JRODOS, and the dispersion distance between the SW and N directions increased to 350 km. As for the dispersion pattern at 72 hours, both codes provided similar dispersion distances in the W, WNW, and NW directions, as presented in Figure. 20(c). However, the NACAC gave a longer dispersion distance than the JRODOS in the other directions, with a maximum of 200 km. In the last 24 hours, Figure 20(d) showed that in the W and WNW directions from the NACAC prediction increased to 700 km, JRODOS gave dispersion distances in the NW, WNW, and W directions increased to 668, 645, and 541 km.

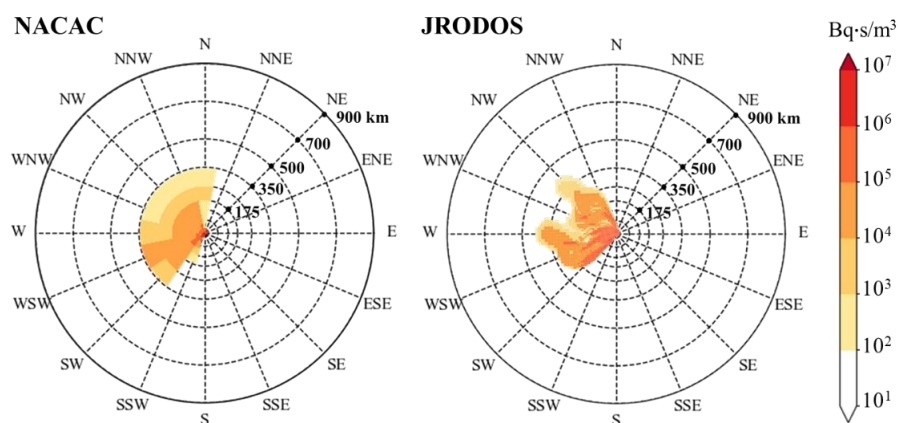
Figures 21(a), 21(b), and 21(c) showed a comparison of the air concentration map after the accident occurred 96 hours in the case of March 20, 2018, 3:00 UTC (Spring season), August 10, 2018, 5:00 UTC (Summer season), and September 19, 2018, 3:00 UTC (Autumn season), respectively. The comparisons showed a reasonable

agreement of the air concentration transportation patterns by NACAC and JRODOS. The dominant dispersion direction was the SW, E, and NNW direction for Spring, Summer, and Autumn, respectively. Nevertheless, a variation in dispersion distance of approximately 200 km was observed in the dominant dispersion direction in the cases of March 20, 2018, at 3:00 UTC and September 19, 2018, at 3:00 UTC. In addition, a variation in dispersion size also found that NACAC provided more widely dispersion in the case of January 18, 2018, 7:00 UTC and March 20, 2018, 3:00 UTC.

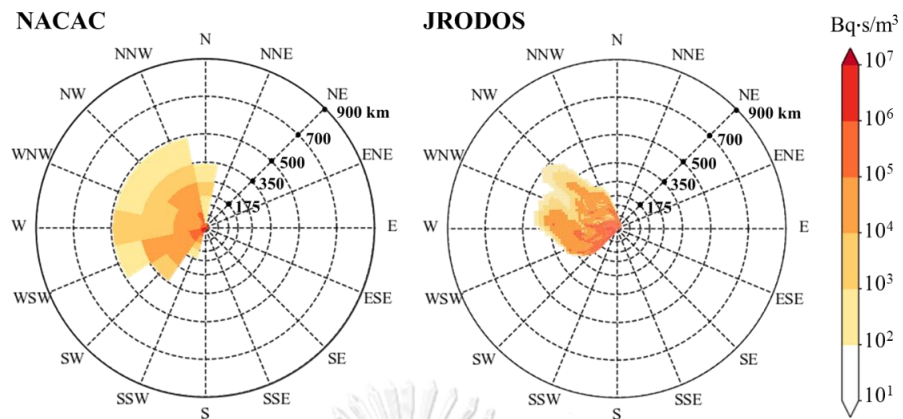
The comparisons above showed that the NACAC could offer a dispersion pattern similar to the predicted results of JRODOS. Most radionuclides dispersed in the same direction in all representative cases. Slight differences in dispersion distance were found in some directions. However, both codes generally showed similar plume transportation patterns in the dominant dispersion direction.



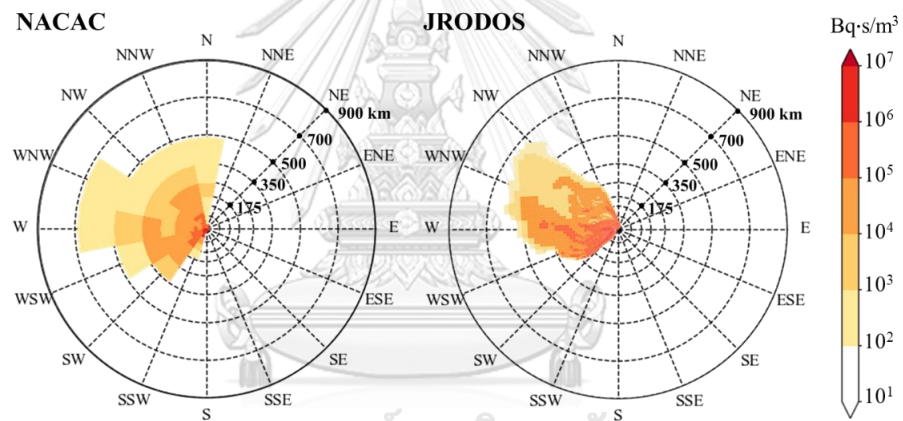
(a) Air concentration map after 24 h



(b) Air concentration map after 48 h

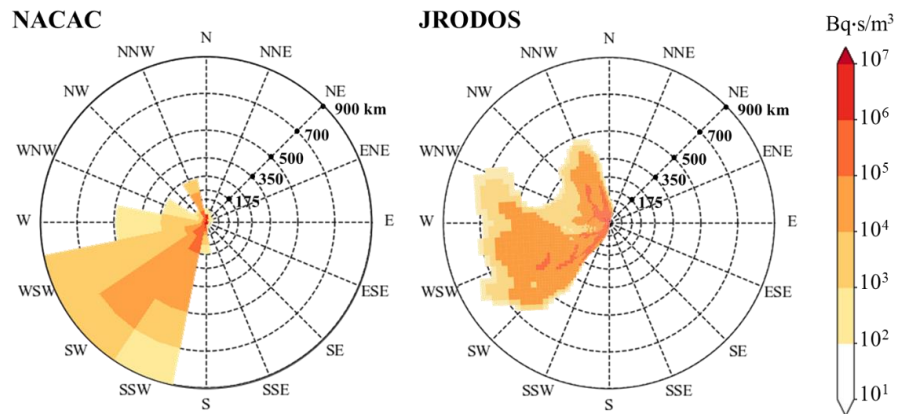


(c) Air concentration map after 72 h

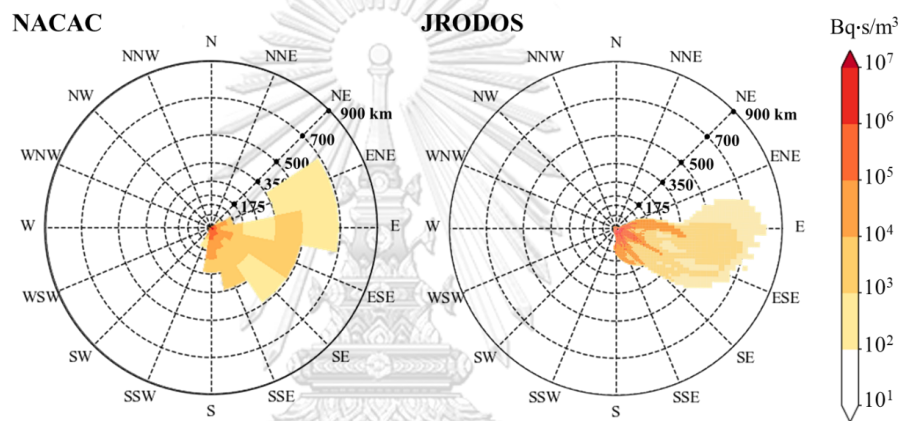


(d) Air concentration map after 96 h

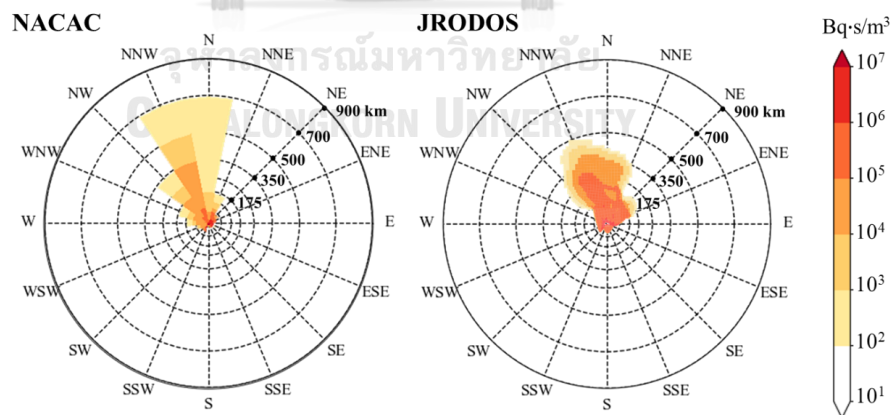
Figure 20 Predicted air concentration of I-131 every 24 h from the NACAC and JRODOS at (a) 24 h, (b) 48 h, (c) 72 h, and (d) 96 h in the case of January 18, 2018, 7:00 UTC[2].



(a) Predicted result of March 20, 2018, 3:00 UTC case



(b) Predicted result of August 10, 2018, 5:00 UTC case



(c) Predicted result of September 19, 2018, 3:00 UTC case

Figure 21 Air concentration of I-131 for 96 hours predicted by the NACAC and JRODOS of (a) March 20, 2018, 3:00 UTC (b) August 10, 2018, 5:00 UTC, and (c) September 19, 2018, 3:00 UTC[2]

4.1.2 Comparisons of calculated results

The preliminary study showed that the predicted results between the JRODOS and NACAC in the four cases were similar. Thus, the first case (January 18, 2018, 7:00 UTC), which best demonstrated the different character of prediction results between the two codes, was used in the investigation. Figure 22 presented the predicted result comparison point by point between both codes in the case of January 18, 2018, at 7:00 UTC. The comparisons of air concentration, ground concentration, and effective dose rate in the dominant dispersion directions (W, WNW, and NW) were shown in Figures 22(a), 22(b), and 22(c), respectively. The triangle and square symbols in Figures 22(a) and 22(b) represented Cs-137 and I-131 predicted results. The solid and open symbols were the results obtained by the NACAC and JRODOS, respectively.

The predicted result comparisons showed that the NACAC gave a similar trend line of dose rate and concentration values as the JRODOS, decreasing with distance. However, variation of these predicted results was found between the two codes of around one order of magnitude. The NACAC predicted lower air concentrations in the W direction and higher ground concentrations in the NW and WNW directions, as shown in Figures 22(a) and 22(b). Meanwhile, dose values predicted by the NACAC were higher than the JRODOS in NW and WNW directions, while lower dose values predicted by the NACAC were found in the W direction, as shown in Figure 22(c).

Table 15 displayed the statistical parameters for the four weather cases at 500 km in a direction with the furthest dispersion and the highest radiation intensity. The results demonstrated that the NACAC gave reasonable agreement with the JRODOS predicted results in long dispersion distance with a maximum correlation coefficient of 0.95, 0.96, 0.72, 0.97, and 0.88 in air concentration of I-131, air concentration of Cs-137, the ground concentration of I-131, the ground concentration of Cs-137, and dose rate, respectively. In addition, AMBE and RMSE also show that the difference in dose rate

between the two codes was lower than 2.47×10^{-7} and 5.95×10^{-9} mSv, respectively. These variations were the result of different computational methods in input data preparation and advection calculation process. These different methods caused variations in meteorological input data and trajectory patterns, leading to variations of activity concentration in each direction and distance, with more detail in section 4.2.

Table 15 Statistical parameters values at 500 km in the dominant dispersion direction of four cases[2]

| Parameters | CC [-] | RMSE [Concentration Unit] | AMBE [Concentration Unit] |
|---|--------------|--|--|
| Air concentration (I-131) [Bqs/m ³] | 0.51 to 0.95 | 5.01×10^2 to 1.03×10^4 | 4.11×10^2 to 8.10×10^3 |
| Air concentration (Cs-137) [Bqs/m ³] | 0.49 to 0.96 | 1.10×10^1 to 2.72×10^3 | 9.11×10^0 to 2.25×10^3 |
| Ground concentration (I-131) [Bq/m ²] | 0.44 to 0.72 | 3.76×10^0 to 1.35×10^1 | 1.58×10^0 to 1.13×10^1 |
| Ground concentration (Cs-137) [Bq/m ²] | 0.56 to 0.97 | 4.56×10^{-1} to 3.15×10^0 | 2.23×10^{-1} to 2.61×10^0 |
| Dose rate (All nuclides) [mSv/h] | 0.33 to 0.88 | 2.91×10^{-7} to 5.95×10^{-9} | 2.45×10^{-9} to 2.47×10^{-7} |

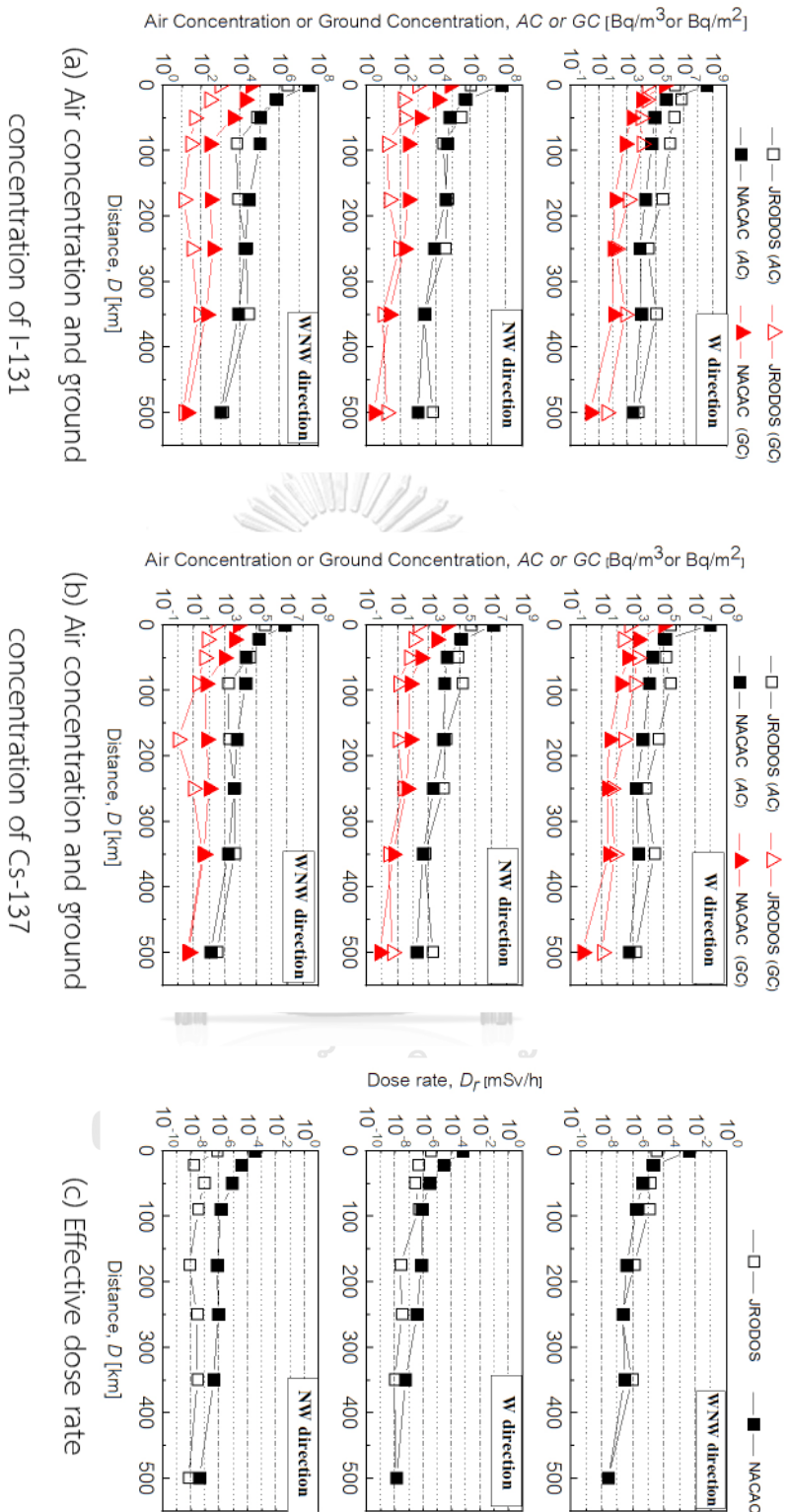


Figure 22 Comparison of the predicted air concentration, ground concentration, and effective dose rate from the MACAC and JRODOS in the dominant dispersion direction in the case of January 18, 2018, 7:00 UTC[2].

4.2 Effects of different computational methods on the predicted results of atmospheric dispersion code.

The aforementioned comparison indicated that the predicted plume characteristics from the NACAC and JRODOS codes were not significantly different. The plume mostly dispersed in the same dominating dispersion direction in each instance. Nevertheless, in some directions, the NACAC still predicted a wider and longer plume dispersion than the JRODOS. As for the concentration results, the predicted radionuclide concentration generally diminished as dispersal distance increased in both codes. However, the magnitude varies by around an order of magnitude at each point. These variations were probably a result of the various computation techniques each code used. As described in section 2.4, both codes prepared meteorological data and calculated advection by different methods. Consequently, these effects were assessed by the following sensitivity analysis.

4.2.1 Effects of input data preparation

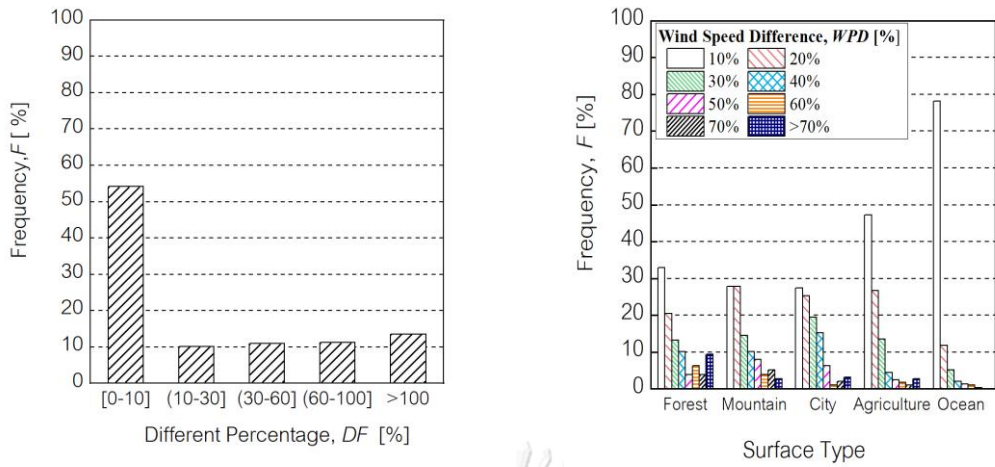
The input data preparation system was designed to prepare the meteorological data according to each code computational pattern. It varied along with computational code design. The data preparation system in the NACAC ignored the terrain effects in generating wind fields and evaluated atmospheric stability class by the Pasquill-Gifford method. A single grid domain resolution was used for all meteorological parameters in the NACAC. In contrast, the JRODOS considered the terrain effects in preparing the wind field, used various methods to evaluate the atmospheric stability class, and prepared all meteorological parameters in five grid domain resolutions.

Consequently, three analyses were conducted to assess the potential impact on the simulated results: grid resolution effects, terrain effects, and effects of atmospheric stability class analyses. As a representative case, the above analyses were based on January 18, 2018, weather data at 7:00 UTC that led to significant differences in

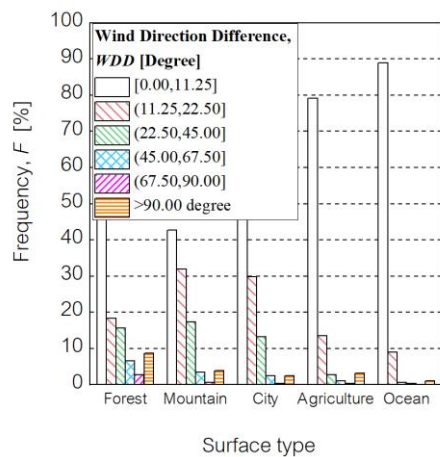
dispersion distance estimates for NACAC and JRODOS. The meteorological data from 15 locations was compared with the various surface types and grid resolutions in analyzing grid resolution and terrain effects, as described in Table 16. The difference (%) between hourly meteorological data from the NACAC and JRODOS data preparation systems were computed and visualized in the histogram graph shown in Figure 23.

Table 16 Representative positions for the meteorological data collection from the different data preparation system evaluations[2].

| Position | Latitude [°] | Longitude[°] | Roughness [m] | Grid resolution [km ²] | |
|-----------------------|--------------|--------------|---------------|------------------------------------|-------------|
| | | | | JRODOS | NACAC |
| Land area: | | | | | |
| City 1 | 21.03 | 105.83 | 1.5 | 32 x 32 | Constant at |
| City 2 | 22.82 | 108.34 | 1.5 | 8 x 8 | 55.5 x 55.5 |
| City 3 | 18.72 | 105.60 | 1.5 | 16 x 16 | |
| Forest 1 | 18.85 | 103.40 | 1.5 | 32 x 32 | |
| Forest 2 | 22.25 | 102.70 | 1.5 | 32 x 32 | |
| Forest 3 | 24.10 | 110.17 | 1.5 | 8 x 8 | |
| Agriculture 1 | 29.00 | 112.60 | 0.2 | 32 x 32 | |
| Agriculture 2 | 15.40 | 103.65 | 0.2 | 32 x 32 | |
| Agriculture 3 | 21.00 | 106.15 | 0.2 | 8 x 8 | |
| Mountain area: | | | | | |
| Mountain 1 | 22.57 | 100.19 | 1.5 | 32 x 32 | Constant at |
| Mountain 2 | 19.50 | 103.00 | 1.5 | 32 x 32 | 55.5 x 55.5 |
| Mountain 3 | 24.50 | 112.00 | 1.5 | 32 x 32 | |
| Ocean area: | | | | | |
| Ocean 1 | 20.67 | 108.90 | 0.01 | 4 x 4 | Constant at |
| Ocean 2 | 21.26 | 107.71 | 0.01 | 8 x 8 | 55.5 x 55.5 |
| Ocean 3 | 18.50 | 108.00 | 0.01 | 16 x 16 | |



(a) Frequency percentage of rain difference (b) Frequency percentage of wind speed difference



(c) Frequency percentage of wind direction difference

Figure 23 Comparison of the different (a) rain, (b) wind speeds, and (c) wind direction obtained from the NACAC and JRODOS data preparation systems in the case of January 18, 2018, 7:00 UTC[2].

As for the grid resolution analysis, rain data directly influenced by varying grid resolutions was utilized in the process. Figure 23(a) displayed the difference (%) in rain data resulting from the preparation processes of both codes. The x-axis displays the

difference (%) of hourly rain data between two codes divided into five groups, and the data frequency (%) in each group was shown in the y-axis.

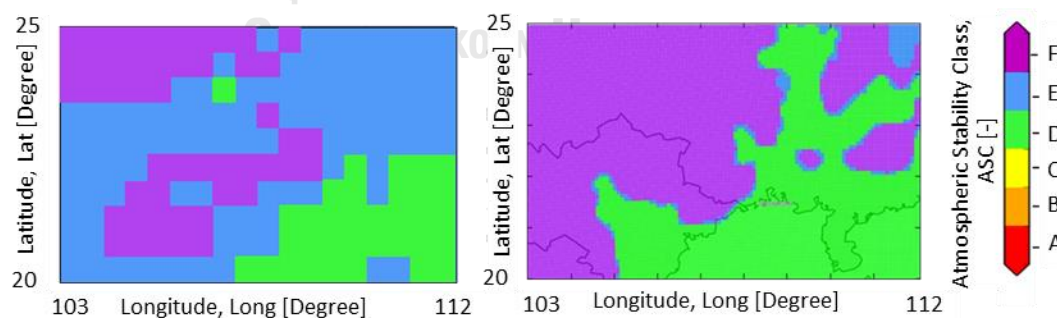
The analysis results suggested that grid resolutions could affect variances in rain intensity between the two codes, even though both codes utilized data from the same source. Approximately 50% of the data generated through NACAC preparation differed from the JRODOS data by approximately 10%. This result was related to the Sekiyama study [101], which revealed that the variation in grid resolution led to slight differences in rain data. Furthermore, the differences in rain data also contributed to variations in the wet deposition coefficient, resulting in differences in concentration values and transportation patterns of radionuclides [45,92].

The terrain effect analysis used the wind data influenced by terrain effects in this process. Figures 23(b) and 23(c) showed the difference (%) of wind speed and wind direction between the data preparation systems of both codes with five surface types: forest, mountain, city, agriculture, and ocean. Each surface type's difference (%) was divided into several groups on the x-axis to increase analysis efficiency. The wind speed difference (%) was categorized into eight groups ranging from 10% up to over 70% by white color without a pattern up to violet color with a pattern, as visualized in Figure 23(b). Meanwhile, the difference (%) in wind direction was categorized into six groups. Each group was incremented by 11.25 degrees with white color without a pattern up to orange color with a pattern, as illustrated in Figure 23(c). The y-axis of both graphs demonstrated each group's frequency (%) of the data.

The results demonstrated that terrain effects significantly influenced both codes' differences in wind speed and wind direction, especially in high-roughness areas. Approximately 50%, 30%, and 20% of wind speed data from both codes differed around 10% to 20%, 30% to 40%, and 50% to 80%, respectively. Regarding wind direction, roughly 50% of the data between the two codes differed by about 11° . Additionally, 40%

of the remaining data differed by about 11° to 45° , while the remaining 10% showed differences from approximately 45° to 90° . This phenomenon correlated to Lim et al. study [102], which demonstrated that the terrain has played an important role in the changing wind direction and speed. The different wind data resulted in an inconsistency in plume transportation and caused a difference in radionuclide dispersion and activity concentration.

The atmospheric stability class data was compared to evaluate the effects of different evaluation methods on the two codes. Figure 24 displayed atmospheric stability class data on January 18, 2018, at 23 UTC, prepared by the NACAC and JRODOS systems. It was categorized into six groups: unstable (class A) to stable stability (class F). The comparison results showed that the NACAC and JRODOS performed with one and three evaluation methods provided a different pattern of the atmospheric stability class data. The evaluation method in the NACAC provides atmospheric stability class E more than the evaluation method in the JRODOS. This was related to prior research that variations in evaluation methods caused discrepancies in atmospheric stability class data [102,103]. The different atmospheric stability class data caused various diffusion coefficients between the two codes, leading to inconsistencies in the plume intensity of each area. The plume dispersion arrival time and dispersion distance were previously reported to vary with the atmospheric stability class data [104].



(a) NACAC atmospheric stability class

(b) JRODOS atmospheric stability class

Figure 24 Atmospheric stability class data on January 18, 2018, 23 UTC derived from the (a) NACAC and (b) JRODOS[2].

4.2.2 Effects of advection calculation

Advection calculation plays an important role in determining the dispersion direction and distance in the atmospheric dispersion code. The total advection at each calculation step was the trajectory line utilized to demonstrate the pathway of the plume. The simulation process in NACAC and JRODOS was performed with different advection calculation schemes. Hence, these differences were investigated to identify the cause of inconsistent predicted results. The plume trajectory of the NACAC was determined using the 2D effective vector derived from the average wind data across ten layers. Figure 25 illustrated the distribution of wind data across ten layers, which were averaged in each trajectory line. These proportions vary according to each area's atmospheric stability class data. The x-axis showed the number of trajectory lines produced by the NACAC. Meanwhile, the y-axis presented the proportion (%) of wind data in each layer, ranging from grey to blue.

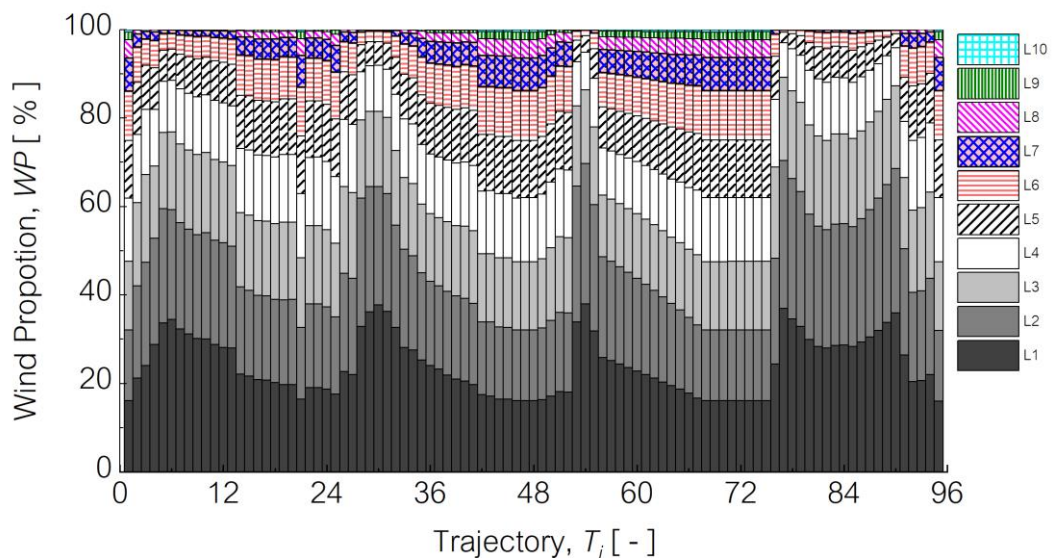


Figure 25 Wind proportion for the trajectory calculation in NACAC in the case of January 18, 2018, 7:00 UTC[2].

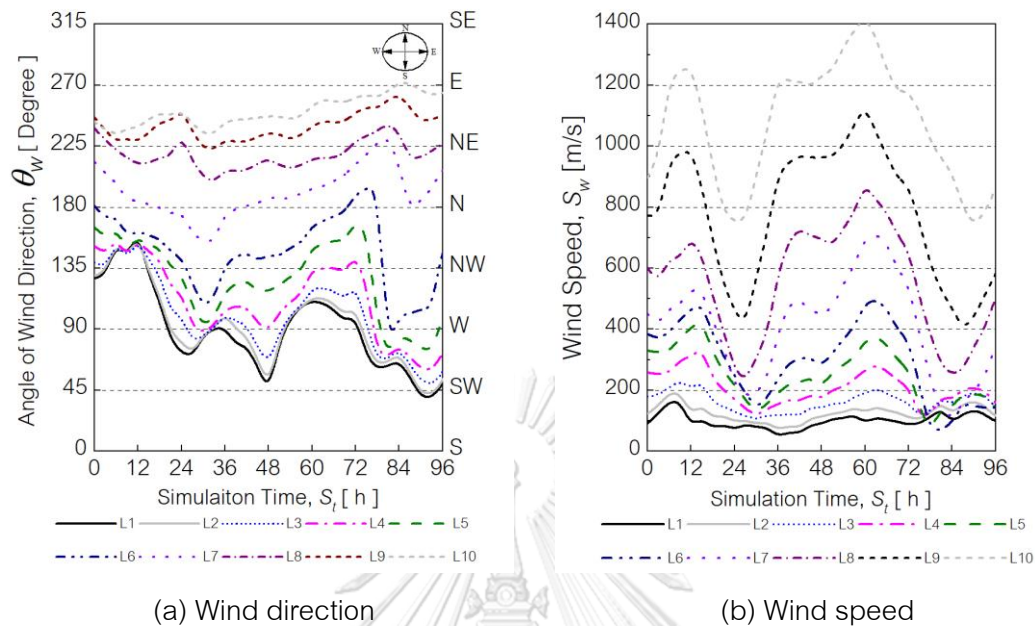


Figure 26 The wind (a) direction and (b) speed obtained from the NACAC using the vector summation at a latitude of 21° to 25° and longitude of 105° to 109° in case of January 18, 2018, 7:00 UTC[2].

The trajectory generated by the NACAC could be categorized into two groups. Firstly, trajectories were generated using wind data from layers 1 to 6 higher than 95%. This pattern was evident in trajectory lines such as 5, 30, 53, and 85. Secondly, trajectories were generated using wind data from layers 1 to 6 lower than 95%. This characteristic was observable in trajectory lines 1, 21, 45, and 75. These trajectories exhibited distinct movement patterns based on the wind data utilized in the calculation process.

Figure 26 displayed wind direction and speed derived from wind vector summation within a latitude of 21° to 25° and a longitude of 105° to 109° . The black solid up to the grey dashed lines demonstrated wind data from the first up to the tenth layer. Figure 26 (a) showed that the dominant wind directions of the first six and the last three

layers were different. Most of the wind blows in the SW to NW directions in the six layers. The wind blows strongly in the N to E direction in the last three layers.

Furthermore, Figure 26(b) demonstrated that wind speed varied with altitude. These phenomena resulted in the trajectories in the first group being affected mainly by the first six wind layers, causing movement towards the SW up to the NW directions. Meanwhile, the trajectories in the second group were influenced by the last three wind layers moving to the N to E directions, with higher wind speeds than in the first six layers. Figure 27 showed an example of the trajectory above the pattern. Open symbols represented the trajectories in the first group, while solid symbols presented the second group's trajectories. Both trajectory groups caused radionuclide transportation from the SW to N directions. However, the number of trajectories in the second group was lower than in the first group, as shown in Figure 25. Consequently, most of the radionuclides predicted by the NACAC were transported along the lower wind.

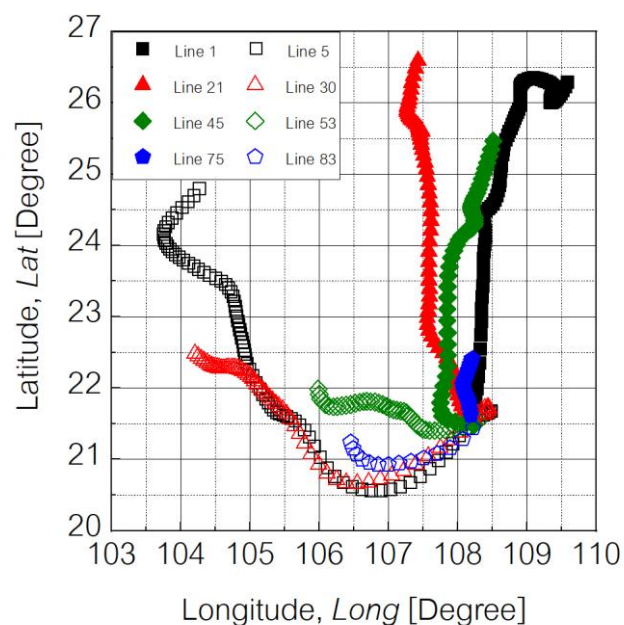


Figure 27 Example of the trajectory characteristic in the first and second groups generated in the NACAC simulation in the case of January 18, 2018, 7:00 UTC[2].

The JRODOS computed the plume trajectories by employing the 3D effective vector of the wind data at the puff position, considering the turbulence from the terrain effects. This approach results in the plume moving both horizontally and vertically. However, the JRODOS imported only the wind components in the y and x directions of the wind surface. Meanwhile, the wind component in the z-direction was calculated utilizing the LINCOM or MCF model, especially notable in high-roughness regions [105]. Consequently, the plume movement in the vertical direction was primarily evident in specific regions, and most of the plumes probably dispersed along with the lower wind. However, limitations on access to JRODOS trajectory data made it difficult to assess the plume movement. Thus, the wind data and radionuclide transportation patterns were compared to investigate this hypothesis. Figure 28 demonstrated that the majority of the plume dispersed in the W up to NNW directions, consistent with the dominant wind direction at 10 meters, illustrated by an arrow. This pointed out that different advection calculation schemes caused different advection patterns. The NACAC, considering average wind data of ten layers in advection calculation, causes a high wind component in the X and Y directions according to the high wind speed of the upper wind. This leads to a high value of the effective vector and subsequently causes a long dispersion distance. Meanwhile, considering wind data at the plume position in the advection calculation of JRODOS causes a shorter dispersion distance than NACAC since most radionuclides are transported along lower wind with low wind speed.

This study revealed that variations in calculation schemes between NACAC and JRODOS resulted in a difference in input data and plume trajectory pattern. These caused variations in the radionuclide dispersion characteristics and activity concentrations predicted by NACAC and JRODOS codes. The advection calculation in NACAC considering ten layers of wind caused a longer dispersion distance than the JRODOS considering wind data at puff position. The further dispersion and higher

concentration in some dispersion directions are found in NACAC prediction. In addition, the variation of activity concentration around one order of magnitude is found. Silva, Krisanungkura [93] suggest that the variation with one order of magnitude is a common difference by the effect of a different computational process that is generally found in comparing predicted results in commercial codes.

Nevertheless, the NACAC also demonstrates significantly faster calculation times than JRODOS, approximately 30 times, within the same computational process since it has a low complexity of data preparation. The further dispersion of radionuclides in NACAC prediction is appropriate for evaluation in conservative cases. In addition, open-source code in NACAC makes the modified evaluation method easier than JRODOS, which is commercial code. This results in NACAC being performed with various evaluation patterns according to user design, while the evaluation pattern in JRODOS is fixed with an original design.

Ultimately, Thailand's objective was to employ the NACAC to evaluate radiation impacts from nuclear power plant accidents in neighboring countries. The comparison of total effective dose rates between the NACAC and JRODOS was examined for the March 20, 2018 scenario, during which radionuclides are clearly dispersed towards Thailand, as shown in Figure 29. This analysis showed that the prediction results derived from NACAC agreed with those generated by JRODOS. Most radionuclides from the LOOP/LB LOCA scenario dispersed to the southwest, covering a radius ranging from approximately 700 to 900 km. These radionuclides covered certain northeastern regions in Thailand. However, the total effective dose equivalence remained below the minimum operational intervention level criteria (1 mSv) [106].

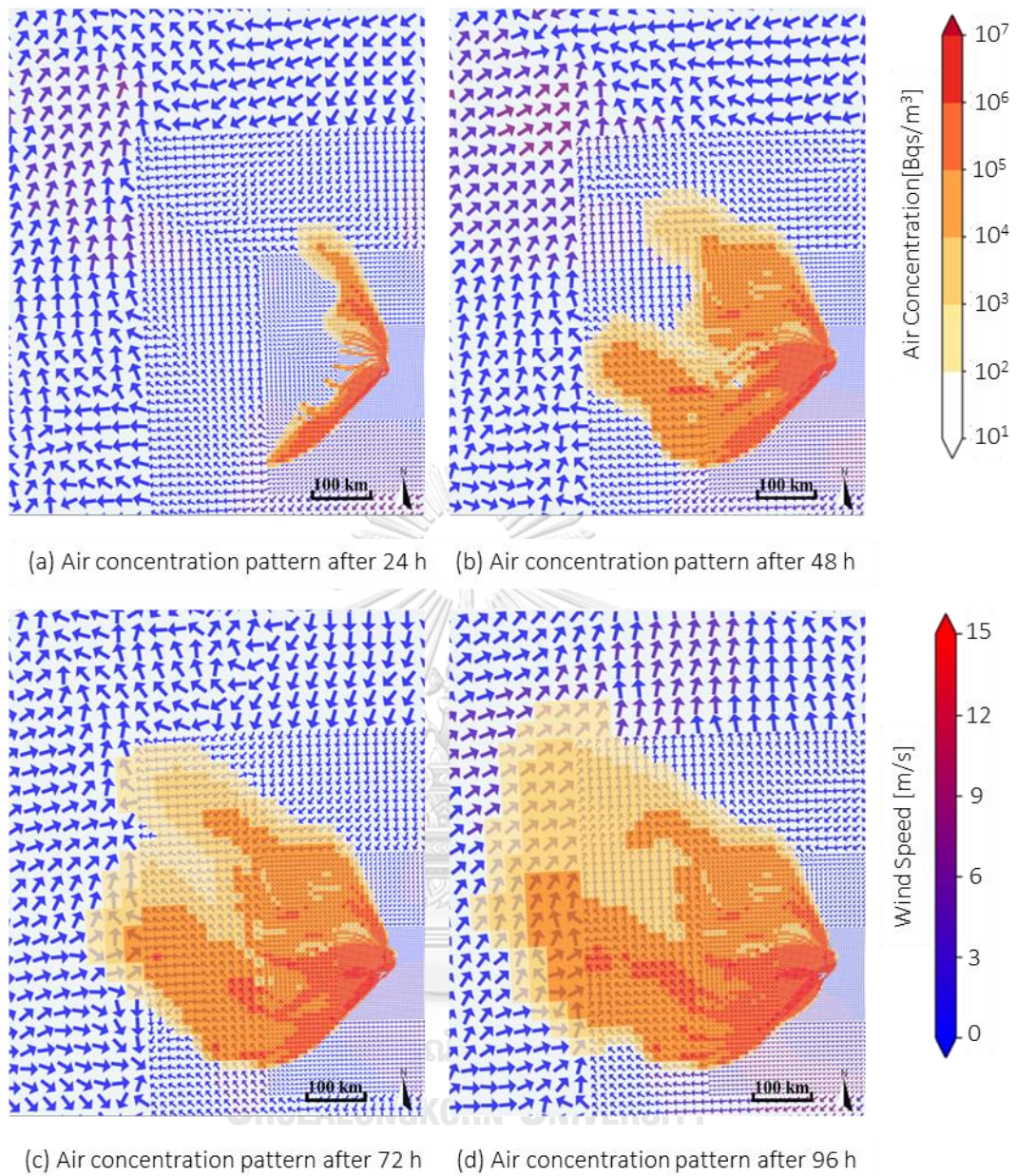


Figure 28 Comparison between the JRODOS predicted I-131 air concentration transportation patterns and wind data at 10 m after (a) 24 h, (b) 48 h, (c) 72 h, and (d) 96 h in the case of January 18, 2018, 7:00 UTC[2].

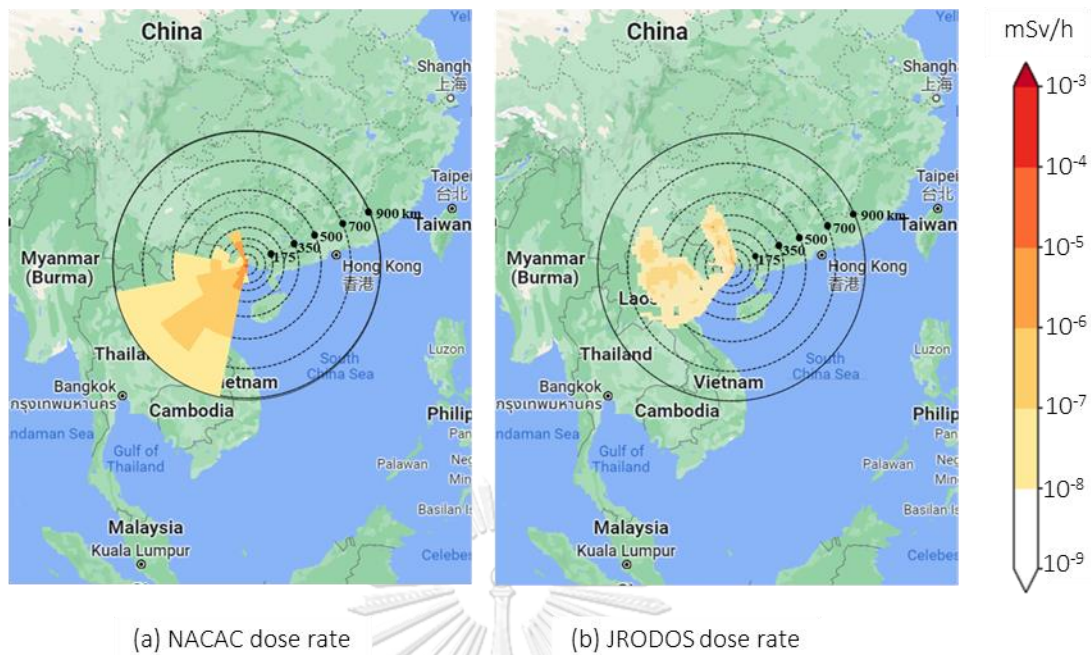


Figure 29 Total dose rate of I-131 and Cs-137 at Fangchenggang NPP after 96 h derived from the (a) NACAC and (b) JRODOS predictions after 96 h in the case of March 20, 2018, 3:00 UTC[2].

4.3 Results of modifying representative data selection

This research aimed to investigate the influences of climate change on the predicted results of an atmospheric dispersion code. However, the investigation required preparing meteorological input data illustrating all aspects of the effects of variations in meteorological data on prediction results for transboundary radiation effect evaluation. Sequential data selection could fulfill this requirement, but challenges were associated with employing excessive computational resources. Thus, representative data selection providing a comprehensive predicted result with less computational resources in the domestic evaluation was modified for transboundary radiation effect evaluation. The analysis results of computational cases in Table 13 were discussed in this section. The effects of selected optional weather parameters, area boundaries, and sampling rate were defined by comparing statistical parameters between the simulations using sequential and representative data selection.

4.3.1 Effects of optional weather parameters and area boundaries

The statistical values of AMBE at the 50th, 90th, and 99.5th percentiles for radial locations up to 900 km were shown in Figures 30(a), 30(b), and 30(c), respectively. The open blue circle, open blue triangular, and open blue rectangular symbols correspond to the AMBE values for cases numbered 2, 3, and 4, respectively. Meanwhile, the solid red diamond, solid red circle, solid red triangular, and solid red rectangular symbols denote the AMBE values for cases No. 5, 6, 7, and 8, respectively.

The comparison showed that all cases generally provided a similar trend of AMBE changing along the locations. Thus, the effects of selected optional parameters and area boundaries in the simulation using representative data selection were insignificant. The TEDE values derived from all cases were similar to those of the simulation using the sequential data selection. The AMBE values of the three percentile levels throughout 900 km radials were found to be lower than 0.1 mSv, which was lower than the minimum requirement of operational intervention levels at 1 mSv [106].

Figure 30(a) suggested it had very close TEDE values at the 50th percentile derived from the simulation using sequential and representative data selection throughout 900 km radials. Meanwhile, a slight variation in TEDE obtained by both simulation processes was identified with a high TEDE, frequently near a release point, as a comparison at the 99.5th percentile in Figure 30(c).

Figures 30(d), 30(e), and 30(f) showed RSME values at the percentile of 50th, 90th, and 99.5th at the radial locations up to 900 km, respectively. Similar symbols used in Figures. 30(a) to 30(c) were applied here. Typically, the RMSE values exhibited similar trend lines to AMBE values in the three percentile levels. It illustrated that the RMSE and AMBE investigation agreed that the differences in optional parameters and selected area boundaries are negligible in predicting the TEDE values.

Figures 30(g), 30(h), and 30(i) showed the CC values at the 50th, 90th, and 99.5th percentiles at the radial locations up to 900 km, respectively. Similar symbols used in Figure. 30(a) to 30(c) were applied here. As shown in Figures 30(g) and 30(i), the CC values at the percentiles of 50th and 99.5th were lower than 0.8 and fluctuated over the radius locations. The trends of CC values at the 90th percentiles for all cases were higher than 0.8 and generally correlated well. This is the effect of the NACAC computational scheme. The NACAC calculates the TEDE values in all locations, even though radionuclides do not entirely affect some locations. These cause those locations to contain a TEDE value of zero (0 mSv) in the predicted result dataset. This results in the prediction results at the 50th percentile being lower than the average and generally approaching the minimum TEDE value.

In addition, the simulation using representative data selection is performed with meteorological input data derived from the sampling method. Consequently, certain meteorological conditions are excluded, especially the conditions causing high and low radiation consequences that are less likely to occur. Hence, the predicted results at the 50th and 99.5th percentile demonstrating almost minimum and maximum TEDE of both simulations are different. This leads to a low CC value at specific locations. The different variations in the predictions at each location contribute to the fluctuation in CC value at specific locations [1]. จุฬาลงกรณ์มหาวิทยาลัย

To confirm these hypotheses, Figure 31 compared the TEDE values predicted by simulation using sequential and representative data selection at a radius of 9 km in the NE direction. Figure 31(a) demonstrated that the TEDE values of zero (0 mSv) contained in the dataset of the predicted results by simulation using sequential and representative data selection 47% and 33%, causing predicted results at the 50th percentile close to the minimum value. Meanwhile, Figure 31(b) showed that the most consistent predicted results between both simulations were found at the 90th percentile, while predicted results at the 50th and 99.5th percentiles had a higher variation.

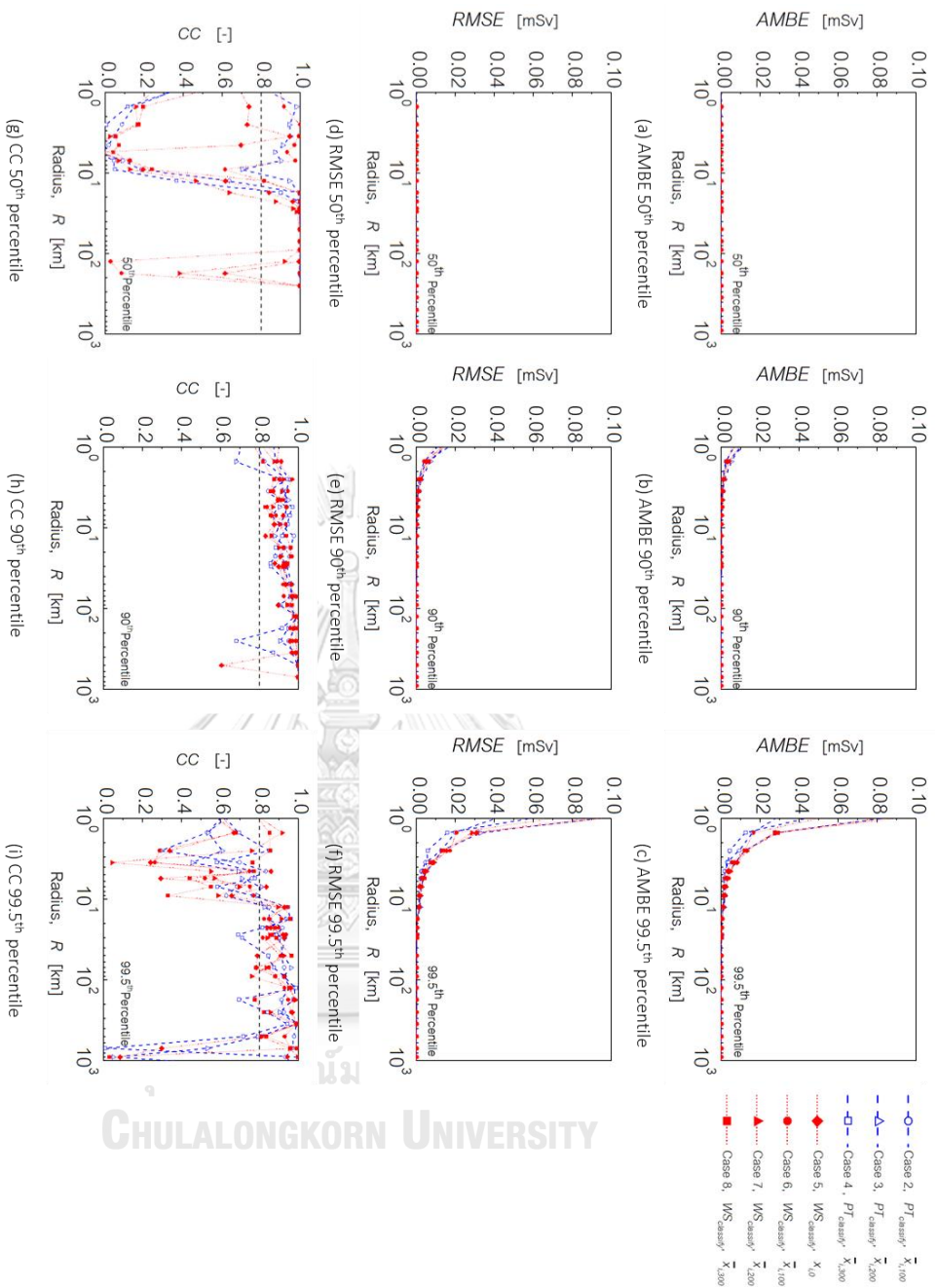


Figure 30 Data consistency investigation of TEDE values after 24 hours at 50th, 90th, and 99.5th percentile between simulation using sequential data selection and representative data selection by case no. 2 to 8 based on statistical values[1].

As mentioned above, the effects of selected optional parameters and area boundaries in the simulation using representative data selection were insignificant to predicted results based on analyzing the statistical parameters across radial locations. Thus, simulation using representative data selection with the computational case requiring the minimum computational resources was probably more favorable than other computational cases.

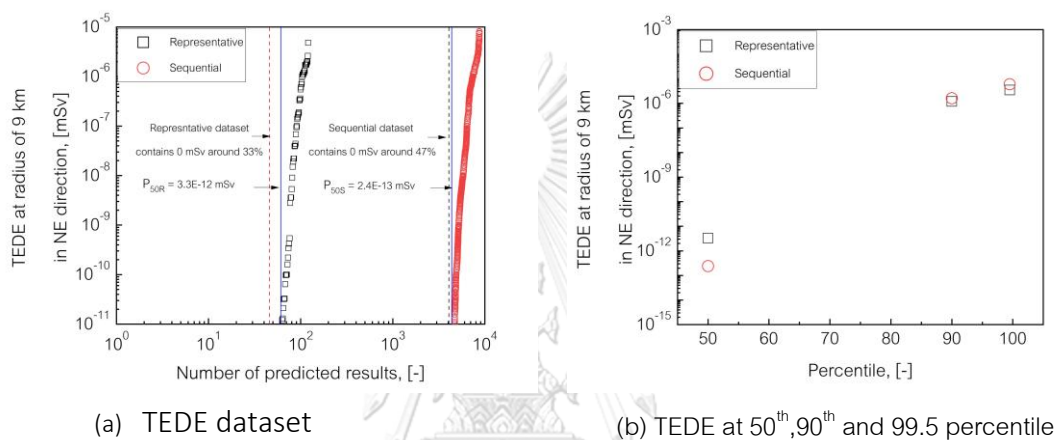


Figure 31 Comparing TEDE value predicted by simulation using sequential and representative data selection at a radius of 9 km in the NE direction

4.3.2 Effects of sampling rates

This section investigated the influences of sampling rates on the predicted results in simulation using representative data selection. Computational case No. 5, using less computational resources, was selected as a representative case. The sensitivity tests were conducted by five sampling rate conditions from high to low sampling rate: at least 1:50, 1:100, 1:200, 1:300, and 1:400. The NACAC conducted the off-site consequence evaluation for 24 hours. The CC values evaluated consistency in predicted simulation results by simulation using sequential and representative data selection. Changing the CC values along the radius locations was utilized to define the sampling rate effect on the predicted results of the simulation using representative data selection.

Figures 32(a), 32(b), and 32(c) demonstrated CC values across 900 km radials at the 50th, 90th, and 99.5th percentiles of each sampling condition, respectively. Each figure contained subfigures illustrating the CC values at each sampling rate condition. Generally, it noted that the CC values were inversely related to distance. The short distance had low CC values, while the long distance had high CC values. This was because the activity concentration near the release point was high, leading to a high difference in predicted results and low CC values. Meanwhile, the depletion phenomena cause the activity concentration to be decreased when distance increased. The low concentration caused a low difference in predicted results, leading to low CC values, Figures 32(a) and 32(b) showed that sampling rates significantly affected predicting TEDE values at the 50th and 90th percentiles of the simulation using representative data selection. The increase in sampling rate caused the higher CC values. However, the CC values at the 99.5th percentile were insignificantly changed, as shown in Figure 32(c).

This evaluation showed that each sampling rate condition may affect the predicted results in each percentile differently. For the 50th and 90th percentile, the higher sampling rate improved the consistent predicted results of the simulation using representative data selection. However, the higher sampling did not improve the data consistency of the predicted results at the 99.5th percentile of data. In addition, It was found that the sampling rate impacted the computational resources of the simulation using representative data selection. Thus, selecting an appropriate sampling rate for the consequence evaluation should be prudent to achieve reasonable predicted results. The optimum condition of the sampling rate should be selected based on specific data stratification characteristics.

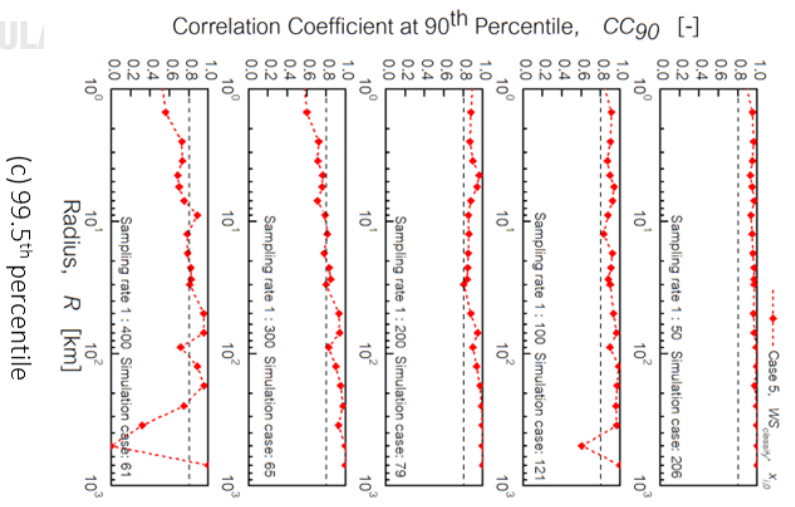
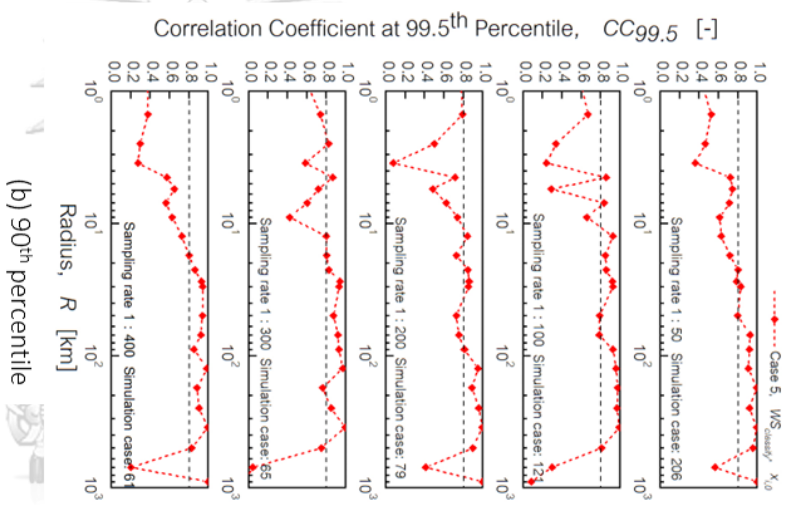
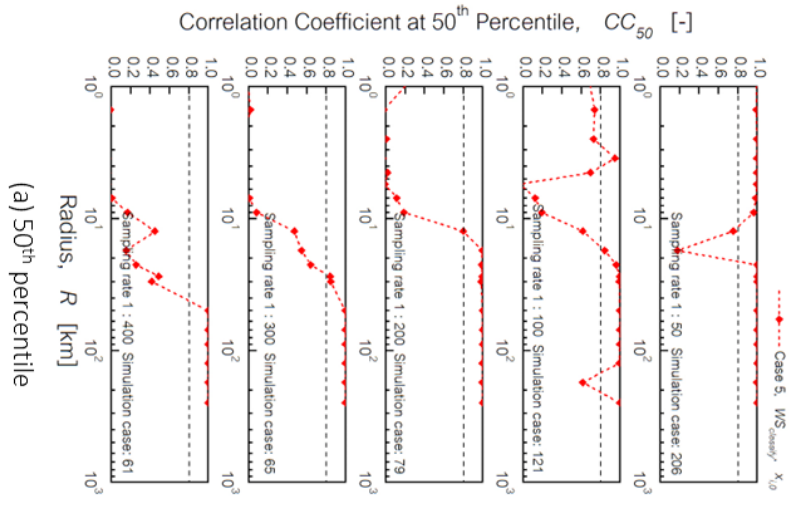


Figure 32 CC values of case no. 5 with five-sampling rate conditions at (a) 50th, (b) 99th, and (c) 99.5th percentile[1].

4.4 Results of investigating appropriate meteorological data selection

The appropriate simulation process to investigate the effects of variations in meteorological data on transboundary radiation effect evaluation was examined. The simulation using modified representative data selection was compared to the simulation using sequential data selection, providing comprehensive predicted results. The hypothetical severe accidents at Fangchenggang NPP in China and hourly meteorological data in 2020 were used as initial conditions.

The simulation using representative data selection was performed with the scheme of data selection of case No.5 with the minimum computational resources. The optional parameter with wind speed and the area boundary of meteorological data at the release point was used. According to the previous analysis, the sampling rate of 1:50, achieving the highest acceptable CC values, was selected. These conditions produced input data containing 206 meteorological data sequences for the simulation. Meanwhile, the simulation using sequential data selection was performed with input data containing 8,760 meteorological data sequences at one-hour intervals throughout a year to produce comprehensive predicted results.

The TEDE values and dispersion characteristic maps of 24 hours at the 50th, 90th, and 99.5th percentiles, demonstrating radiation consequences at medium, severe, and critical, were compared. One of the simulation processes was selected to demonstrate the effects of variations in meteorological data on the transboundary radiation effect with reasonable computational resources in section 4.6.

4.4.1 Total Effective Dose Equivalence (TEDE)

Figures 33 to 35 compared the TEDE values for 24 hours in 16 directions at the 50th, 90th, and 99.5th percentiles produced by the simulation using representative and sequential data selection with the open red rectangular and black triangular symbols, respectively. Generally, both simulation processes provided similar TEDE trends with

TEDE values less than 1 mSv. The TEDE values decreased along the radius location depending on the direction. The TEDE values reached near-zero values at a specific radius location (dispersion distance) depending on the direction. However, some differences in TEDE values and dispersion distances were also found. The differences in TEDE values were generally found at almost the end of the dispersion distance.

As for the comparison at the 50th percentile, Figure 33 showed that both simulations provided similar predicted results, with most radionuclides dispersed in 8 directions from 16 directions. However, simulation using representative data selection gave a shorter dispersion distance in 5 directions with a maximum difference of around 100 km. Meanwhile, the differences in the TEDE values of both simulations were found in period 1 up to 5 orders of magnitude in SSE, S, NW, and NNW directions. As for the comparisons at the 90th percentile, Figure 34 showed that the highest consistency predicted results between both simulations were found in this percentile. However, the NE and NNW directions have slightly different dispersion distances, with a maximum value of 150 km. Meanwhile, different TEDE values of around 1 up to 2 orders of magnitude were found in E, ESE, SE, W, and WNW directions. In contrast, the lowest consistency predicted results between both simulations was found in the 99.5th percentile. The high difference was shown in the E up to the SSE directions, as shown in Figure 35. The maximum difference in TEDE values and dispersion distances in these directions was found at 6 orders of magnitude and 200 km, respectively.

4.4.2 Dispersion characteristics

Figure 36 compared the dispersion characteristic maps of TEDE values at the 50th, 90th, and 99.5th percentiles produced by the simulation using representative and sequential data selection. Generally, the dispersion characteristics of both simulations agreed well. Most radionuclides of the three percentiles dispersed in the same direction. The most consistent predicted results were found at the 90th percentile, as shown in

Figured 36 (b) and (e). However, as mentioned above, the differences in dispersion distances and concentration of the TEDE values caused a difference in dispersion characteristics. The highest difference was found at the 99.5th percentile, as shown in Figured 36 (c) and (f). The simulation using representative data selection did not show some part of the radiation impact in the directions of ENE up to SSE compared with the simulation using sequential data selection.

Conclusively, simulation using representative data selection could provide high consistency in predicted results compared with simulation using sequential data selection. The predicted results at the 90th percentile were the most consistent. However, comparing predicted results at the 50th and 99.5th percentile also showed high differences in dispersion distances and TEDE values. This was the effect of different schemes in preparing meteorological input data. The representative data selection prepares meteorological data by sampling method. It caused certain meteorological conditions to be excluded, especially the conditions causing low and high radiation consequences that were less likely to occur. Hence, the representative data selection yielded only good predictions that reflected most of the climate data that occurred in a year. Meanwhile, the ineffective prediction result was found in rare cases, such as the predicted result at the 99.5th percentile.

This demonstrated that simulation using representative data selection was suitable for emergency impact assessment, which required the preliminary impact locations and preliminary level of radiation impacts in a short period of time. However, the investigation of the effects of meteorological data variations on prediction results required all aspects of meteorological behavior to demonstrate the effect of each meteorological characteristic change. The loss-effective predicted result in rare meteorological data cases in the representative data selection might be inappropriate for this investigation.

Consequently, simulation by sequential data selection providing a comprehensive prediction result was used for the investigation of the effects of meteorological data variations on prediction results.

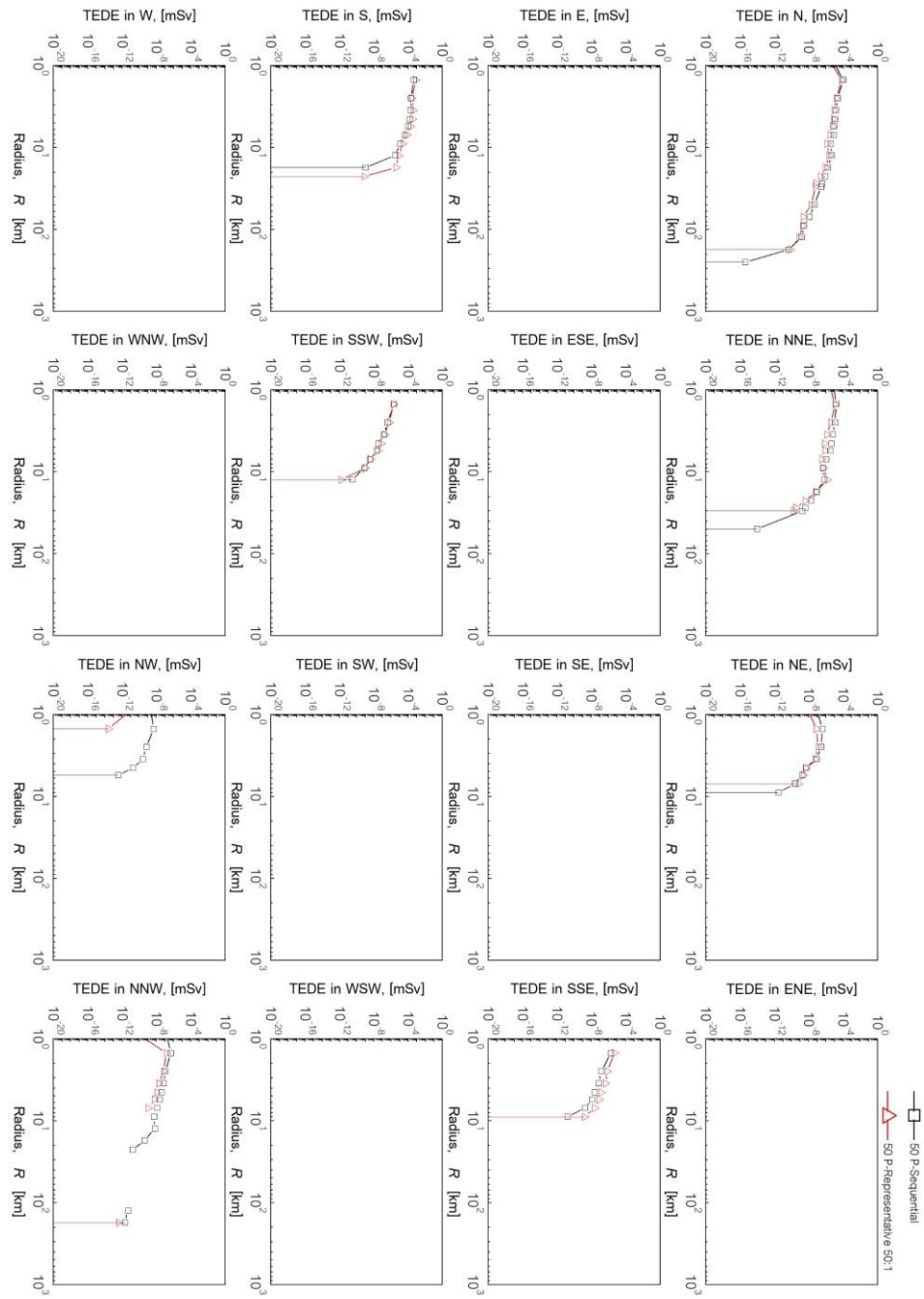


Figure 33 Comparing TEDE values after 24 hours at the 50th percentile within a radial of 900 km in 16 directions predicted by simulation using representative and sequential data sections.

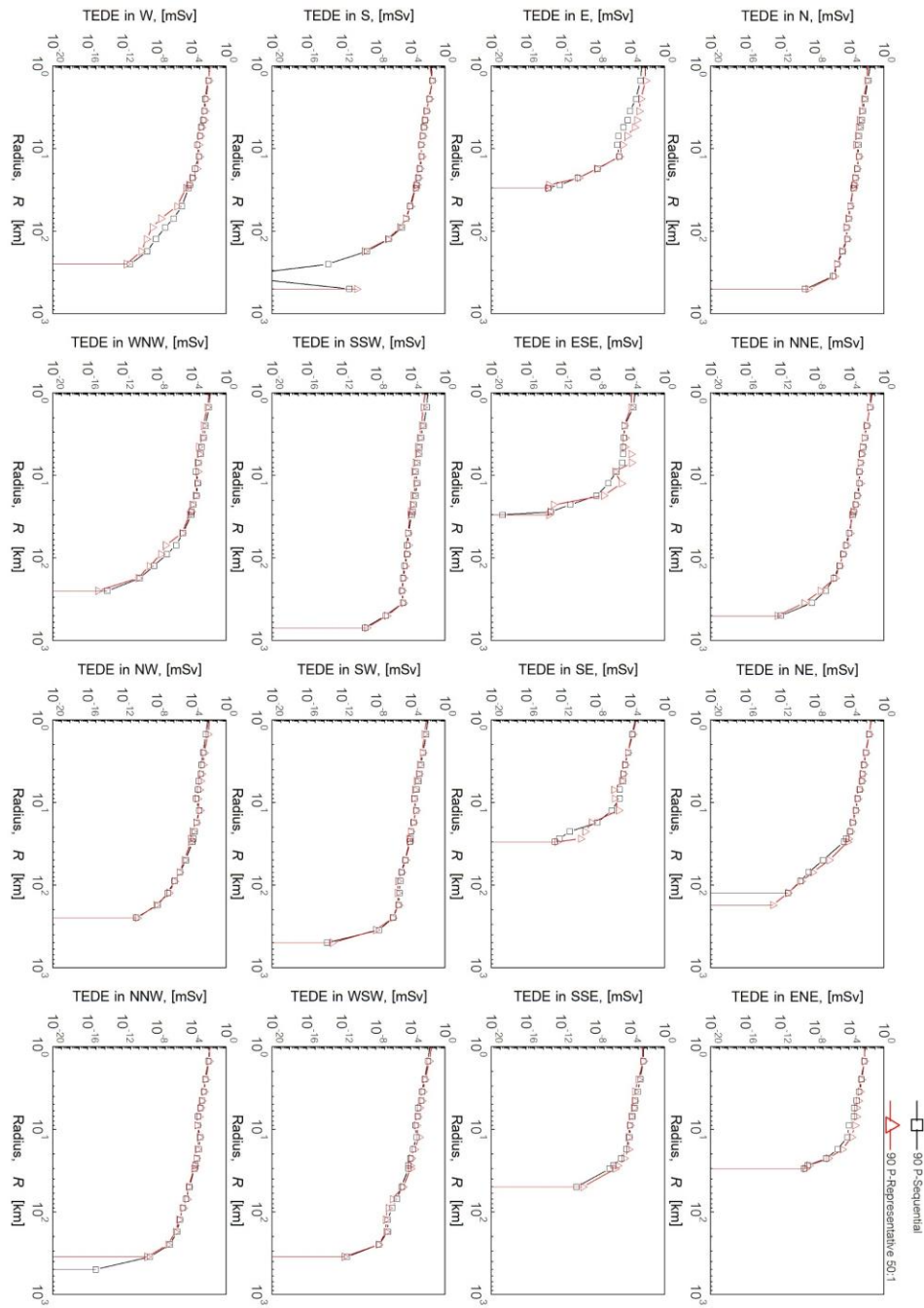


Figure 34 Comparing TEDE values after 24 hours at the 90th percentile within a radial of 900 km in 16 directions predicted by simulation using representative and sequential data sections.

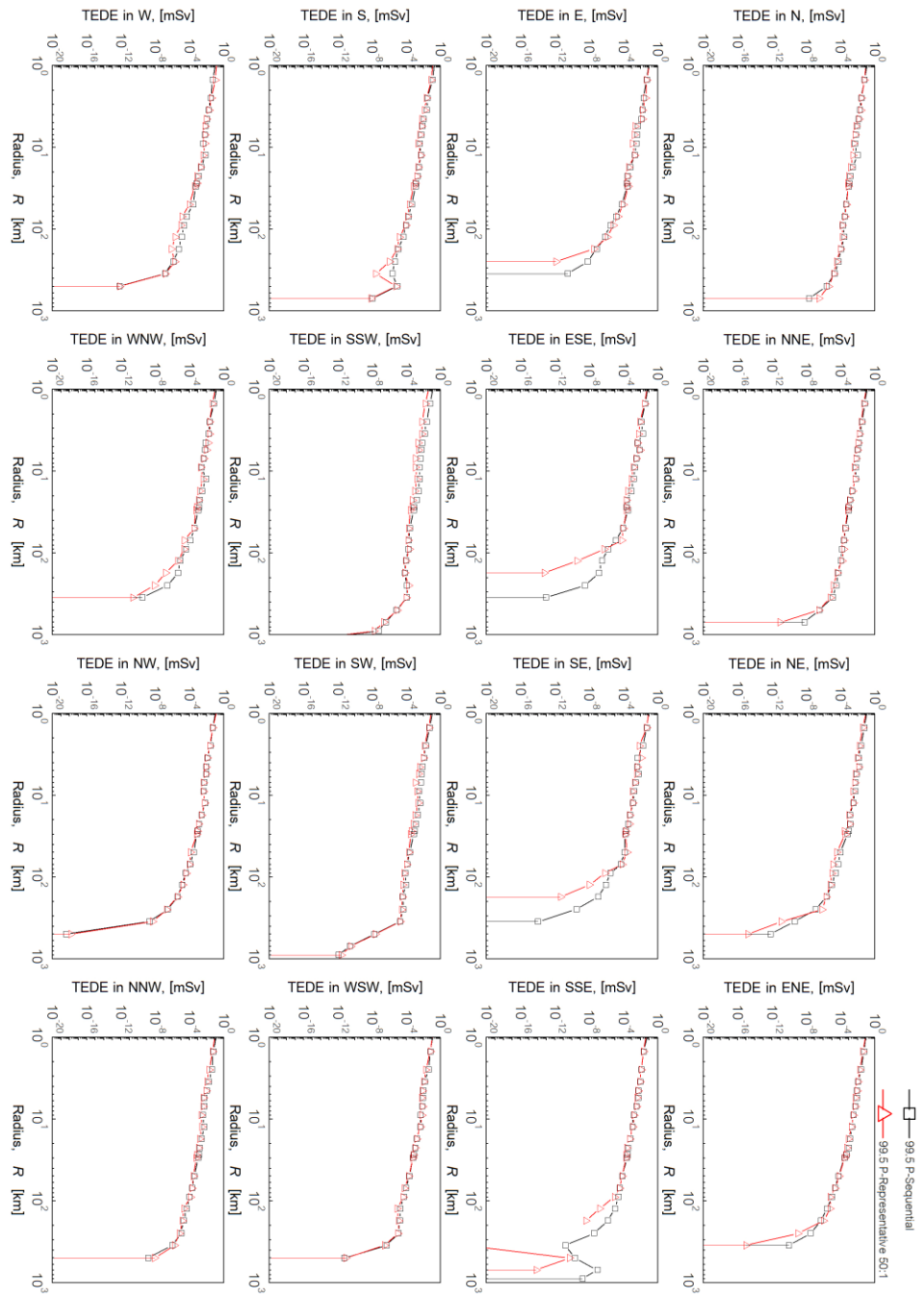


Figure 35 Comparing TEDE values after 24 hours at the 99.5th percentile within a radial of 900 km in 16 directions predicted by simulation using representative and sequential data sections.

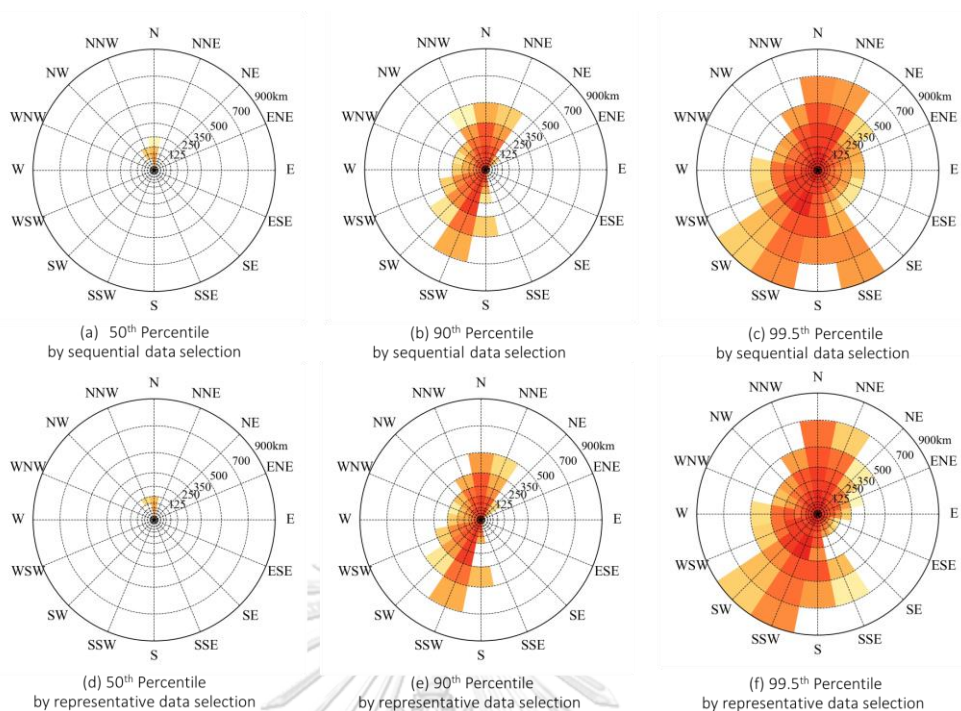


Figure 36 Comparing dispersion characteristics at the 50th, 90th, and 99.5th percentile by simulation using sequential and representative data selection

4.5 Results of investigating influences of meteorological data on NACAC computational

Understanding the influences of meteorological parameters at each computational step in NACAC was essential for discussions about investigating the effects of variations of meteorological data on prediction results. As mentioned in section 2.6.1, NACAC calculated atmospheric dispersion with 16 main calculation parameters in three sub-calculation parts: depletion, dispersion, and concentration calculations. To investigate the influences of each meteorological parameter on these calculation parameters, a sensitivity test was performed by varying meteorological input data in 12 cases, according to Table 14.

Figures 37 to 39 showed the average values for 24 hours of each calculation parameter of depletion, dispersion, and concentration calculation parts, respectively. The open and solid symbols represented conditions of no rain and heavy rain. The black

and red colors represented conditions of low and high wind speeds. The square, circle, and triangle represented atmospheric stability class A, D, and F, respectively.

As for depletion calculation, the depletion of the emission concentration rate was calculated by decay, wet, and dry deposition phenomena. However, this study was performed by Cs-137 with a long half-life. Thus, depletion with decay was low, as shown in Figure 37(a). Meanwhile, wet deposition was considered the main effect, followed by dry deposition. Thus, the rain intensity was the main parameter causing the depletion of the emission concentration rate in this part.

This investigation had 6 cases of meteorological input data considering heavy rain. It was noted that case No. 4, with low wind speed (0.3 m/s), heavy rain (7.6 mm/h), and unstable atmospheric stability class (A), caused the highest depletion. The low wind speed and unstable atmospheric stability class caused short dispersion distance and high diffusion coefficient in both horizontal and vertical directions. The high diffusion coefficient in a vertical direction caused great radionuclide dispersion in the atmosphere, leading to a low dry deposition coefficient, as shown in Figure 37(b). Meanwhile, the high diffusion coefficient in the horizontal direction and low dispersion distance caused a high advection time, according to Equations 12 and Figure 37(d). However, the high rain intensity produced a high wet depletion coefficient. These conditions caused the lowest depletion fraction, leading to the highest depletion in the emission concentration rate, as shown in Figures 37(c), 37(e), and 37(f), respectively.

On the other hand, the case causing the lowest depletion was found in case No. 7 with high wind speed (10.8 m/s), no rain (0 mm/h), and unstable atmospheric stability class (A). This was because no rain does not cause wet deposition, which was the main parameter of the depletion calculation. In addition, the high wind speed and unstable atmospheric stability class were a combination, causing a short travel time. These conditions caused depletion fractions close to one, demonstrating the lowest depletion.

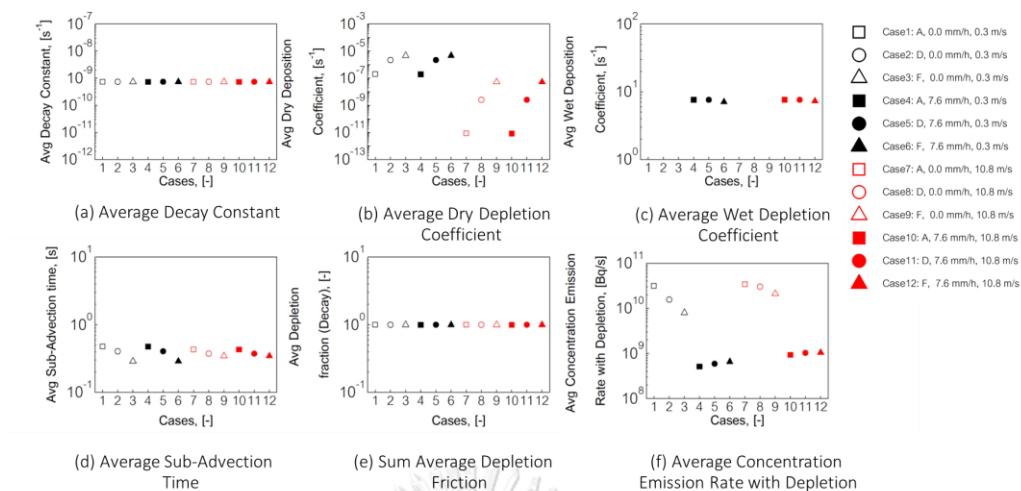


Figure 37 Depletion parameters

As for the dispersion calculation, it was noted that the change in wind speed and atmospheric stability class significantly affected the calculation parameters in this part. Meanwhile, the change in rain intensity indirectly affected these parameters with the depletion of the emission concentration rate, as mentioned above. Case No. 7, with high wind speed (10.8 m/s), no rain, and unstable atmospheric stability class (A), caused long and wide dispersion distances. The high wind speed and unstable atmospheric stability class caused the high diffusion coefficient in both horizontal and vertical directions, as shown in Figure 38(a) and (b).

Effective dispersion in the vertical direction enabled radionuclides to disperse across multiple layers of wind, leading to high plume density in each layer. It resulted in the high wind speeds commonly observed at higher altitudes employed in advection calculations, contributing to extended dispersion distances, as shown in Figures 38 (c-e). Meanwhile, effective dispersion in a horizontal direction caused a wide dispersion boundary, causing more calculation receptors in several directions and radii to be selected, as shown in Figures 38 (f-i). These conditions allowed radionuclides to disperse far and wide.

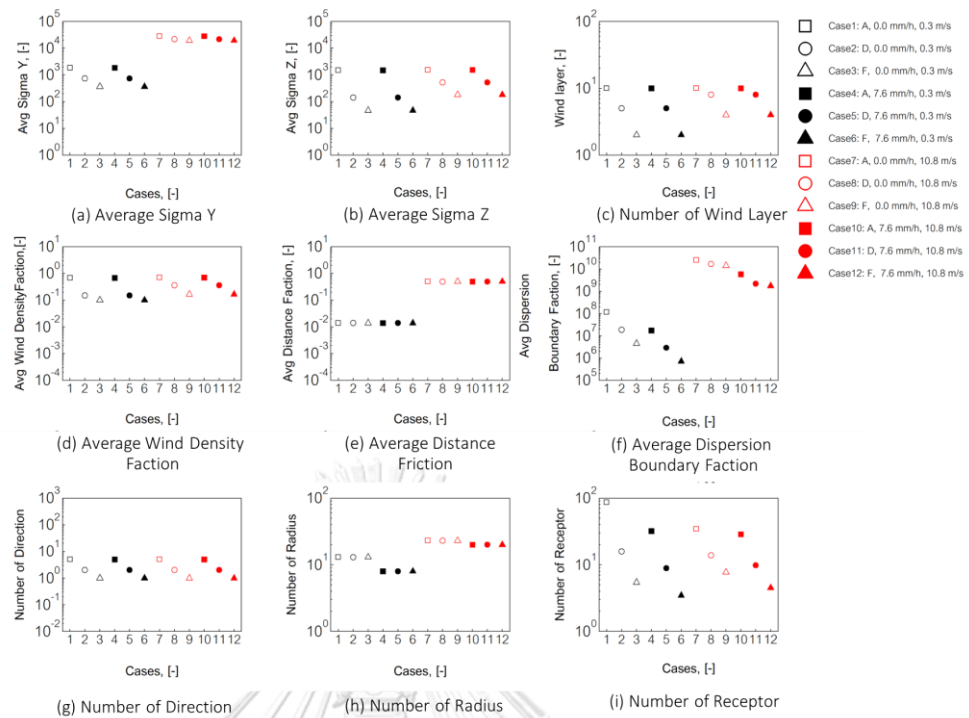


Figure 38 Dispersion parameters

In contrast, the condition causing the opposite character was observed in case No. 6 with low wind speed (0.3 m/s), heavy rain (7.6 mm/h), and stable atmospheric stability class (F). The low wind speed and stable atmospheric stability class resulted in inefficient dispersion coefficients in both horizontal and vertical directions. These conditions caused narrow and shot dispersion of radionuclides. In addition, heavy rain also led to high depletion in the concentration emission rate, causing the shortest dispersion distance in this case. The dispersion characteristic of the 12 cases was shown in Appendix A.

As for concentration calculation, the depleted emission concentration rate and selected receptor from the above-mentioned were utilized. Case No. 3, with low wind speed (0.3 m/s), no rain (0 mm/h), and stable atmospheric stability class (F), caused the height average air concentration, ground concentration, and total effective dose equivalence. The low wind speed and stable atmospheric stability class caused low diffusion coefficients in horizontal and vertical directions, leading to narrow and shot

dispersion of radionuclides. This demonstrated that the calculation receptors selected were low. In addition, no rain caused a low wet deposition coefficient, leading to low depletion in the emission concentration rate. The low number of calculation receptors and low depletion in the emission concentration rate caused the high average air concentration, as shown in Figure 39 (a). Meanwhile, the ground concentration was calculated by considering air concentration and deposition coefficient. However, the air concentration was the main effect. It caused a high average ground concentration in case No. 3, even though there was no rainfall, as shown in Figure 39(b). Finally, the high air and ground conditions in case No. 3 led to high total effective dose equivalence, as shown in Figure 39 (c).

In contrast, the lowest average activity concentrations and total effective dose equivalence were found in Case No.10 with high wind speed (10.8 m/s), heavy rain (7.6 mm/h), and unstable atmospheric stability class (A). The high wind speed and unstable atmospheric stability class caused wide and long dispersions. This led to a large selection of calculation receptors. In addition, heavy rain caused high depletion. These conditions resulted in low average air concentration, leading to low average ground concentration and total effective dose equivalence.

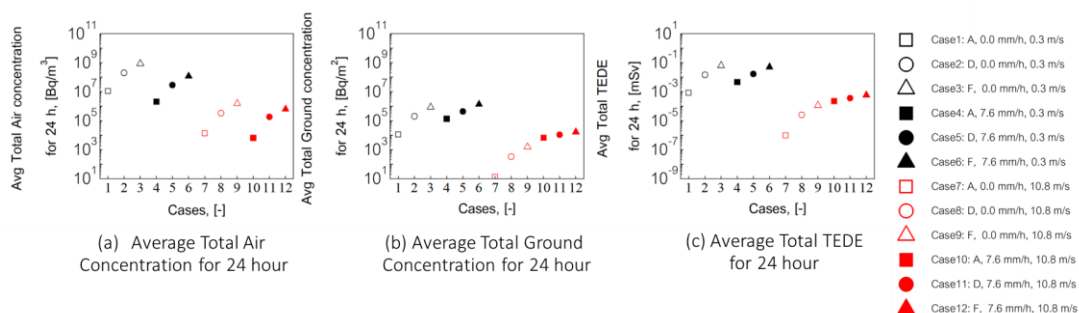


Figure 39 Concentration parameters

Figure 40 showed the prediction results of 12 meteorological input data sorted in ascending order concentration parameters and categorized according to the number of

dispersion directions. Since the dispersion characteristics of air concentration, ground concentration, and TEDE are the same, the dispersion characteristics of TEDE are used as representatives in Figure 40.

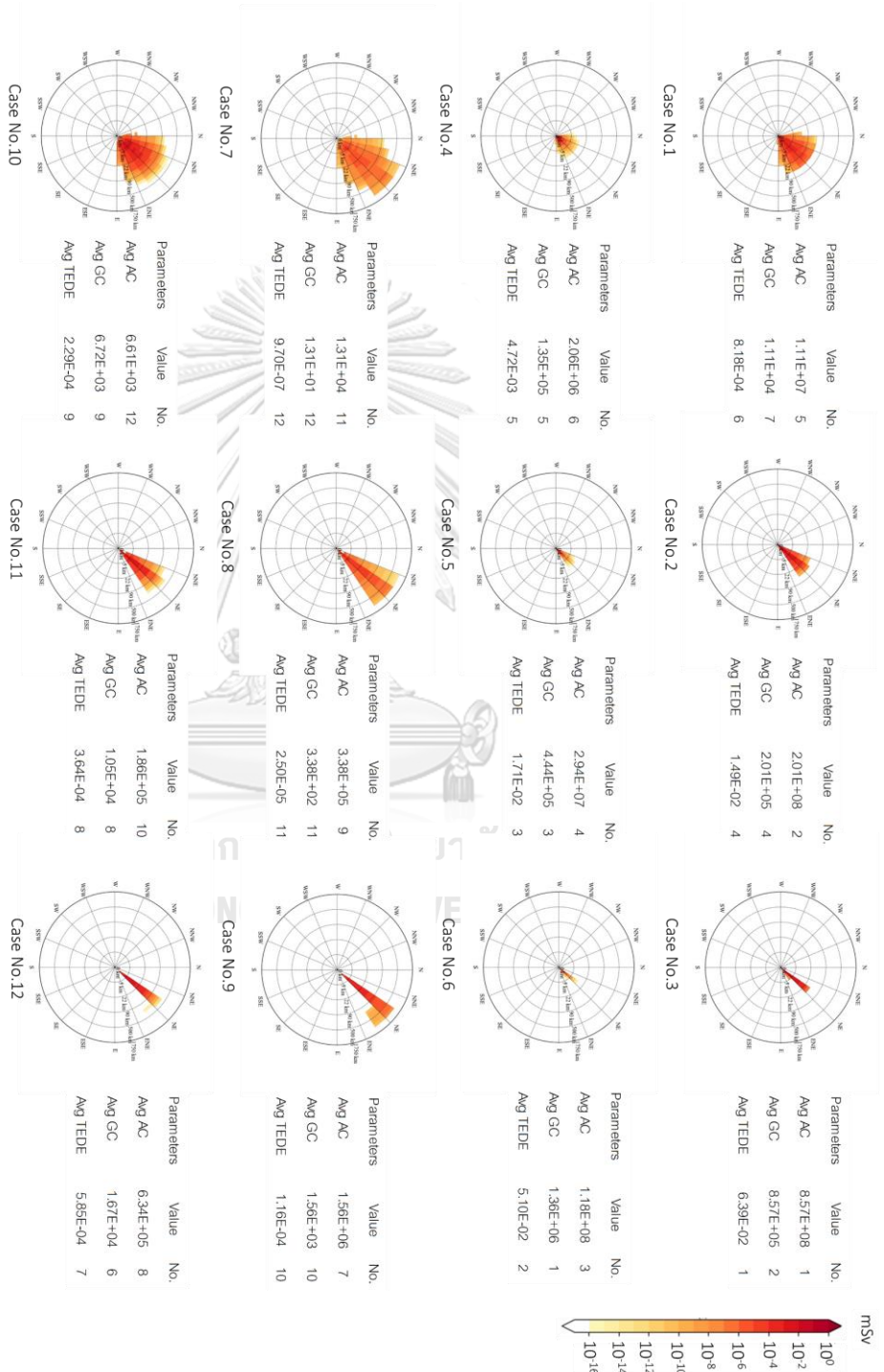


Figure 40 Prediction results of 12 meteorological input data sorted in ascending order concentration parameters where Avg AC, Avg GC, and Avg TEDE are average total for 24 hours of air concentration $[\text{Bq}/\text{m}^3]$, ground concentration $[\text{Bq}/\text{m}^2]$, and total effective dose equivalent $[\text{mSv}]$

As mentioned above, it demonstrated that each type of meteorological parameter had different influences on calculation parameters in NACAC. The atmospheric stability class and wind speed were used in calculating the diffusion coefficient in the horizontal and vertical directions. The unstable atmospheric stability class and high wind speed were a combination causing the highest diffusion coefficient.

The high diffusion coefficient in the vertical direction provided effective vertical dispersion of radionuclides. This resulted in the average wind speed being high since the high wind speed at high altitudes was used in the calculation. The high average wind speed led to a long dispersion distance. In addition, effective vertical dispersion also caused great dispersion in the atmosphere. The radionuclides were low deposited from the puff center to the ground. Meanwhile, the high diffusion coefficient in the horizontal direction provided further dispersion of radionuclides. This caused the high dispersion boundary fraction and many calculation receptors to be selected. In addition, this condition led to a long advection time, causing high depletion in the emission concentration rate. As for rain intensity, this parameter affected depletion and ground concentration calculations. The high rain intensity caused high depletion by wet deposition, leading to decreased concentration emission rates. Meanwhile, this condition caused a high deposition coefficient, leading to high ground concentration.

As for average air concentration, ground concentration, and total effective equivalent dose, these parameters depended on the emission concentration rates and the number of receptors. They had a high value with the meteorological parameter sets, causing low depletion and dispersion, such as low wind speed, low rain intensity, and stable atmospheric stability class. In contrast, these parameters had a low value with the meteorological parameter sets, causing high depletion and dispersion, such as high wind speed, high rain intensity, and unstable atmospheric stability class. Figure 41

shows combinations of meteorological parameters causing the highest value of each calculation parameter in NACAC.

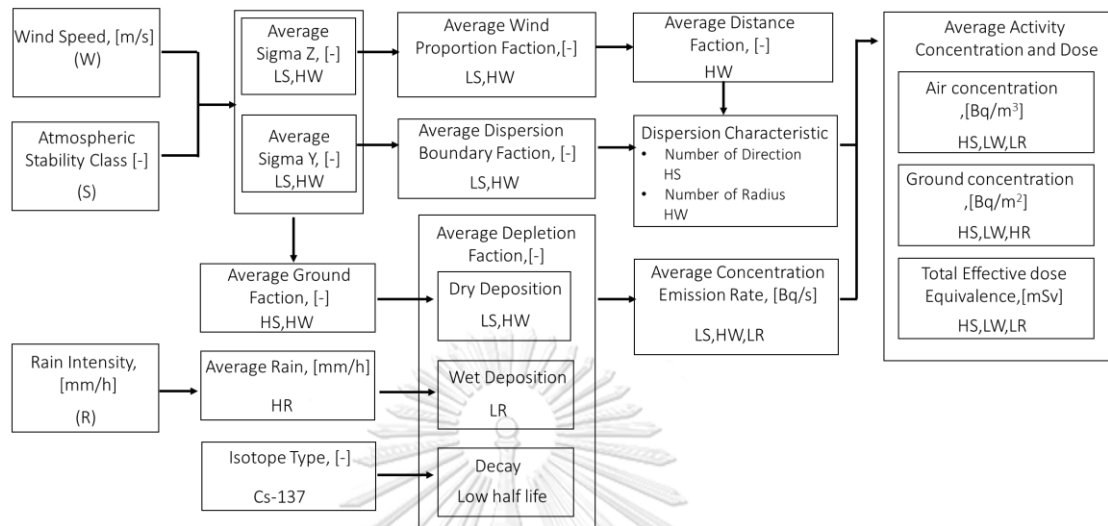


Figure 41 Combinations of meteorological parameters causing the highest value of each calculation parameter in NACAC

4.6 Results of investigating the influences of variations in meteorological data on the predicted results

This section demonstrated results according to the investigation process described in section 3.6. the influences of variations in meteorological data on predicted results were investigated for a year and five years, as detailed in sections 4.6.1 and 4.6.2, respectively.

4.6.1 Influences of variations in meteorological data on predicted results for a year

4.6.1.1. Change in meteorological data over one year

Hourly meteorological data in 2016 within a radius of 900 km was collected to use as sample data for investigating meteorological change in a year. The frequency distribution of wind directions and the average values of wind speed, rain, and atmospheric stability class in each month were plotted to obtain characteristics of these parameters in each season.

As for changes in wind direction, Figure A-4 in Appendix A showed the frequency distribution of wind directions of 10 layers in 2016. It was found that wind directions were separated into two patterns: wind directions of the first seven layers and the last three layers. To simplify the analysis, the two groups' wind directions were plotted by the wind pathway form, as shown in Figure 42. The green and blue colors represented the wind pathways in the first seven and last three layers.

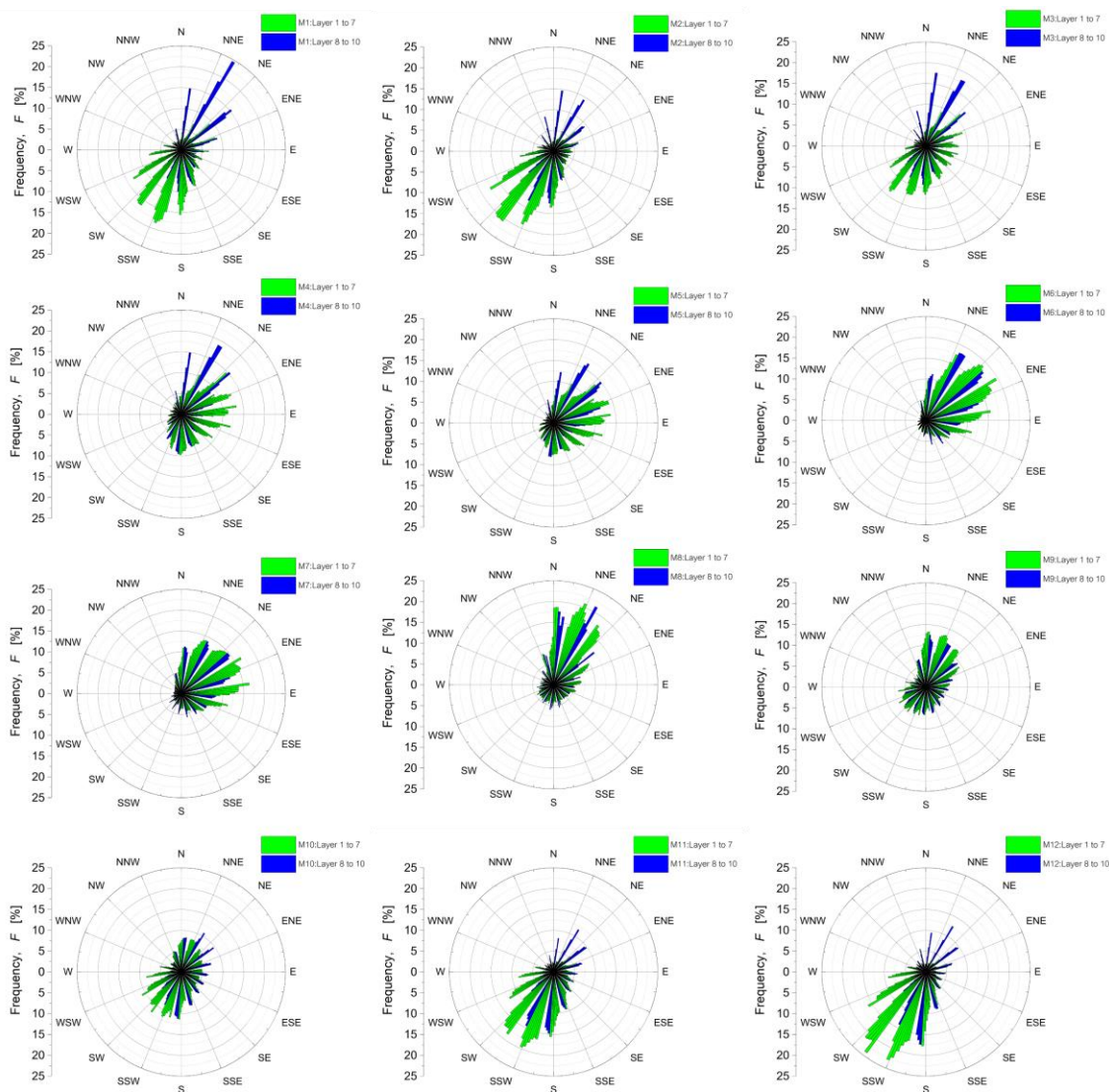


Figure 42 Wind pathway in the first seven and last three layers in each month in 2016

It was noted that the wind directions of the first seven layers changed more than the wind directions of the last three layers. As for the first seven layers, the dominant wind directions changed clockwise. It started with the SW direction in the period 1st to 3rd month. Then, it moved to the N up to NE directions from 4th to 6th month and changed to the NE up to E directions from 7th to 9th month. Finally, it moved to the SW direction from 10th to 12th month. As for the last three layers, the NNE direction was the dominant wind direction in the first three months. Meanwhile, the ENE and E directions have been the dominant wind directions for the 4th to 9th months. As for the last three months, it noted that most wind moved to SSW and S direction. This investigation showed that changing wind direction could separate into stable and unstable wind direction parts. The 4th and 9th months were transition periods between both parts with more change in wind direction than the other periods.

As for changes in wind speed, Figure 43 showed each layer's monthly average wind speed values in 2016. It was found that the average wind speed varied with altitude. Changing the characters of the average wind speed values in each layer was similar. The high average value was found in the first and last three months. Meanwhile, the low average value was found in the 4th to 9th month period. As for changes in rain intensity and atmospheric stability class, it was noted that the changing behavior of both parameters on a monthly had a similar trend line, as shown in Figure 44. The average values of both parameters decreased in the first and last three months. In contrast, they increased in the 4th to 9th months.

The above investigation noted that changing meteorological data in a year could be categorized into two parts according to changes in the dominant wind direction of the first seven layers. Firstly, the stable wind direction occurs in the year's first and last three months. The trend line of average wind speed was increased. Meanwhile, the

trend line of average atmospheric stability class and rain intensity was decreased. The dominant wind directions of the first seven layers were stable in the SW direction. Meanwhile, the dominant wind direction of the last three layers was the NNE direction in the first three months and the SSW and S directions in the last three months.

Secondly, the unstable wind direction part occurred from 4th to 9th month of the year. The trend line of average wind speed was decreased while average atmospheric stability and rain intensity was increased. The dominant wind direction changed clockwise for the first seven layers. It transfers from SW to N directions, changes between N up to E directions, and moves from E to SW directions, respectively. The dominant directions for the last three layers were between ENE and E directions.

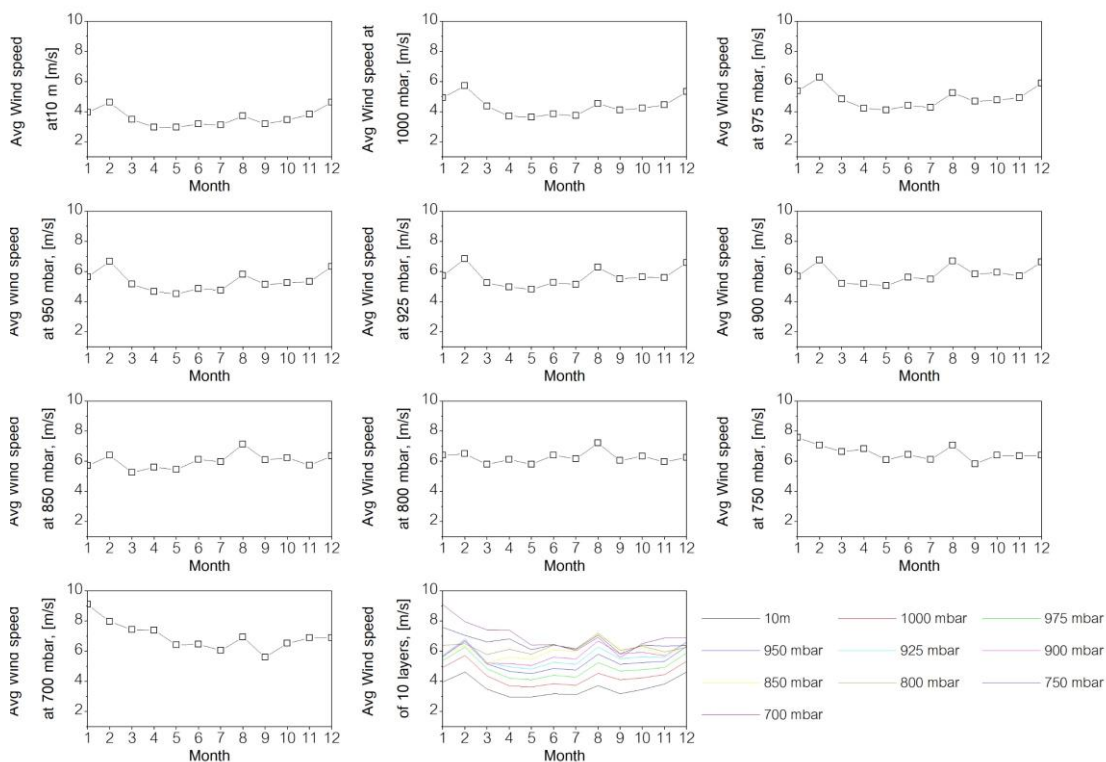


Figure 43 Monthly average wind speed value of each layer in 2016

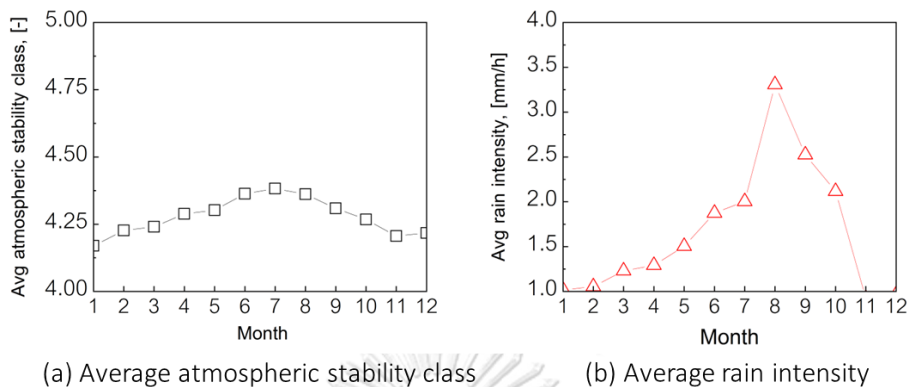


Figure 44 Monthly average (a) atmospheric stability class and (b) rain intensity in 2016

4.6.1.2 Change in projected results over one year

Dispersion characteristics

Simulation using sequential data selection was used to evaluate the radiation effect for 24 hours of the hypothetical accident at Fangchenggang NPP. The simulation was performed with meteorological data in 2016. The predicted results at the 50th, 90th, and 99.5th percentile of air concentration, ground concentration, and TEDE values were used to analyze changing dispersion characteristics and concentration values. As mentioned in section 4.5, air concentration, ground concentration, and TEDE dispersion maps were the same pattern. Thus, the dispersion maps of TEDE were used as the representative in this investigation. Figures 45, 46, and 47 showed the TEDE dispersion maps for 24 hours at the 99.5th, 90th, and 50th percentile in each month in 2016.

The result comparison showed that the predicted results at the 99.5th percentile had the greatest dispersion and the highest TEDE values, followed by the predicted results at the 90th and 50th percentile, respectively. Generally, the dispersion maps of the three percentile are consistent with meteorological data in each month. As for dispersion maps at the 99.5th percentile,

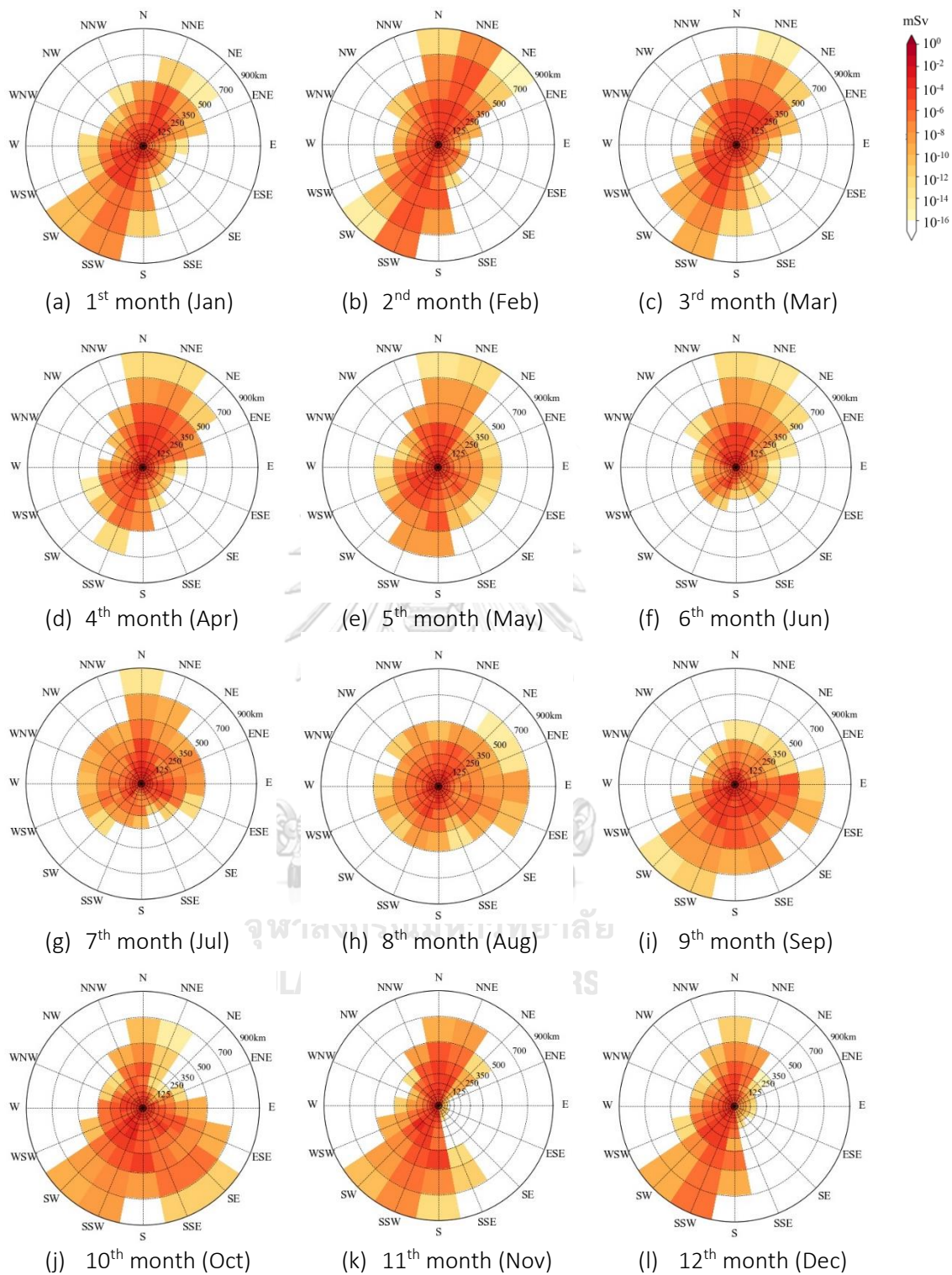


Figure 45 TEDE in 2016 at 99.5th percentile

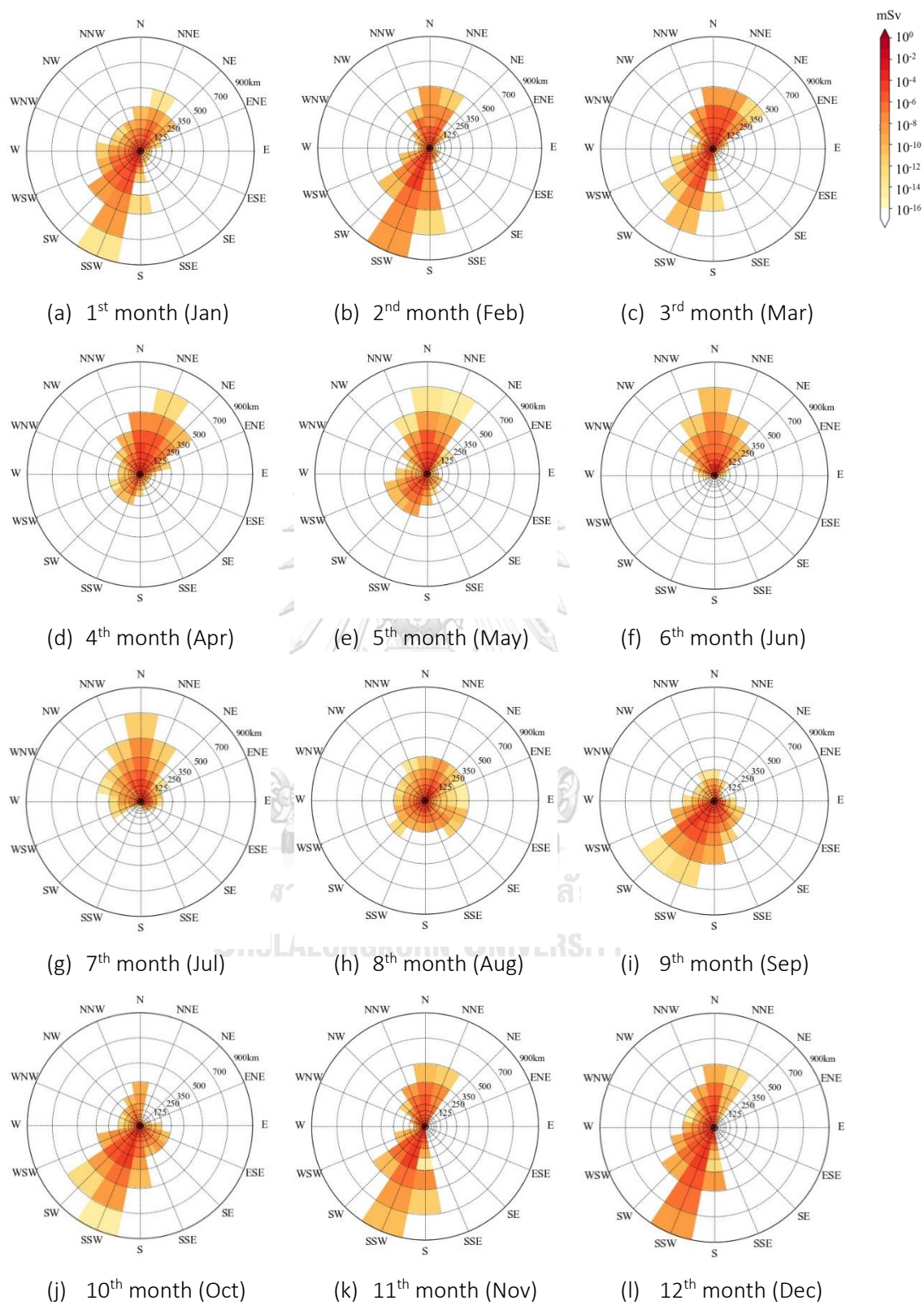


Figure 46 TEDE in 2016 at 90th percentile

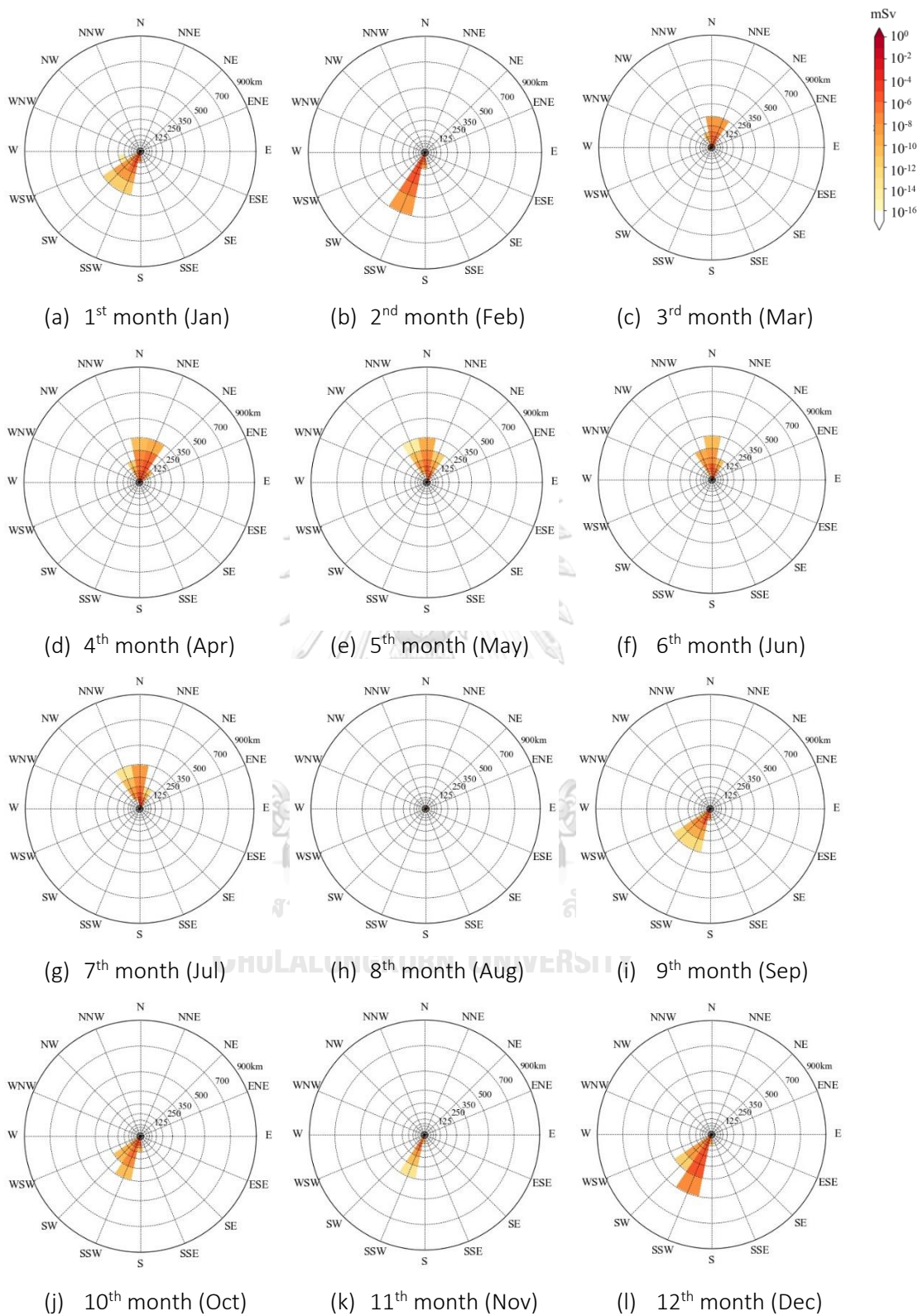


Figure 47 TEDE in 2016 at 50th percentile

Figure 45 showed that changing dispersion characteristics at the 99.5th percentile correlated with changing meteorological parameters, as mentioned in section 4.6.1.1. Figures 45 (a-c) and 45 (j-l) showed that the dispersion of radionuclides in the 1st up to 3rd and 10th up to 12th month was wide and long. Most of the radionuclides dispersed to SSW up to SW directions and N up to NNE directions with high concentration.

This is because the meteorological characteristic in these periods was the stable wind direction part consisting of low rain intensity, low atmospheric stability class, and high wind speed. These conditions correlated to the nature of case No. 7 in section 4.6. The high wind speed and low atmospheric stability class caused wide and long dispersion. The low rain intensity caused a low depletion of the emission concentration rate, leading to a high concentration value in each dispersion location. In addition, the low atmospheric stability class caused a high diffusion coefficient in the vertical direction. Hence, wind in the low and high layers was used in advection calculation. It caused most of the radionuclides to disperse to the SW and NNE directions, which were dominant wind directions of the first seven and last three wind layers of the first and last three months in 2016.

Meanwhile, Figures 45 (d-i) showed that the concentration of TEDE and dispersion distance from the 4th up to 9th months was lower and shorter than those of the first and last three months. Most radionuclides disperse from SSW to N directions and move from N up to E directions and from E to SSW directions, respectively. This is the influence of meteorological characteristics in the unstable wind direction period.

In the 4th up to 9th months, meteorological characteristics in this period were high rain intensity, high atmospheric stability class, and low wind speed correlating to the nature of case No. 6 in section 4.6. The low wind speed and high atmospheric stability class caused short and narrow dispersion. Meanwhile, the high rain intensity caused high depletion, resulting in a low concentration value, especially in the eighth month with the highest rain intensity. The dispersion distances in this month were the shortest, and the TEDE values were the lowest, especially the predicted results at the

50th percentile, as shown in Figure 47 (h). The high atmospheric stability class caused a low diffusion coefficient in the vertical direction. Thus, the wind data in the low layer was likely to be used in advection calculation.

As for the dispersion direction, the 4th month was the transition from the stable to unstable wind direction parts. Thus, most radionuclides used to disperse in SSW and NNE directions move to the N direction, which was the dominant wind direction of the first seven layers of this month. In the 5th up to 8th month, most radionuclides dispersed between N up to E directions correlated with the dominant wind directions of the first seven layers in this period. In the 9th month, this month was the transition from the unstable to stable wind direction parts. Thus, the dispersion of most radionuclides moves from E to SSW direction. Meanwhile, dispersion characteristics at the 90th and 50th percentile correlated with dispersion characteristics at the 99.5th percentile with the dominate dispersion direction. However, the concentration values in some directions were decreased according to percentile levels, leading to the disappearance of some dispersion directions, as shown in Figures 46 and 47.

Activity concentrations

As for activity concentration, average air concentration, ground concentration, and TEDE values in each radius location of each month were calculated to investigate changing activity concentration at the 50th, 90th, and 99.5th percentile. Since the trend lines of activity concentration by Cs-137 and I-131 were the same, predicted results by I-131 with higher activity concentration were used as representative results for the investigation. Figure 48 showed the average air concentration values of I-131, the ground concentration values of I-131, and TEDE values by I-131 and Cs-137 at the 50th, 90th, and 99.5th percentile in each month. The dashed blue and green lines represented the stable wind direction part in the period of 1st to 3rd and 10th to 12th month. The dotted red lines represented the unstable wind direction part in the 4th to 9th month period. The

solid black line was an average value in a year. The symbols from a square to a pentagon in each color presented the order of the months in each range.

It was noted that the trend lines of air concentration values, ground concentration values, and TEDE values in each percentile were similar. Generally, a concentration value of predicted results in the stable wind direction part with low rain intensity was close to the average in a year. Meanwhile, a concentration of predicted results in the unstable wind direction part with high rain intensity was lower than the average value in a year, especially a result of the 8th month with the highest rain intensity.

As for air concentration, it was found that the predicted results for each month at the 90th and 99.5th percentile were rather consistent within a radius of 100 km. Contrarily, the difference in predicted results about 1 up to 6 and 1 up to 5 orders of magnitude was found in a radius of more than 100 km of predicted results at 90th and 99.5th percentile. As for predicted results at the 50th percentile, the most consistently predicted results with the average value of a year were found within a radius of 10 km, while different predicted results of about 1 up to 7 orders of magnitude were found after that. The most differences were found in the unstable wind direction part with high rain intensity.

As for ground concentration and TEDE values, the trend lines of both parameters were consistent with the trend lines of the air concentration. The maximum difference in both parameters at the 90th and 99.5th percentile was around 6 orders of magnitude, while the maximum difference at the 50th percentile was around 7 orders of magnitude.

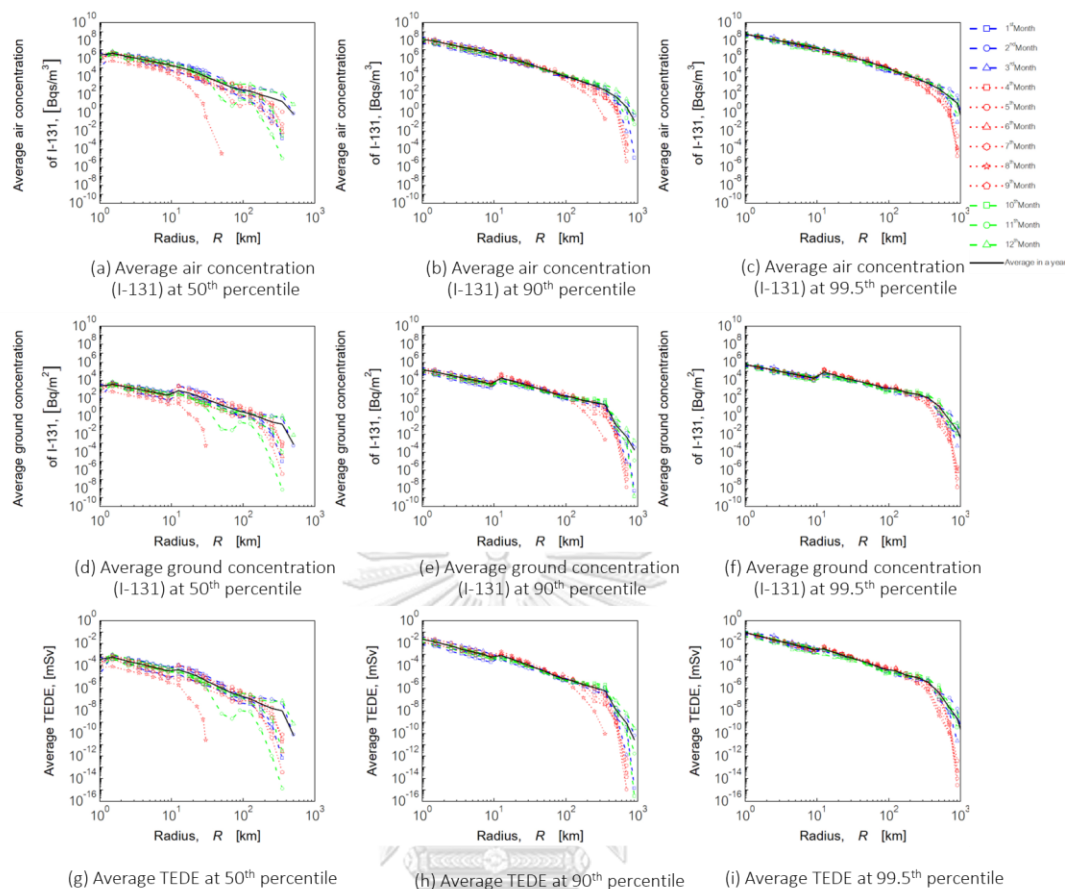


Figure 48 Monthly average activity concentration in each radius location at 50th, 90th, and 99.5th percentile in 2016

จุฬาลงกรณ์มหาวิทยาลัย

4.6.2 Influences of variations in meteorological data on predicted results for five years

4.6.2.1 Change in meteorological data over five years

Hourly meteorological data from 2016 up to 2020 within a radius of 900 km was collected and compared by averaged value to demonstrate the different characteristics of meteorological data in each year. The wind data at 10 m most significantly affected advection calculation in NACAC, as mentioned in section 4.2.2. Thus, wind speed and wind direction at 10 m were used as representatives from the ten layers of wind in this investigation.

Figures 49 (a), (b), and (c) showed the average atmospheric stability class, rain intensity, and wind speed at 10 m within a radius of 900 km. Meanwhile, Figure 50 showed the frequency distribution of wind directions at 10 m each year. Generally, it was found that meteorological characteristics in each year were similar, corresponding to changing meteorological data in a year described in section 4.6.1.1. The meteorological characteristics at the beginning and end of the year had low atmospheric stability class, low rain intensity, and high wind speed. Most of the wind blew in the SW direction. In contrast, the meteorological characteristics of the middle of the year were opposite: high atmospheric stability class, high rain intensity, low wind speed, and dominant direction change clockwise from SW to NE and NE to SW directions.

However, some differences in meteorological characteristics of each year were also found. The obvious difference was shown in the average rain intensity in Figure 49 (b). The high average rain intensity was found from the 6th to 9th month in 2017 to 2019, but this kind of weather was delayed for a month in 2016 and 2020. The average wind speed of 10 m in 2020 was the lowest in the 6th to 9th month but highest in the 10th month, as shown in Figure 49 (c). In addition, the proportion of wind in each direction in each year was different. It was clearly found in the 4th to the 9th month, as shown in Figures 50(e-j). Although the dominant wind direction in each year changed clockwise, the change period of each year was different.

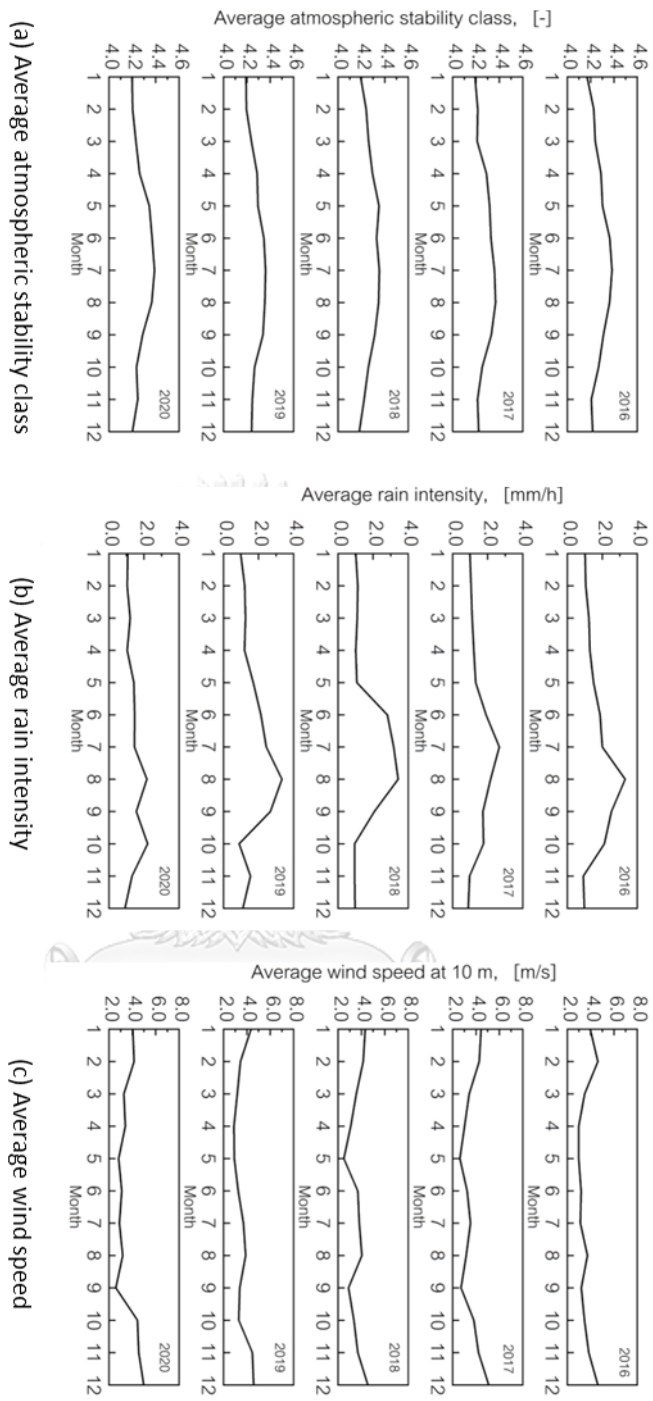


Figure 49 Average hourly meteorological parameter in each year within a radius of 900 km from Fanhchengang NPP

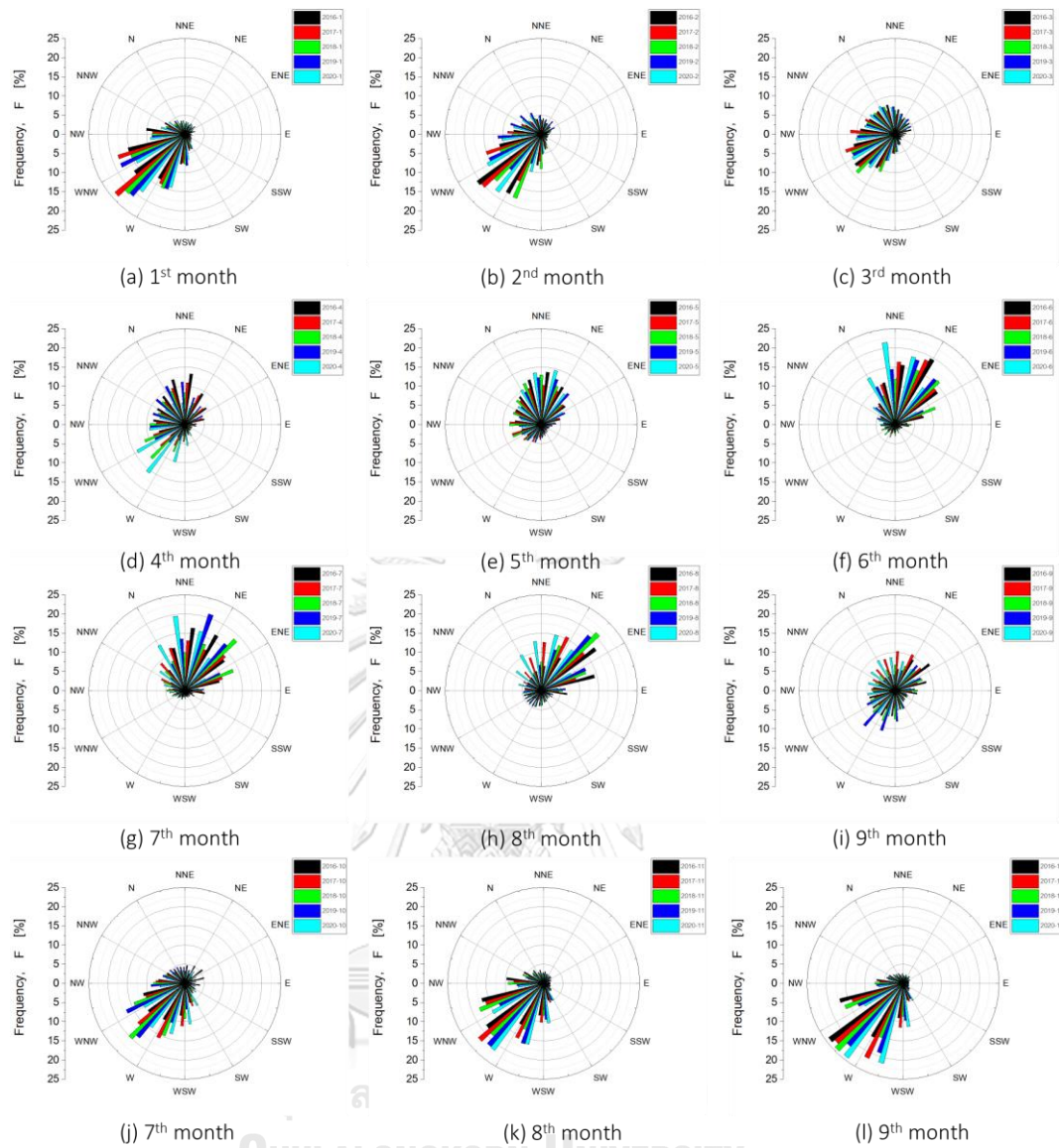


Figure 50 Frequency of wind direction at 10 m of each year within a radius of 900 km from Fangchenggang NPP

These differences were identified with AMBE, RMSE, and CC statistical methods by comparing hourly meteorological data in each year and average value over five years, as shown in Figure 51.

The result comparison shows that the atmospheric stability class of each year has similar changes, with a maximum AMBE of 0.33, maximum RMSE of 0.48, and minimum CC of 0.94, as shown in Figure 51 (a), 51 (b), and 51 (c), respectively. In contrast, the other parameters were rather different. Most differences were found in the unstable wind direction part (the 4th and 9th months). The wind direction was the highest difference, followed by rain intensity and wind speed. It was noted that the frequency distribution of wind direction in each year was different every month, with a maximum AMBE of 2.15% and RMSE of 2.76 %, as shown in Figures 51 (d) and 51 (e). Meanwhile, CC showed that the transition between stable and unstable wind direction was the most different, with a CC value of about 0.7%, as shown in Figure 51 (f).

As for the rain intensity, the most difference was found in the period of the 5th to 10th month with rainfall occurring. Figures 51 (g), 51 (h), and 51 (i) showed that the maximum AMBE, maximum RMSE, and minimum CC are 1.64 mm/h, 2.75 mm/h, and 0.45, respectively. The differences in wind speed were not much different but found throughout a year with a maximum AMBE of 1.37 m/s, maximum RMSE of 2.94 m/s, and minimum CC of 0.72, as shown in Figures 51 (j), 51 (k), and 51 (l).

These comparisons showed that meteorological parameters in each year changed with a similar pattern but did not change with the same ratio. The consistency in each meteorological parameter between a single year and the five-year average was medium up to high correlate.

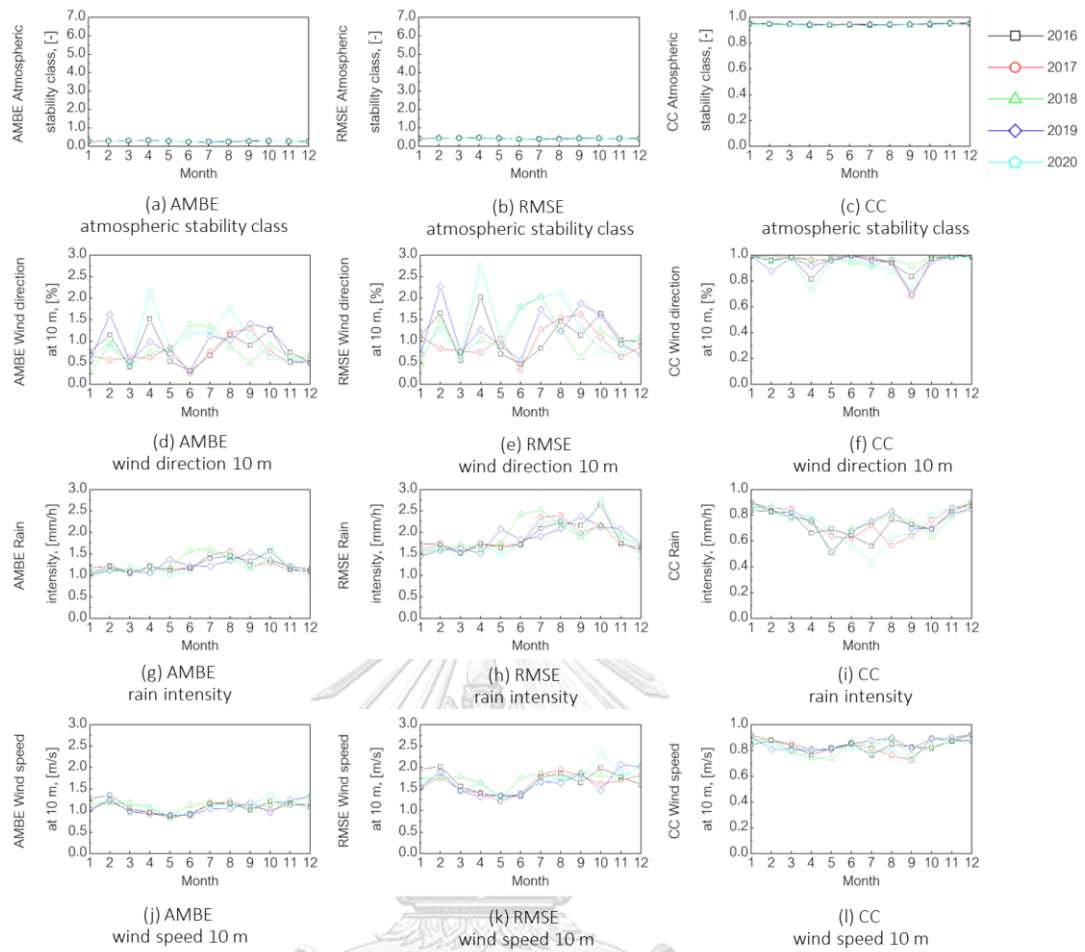


Figure 51 Monthly statistical values of AMBE, RMSE, and CC, demonstrating differences in each meteorological parameter in each year from the average value over five years.

4.6.2.2 Change in predicted results over five years

To demonstrate the influences of variation in meteorological data from each year on predicted results, simulations were conducted using sequential data selection with monthly meteorological data for each year and over five years. The simulation was carried out with the hypothetical severe accident at Fangchenggang NPP to evaluate the radiation effect for 24 hours. The predicted results of air concentration, ground concentration, and TEDE at the 50th, 90th, and 99.5th percentile were calculated to demonstrate radiation effect at medium, severe, and critical consequence levels. The effects of variation in meteorological data on dispersion characteristics and activity concentration were examined.

Dispersion characteristics

The influences of meteorological data variation on dispersion characteristics were investigated. As mentioned in section 4.5, the dispersion characteristics of air concentration, ground concentration, and TEDE were the same. Thus, the dispersion characteristic maps of TEDE were used as a representative in this investigation, as shown in section A5 in Appendix A. Typically, the dispersion characteristics of predicted results at 50th, 90th, and 99.5th percentile were correlated. However, some dispersion parts in the 99.5th percentile disappear in the 90th and 50th percentages according to the consequence level. The disappearance of some dispersion parts in predicted results at the 90th and 50th percentile might cause a misinterpretation of the effects of meteorological data variation. Thus, the dispersion characteristics at the 99.5th percentile, providing clear variation from the influence of different meteorological data, were considered.

Generally, the dispersion characteristics of each year were similar and related to the dispersion characteristics of a year described in section 4.6.1.2. They changed according to meteorological characteristics each month. The low atmospheric stability class, low rain intensity, and high wind speed in the first and last three months corresponded to Case No. 7 or 8, causing wide and long dispersion distances. Most radionuclides dispersed to the dominant wind directions of the first seven and last three

layers: S to WSW and ENE to NNW direction, respectively, as shown in section A6 of Appendix A. Meanwhile, the high atmospheric stability class, high rain intensity, and low wind speed in the middle of the year (4th to 9th month) corresponded to Case No. 5 or 6, causing narrow and short dispersion distances. Most radionuclides dispersed along with the dominant wind directions of the first seven layers of wind, changing clockwise between SW and NW directions.

However, variations in meteorological data of each year also caused variations in the monthly dispersion characteristic. The comparison results showed that the obvious difference is found in the 4th to 10th month, with a high variant of each meteorological parameter. In the 4th month, Figure A-9 showed that the dispersion characteristics of 2016 and 2019 differed from the others, with shorter dispersion distances in the SW and SSW directions. Generally, each year's average rain intensity, atmospheric stability class, and wind speed were not much different. However, the investigation of the dominant wind direction showed that the frequency of wind direction in SW and SSW directions in 2016 and 2019 was lower than the others, as shown in section A6 in Appendix A. This resulted in the transportation of radionuclides in 2016 and 2019 being lower than the others in those directions.

In the 5th month, Figure A-10 showed that the dispersion characteristics of 2018 were different from the others. The radionuclide did not disperse in the S up to SSW directions. This was the effect of differences in atmospheric stability class. Figure 49 showed that the average stability class in the 5th month of 2018 was the highest, with a value of 4.35. This resulted in a low diffusion coefficient in a vertical direction. It caused low wind in the last three layers used in the advection calculation. However, the dominant wind direction of the first seven layers in the 5th month of 2018 was mainly found from the NW up to NNW directions, while the E up to SSW directions had a lower occurrence rate than the other. Consequently, the radionuclides in the 5th month of 2018 were low dispersed in the S up to SSW directions.

In the 6th month, predicted results of each year showed that most radionuclides were dispersed in the N direction, as shown in Figure A-11. However, predicted results in 2018 indicated that some radionuclides dispersed in the E direction. This was the effect of different atmospheric stability class and different wind direction. Since the average stability class in the 6th month of 2018 was low, the wind data at the last three of the ten layers were used in the advection calculation. The wind data in 2018 had the highest occurrence in the E direction. This resulted in some parts of the radionuclides in 2018 being dispersed in the E direction.

In the 7th month, since the frequency of wind direction in each direction was similar in this month, radionuclides disperse in all directions, as shown in Figure A-12. However, the dispersion characteristic of 2020 differed from the others, with low dispersion in the W to NW directions and the ENE to ESE directions. This was the effect of different atmospheric stability classes and wind direction. The average stability class in the 7th month of 2020 was the lowest, with a value of 2.88. The wind data at the last three-layer was used in the advection calculation. However, the characteristics of the wind in 2020 differed from the others. More winds moved to the N to NW directions than in other years, while fewer winds blew in the other direction every year. This resulted in the dispersion distance of 2020 being longer than the others in N up to NW directions but lower than the others in other directions.

In the 8th month, the dispersion distances in each year were short because of the high rain intensity effect, as shown in Figure A-13. However, the dispersion characteristic in each year was quite different in this month. A dominant dispersion direction in 2017 and 2020, 2016 and 2018, and 2019 was the N, E, and SSW direction, respectively. This was because each year had a different wind pattern. The wind pattern of 2017 and 2020 was similar, with a higher frequency of wind in NNE up to WNW directions than the other years. Meanwhile, the wind patterns of 2016 and 2018 had a high frequency of wind direction in the E up to NE directions. The frequency of wind direction in 2019 was higher than the others in W up to S directions. This resulted in the dominant dispersion direction of each year being different.

In the 9th month, Figure A-14 showed that the dispersion characteristics in each year were all different. Since the wind direction patterns of each year in this month were quite inconsistent compared with the other months. This led to the dispersion direction in each year being quite different. However, it also obtained that most radionuclides each year dispersed to the SSW direction.

In the 10th month, Figure A-15 showed that the dispersion characteristic of 2016 and 2017 was rather different than the others. They have high dispersion in the SSE up to ESE directions. In addition, the radionuclides in 2016 dispersed in the N direction higher than in other years. Meanwhile, the radionuclides in 2017 dispersed in the N direction lower than in the other years. This was the effect of different wind direction patterns. Although the wind direction pattern of each year in this month is similar with high frequency in the NW to SSW directions, the frequency of data in this period of 2016 and 2017 was lower than the others. However, frequencies in the S up to N directions and SSW up to ESE directions of 2016 and 2017 were the highest, respectively. This difference led to inconsistent dispersion characteristics each year.

As for dispersion characteristics by five years of meteorological data, the comparison result showed that the simulation with monthly meteorological data over five years provided more comprehensive dispersion characteristics than the simulation with monthly meteorological data of a single year. It gave dispersion characteristics similar to dispersion characteristics by an average of a single year that showed predominant characteristics of each year. However, the high consistency of dispersion characteristics by the average and the five years was found in the month with a low variation of meteorological data.

As for the month with a high variation of meteorological data, the simulations with the five years yielded results consistent with most of the yearly simulation results. A level of result consistency varied across a percentile level. The predicted results at the 99.5th percentile provided the most consistency. For example, the yearly dispersion characteristic in the 8th month was quite different by a high variant of wind patterns. The

high frequency of wind direction in 2017 and 2020 was the E up to NE directions, while in 2016 and 2018 was the NNE up to WNW directions. The wind pattern in 2019 was similar to 2016 and 2018 but higher than the others in W up to S directions. This resulted in the dominant dispersion direction of each year being different. However, the predicted results at the 99.5th percentile of simulation with the five years of meteorological data covered all dominant dispersion directions.

The predicted results at the 90th percentile of simulation by the five years were less consistent with the yearly predicted results than the 99.5th percentile. It demonstrated that most radionuclides dispersed to the NE up to NW directions, which were the overlapping directions of the three different wind patterns. However, the unique predicted results of each year were not demonstrated, such as dispersion in the E direction in 2018. Meanwhile, the predicted results at the 50th percentile of simulation with five years of meteorological data were close to zero. This was consistent with the 50th percentile of yearly predictions, where more than 50 % of the predicted results every year were close to zero by the high rain intensity effect.

In general, predictions using five-year data yielded results that were consistent with most of the data found in the annual predictions. However, high-specificity data that occurred only in one year over a five-year period will be found in predicted results at the 99.5th percentile but might not be found in predicted results at the 90th and 50th percentiles of five-year prediction results. The data presentation by percentile provided a less comprehensive dispersion characteristic than the data presentation by average in some months. However, the data presentation by percentile clearly demonstrated the radiation effect according to all consequence levels.

Activity concentrations

The influences of variations in meteorological data on activity concentration were investigated. The monthly air concentration, ground concentration, and TEDE values by a single year, average single year, and five years of meteorological data in the dominant dispersion direction of the average single-year dispersion characteristic within a radial

of 900 km were shown in section A7 in Appendix A. It was noted that trend lines of air concentration, ground concentration, and TEDE values were the same pattern. Thus, the predicted results of the TEDE values at the 50th, 90th, and 99.5th percentile were representative of this investigation, as shown in Figures 52 to 54.

Generally, The result comparisons showed that the distribution of predicted results from 2016 to 2020 was a positive skew in all months of the three percentiles. Thus, the TEDE values by average were close to the maximum value found from the predicted results of every single year. Meanwhile, the TEDE values for the five years were varied according to percentile levels. The predicted results in each year at the 99.5th percentile were the most correlated with the predicted results by an average single year and the five years, followed by the predicted result at the 90th and 50th percentile, respectively.

The predicted results at the 99.5th percentile had the longest dispersion distance. The radionuclide could disperse in the dominant dispersion direction of almost 900 km every month. The TEDE values by the five years at the 99.5th percentile were a few higher than the TEDE values by average, as shown in Figure 52. The main difference in comparing predicted results at 99.5th was found in the 7th up to 9th months in a period of 100 to 1000 km, with less TEDE values and short dispersion distances. As mentioned in section 4.5, low wind speed caused ineffective radionuclide transportation. In addition, high rain intensity led to a high depletion of the emission concentration rate, subsequently causing a short dispersion distance. The period of the 7th up to 9th months had a high variation of these parameters, as shown in Figure 49

The dispersion distance and TEDE values of 2017 and 2018 in the 7th and 8th months were the shortest and lowest compared with the other years by the influences of the highest rain intensity in that month. Meanwhile, the influences of the lowest wind speed in 2017 and 2020 of the 9th month caused the short dispersion distance. However, It was noted that the TEDE values by each year in the other months were quite correlated with the TEDE values by average and the five years. A slight difference with

a lower TEDE value was found at almost the end of a dispersion distance of around 500 to 1000 km.

The predicted results at the 90th percentile had a few shorter dispersion distances than the predicted results at the 99.5th percentile, as shown in Figure 53. The TEDE values by average were slightly higher than the TEDE values by five years. This was in contrast to the results predicted at the 99.5th percentile. However, the main difference was still found in the 7th up to 9th months in 50 to 1000 km, with the same characteristics as the 99.5th percentile comparison. Meanwhile, the TEDE values in the other months differed slightly from 500 to 1000 km.

In contrast, the predicted results at the 50th percentile were different from the other percentiles. The dispersion distances and the TEDE values were the lowest, as shown in Figure 54. The TEDE values by five years had a value in the medium found from every year's predicted result. It is clearly lower than the TEDE by average, which was close to the maximum value. As mentioned in section 4.3.1, the prediction results at the 50th percentile were lower than the average and generally close to the minimum value by the effect of the NACAC calculation pattern. This caused a high difference in the monthly TEDE values at the 50th percentile. The TEDE values by single year differed from the TEDE values by average and the five years throughout a dispersion distance with an unclear pattern. However, the highest difference was also found in the period of the 7th up to 9th month by the effects of different rain intensities and wind speeds.

As mentioned above, it noted that the predicted results of an atmospheric dispersion code depend on meteorological data. The meteorological data changed throughout the year, with the stable and unstable wind direction periods occurring from October to March and April to September. The stable and unstable wind direction periods were related to the northeast and southwest monsoon periods. Thus, it could be concluded that the radionuclide dispersion in the northeast monsoon was wide and long. Most radionuclides dispersed in the SW direction. Meanwhile, the dispersion of radionuclides in the southwest monsoon period had a short dispersion distance due to

the effects of high rain intensity. The dominant dispersion direction varied between SW and NW directions. Predicted results in each year had more variations in the southwest monsoon period than in the northeast monsoon periods.

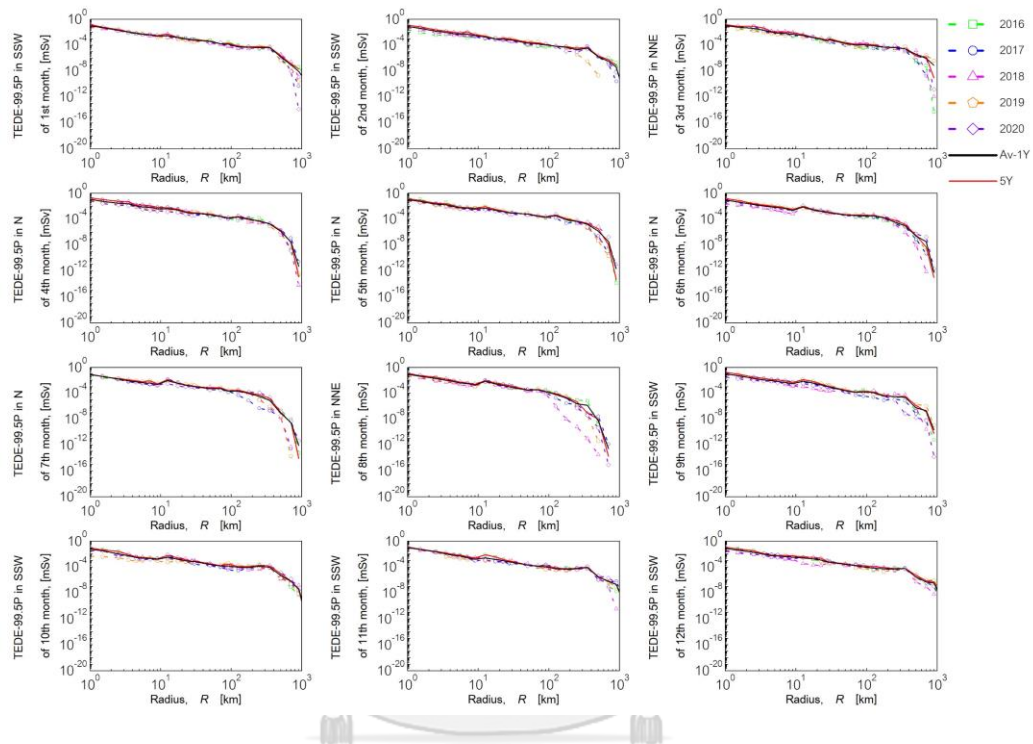


Figure 52 TEDE values at 99.5th percentile comparison in dominant dispersion direction of the yearly average dispersion characteristic

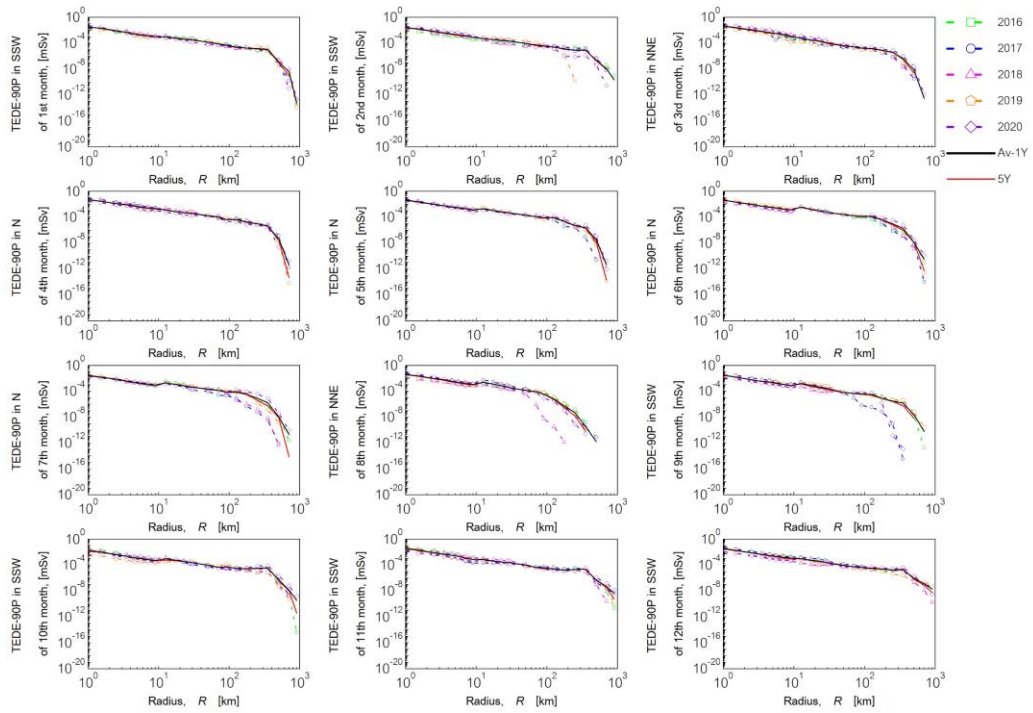


Figure 53 TEDE values at 90th percentile comparison in dominant dispersion direction of the yearly average dispersion characteristic

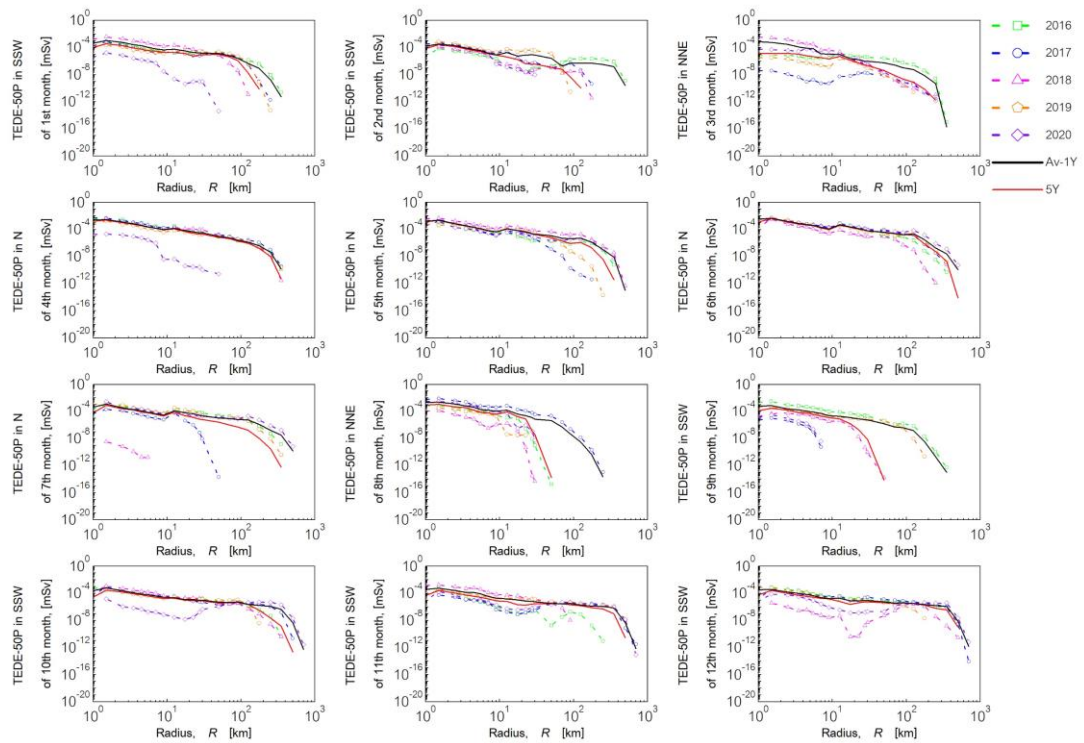


Figure 54 TEDE values at 50th percentile comparison in dominant dispersion direction of the yearly average dispersion characteristic

4.6.3 Variability of the predicted results

To quantify the variability of the predicted results from the influences of the variations in meteorological data. The predicted results at 50th, 90th, and 99.5th percentile of air concentration, ground concentration, and TEDE values by single year were compared with those by an average of every single year and five years through AMBE, RMSE, and CC methods to investigate different predicted results in each year and five years. The investigation was performed in all directions with three distances: short (0-10km), medium (10-100km), and long (100-1000 km) periods. Section A 8 in Appendix A showed statistical values in comparing the predicted results by single year and average. Meanwhile, section A 9 in Appendix A showed statistical values in comparing the predicted results by single year and five years. It was noted that the trend lines character of AMBE, RMSE, and CC of air concentration, ground concentration, and TEDE were the same. Thus, the AMBE, RMSE, and CC of TEDE were used as representatives in the investigation to demonstrate different predicted results for each year and five years.

4.6.3.1 Variation of predicted results for each year and average

Figures 55 to 57 showed AMBE, RMSE, and CC of TEDE values by a single year of meteorological data compared to averaged TEDE values over five years. Each symbol presented statistical values comparing TEDE values in each year with the average TEDE values. As mentioned above, the predicted results at the 99.5th percentile were almost the highest of all simulation results, followed by the 90th and 50th percentile. Thus, the difference in concentration of predicted results at the 99.5th percentile by a single year of meteorological data and the average TEDE values were the highest, resulting in AMBE and RMSE being the highest, as shown in Figures 55 (c, f, i) and 56 (c, f, i).

Figures 55(c) and 56(c) showed that the short distance period with the highest TEDE values had the highest variant in the 99.5th percentile with an average AMBE and RMSE of 1.85E-2 and 5.02E-2 mSv, respectively. Meanwhile, the variations of the TEDE values in the medium and long distances decreased according to the concentration levels. This resulted in average AMBE and RMSE values in medium and long distances being dropped by around 2 and 4 orders of magnitude, as shown in Figures 55(f, i) and 56 (f, i).

As for result comparisons at the 90th percentile, the high concentration of TEDE values also caused a high variation of predicted results each year. However, the variances in the TEDE values were decreased from the 99.5th percentile by lower average AMBE and REME around one order of magnitude, as shown in Figures 55(b, e, h) and 56(b, e, h). Meanwhile, the low concentration of TEDE values at the 50th percentile caused the low variation. The AMBE and RMSE values of the 8th and 9th months were the lowest by the effect of high rain intensity. It caused a high deposition of radionuclides, leading to a low concentration over a long distance. The decreased concentration caused a low variation of prediction results. Generally, It noted that the 50th percentile variance was two orders of magnitude smaller than the 99.5th percentile, as shown in Figure 55(a, d, g) and 56(a, d, g).

However, the variation investigation by the CC method demonstrated that the predicted results at the 99.5th percentile had the highest correlation, followed by the predicted results at the 90th and 50th percentile, as shown in Figure 57. The comparison results at the 99.5th percentile showed that the most consistent predicted results were found in the short distance, followed by the medium and long distance, with the minimum CC values of 0.66, 0.65, and 0.44, as shown in Figure 57(c, f, i). Generally, the lowest correlation was found in the 4th up to 9th months, with a high variation of meteorological data, as mentioned in section 4.6.2.1. This caused inconsistent

dispersion characteristics and activity concentrations each year, as mentioned in section 4.6.2.2.

The predicted results at the 90th percentile had a lower CC value than the predicted results at the 99.5th percentile. The high variation of meteorological data from the 4th up to 9th months also caused the lowest correlation in the long distance. However, it noted that predicted results by each year at the medium distance had the highest correlation, followed by the short and long distances with the minimum CC value of 0.68, 0.30, and 0.18, respectively.

This was the effect of variation in yearly wind direction patterns. The frequency distribution of wind direction from 2016 up to 2020 in section A6 of Appendix A showed that the wind data for each year tend to have a consistent frequency of wind in the main direction. However, the frequency of wind in the minor direction was different. Typically, the radionuclide was dispersed more by the main wind direction than by the minor wind direction. It caused the highest radionuclide concentration in the main wind direction. Hence, the CC values in the predicted results at the 99.5th percentile, almost the maximum value, were high. Since the dispersion characters of the predicted results in each year were highly correlated according to the main wind direction.

In contrast, the predicted results at the 90th percentile with concentrations lower than the maximum value were dispersed in the minor wind direction. The low correlation of the minor wind direction each year caused a lower correlation of the predicted results than the 99.5th percentile throughout the dispersion distance, as shown in Figures 57(e, b, h). To demonstrate this phenomenon, predicted results in the 1st month with the lowest possible variance of meteorological parameters were used.

Figure 58 showed the yearly average TEDE at the 90th percentile in short, medium, and long in the 1st month. Figure 58 (a) showed that the predicted results near the release point had the highest concentration. The dispersion of the highest

concentration in the minor wind direction caused high variation between each year, leading to low CC values, as shown in Figure 57 (b). However, the concentration of the predicted results decreased with the dispersion distance increased. It caused a close of predicted results in each direction of each year at a medium distance, as shown in Figure 58 (b). This decreased the effects of variation in minor wind direction and caused a higher CC value than a short distance, as shown in Figure 57 (e). As for the long distance, Figure 58 (c) showed that the low concentration of the predicted result was more influenced by variation in minor wind direction. This caused variations in predicted results each year, leading to a low CC value, as shown in Figure 57 (h).

As for the predicted result at the 50th percentile, it had the lowest correlation with the average value, as shown in Figures 57 (a, d, g). the CC values in the long distance were the lowest with 0 because the radionuclide could not disperse to such a distance. Meanwhile, the effects of variation in minor wind direction also caused a low CC value in the short distance. As for the medium distance, it was noted that the high rain intensity in the period of the 7th up to 8th month caused a low CC value. The minimum CC value of TEDE in the short, medium, and long distances was around 0.02, 0.01, and 0, respectively.

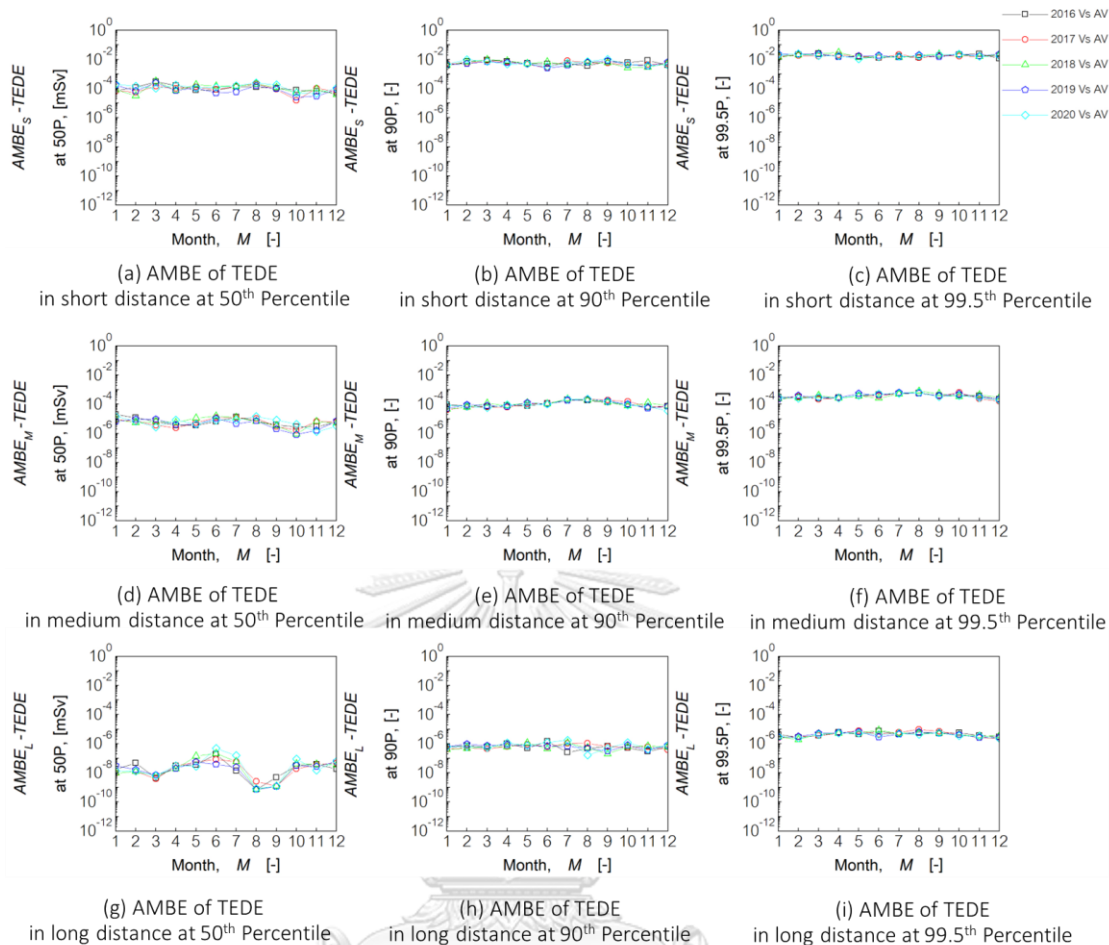


Figure 55 AMBE values in each single year of TEDE at 50th, 90th, and 99.5th percentiles compared with an average value over five years in short, medium, and long distances.

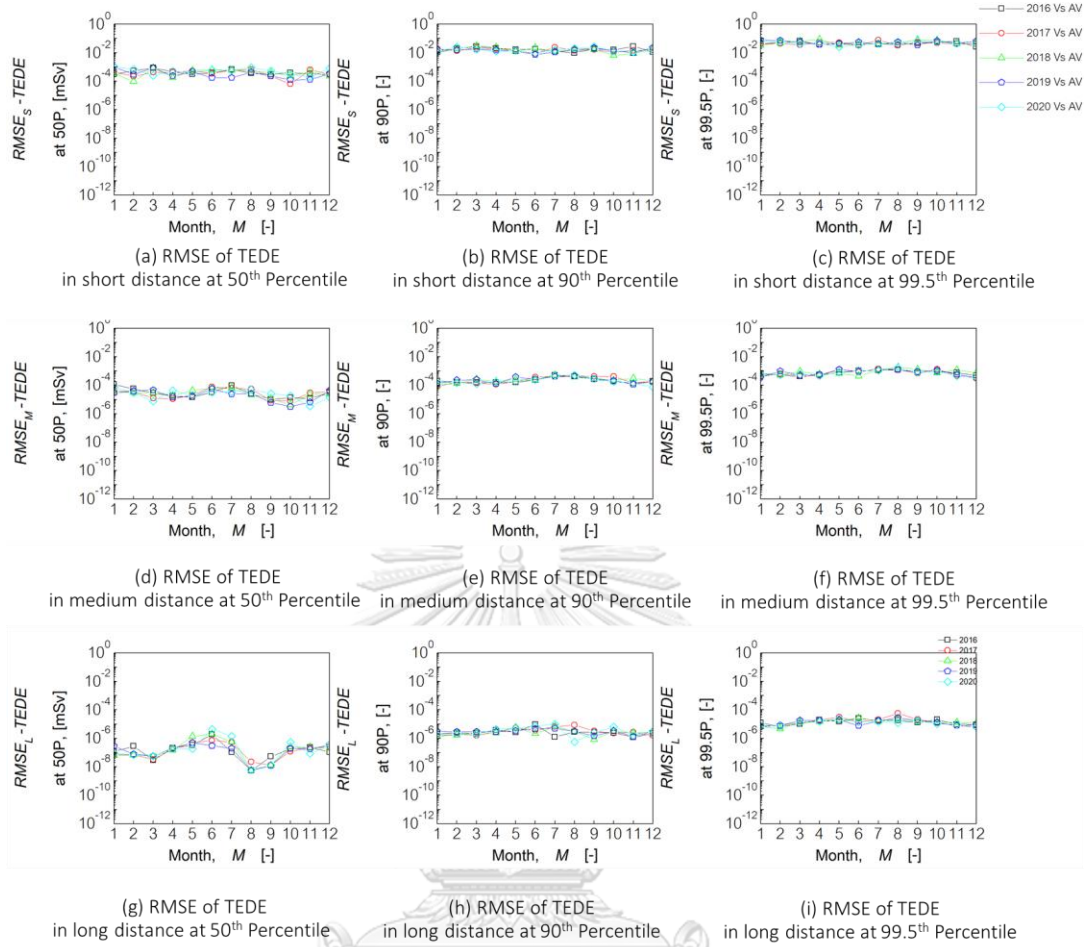


Figure 56 RMSE values in each single year of TEDE at 50th, 90th, and 99.5th percentiles compared with an average value over five years in short, medium, and long distances.

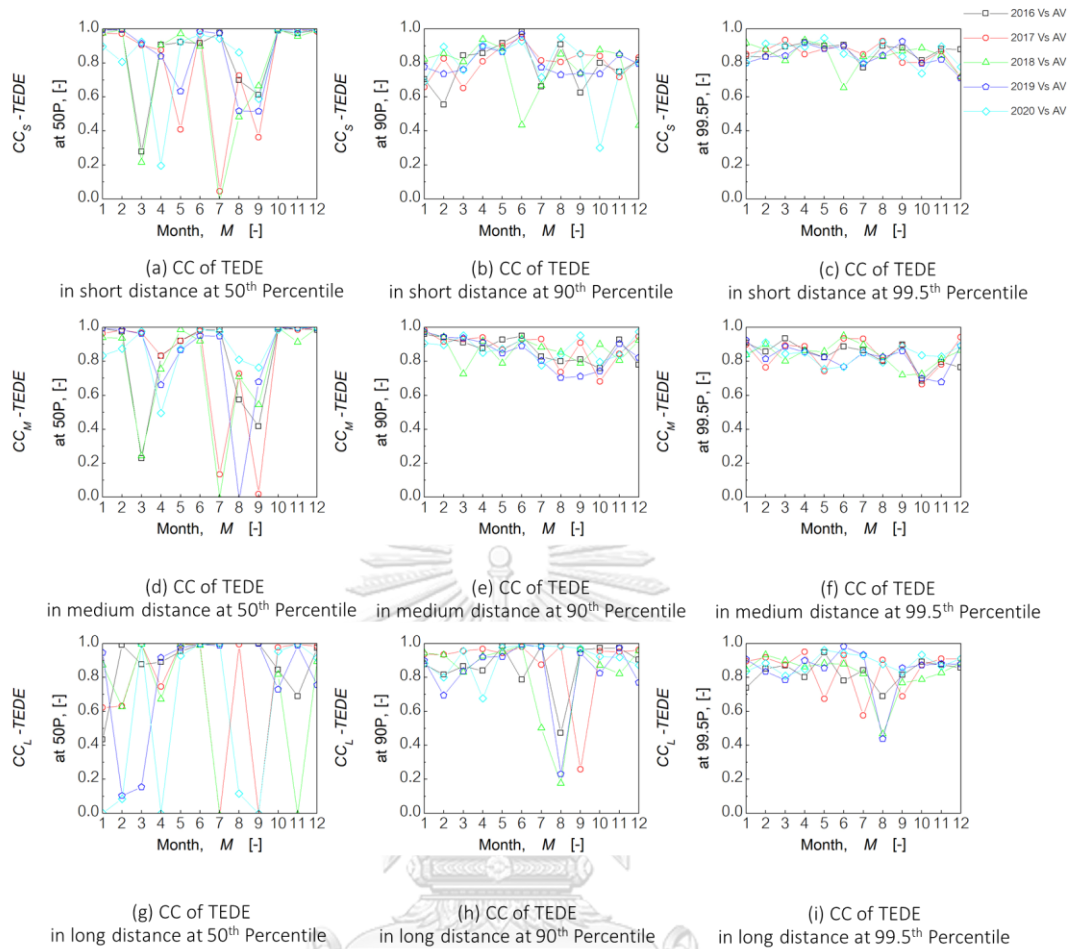


Figure 57 CC values in each single year of TEDE at 50th, 90th, and 99.5th percentiles compared with an average value over five years in short, medium, and long distances.

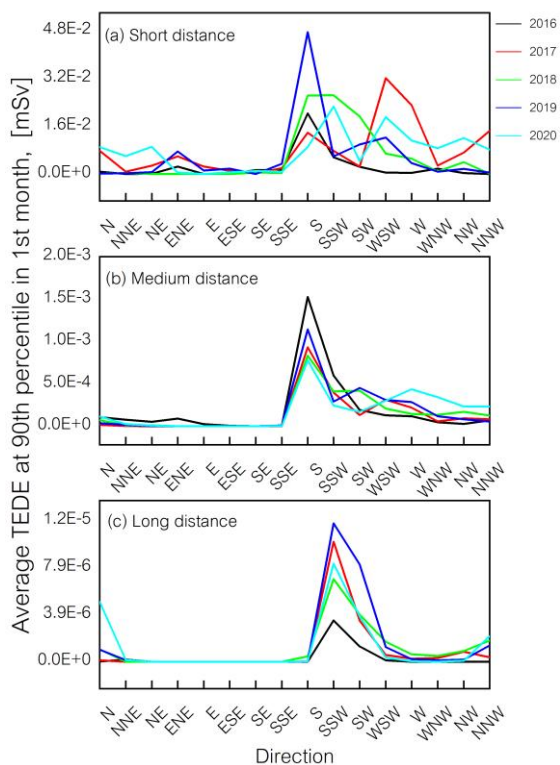


Figure 58 Yearly average TEDE values at the 90th percentile in short, medium, and long in the 1st month

4.6.3.2 Variation of predicted results for each year and five years

Figures 59 to 61 compared TEDE values for single and five years of meteorological data using AMBE, RMSE, and CC methods. The similar colors and symbols used in section 4.6.3.1 were applied here. Generally, it noted that comparing predicted results by a single year and five years was similar to comparing predicted results by a single year and the average.

As for the AMBE and RMSE investigation, the differences in predicted results at the 99.5th percentile were the highest, followed by the 90th and 50th percentile. Figures 59 and 60 showed that the highest concentration near the release point caused the highest variation in the short distance of all percentile levels. Meanwhile, a lower variation in medium and long distances was found from decreased concentration along the distance. The predicted results at the 99.5th percentile, with the highest variation,

had an average AMBE in the short, medium, and long distances of $3.07\text{E-}02$, $5.78\text{E-}04$, and $5.43\text{E-}06$ mSv, respectively. An average RMSE value in the short, medium, and long distances was found with $8.64\text{E-}02$, $1.29\text{E-}03$, and $1.82\text{E-}05$ mSv. Meanwhile, the average AMBE and RMSE values of the predicted results at the 90th and 50th percentile were lower than the predicted result at the 99.5th percentile of around one and two orders of magnitude in all distance periods. The lowest variation was found in the long distance at the 50th percentile with the 7th up to 9th month. It was lower than the variation by comparing the TEDE values by a single year and the average value of around one up to five orders of magnitude. This was because, during the 7th to the 8th month, there was a high rainfall variability between the five years. It caused different predicted results from year to year with a positive skew. Hence, the average value differed from the predicted results at the 50th percentile value.

As for the CC investigation, Figure 61 showed that the highest correlation between the predicted results by each single and five years was the 99.5th percentile, followed by the 90th and 50th percentile. The high variation of rain intensity in periods of the 7th to 9th month also caused low consistency in all percentile levels. It clearly affected the long distance with high variation due to the radionuclide not reaching it. In addition, a low consistency in the short distance of the predicted result at the 90th and 50th percentile was also a result of the variation in minor wind direction, as noted before. Meanwhile, the lowest correlation was found at the long distance of the 50th percentile by the low dispersion distance effect.

The explanation above highlighted a similar pattern between the variation of the TEDE between a single year and five years and the variation of the TEDE between each year. However, the difference between both variations was found. Most differences were shown at the TEDE values at the 99.5th percentile. Comparing TEDE values between the single year and five years had an average AMBE and RMSE values higher of around 60-70 %, 50-60 %, and 20 % in short, medium, and long distances. The average CC values

were around 2% in long distances and 6 % in short and medium distances. Meanwhile, the difference in comparing TEDE values at the 90th and 50th percentile was lower than 4% of the average CC value and 10% of the average AMBE and REME value throughout the dispersion distance. This was because simulation by five years of meteorological data provided a comprehensive predicted result more than simulation by one year of meteorological data in all radiation consequence levels.

Generally, evaluating radiation consequences at a critical level between each year, considering predicted results at the 99.5th percentile, exhibited a high variation of predicted results. This was because the meteorological data that caused the impact at the 99.5th percentile had a low occurrence rate (Rare case). The rare cause of each year caused a high variation of predicted results, as shown in Figure 62. Figure 62 showed the variation of TEDE values at the 99.5th percentile in short, medium, and long distances on the 11th month of each year. The low average wind speed of 10 m in 2016 caused a higher concentration in the short and medium distances, while a lower concentration in the long distance was found compared with the others. This clearly showed variation in predicted results from different rare case characteristics in each year.

However, evaluating radiation consequences at a critical level for five years provided a more comprehensive evaluation result, as shown in the pink line in Figure 62. It covered all characteristics of rare cases in each year causing the highest concentration. Hence, the evaluation of five years covering all phenomena was very different from the evaluation of each year covering some phenomena, especially at the short distance with the highest variation of predicted results each year.

Meanwhile, evaluating radiation consequences at a severe and medium level, considering predicted results at the 90th and 50th percentile, was a lower variation between each year and five years. This was because meteorological conditions causing radiation effects at the 90th and 50th percentile were less specific than those at the 99.5th

percentile. It led to a lower variation of meteorological phenomena, causing radiation at the 90th and 50th percentile each year. Thus, the evaluation of five years covering all phenomena and the evaluation of each year with similar phenomena had a low variation.

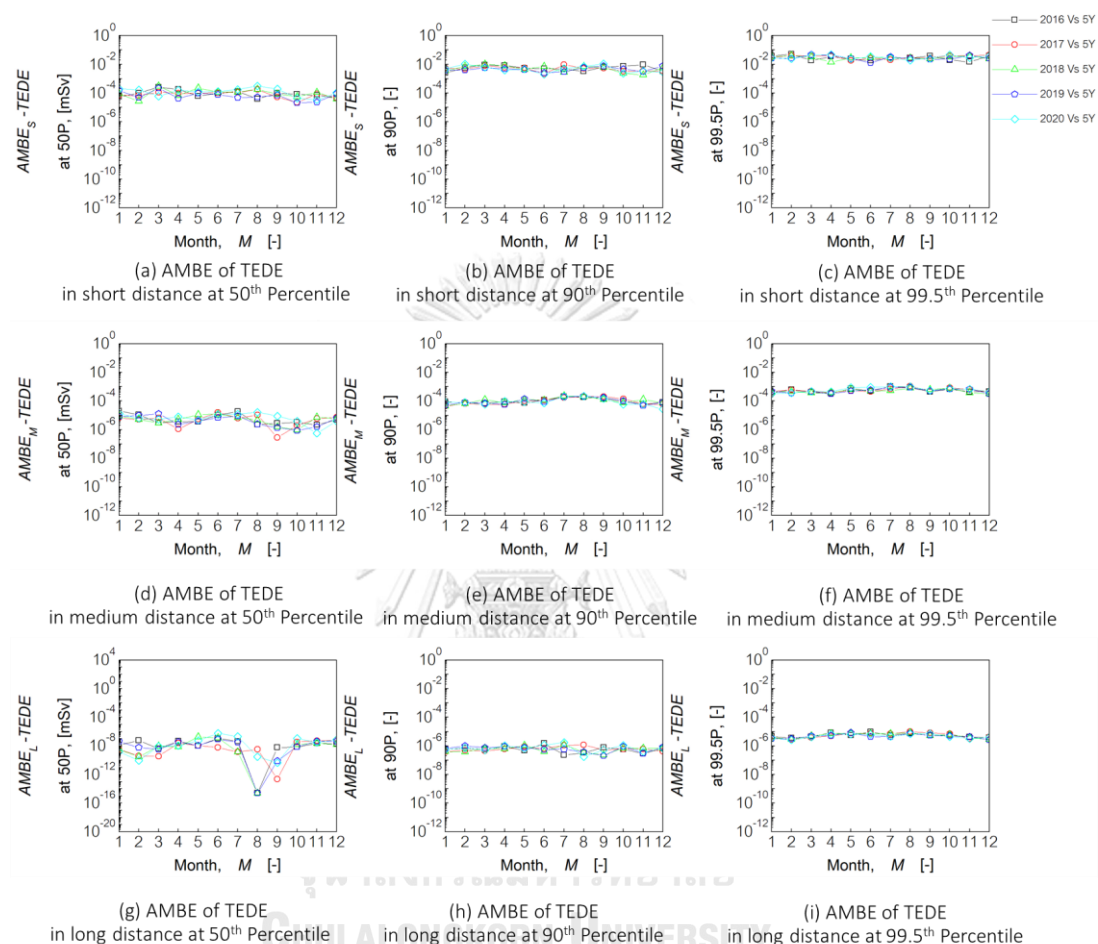


Figure 59 AMBE values in each single year of TEDE at 50th, 90th, and 99.5th percentiles compared with five years in short, medium, and long distances.

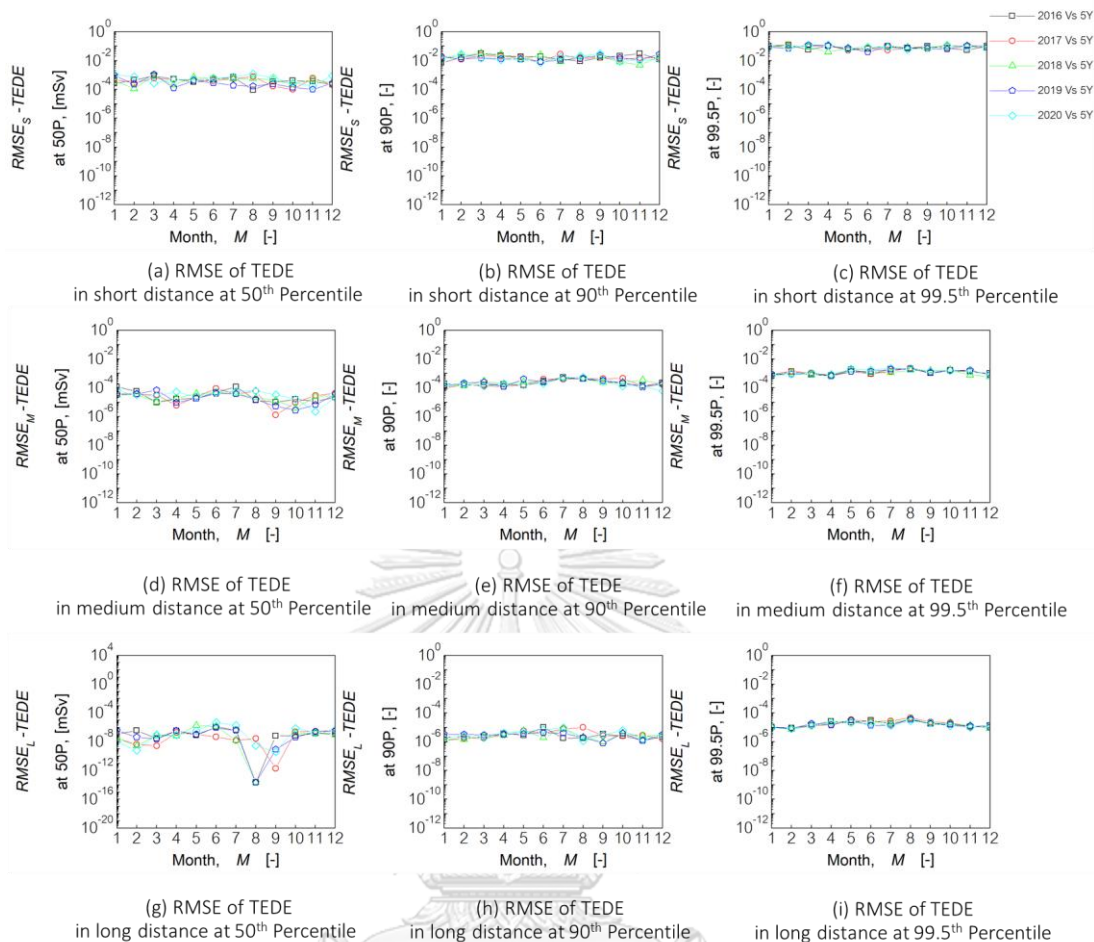


Figure 60 RMSE values in each single year of TEDE at 50th, 90th, and 99.5th percentiles compared with five years in short, medium, and long distances.

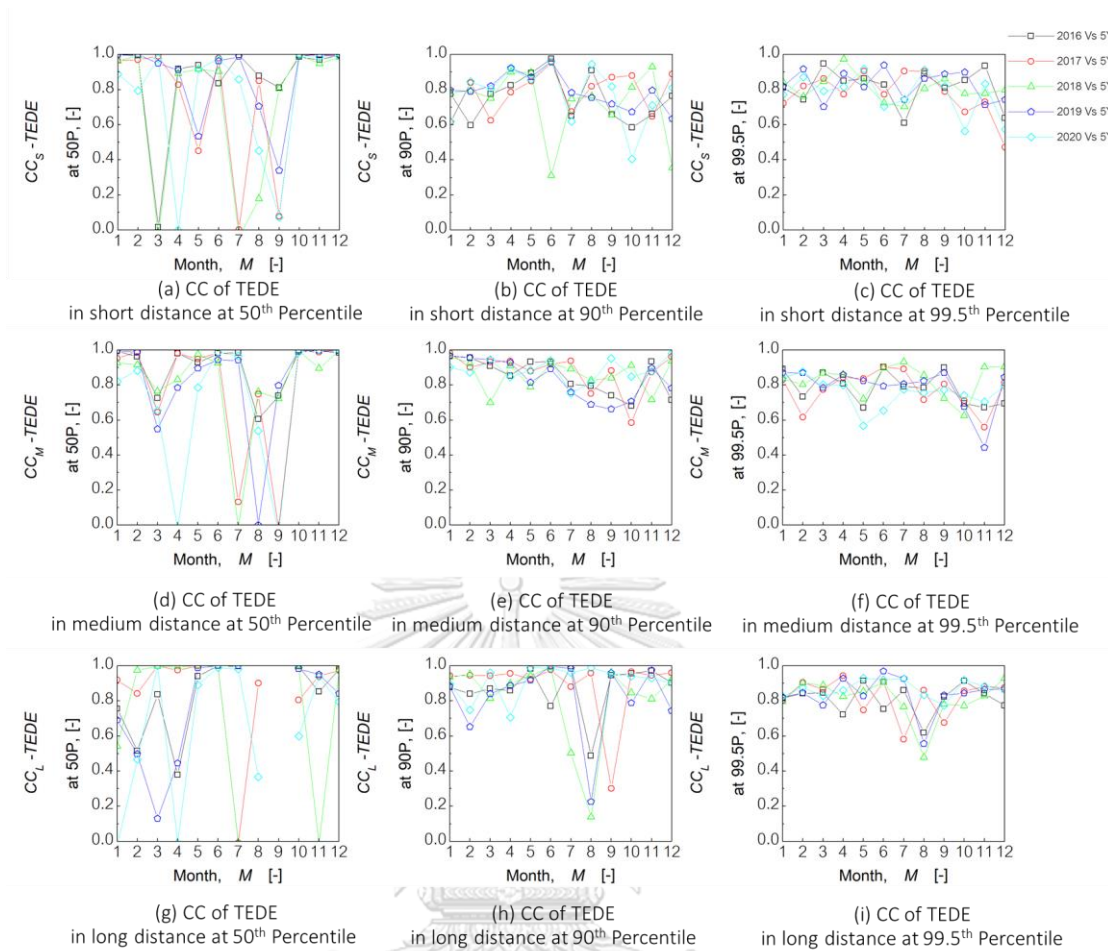


Figure 61 CC values in each single year of TEDE at 50th, 90th, and 99.5th percentiles compared with five years in short, medium, and long distances.

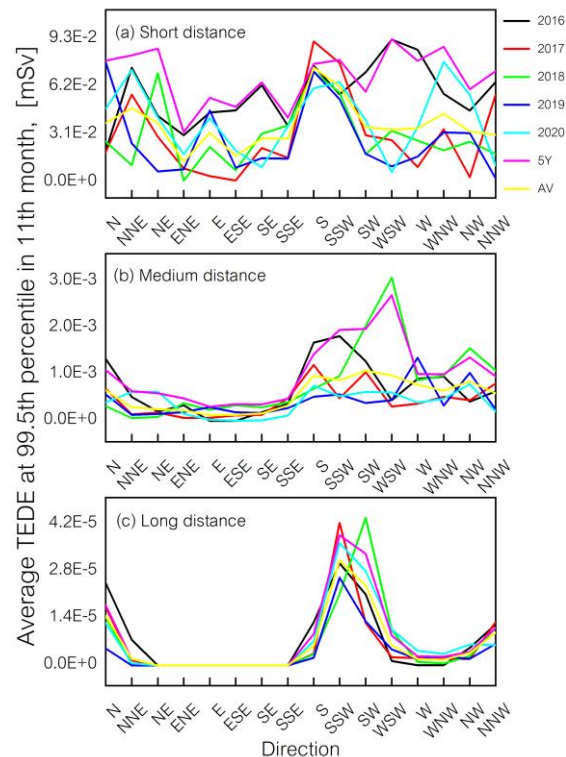


Figure 62 Variation of TEDE values at the 99.5th percentile in short, medium, and long distances on the 11th month of each year

All details mentioned above could be summarized as follows. This research was carried out in four parts. Firstly, the verification of calculation performance in NACAC was performed with methods in section 3.3. Results and discussions were demonstrated in sections 4.1 and 4.2. Secondly, appropriate meteorological data selection was investigated to define the meteorological data preprocessing process that was appropriate to examine the influences of variations in meteorological data on predicted results. This research part was conducted according to the method in section 3.4. Results and discussions were shown in sections 4.3 and 4.4. Thirdly, the influences of meteorological data on NACAC calculations were evaluated to illustrate the impact of changes in each meteorological parameter on the predicted results of the atmospheric dispersion code. The methods and results were shown in sections 3.5 and 4.5, respectively. Fourthly, The influences of variations in meteorological data on predicted

results were investigated to determine variations of predicted results in atmospheric dispersion code by the influences of variations in meteorological data in a year and five years. The critical points found in each research part were summarized in Table 17.

Table 17 Summary of research results

| Research parts | Methodology | Results |
|--|--|--|
| Verifications of calculation performances in NACAC | <ul style="list-style-type: none"> Comparing predicted results between NACAC and JRODOS | <ul style="list-style-type: none"> NACAC could offer a similar character of radionuclide concentration and transportation to the JRODOS predicted results. Differences in meteorological data preparation schemes caused different input data. Differences in the advection calculation scheme caused differences in plume trajectories. These caused variations in dispersion distances around 200 km and variations in activity concentration around one order of magnitude. |

| Research parts | Methodology | Results |
|--|---|---|
| Investigation of appropriate meteorological data selection | <ul style="list-style-type: none"> ● Representative data selection was modified for the transboundary radiation effects. ● Comparing the predicted results of simulation using representative and sequential data selection was performed to find the method that gave the most comprehensive predicted results. ● The appropriate process was used to investigate the influences of variations in meteorological data on predicted results (the fourth part of the research). | <ul style="list-style-type: none"> ● For modification of the representative data selection, the selected area boundary and the optional meteorological parameter insignificantly affected the simulation using representative data selection. ● A high sampling rate improved the accuracy of the simulation using representative data selection. ● However, preparing meteorological data by sampling method in representative data selection caused ineffective prediction results in rare cases. ● Simulation using sequential data selection providing higher comprehensive predicted results was selected. |

| Research parts | Methodology | Results |
|---|--|---|
| Influences of meteorological data on NACAC calculations | <ul style="list-style-type: none"> • Various meteorological input data were used to predict the radiation effects for 24 hours in NACAC with the same condition. • Predicted results of each meteorological input data were compared to demonstrate the effects of rain, wind, and atmospheric stability class data on atmospheric dispersion calculation. | <ul style="list-style-type: none"> • Rain data affected the depletion of emission concentration. • High rain intensity caused low concentrations of radionuclides in the atmosphere. • Wind data affected the dispersion distance of radionuclides. • High wind speed data caused long dispersion distances of the radionuclides. • Atmospheric stability class affected the boundary of radionuclide dispersion. • The unstable atmospheric stability class caused wide dispersion characteristics. • Low rain intensity, low wind seed, and stable atmospheric stability class caused the highest average TEDE values. |

| Research parts | Methodology | Results |
|---|---|--|
| <p>Influences of variations in meteorological data on predicted results</p> | <ul style="list-style-type: none"> ● The simulation using sequential data selection was performed with a single year and five years of meteorological data. ● Variations in meteorological data for a year and five years of meteorological data were investigated. ● The consistency of changes in predicted results and climate data was evaluated. ● AMBE, RMSE, and CC methods investigated the variations of predicted results in each year by comparing yearly and average predicted results over five years. ● AMBE, RMSE, and CC methods investigated the variations of predicted results in each year and five years by comparing single-year | <ul style="list-style-type: none"> ● Meteorological data in a year changed with two patterns: stable and unstable wind direction part. ● The stable wind direction occurred around the year's first and last three months. ● This period had low rain intensity, low atmospheric stability class, and high wind speed. ● Wind direction was stable at around the SW direction for the first seven layers and varied between NNE and SSW directions for the last three layers. ● The unstable wind direction occurred around the middle of the year. It had the opposite climatic characteristics as in the first pattern. ● Predicted results had high variation in the unstable wind direction pattern period. ● As for variation in |

and five-year predicted results.

predicted results by a single year, the highest average AMBE and RMSE value throughout a year was found in the short distance of predicted results at the 99.5th percentile. Meanwhile, the lowest average CC value was found in the long distance of predicted results at the 50th percentile.



- As for variation in predicted results by a single year and five years, it had a similar pattern to the variation in predicted results by a single year with a higher variation.
 - The average over a year of AMBE, RMSE, and CC values in the short and long distance of predicted results at the 50th and 99.5th percentile were calculated and shown in Tables 18 and 19.
-

Table 18 Average over a year of statistical values demonstrating variation between predicted results by each year and the average predicted results over five years.

| Parameters (1Y vs Av) | The long distance at the 50 th percentile | | | The short distance at the 99.5 th percentile | | |
|--|--|-----------------------|-----------------------|---|-----------------------|-----------------------|
| | AMBE _{Avg} | RMSE _{Avg} | CC _{Avg} | AMBE _{Avg} | RMSE _{Avg} | CC _{Avg} |
| Air concentration of I-131 [Bqs/m ³] | 5.35X10 ¹ | 4.02X10 ² | 6.94X10 ⁻¹ | 1.21X10 ⁸ | 3.29X10 ⁸ | 8.53X10 ⁻¹ |
| Air concentration of Cs-137 [Bqs/m ³] | 9.65X10 ⁰ | 7.43X10 ¹ | 6.92X10 ⁻¹ | 2.26X10 ⁷ | 6.13X10 ⁷ | 8.53X10 ⁻¹ |
| Ground concentration of I-131 [Bq/m ²] | 9.38X10 ⁻¹ | 7.89X10 ⁰ | 6.75X10 ⁻¹ | 1.19X10 ⁵ | 3.24X10 ⁵ | 8.53X10 ⁻¹ |
| Ground concentration of Cs-137 [Bq/m ³] | 1.83X10 ⁻¹ | 1.54X10 ⁰ | 6.74X10 ⁻¹ | 2.26X10 ⁴ | 6.13X10 ⁴ | 8.53X10 ⁻¹ |
| TEDE [mSv] | 4.30X10 ⁻⁸ | 3.49X10 ⁻⁷ | 6.82X10 ⁻¹ | 1.85X10 ⁻² | 5.02X10 ⁻² | 8.53X10 ⁻¹ |

Table 19 Average over a year of statistical values demonstrating variation between predicted results by each year and the predicted by five years.

| Parameters (1Y vs 5Y) | The long distance at the 50 th percentile | | | The short distance at the 99.5 th percentile | | |
|--|--|-----------------------|-----------------------|---|-----------------------|-----------------------|
| | AMBE _{Avg} | RMSE _{Avg} | CC _{Avg} | AMBE _{Avg} | RMSE _{Avg} | CC _{Avg} |
| Air concentration of I-131 [Bqs/m ³] | 4.79X10 ¹ | 3.67X10 ² | 6.72X10 ⁻¹ | 2.02X10 ⁸ | 5.68X10 ⁸ | 8.01X10 ⁻¹ |
| Air concentration of Cs-137 [Bqs/m ³] | 8.50X10 ⁰ | 6.65X10 ¹ | 6.64X10 ⁻¹ | 3.76X10 ⁷ | 1.06X10 ⁸ | 8.01X10 ⁻¹ |
| Ground concentration of I-131 [Bq/m ²] | 8.42X10 ⁻¹ | 7.41X10 ⁰ | 6.50X10 ⁻¹ | 1.99X10 ⁵ | 5.59X10 ⁵ | 8.01X10 ⁻¹ |
| Ground concentration of Cs-137 [Bq/m ³] | 1.64X10 ⁻¹ | 1.45X10 ⁰ | 6.42X10 ⁻¹ | 3.76X10 ⁴ | 1.06X10 ⁵ | 8.01X10 ⁻¹ |
| TEDE [mSv] | 3.85X10 ⁻⁸ | 3.26X10 ⁻⁷ | 6.59X10 ⁻¹ | 3.07X10 ⁻² | 8.64X10 ⁻² | 8.01X10 ⁻¹ |

CHAPTER 5

CONCLUSIONS AND SUGGESTIONS

This research investigated the variability of radiation consequence evaluation for transboundary radiation effects from the influences of variation in meteorological data. Historical meteorological data from 2016 to 2020 by NCEP was used to examine meteorological behavior change. Fangchenggang NPP, located in western China and surrounded by many ASEAN countries, was considered as a study location. The investigation was performed by the overlap hypothetical severe accident loss of off-site power and large-break loss of coolant to provide conservative predicted results. The NACAC code was employed as a computational tool for the investigation process. The study findings could be summarized as follows:

- (1) The NACAC was verified before investigating the variability of radiation consequence evaluation. Comparing predicted results with JRODOS code was performed to evaluate the prediction performance in NACAC. The four representative causes with highly fluctuating wind direction in each season were used to increase verification performance. Simulation for 96 hours with the hypothetical severe accident of LB LOCA and LOOP scenarios at Fangchenggang NPP was conducted.

The comparison result showed that the NACAC could offer a dispersion pattern similar to the predicted results of JRODOS. Most radionuclides dispersed in the same direction in all representative cases. In addition, a similar trend line of dose rate and concentration values was shown. However, slight differences in dispersion distance and variation around one order of magnitude in predicting activity concentration and dose rate were found.

Different data preparation and advection calculation schemes were considered as possible factors causing the variation in simulation results. Three analyses of the grid resolution effects, terrain effects, and effects of atmospheric stability class

evaluation were performed to evaluate the potential effects of different data preparation schemes. Meanwhile, the effects of various advection calculation schemes were identified by comparing trajectory patterns. It was noted that differences in grid resolution, terrain data, and evaluation method caused variations in preparing data of rain, wind, and atmospheric stability class data, respectively. In addition, the different advection calculations led to different trajectory patterns. These caused variations in the radionuclide dispersion characteristic and activity concentration predicted by NACAC and JRODOS codes.

However, the NACAC code, with significantly faster calculation times, also provided consistent dose consequence evaluation compared to JRODOS. They agreed that radionuclides probably cover certain northeastern regions in Thailand, with a lower total effective dose equivalence than 1 mSv.

- (2) Appropriate meteorological data selection for investigating the influences of variation in meteorological data on predicted results was investigated. This process was required to demonstrate the effects of the variations in meteorological data of the transboundary radiation effect with reasonable computational resources. Representative data selection providing comprehensive predicted results for domestic radiation effect evaluation with computational resources was considered. It was improved to be appropriate for transboundary radiation effect evaluation. The meteorological classification was modified by categorizing data according to percentile level instated of specific value.

The optimum condition for the transboundary radiation effect of selected area boundaries, optional parameters, and the sampling rate was examined. Simulation with the hypothetical accident of LB LOCA and LOOP scenarios at Fangchenggang NPP was performed by considering meteorological data prepared by representative and sequential data selection. Comparing predicted results with simulation using sequential data selection providing comprehensive prediction results for

transboundary radiation effect with large computational resources was conducted. Statistical methods investigated the consistency of predicted results between both simulations to define appropriate data preparation methods for investigating the influence of variations in meteorological data on predicted results.

The result revealed that differences in selected area boundaries and optional parameters insignificantly affected the prediction of simulation using representative data selection. Meanwhile, higher sampling rates increased the consistency of predicted results at the 50th and 90th percentile compared with simulation using sequential data selection. In addition, it noted that simulation using representative data selection with optimum conditions could reduce computational resources by around 42 times.

However, preparing meteorological data by sampling method in representative data selection caused certain meteorological conditions to be excluded. As a result, simulation using representative data provided an ineffective prediction result in rare cases, such as the predicted result at the 99.5th percentile. This disadvantage caused simulation using representative data selection to be inappropriate for the investigation of the effects of variations in meteorological data on prediction results requiring all aspects of meteorological behavior in a discussion. Consequently, simulation by sequential data selection providing a comprehensive prediction result was considered an appropriate process for the investigation of variations in meteorological data on prediction results.

- (3) The influence of wind, rain, and atmospheric stability class on NACAC predicted results was investigated. Simulations with 12 cases of meteorological input data were conducted to evaluate radiation consequences for 24 hours. Each meteorological input case consisted of rain intensity, wind speed, and atmospheric stability class varied between 0 to 7.6 mm/h, 0.0 to 10.8 m/s, and class A, D, and F,

respectively. Meanwhile, the wind direction was fixed in the northeast direction. Predicted results in each case were compared to demonstrate the impact on computational processes in NACAC.

The result comparison showed that rain intensity significantly affected the depletion of emission concentration. The dispersion distance of the radionuclide varied with wind speed. Meanwhile, the atmospheric stability class influenced the dispersion width of radionuclides. The meteorological data case with low rain intensity (0 mm/h), low wind speed (0.3 m/s), and stable atmospheric stability class (F class) caused low depletion and dispersion of radionuclides. These conditions caused the high radionuclide concentration. The dispersion characteristic is short and narrow dispersion characteristics. The average TEDE value is the highest.

In contrast, the meteorological data with high rain intensity (7.6 mm/h), high wind speed (10.8 m/s), and unstable atmospheric stability class (A class) caused high depletion and dispersion of radionuclide. These conditions caused the low radionuclide concentration to disperse in long and wide dispersion characteristics, leading to the lowest average TEDE value.

- (4) The influences of variations in meteorological data on NACAC predicted results were investigated. The meteorological in 2016 was used as a representative to demonstrate monthly climate changes in a year. The behavior of wind direction, wind speed, rain intensity, and atmospheric stability class was investigated. It was noted that changing meteorological data in a year could be categorized into two parts.

Firstly, the stable wind direction part occurred in the year's first and last three months. The dominant wind direction of the first seven layers was stable in the SW direction. Meanwhile, the dominant wind direction of the last three layers was the NNE and SSW direction in the first and last three months, respectively. The average wind speed was high, while the average rain intensity and atmospheric stability

class were low. Secondly, the unstable wind direction part occurred in the middle of the year. The dominant wind direction in the first seven layers changed clockwise between NE and SW direction. The dominant direction for the last three layers was between ENE and E directions. The average wind speed was low, while the average rain intensity and atmospheric stability class were high.

The simulation using sequential data selection to evaluate radiation consequences for 24 hours with meteorological data in 2016 was performed. The consistency of the predicted results and climate data change trends were analyzed. It was noted that changing dispersion characteristics and activity concentration of radionuclides correlate with changing meteorological data. As for dispersion characteristics, the high wind speed data and low atmospheric stability class in the first and last three months caused long and wide dispersion of radionuclides. Most of the radionuclides dispersed to SSW up to SW directions and N up to NNE directions with high concentration values. In the middle of the year, the effects of high rain intensity caused the short dispersion distance. The unstable wind direction resulted in most radionuclides dispersing from SSW to N directions. Then, it moved from N to E directions and from E to SSW directions, respectively.

As for activity concentration, the trend lines of air concentration, ground concentration, and TEDE values were similar. Generally, a concentration of predicted results in the stable wind direction part with low rain intensity was rather close to an average value in a year. Meanwhile, a concentration of predicted results in the unstable wind direction part with high rain intensity is lower than an average value in a year, especially a result of the 8th month with the highest rain intensity.

- (5) The influence of variations in meteorological data between five years on NACAC predicted results was investigated. The meteorological data from 2016 to 2020 was used to demonstrate monthly variations in meteorological data between a year. The statistical methods identified variations between each year and the average value

over five years. It was noted that meteorological characteristics in each year changed with a similar pattern but did not change with the same ratio. Most differences were found in the unstable wind direction part. The consistency in medium up to high correlation was found by comparing meteorological data each year and the average value. The wind direction had the highest difference, followed by rain intensity, wind speed, and atmospheric stability class.

Simulation using sequential data selection with meteorological data for a single year and five years was performed. Investigation of radiation effects for 24 hours at predicted results at the 50th, 90th, and 99.5th percentile was carried out. It was noted that the most consistent predicted result was found at the 99.5th percentile, followed by the 90th and 50th percentile, respectively. Each year's dispersion characteristic of radionuclides was similar and related to the changing prediction results in a year with stable and unstable wind direction parts.

However, inconsistent meteorological data each year also caused variations in the monthly dispersion characteristic and activity concentration. Most differences were found in the unstable wind direction part with a period of the 7th up to 9th months. The discrepancy in rain intensity during this period significantly caused variations in predicted results. Meanwhile, the simulation using five years of meteorological data provided more comprehensive predicted results than the simulation using a single year of meteorological data. It yielded predicted results that align with most of the data found in the annual predictions.

- (6) Variations of predicted results in short (0-10 km), medium (10-100 km), and long (100-900 km) distances between simulations with a single year and five years of meteorological data were analyzed by three statistical methods: AMBE, RMSE, and CC. As for variations in every single year, AMBE and RMSE values showed that a difference in concentration of predicted results at the 99.5th percentile was the highest, followed by the 90th and 50th percentile. The highest concentration near the

release point caused the highest variation in the short distance of all percentile levels. Meanwhile, a lower variation in medium and long distances was found from decreased concentration along the distance.

Average AMBE and RMSE values in comparing TEDE values by a single year and the average value at the 99.5th percentile in the short distance were found at 1.85E-2 and 5.02E-2 mSv, respectively. Meanwhile, the average values of AMBE and RMSE dropped by around 2 and 4 orders of magnitude in the medium and long distances. Decreasing the concentration of predicted results at the 90th and 50th percentile caused average AMBE and RMSE of TEDE throughout dispersion distance to drop from those at the 99.5th percentile of around 1 and 2 orders of magnitude, respectively.

CC values showed that the highest correlation between the predicted result by each year of meteorological data and the average value was the 99.5th percentile, followed by the 90th and 50th percentile. The high variation of rain intensity in periods of the 7th to 9th month caused low consistency in all percentile levels. It clearly affected the long distance with high variation due to the radionuclide not reaching it. In addition, a low consistency in the short distance of the predicted results at the 90th and 50th percentile was a result of the variation in minor wind direction. Meanwhile, the low dispersion distance effects caused the low correlation in the long distance at the 50th percentile.

As for variation between predicted results by a single year and five years, it had a similar pattern to the variation in every single year. However, simulation using five years of meteorology providing a higher comprehensive predicted result caused a higher variation. The predicted result at the 99.5th percentile was the most different. The higher average AMBE and RMSE values were found at around 60-70 %, 50-60 %, and 20 % at short, medium, and long distances. Meanwhile, the average CC values were lower, around 2% in long distances and 6 % in short and medium distances.

As for the predicted results at the 90th and 50th percentile, they had a closer variation to the variation in every single year. A difference in average AMBE and RMSE values of TEDE values was lower than around 10% throughout the dispersion distance. Meanwhile, A difference in average CC values of TEDE value was lower than 4% throughout the dispersion distance.

- (7) As mentioned above, it has been shown that variations in meteorological data caused significant variations in the predicted results. It was noted that the radiation effect evaluation in the unstable wind direction period with large variations in meteorological data led to a high discrepancy in dispersion characteristics and activity concentration from year to year, especially at long dispersion distances. In addition, the high depletion with wet deposition in this period also caused a low concentration of the TEDE values. Therefore, in order to obtain comprehensive assessment results, it was preferable to carry out a radiation effect evaluation with several years of meteorological data in the unstable wind direction period. Meanwhile, low variation in meteorological data in the stable wind direction period caused minimal variation in the evaluation results from year to year at all distances. Low rain intensity in this period also caused the high TEDE values. Therefore, radiation effect evaluation with one year of meteorological data was sufficient to provide comprehensive prediction results in this period with a conservative situation.

REFERENCES

1. Khunsrimek N, Vechgama W, Silva K, et al. Simulation using representative data selection for transboundary radiation effect evaluation by Nuclear Accident Consequence Analysis Code (NACAC). *Journal of Nuclear Science and Technology*. 2023:1-16.
2. Khunsrimek N, Krisanungkura P, Vechgama W, et al. Verification of the NACAC atmospheric dispersion calculation using a hypothetical accident in a neighboring nuclear power plant. *Progress in Nuclear Energy*. 2023 2023/02/01;156:104532.
3. Marzo GA. Atmospheric transport and deposition of radionuclides released after the Fukushima Dai-chi accident and resulting effective dose. *Atmospheric Environment*. 2014 2014/09/01;94:709-722.
4. Povinec PP, Gera M, Holý K, et al. Dispersion of Fukushima radionuclides in the global atmosphere and the ocean. *Applied Radiation and Isotopes*. 2013 2013/11/01;81:383-392.
5. Nakano M, Povinec PP. Long-term simulations of the ¹³⁷Cs dispersion from the Fukushima accident in the world ocean. *Journal of Environmental Radioactivity*. 2012 2012/09/01;111:109-115.
6. Long NQ, Truong Y, Hien PD, et al. Atmospheric radionuclides from the Fukushima Dai-ichi nuclear reactor accident observed in Vietnam. *Journal of Environmental Radioactivity*. 2012 2012/09/01;111:53-58.
7. Leung WH, Ma WM, Chan PKY. Nuclear accident consequence assessment in Hong Kong using JRODOS. *Journal of Environmental Radioactivity*. 2018 2018/03/01;183:27-36.
8. Min JS, Kim HR. Environmental impact on the Korean peninsula due to hypothetical accidental scenarios at the Haiyang nuclear power plant in China. *Prog Nuclear Energy*. 2018:254-262.
9. Klein H, Bartnicki J, Brown JE, et al. Consequences for Norway from a hypothetical accident at the Sellafield reprocessing plant: Atmospheric

- transport of radionuclides. *Journal of Environmental Radioactivity*. 2021
2021/10/01;237:106703.
10. Webster PJ. The coupled monsoon system. In: Wang B, editor. *The Asian Monsoon*. Berlin, Heidelberg: Springer Berlin Heidelberg; 2006. p. 3-66.
 11. Dean A, Green D. Climate change, air pollution and human health in Sydney, Australia: A review of the literature. *Environmental Research Letters*. 2018
2018/05/10;13(5):053003.
 12. Mickley LJ, Jacob DJ, Field BD, et al. Effects of future climate change on regional air pollution episodes in the United States
[\[https://doi.org/10.1029/2004GL021216\]](https://doi.org/10.1029/2004GL021216). *Geophys Res Lett*. 2004
2004/12/01;31(24).
 13. Jacob DJ, Winner DA. Effect of climate change on air quality. *Atmos Environ*.
2009 2009/01/01;43(1):51-63.
 14. Liu JC, Mickley LJ, Sulprizio MP, et al. Particulate air pollution from wildfires in the Western US under climate change. *Clim Change*. 2016
2016/10/01;138(3):655-666.
 15. Suzhou Thermal Research Institute. Fangchenggang Nuclear Power Plant Phase II (2 × HL1000-1) Project Environmental Impact Report for Units 3 and 4 (site selection stage). 2014. p. 436-445.
 16. Dvorzhak A, Puras C, Montero M, et al. Spanish Experience on Modeling of Environmental Radioactive Contamination Due to Fukushima Daiichi NPP Accident Using JRODOS. *Environ Sci Technol*. 2012 2012/11/06;46(21):11887-11895.
 17. Landman C, Päsler-Sauer J, Raskob W. RODOS and the Fukushima Accident. In: Kessler G, Veser A, Schlüter F-H, et al., editors. *The Risks of Nuclear Energy Technology: Safety Concepts of Light Water Reactors*. Berlin, Heidelberg: Springer Berlin Heidelberg; 2014. p. 349-352.
 18. Bal RS. Chapter 5 - Fission Product Release and Transport. In: Sehgal BR, editor. *Nuclear Safety in Light Water Reactors*. Boston: Academic Press; 2012. p. 425-517.
 19. Le Bot P. Human reliability data, human error and accident models—illustration

- through the Three Mile Island accident analysis. *Reliab Eng Syst Saf*. 2004
2004/02/01/;83(2):153-167.
20. Paatero J, Hämeri K, Jaakkola T, et al. Airborne and deposited radioactivity from the Chernobyl accident: a review of investigations in Finland. *Boreal Environ Res*. 2010;15(1):19-33.
 21. Steinhauser G, Brandl A, Johnson TE. Comparison of the Chernobyl and Fukushima nuclear accidents: a review of the environmental impacts. *Sci Total Environ*. 2014;470:800-817.
 22. Chapter 5 - Fission Product Release and Transport. In: Sehgal BR, editor. *Nuclear Safety in Light Water Reactors*. Boston: Academic Press; 2012. p. 425-517.
 23. Richard Chang JS, Tina Ghosh,, Jonathan Barr CT, and Martin Stutzke. State-of-the-Art Reactor Consequence Analyses (SOARCA). Office of Nuclear Regulatory Research U.S. Nuclear Regulatory Commission Washington, DC 20555-00012012.
 24. Commission UNR. Severe Accident Risks: An Assessment of Five US Commercial Nuclear Power Plants (NUREG-1150). Office of Nuclear Regulatory Research U.S. Nuclear Regulatory Commission Washington, DC 205551990.
 25. Suzhou Thermal Research Institute. Fangchenggang Nuclear Power Plant Phase II (2 × HL1000-1) Project Environmental Impact Report for Units 3 and 4 (site selection stage). 2014. p. 436-445.
 26. Hanrahan G. Chapter 6 - The Atmosphere and Associated Processes. In: Hanrahan G, editor. *Key Concepts in Environmental Chemistry*. Boston: Academic Press; 2012. p. 179-211.
 27. Childs PRN. Chapter 8 - Atmospheric and Oceanic Circulations. In: Childs PRN, editor. *Rotating Flow*. Oxford: Butterworth-Heinemann; 2011. p. 299-366.
 28. Philander SGH. El Niño and La Niña. *J Atmos Sci*. 1985 01 Dec. 1985;42(23):2652-2662.
 29. Chapter 18 - Meteorology and Air Pollution. In: Weiner RF, Matthews RA, editors. *Environmental Engineering (Fourth Edition)*. Burlington: Butterworth-Heinemann; 2003. p. 351-374.
 30. Repace J. Analysis of the Air Quality Impact of Hoyvik Heating Plant Parts I, II, & III. 2015.

31. Kahl JDW, Chapman HL. Atmospheric stability characterization using the Pasquill method: A critical evaluation. *Atmos Environ*. 2018 2018/08/01/;187:196-209.
32. Azevedo JA, Chapman L, Muller CL. Quantifying the daytime and night-time urban heat island in Birmingham, UK: A comparison of satellite derived land surface temperature and high resolution air temperature observations. *Remote Sensing*. 2016;8(2):153.
33. Schnadt H, Ivanov I. Chapter 7 - Environmental Consequences and Management of a Severe Accident. In: Sehgal BR, editor. *Nuclear Safety in Light Water Reactors*. Boston: Academic Press; 2012. p. 589-624.
34. International Atomic Energy Agency V. Generic models for use in assessing the impact of discharges of radioactive substances to the environment. International Atomic Energy Agency (IAEA): IAEA; 2001.
35. Vetter RJ. ICRP Publication 103, The Recommendations of the International Commission on Radiological Protection. *Health Physics*. 2008;95(4).
36. Food, Agriculture Organization of the United Nations R. Criteria for use in preparedness and response for a nuclear or radiological emergency General safety guide. International Atomic Energy Agency (IAEA): IAEA; 2011.
37. Khunsrimek N. ATMOSPHERIC DISPERSION SIMULATION OF CESIUM-137 RELEASE FROM A HYPOTHETICAL ACCIDENT AT NUCLEAR POWER PLANTS: CASE STUDY IN CHINA AND VIETNAM. Chulalongkorn University 2017.
38. IAEA. Generic Procedures for Monitoring in a Nuclear or Radiological Emergency. Vienna: INTERNATIONAL ATOMIC ENERGY AGENCY; 1999.
39. de la Rosa Blul JC. Determination of Emergency Planning Zones distances and scaling-based comparison criteria for downsized Nuclear Power Plants. *Nuclear Engineering and Design*. 2021 2021/10/01/;382:111367.
40. Hummel DW, Chouhan S, Lebel L, et al. Radiation dose consequences of postulated limiting accidents in small modular reactors to inform emergency planning zone size requirements. *Annals of Nuclear Energy*. 2020 2020/03/01/;137:107062.
41. Carless TS, Talabi SM, Fischbeck PS. Risk and regulatory considerations for small modular reactor emergency planning zones based on passive decontamination

- potential. *Energy*. 2019 2019/01/15/;167:740-756.
42. Collins HE, Grimes BK, Galpin F. Planning basis for the development of state and local government radiological emergency response plans in support of light water nuclear power plants. Nuclear Regulatory Commission, Washington, DC (USA). 1978.
 43. Park S-U, Lee I-H, Joo SJ, et al. Emergency preparedness for the accidental release of radionuclides from the Uljin Nuclear Power Plant in Korea. *Journal of Environmental Radioactivity*. 2017 2017/12/01/;180:90-105.
 44. Yoshikane T, Yoshimura K. Dispersion characteristics of radioactive materials estimated by wind patterns. *Scientific Reports*. 2018 2018/07/02;8(1):9926.
 45. Leadbetter SJ, Hort MC, Jones AR, et al. Sensitivity of the modelled deposition of Caesium-137 from the Fukushima Dai-ichi nuclear power plant to the wet deposition parameterisation in NAME. *Journal of Environmental Radioactivity*. 2015 2015/01/01/;139:200-211.
 46. Srinivas CV, Hari Prasad KBRR, Naidu CV, et al. Sensitivity Analysis of Atmospheric Dispersion Simulations by FLEXPART to the WRF-Simulated Meteorological Predictions in a Coastal Environment. *Pure and Applied Geophysics*. 2016 2016/02/01/;173(2):675-700.
 47. Leelóssy Á, Lagzi I, Kovács A, et al. A review of numerical models to predict the atmospheric dispersion of radionuclides. *Journal of Environmental Radioactivity*. 2018 2018/02/01/;182:20-33.
 48. Talerko N. Mesoscale modelling of radioactive contamination formation in Ukraine caused by the Chernobyl accident. *Journal of Environmental Radioactivity*. 2005 2005/03/01/;78(3):311-329.
 49. Stohl A, Seibert P, Wotawa G, et al. Xenon-133 and caesium-137 releases into the atmosphere from the Fukushima Dai-ichi nuclear power plant: determination of the source term, atmospheric dispersion, and deposition. *Atmospheric Chemistry and Physics*. 2012;12(5):2313-2343.
 50. Baró R, Maurer C, Brioude J, et al. The environmental effects of the April 2020 wildfires and the Cs-137 re-suspension in the Chernobyl exclusion zone: a multi-

- hazard threat. *Atmosphere*. 2021;12(4):467.
51. Muswema JL, Darko EO, Gbadago JK, et al. Atmospheric dispersion modeling and radiological safety analysis for a hypothetical accident of Ghana Research Reactor-1 (GHARR-1). *Ann Nucl Energy*. 2014 2014/06/01;68:239-246.
 52. Veigele WJ, Head JH. Derivation of the Gaussian Plume Model. *J Air Pollut Control Assoc*. 1978 1978/11/01;28(11):1139-1140.
 53. Arya SP. *Air pollution meteorology and dispersion*. Vol. 310. Oxford University Press New York; 1999.
 54. Thykier-Nielsen S, Deme S, Mikkelsen T. Description of the atmospheric dispersion module RIMPUFF. Riso National Laboratory, PO Box. 1999;49.
 55. Stohl A, Forster C, Frank A, et al. The Lagrangian particle dispersion model FLEXPART version 6.2. *Atmospheric Chemistry and Physics*. 2005;5(9):2461-2474.
 56. IAEA. *Generic Models for Use in Assessing the Impact of Discharges of Radioactive Substances to the Environment*. Vienna: INTERNATIONAL ATOMIC ENERGY AGENCY; 2001.
 57. Thiessen KM, Napier BA, Filistovic V, et al. Model testing using data on ¹³¹I released from Hanford. *Journal of Environmental Radioactivity*. 2005 2005/01/01;84(2):211-224.
 58. Thiessen KM, Sazykina TG, Apostoaei AI, et al. Model testing using data on ¹³⁷Cs from Chernobyl fallout in the Iput River catchment area of Russia. *Journal of Environmental Radioactivity*. 2005 2005/01/01;84(2):225-244.
 59. Homma T, Tomita K, Hato S. Uncertainty and sensitivity studies with the probabilistic accident consequence assessment code OSCAAR. *Nuclear Engineering and Technology*. 2005;37(3):245-258.
 60. Barsotti S, Neri A, Scire J. The VOL-CALPUFF model for atmospheric ash dispersal: 1. Approach and physical formulation. *Journal of Geophysical Research: Solid Earth*. 2008;113(B3).
 61. Evans JS, Abrahamson S, Bender M, et al. *Health effects models for Nuclear power plant accident consequence analysis*. 1993.
 62. Kocher D. Dose-rate conversion factors for external exposure to photon and

- electron radiation from radionuclides occurring in routine releases from nuclear fuel cycle facilities. *Health Phys.* 1980;38(4):543-621.
63. Ievgen I, Dmytro T, Christian S, et al. *JRodos User Guide*. Karlsruhe Institute of Technology; 2018.
 64. Wengert A. *JRodos: An Offsite Emergency Management System for Nuclear Accidents*. Karlsruhe Institute of Technology (KIT); 2017.
 65. Landman C, Päsler-Sauer J, Raskob W. The Decision Support System RODOS. In: Kessler G, Veser A, Schlüter F-H, et al., editors. *The Risks of Nuclear Energy Technology: Safety Concepts of Light Water Reactors*. Berlin, Heidelberg: Springer Berlin Heidelberg; 2014. p. 337-348.
 66. Andronopoulos S, Bartzis JG. Model description of the RODOS meteorological pre-processor. Report RODOS (RA2)-TN (09)2009.
 67. Thykier-Nielsen S, Deme S, Mikkelsen T. Description of The Atmospheric Dispersion Module RIMPUFF. Riso National Laboratory, PO Box, 49.1999.
 68. Liu X, Tomita K, Homma T. Study on a new meteorological sampling scheme developed for the OSCAAR code system. Japan Atomic Energy Research Inst.; 2002.
 69. Kimura M, Takahara S, Homma T. Evaluation of the precautionary action zone using a probabilistic consequence analysis. *Journal of Nuclear Science and Technology*. 2013;50(3):296-303.
 70. Dvorzhak A, Mora JC, Robles B. Probabilistic risk assessment from potential exposures to the public applied for innovative nuclear installations. *Reliab Eng Syst Saf*. 2016 2016/08/01/;152:176-186.
 71. Choi G-S, Lim J-M, Lim K-SS, et al. Characteristics of regional scale atmospheric dispersion around Ki-Jang research reactor using the Lagrangian Gaussian puff dispersion model. *Nuclear Engineering and Technology*. 2018;50(1):68-79.
 72. Kaviani F, Memarian MH, Eslami-Kalantari M. Radioactive impact on Iran and the world from a postulated accident at Bushehr Nuclear Power Plant. *Prog Nuclear Energy*. 2021;142:103991.
 73. Rudas C, Pázmándi T. Consequences of selecting different subsets of meteorological data to utilize in deterministic safety analysis. *Journal of*

- Environmental Radioactivity. 2020 2020/12/01/;225:106428.
74. European C, Directorate-General for Employment SA, Inclusion, et al. Methods for assessing the off-site radiological consequences of nuclear accidents. Publications Office; 1990.
 75. Silva K, Ishiwatari Y, Takahara S. Cost per severe accident as an index for severe accident consequence assessment and its applications. Reliability Engineering & System Safety. 2014 2014/03/01/;123:110-122.
 76. Takahara S, Homma T, editors. Analysis for relocation strategy using the method of probabilistic accident consequence assessment. Proceedings of IRPA12: 12. Congress of the International Radiation Protection Association: Strengthening Radiation Protection Worldwide-Highlights, Global Perspective and Future Trends; 2010.
 77. Van Wonderen E, Van der Steen, I. and Hasemann, I. COSYMA: Users Intercomparison Exercise. EUR 15108, European Communities; 1994. (EUR 15108).
 78. Panitz H-J, Matzerath C, Päsler-Sauer J. UFOMOD-atmospheric dispersion and deposition. Kernforschungszentrum Karlsruhe GmbH (Germany; 1989.
 79. Kelly GN. Cosyma A new programme package for accident consequence assessment. EUR 13028, Commission of the European Communities; 1990.
 80. Homma T, Tomita, K., Hato, S. Uncertainty and sensitivity studies with the probabilistic accident consequence assessment code OSCAAR. Nuclear Engineering and Technology. 2005;37(3):245-258.
 81. Berge E, Andronopoulos S, Klein H, et al. Uncertainties in short term prediction of atmospheric dispersion of radionuclides. A case study of a hypothetical accident in a nuclear floating power plant off the West coast of Norway. Journal of Environmental Radioactivity. 2021;233:106587.
 82. Sørensen JH, Bartnicki J, Blixt Buhr AM, et al. Uncertainties in atmospheric dispersion modelling during nuclear accidents. Journal of Environmental Radioactivity. 2020 2020/10/01/;222:106356.
 83. Wang Q. China needing a cautious approach to nuclear power strategy. Energy Policy. 2009 2009/07/01/;37(7):2487-2491.

84. Christoudias T, Proestos Y, Lelieveld J. Global risk from the atmospheric dispersion of radionuclides by nuclear power plant accidents in the coming decades. *Atmos Chem Phys*. 2014;14(9):4607-4616.
85. Yu R, Wang B, Zhou T. Tropospheric cooling and summer monsoon weakening trend over East Asia. *Geophys Res Lett*. 2004;31(22).
86. Yang F, Lau KM. Trend and variability of China precipitation in spring and summer: linkage to sea-surface temperatures. *International Journal of Climatology: A Journal of the Royal Meteorological Society*. 2004;24(13):1625-1644.
87. Zhu C, Wang B, Qian W, et al. Recent weakening of northern East Asian summer monsoon: A possible response to global warming. *Geophys Res Lett*. 2012;39(9).
88. Chen L, Zhu J, Liao H, et al. Meteorological influences on PM_{2.5} and O₃ trends and associated health burden since China's clean air actions. *Sci Total Environ*. 2020;744:140837.
89. Hu C, Kang P, Jaffe DA, et al. Understanding the impact of meteorology on ozone in 334 cities of China. *Atmos Environ*. 2021;248:118221.
90. Xu Y, Xue W, Lei Y, et al. Spatiotemporal variation in the impact of meteorological conditions on PM_{2.5} pollution in China from 2000 to 2017. *Atmos Environ*. 2020;223:117215.
91. Rakesh PT, Venkatesan R, Hedde T, et al. Simulation of radioactive plume gamma dose over a complex terrain using Lagrangian particle dispersion model. *Journal of Environmental Radioactivity*. 2015 2015/07/01/;145:30-39.
92. Arnold D, Maurer C, Wotawa G, et al. Influence of the meteorological input on the atmospheric transport modelling with FLEXPART of radionuclides from the Fukushima Daiichi nuclear accident. *Journal of Environmental Radioactivity*. 2015 2015/01/01/;139:212-225.
93. Silva K, Krisanungkura P, Khunsrimek N, et al. Inter-comparison of transboundary atmospheric dispersion calculations: A summary of outputs from the ASEAN NPSR benchmark exercise. *Progress in Nuclear Energy*. 2021 2021/05/01/;135:103718.

94. Ievdin IO, Khalchenkov OV, Kovalets IV, et al. Application of decision support system JRODOS for assessments of atmospheric dispersion and deposition from Fukushima Daiichi nuclear power plant accident. *International Journal of Energy for a Clean Environment*. 2012;13(1-4).
95. Saha S, Moorthi S, Wu X, et al. NCEP Climate Forecast System Version 2 (CFSv2) 6-hourly Products. Boulder, CO: Research Data Archive at the National Center for Atmospheric Research, Computational and Information Systems Laboratory; 2011.
96. Nitoi M. Investigating the recurrence of meteorological hazards. *Progress in Nuclear Energy*. 2016 2016/05/01/;89:39-45.
97. Bijlholt J, Constantinou C, Janssens A, et al. HERCA-WENRA Approach for a better cross-border coordination of protective actions during the early phase of a nuclear accident. 2014.
98. Leute J, Walton F, Mitchell R, et al. MACCS (MELCOR Accident Consequence Code System) User Guide–Version 4.0. 2021.
99. MANOBS. Manual of surface weather observation standards. Meteorological Service of Canada: Meteorological Service of Canada; 2021. Available from: <https://publications.gc.ca/site/eng/9.907779/publication.html>.
100. Liu X, Homma T. Variation of radiological consequences under various weather conditions. *Japan Atomic Energy Research Inst*; 2001. p. 57.
101. Sekiyama TT, Kunii M, Kajino M, et al. Horizontal resolution dependence of atmospheric simulations of the Fukushima nuclear accident using 15-km, 3-km, and 500-m grid models. *Journal of the Meteorological Society of Japan Ser II*. 2015;93(1):49-64.
102. Lim K-SS, Lim J-M, Lee J, et al. Impact of boundary layer simulation on predicting radioactive pollutant dispersion: A case study for HANARO research reactor using the WRF-MMIF-CALPUFF modeling system. *Nuclear Engineering and Technology*. 2021;53(1):244-252.
103. Caputo M, Giménez M, Schlamp M. Intercomparison of atmospheric dispersion models. *Atmospheric environment*. 2003;37(18):2435-2449.
104. Periañez R, Thiessen KM, Chouhan SL, et al. Mid-range atmospheric dispersion

- modelling. Intercomparison of simple models in EMRAS-2 project. Journal of Environmental Radioactivity. 2016 2016/10/01;162-163:225-234.
105. Astrup P, Jensen NO, Mikkelsen T. Surface roughness model for LINCOM. 1996.
106. IAEA. Actions to Protect the Public in an Emergency due to Severe Conditions at a Light Water Reactor. Vienna: INTERNATIONAL ATOMIC ENERGY AGENCY; 2013.





APPENDIX A
EXTENDED RESULTS

จุฬาลงกรณ์มหาวิทยาลัย
CHULALONGKORN UNIVERSITY

A1. Average values for 24 hours of each meteorological parameter in the NACAC calculation process

Table A-1. Average values for 24 hours of each meteorological parameters in depletion calculation part

| Cases | Meteorological conditions | | | | Dispersion calculation part | | | | | | | |
|-------|-------------------------------|----------------------|-----------------------|---------------------------------|-----------------------------|----------------------|------------------|-----------------------------|------------------------------|---|---|------------------|
| | Wind direction, $^{\circ}$ | Wind Speed, [m/s] | Rain Intensity [mm/h] | Atmospheric Stability/Class [1] | Average Sigma Y, [1] | Average Sigma Z, [1] | Plume Layer, [1] | Average density Factor, [1] | Average Distance Factor, [1] | Average Dispersion Boundary Factor, [1] | Dispersion Characteristic Number of Direction | Number of Radius |
| 1 | North-east (Light air) | 0.3 (No rain) | 0.0 | A (Unstable) | 1.84×10^3 | 1.49×10^3 | 10 | 6.82×10^{-1} | 1.40×10^{-2} | 1.15×10^8 | 5 | 13 |
| 2 | North-east (Light air) | 0.3 (No rain) | 0.0 | D (Natural) | 7.41×10^2 | 1.43×10^2 | 5 | 1.49×10^{-1} | 1.40×10^{-2} | 1.86×10^7 | 2 | 13 |
| 3 | North-east (Light air) | 0.3 (No rain) | 0.0 | F (Stable) | 3.64×10^2 | 4.69×10^1 | 2 | 1.00×10^{-1} | 1.40×10^{-2} | 4.53×10^6 | 1 | 13 |
| 4 | North-east (Light air) | 0.3 (Heavy rain) | 7.6 | A (Unstable) | 1.84×10^3 | 1.49×10^3 | 10 | 6.82×10^{-1} | 1.40×10^{-2} | 1.73×10^7 | 5 | 8 |
| 5 | North-east (Light air) | 0.3 (Heavy rain) | 7.6 | D (Natural) | 7.41×10^2 | 1.43×10^2 | 5 | 1.49×10^{-1} | 1.40×10^{-2} | 2.90×10^6 | 2 | 8 |
| 6 | North-east (Light air) | 0.3 (Heavy rain) | 7.6 | F (Stable) | 3.64×10^2 | 4.69×10^1 | 2 | 1.00×10^{-1} | 1.40×10^{-2} | 7.08×10^5 | 1 | 8 |
| 7 | North-east (Strong breeze) | 10.8 (No rain) | 0.0 | A (Unstable) | 2.83×10^4 | 1.54×10^3 | 10 | 6.98×10^{-1} | 4.69×10^{-1} | 2.55×10^{10} | 5 | 23 |
| 8 | North-east (Strong breeze) | 10.8 (No rain) | 0.0 | D (Natural) | 2.18×10^4 | 5.20×10^2 | 8 | 3.60×10^{-1} | 4.69×10^{-1} | 1.66×10^{10} | 2 | 23 |
| 9 | North-east (Strong breeze) | 10.8 (No rain) | 0.0 | F (Stable) | 1.96×10^4 | 1.81×10^2 | 4 | 1.67×10^{-1} | 4.69×10^{-1} | 1.41×10^{10} | 1 | 23 |
| 10 | North-east (Strong breeze) | 10.8 (Heavy rain) | 7.6 | A (Unstable) | 2.83×10^4 | 1.54×10^3 | 10 | 6.98×10^{-1} | 4.69×10^{-1} | 5.80×10^9 | 5 | 20 |
| 11 | North-east (Strong breeze) | 10.8 (Heavy rain) | 7.6 | D (Natural) | 2.18×10^4 | 5.20×10^2 | 8 | 3.60×10^{-1} | 4.69×10^{-1} | 2.18×10^9 | 2 | 20 |
| 12 | North-east (Strong breeze) | 10.8 (Heavy rain) | 7.6 | F (Stable) | 1.96×10^4 | 1.81×10^2 | 4 | 1.67×10^{-1} | 4.69×10^{-1} | 1.76×10^9 | 1 | 20 |

Table A-2. Average values for 24 hours of each meteorological parameters in dispersion calculation part

| Cases | Meteorological conditions | | | | Depletion calculation part | | | | | | | |
|-------|---------------------------|-------------------------|-----------------------|---------------------------------|----------------------------|------------------------------|--|--------------------|-------------------------------------|--|--------------------|-----------------------|
| | Wind direction, [°] | Wind Speed, [m/s] | Rain Intensity [mm/h] | Atmospheric Stability Class [°] | Decay constant | Average Dry Coefficient, [°] | Average Wet Deposition Coefficient, [mm/h] | Depletion fraction | Sum Average Depletion fraction, [°] | Average Concentration Emission Rate with Depletion, [Bq/s] | | |
| 1 | Northeast | 0.3 (Light air) | 0.0 (No rain) | A (Unstable) | 7.32×10^{-10} | 1.96×10^{-7} | 0.00×10^0 | 1.00×10^0 | 9.99×10^{-1} | 1.00×10^0 | 3.00×10^0 | 3.15×10^{10} |
| 2 | Northeast | 0.3 (Light air) | 0.0 (No rain) | D (Neutral) | 7.32×10^{-10} | 2.20×10^{-4} | 0.00×10^0 | 1.00×10^0 | 9.92×10^{-1} | 1.00×10^0 | 2.99×10^0 | 1.57×10^{10} |
| 3 | Northeast | 0.3 (Light air) | 0.0 (No rain) | F (Stable) | 7.32×10^{-10} | 4.67×10^{-4} | 0.00×10^0 | 1.00×10^0 | 9.85×10^{-1} | 1.00×10^0 | 2.98×10^0 | 8.04×10^9 |
| 4 | Northeast | 0.3 (Light air) | 7.6 (Heavy rain) | A (Unstable) | 7.32×10^{-10} | 1.96×10^{-7} | 1.00×10^{-3} | 1.00×10^0 | 9.99×10^{-1} | 4.12×10^{-1} | 2.42×10^0 | 5.14×10^9 |
| 5 | Northeast | 0.3 (Light air) | 7.6 (Heavy rain) | D (Neutral) | 7.32×10^{-10} | 2.20×10^{-4} | 1.00×10^{-3} | 1.00×10^0 | 9.92×10^{-1} | 4.81×10^{-1} | 2.49×10^0 | 5.88×10^9 |
| 6 | Northeast | 0.3 (Light air) | 7.6 (Heavy rain) | F (Stable) | 7.32×10^{-10} | 4.67×10^{-4} | 9.30×10^{-4} | 1.00×10^0 | 9.85×10^{-1} | 6.30×10^{-1} | 2.63×10^0 | 6.55×10^9 |
| 7 | Northeast | 10.8 (Strong breeze) | 0.0 (No rain) | A (Unstable) | 7.32×10^{-10} | 8.32×10^{-12} | 0.00×10^0 | 1.00×10^0 | 9.99×10^{-1} | 1.00×10^0 | 3.00×10^0 | 3.40×10^{10} |
| 8 | Northeast | 10.8 (Strong breeze) | 0.0 (No rain) | D (Neutral) | 7.32×10^{-10} | 2.57×10^{-2} | 0.00×10^0 | 1.00×10^0 | 9.98×10^{-1} | 1.00×10^0 | 3.00×10^0 | 3.02×10^{10} |
| 9 | Northeast | 10.8 (Strong breeze) | 0.0 (No rain) | F (Stable) | 7.3×10^{-10} | 5.20×10^{-4} | 0.00×10^0 | 1.00×10^0 | 9.95×10^{-1} | 1.00×10^0 | 2.99×10^0 | 2.11×10^{10} |
| 10 | Northeast | 10.8 (Strong breeze) | 7.6 (Heavy rain) | A (Unstable) | 7.3×10^{-10} | 8.32×10^{-12} | 1.00×10^{-3} | 1.00×10^0 | 9.99×10^{-1} | 4.55×10^{-1} | 2.47×10^0 | 9.30×10^9 |
| 11 | Northeast | 10.8 (Strong breeze) | 7.6 (Heavy rain) | D (Neutral) | 7.3×10^{-10} | 2.57×10^{-2} | 1.00×10^{-3} | 1.00×10^0 | 9.98×10^{-1} | 5.14×10^{-1} | 2.53×10^0 | 1.03×10^9 |
| 12 | Northeast | 10.8 (Strong breeze) | 7.6 (Heavy rain) | F (Stable) | 7.3×10^{-10} | 5.20×10^{-4} | 9.58×10^{-4} | 1.00×10^0 | 9.95×10^{-1} | 5.53×10^{-1} | 2.56×10^0 | 1.05×10^9 |

Table A-3. Average values for 24 hours of each meteorological parameters in concentration calculation part

| Cases | Meteorological conditions | | | | Concentration calculation part | | |
|-------|---------------------------|-------------------------|------------------------|---------------------------------|---|--|---|
| | Wind direction, [°] | Wind Speed, [m/s] | Rain Intensity, [mm/h] | Atmospheric Stability Class [-] | Air concentration, [Bq/m ³] | Ground concentration, [Bq/m ²] | Total Effective dose Equivalence, [mSv] |
| 1 | Northeast | 0.3 (Ligh air) | 0.0 (No rain) | A (Unstable) | 1.11×10 ⁷ | 1.11×10 ⁴ | 8.18×10 ⁻⁴ |
| 2 | Northeast | 0.3 (Ligh air) | 0.0 (No rain) | D (Natural) | 2.01×10 ⁸ | 2.01×10 ⁵ | 1.49×10 ⁻² |
| 3 | Northeast | 0.3 (Ligh air) | 0.0 (No rain) | F (Stable) | 8.57×10 ⁸ | 8.57×10 ⁵ | 6.39×10 ⁻² |
| 4 | Northeast | 0.3 (Ligh air) | 7.6 (Heavy rain) | A (Unstable) | 2.03×10 ⁴ | 1.35×10 ⁵ | 4.72×10 ⁻³ |
| 5 | Northeast | 0.3 (Ligh air) | 7.6 (Heavy rain) | D (Natural) | 2.94×10 ⁷ | 4.44×10 ⁵ | 1.71×10 ⁻² |
| 6 | Northeast | 0.3 (Ligh air) | 7.6 (Heavy rain) | F (Stable) | 1.18×10 ⁸ | 1.36×10 ⁶ | 5.10×10 ⁻² |
| 7 | Northeast | 10.8 (Strong breeze) | 0.0 (No rain) | A (Unstable) | 1.31×10 ⁴ | 1.31×10 ⁵ | 9.70×10 ⁻⁷ |
| 8 | Northeast | 10.8 (Strong breeze) | 0.0 (No rain) | D (Natural) | 3.38×10 ⁴ | 3.38×10 ⁵ | 2.50×10 ⁻⁵ |
| 9 | Northeast | 10.8 (Strong breeze) | 0.0 (No rain) | F (Stable) | 1.56×10 ⁸ | 1.56×10 ³ | 1.16×10 ⁻⁴ |
| 10 | Northeast | 10.8 (Strong breeze) | 7.6 (Heavy rain) | A (Unstable) | 6.61×10 ³ | 6.72×10 ³ | 2.29×10 ⁻⁴ |
| 11 | Northeast | 10.8 (Strong breeze) | 7.6 (Heavy rain) | D (Natural) | 1.86×10 ⁵ | 1.05×10 ⁵ | 3.64×10 ⁻⁴ |
| 12 | Northeast | 10.8 (Strong breeze) | 7.6 (Heavy rain) | F (Stable) | 6.34×10 ⁵ | 1.67×10 ⁴ | 5.85×10 ⁻⁴ |

A2. Dispersion characteristics from sensitivity test of varying meteorological input data in 12 cases

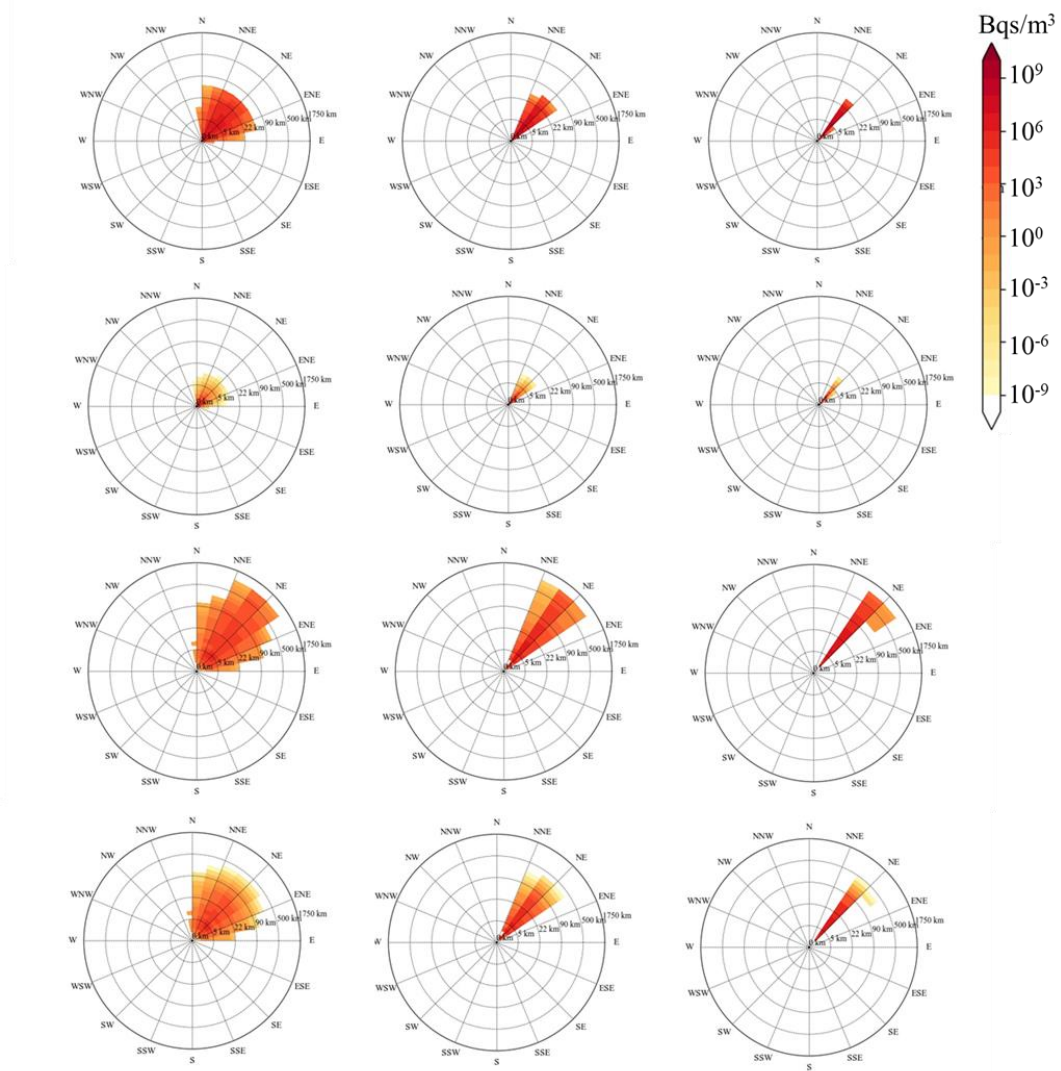


Figure A-1 Total air concentration for 24 hours of Cs-137

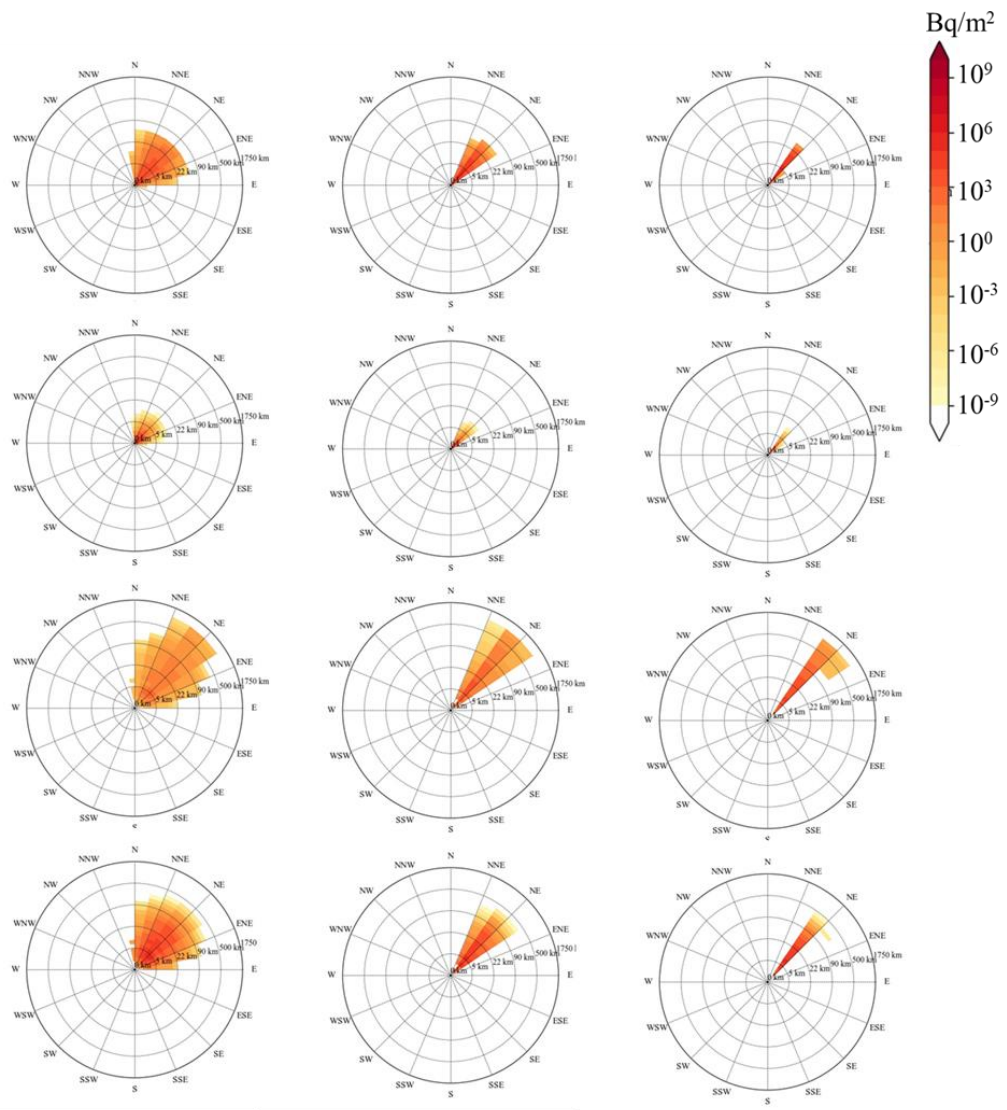


Figure A-2 Total ground concentration for 24 hours of Cs-137

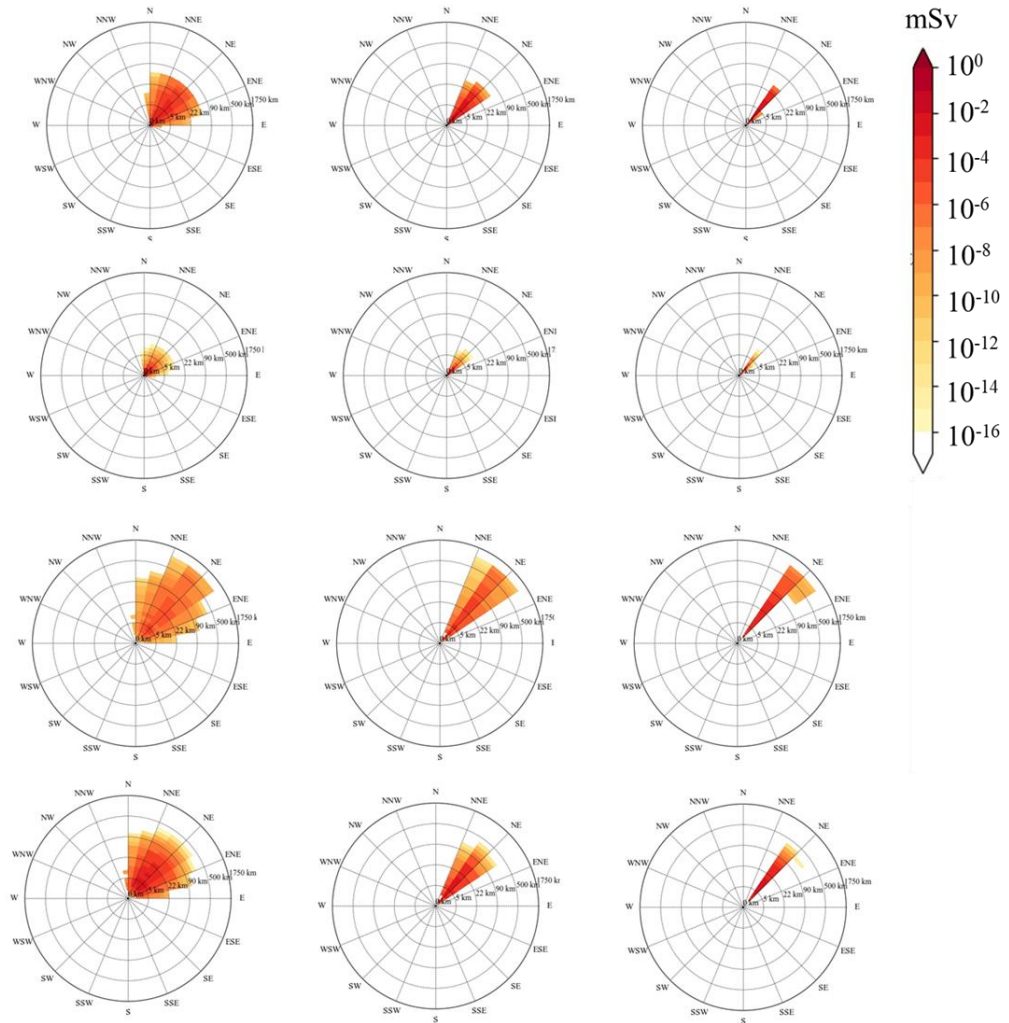


Figure A-3 Total effective dose equivalent for 24 hours

A3.Frequency distribution of wind direction of ten layers in each month

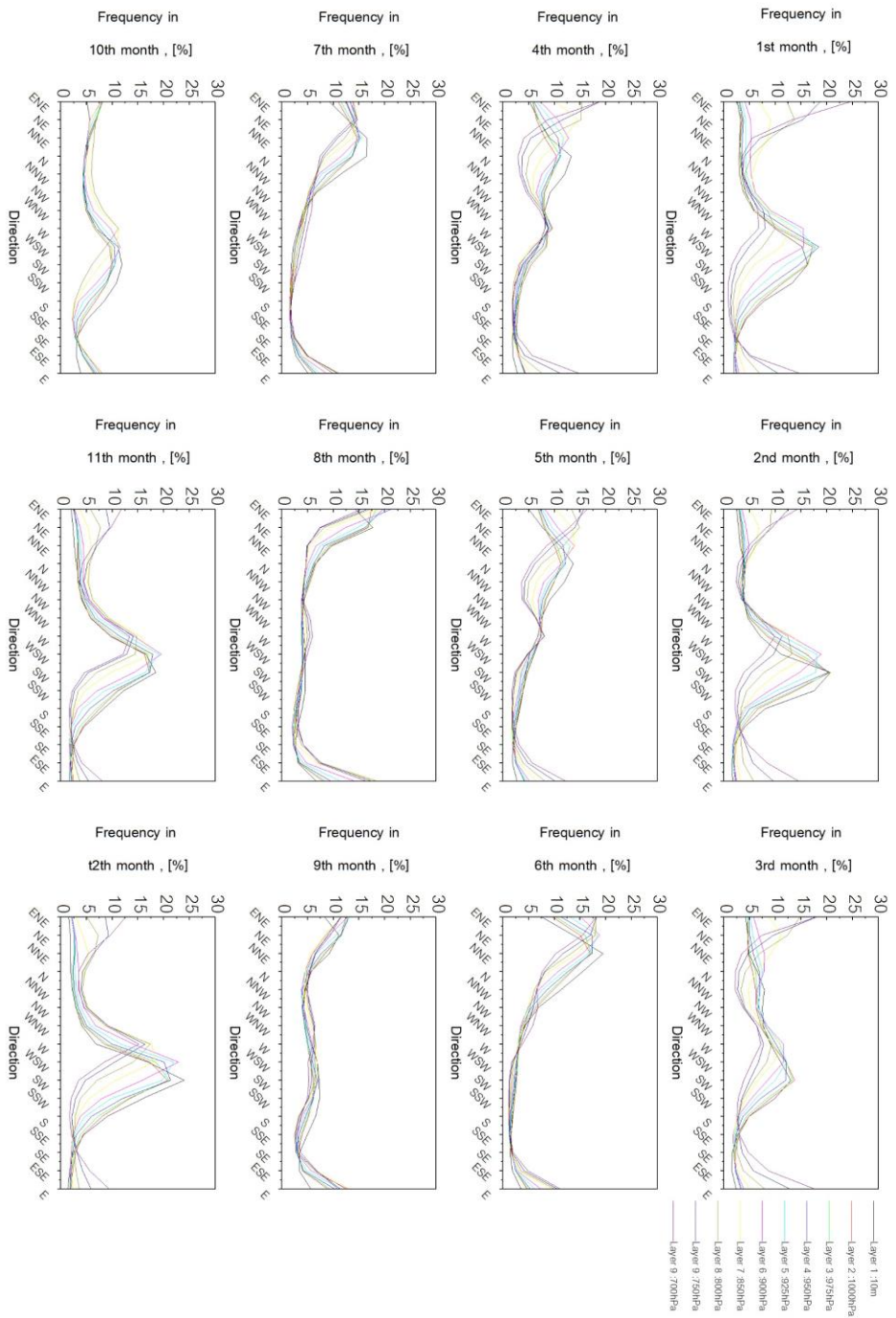


Figure A-4 Frequency distribution of wind direction of 10 layers in 2016

A4. Monthly average activity concentration of Cs-137

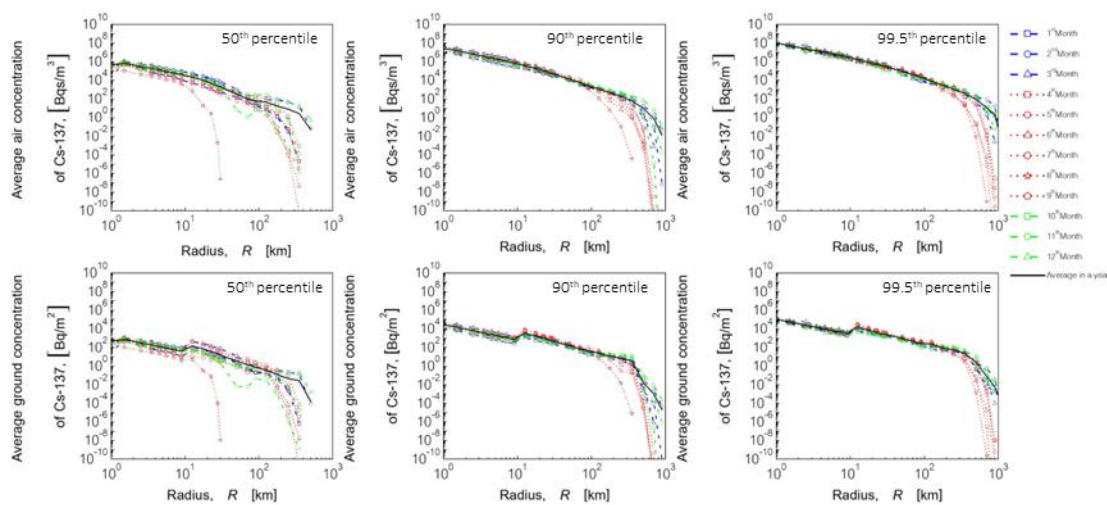
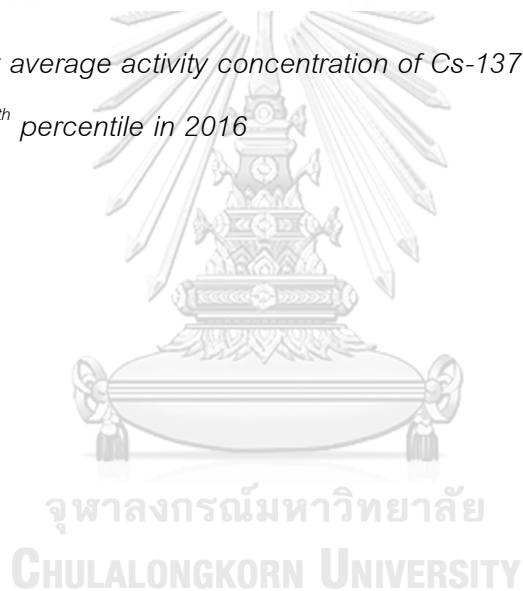


Figure A-5 Monthly average activity concentration of Cs-137 in each radius location at 50th, 90th, and 99.5th percentile in 2016



A5. Dispersion characteristics of TEDE after the accident for 24 hours

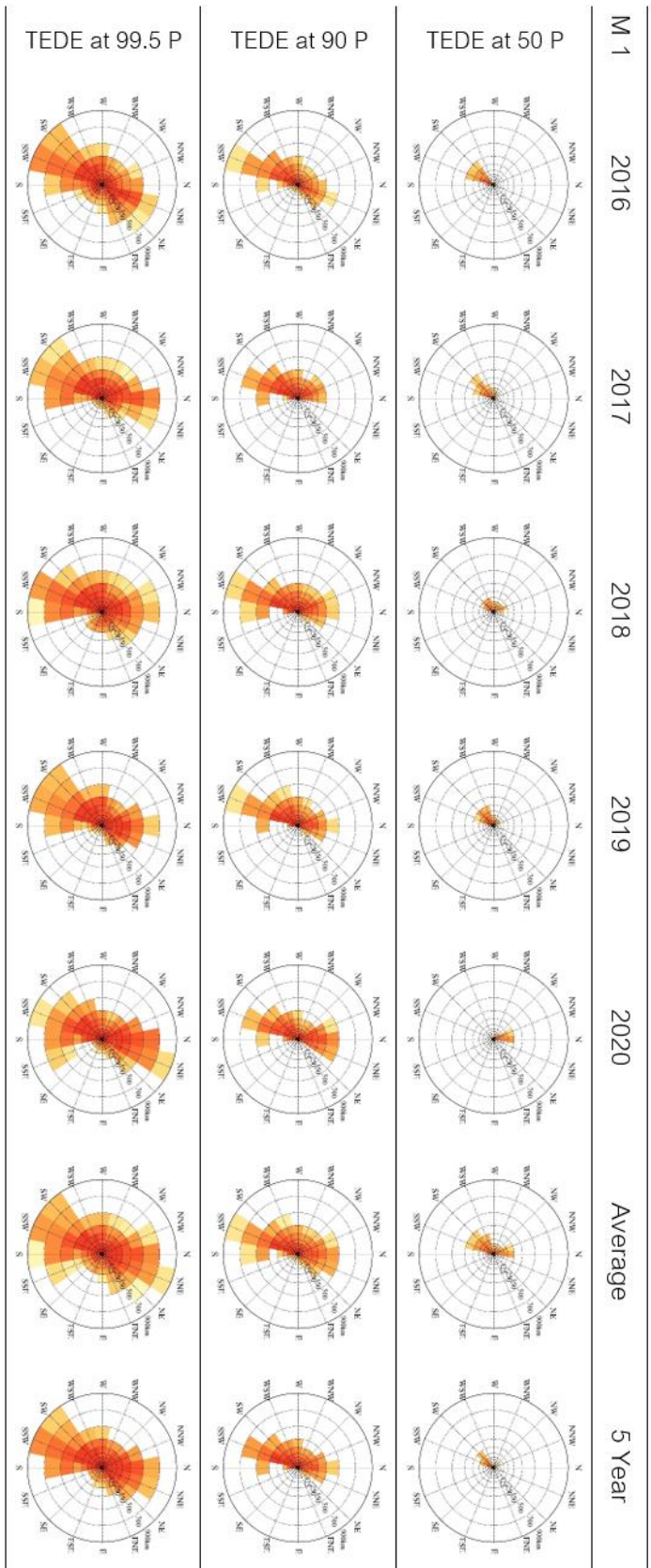


Figure A-6 Dispersion characteristic of TEDE after the accident for 24 hours on 1st month

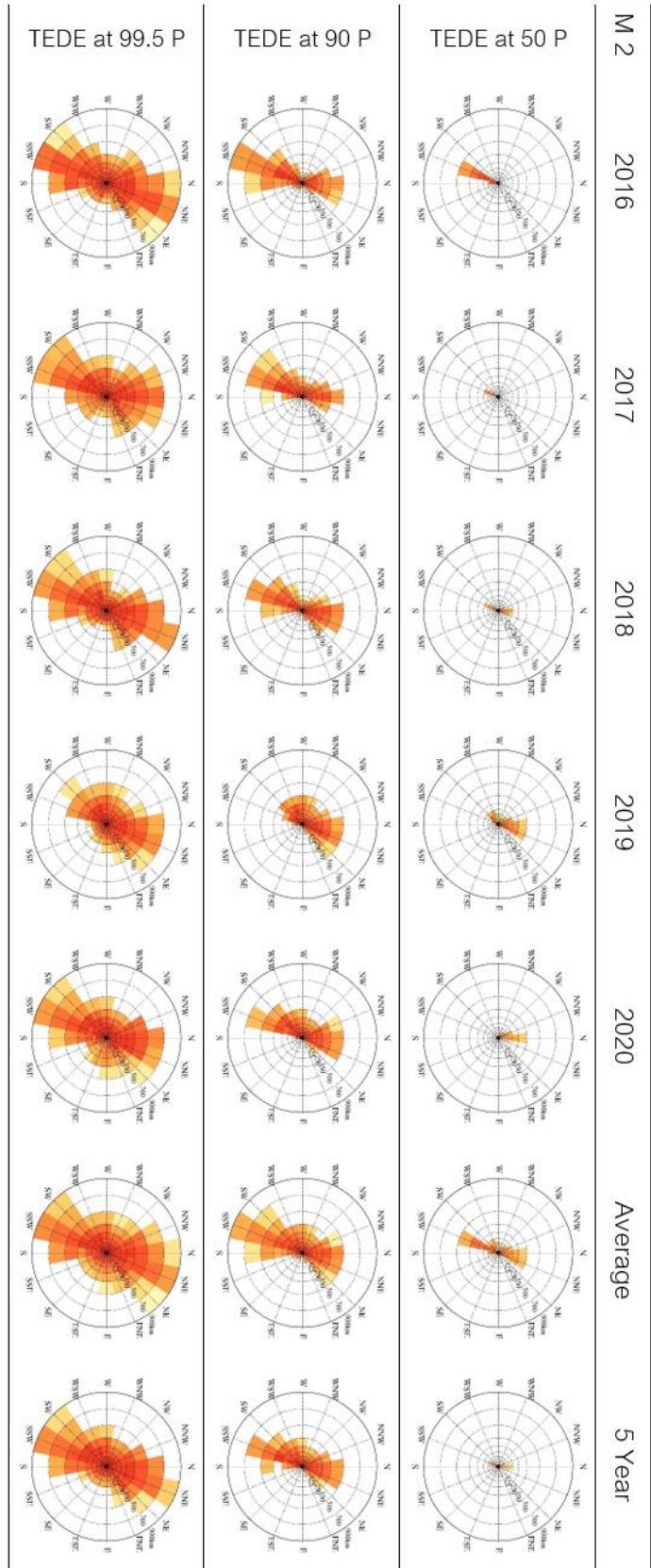


Figure A-7 Dispersion characteristic of TEDE after the accident for 24 hours on 2nd month

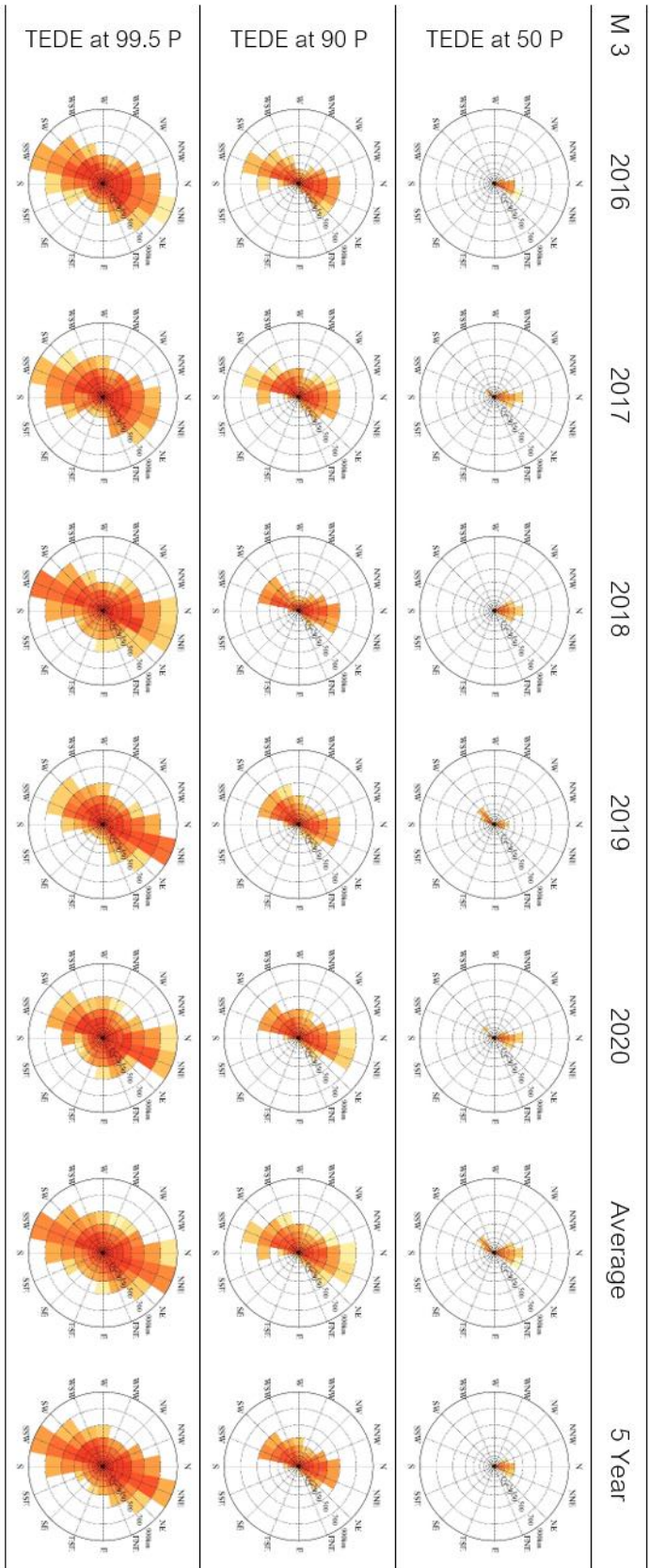


Figure A-8 Dispersion characteristic of TEDE after the accident for 24 hours on 3rd month

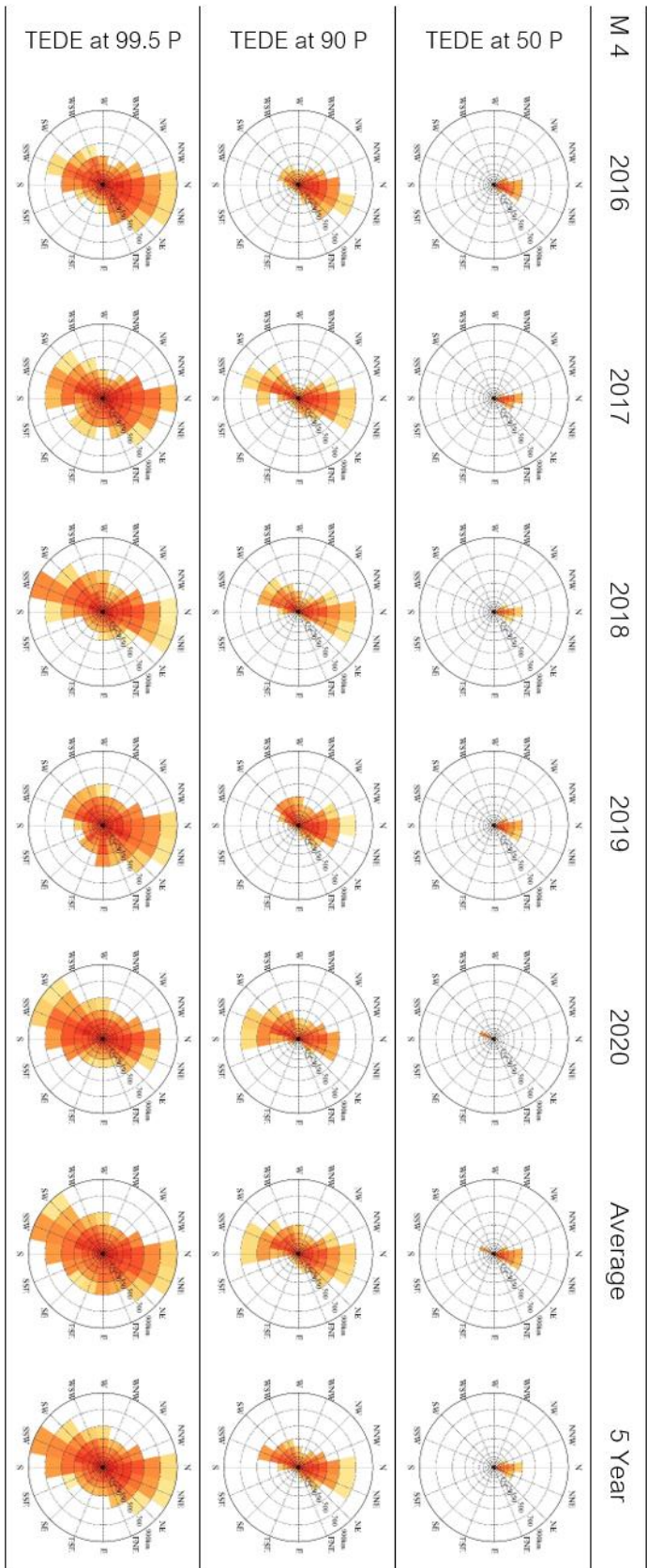


Figure A-9 Dispersion characteristic of TEDE after the accident for 24 hours on 4th month

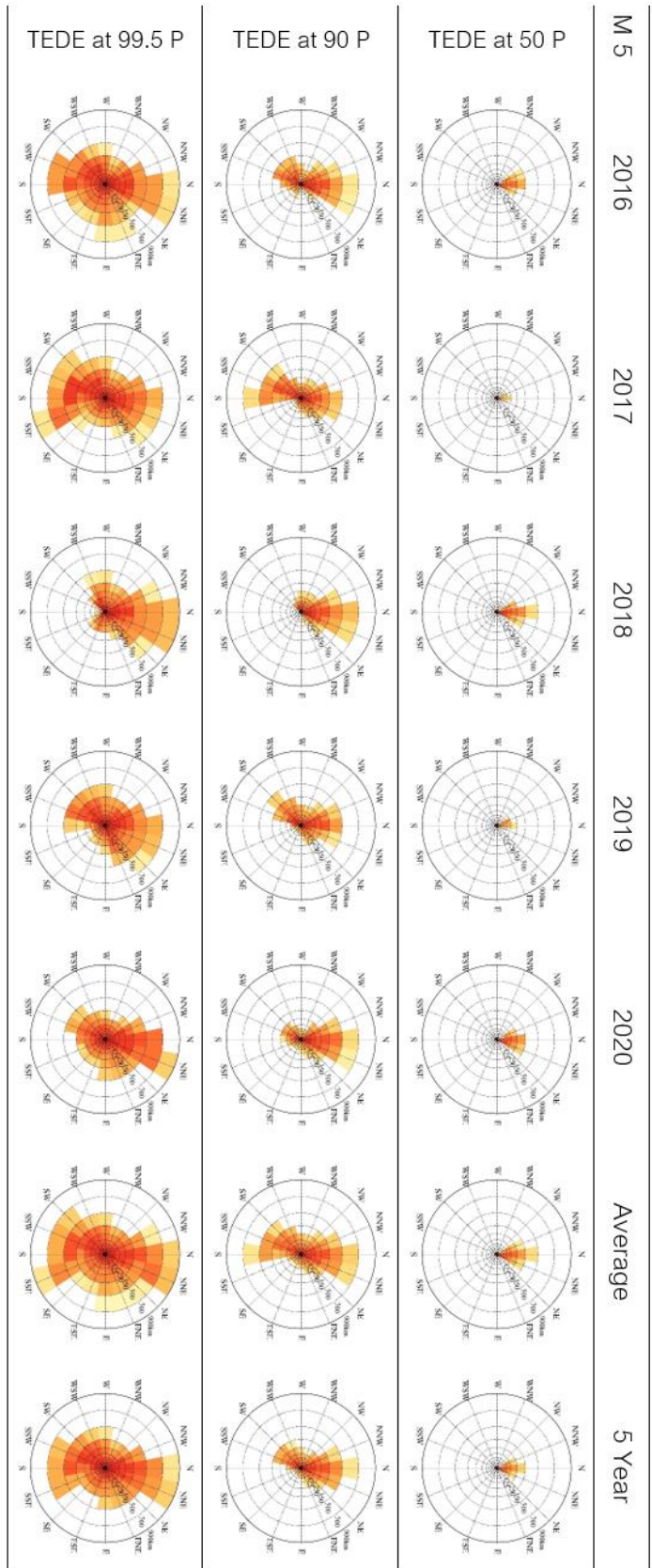


Figure A-10 Dispersion characteristic of TEDE after the accident for 24 hours on 5th month

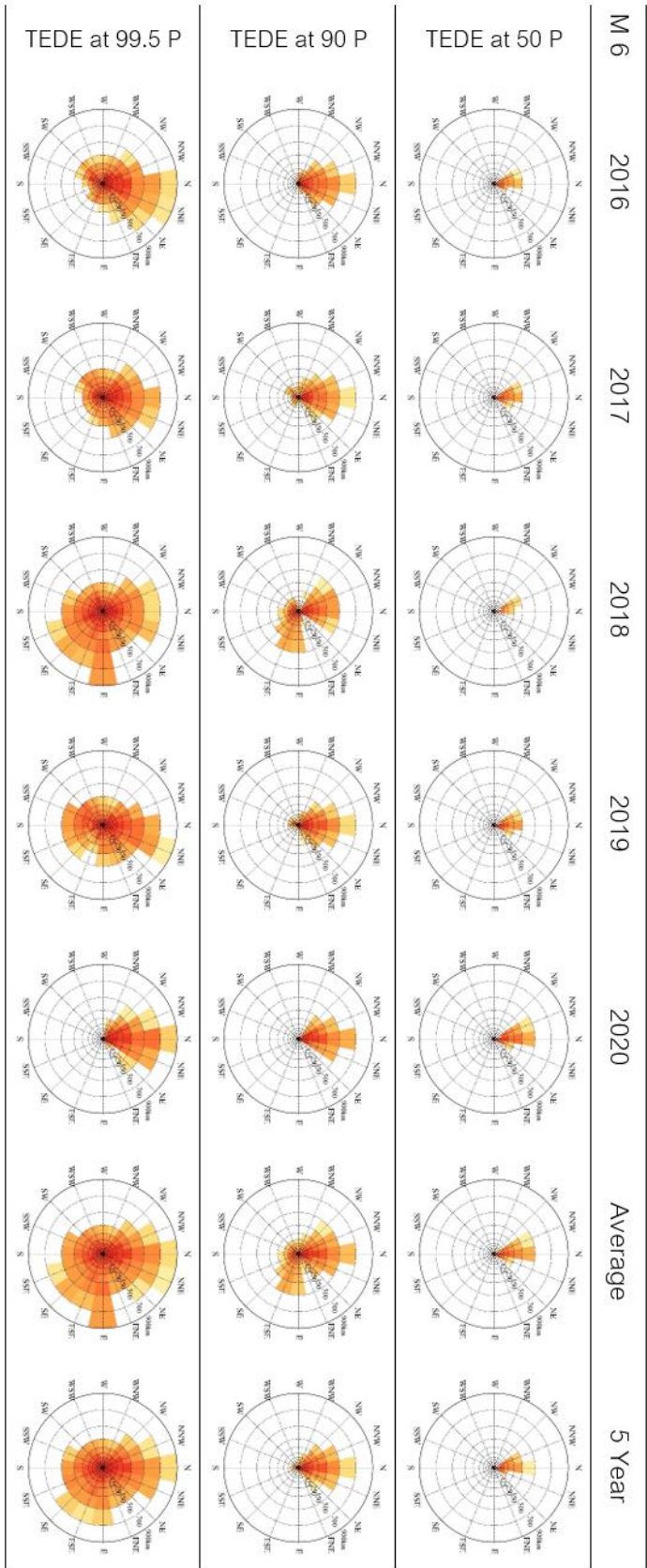


Figure A-11 Dispersion characteristic of TEDE after the accident for 24 hours on 6th month

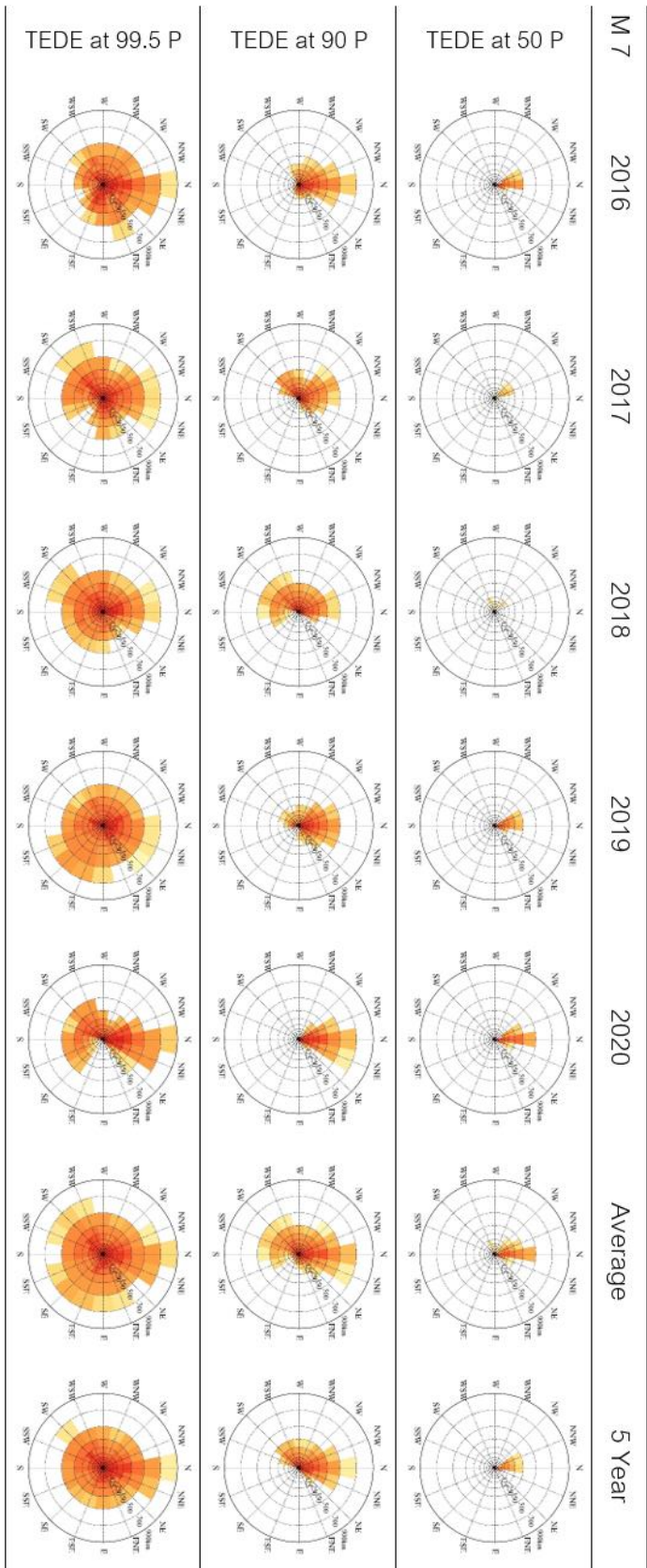


Figure A-12 Dispersion characteristic of TEDE after the accident for 24 hours on 7th month

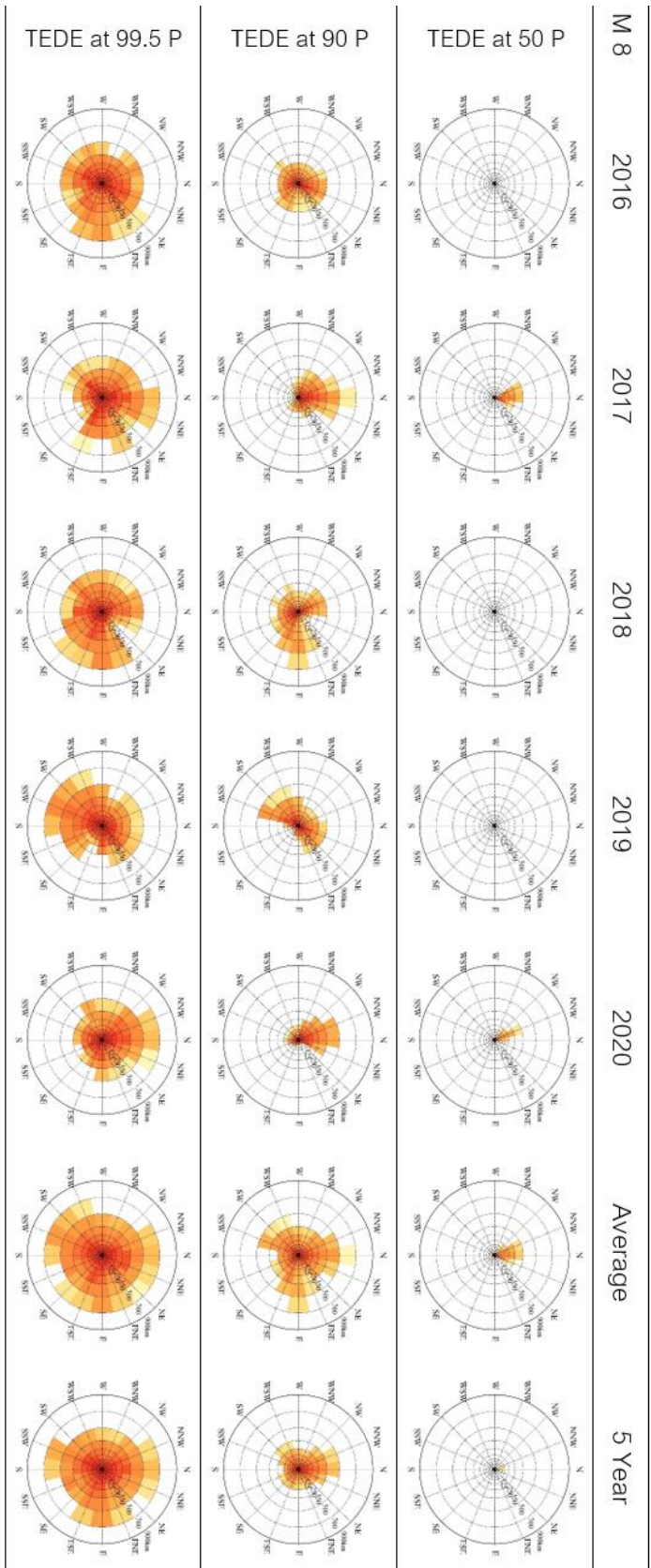


Figure A-13 Dispersion characteristic of TEDE after the accident for 24 hours on 8th month

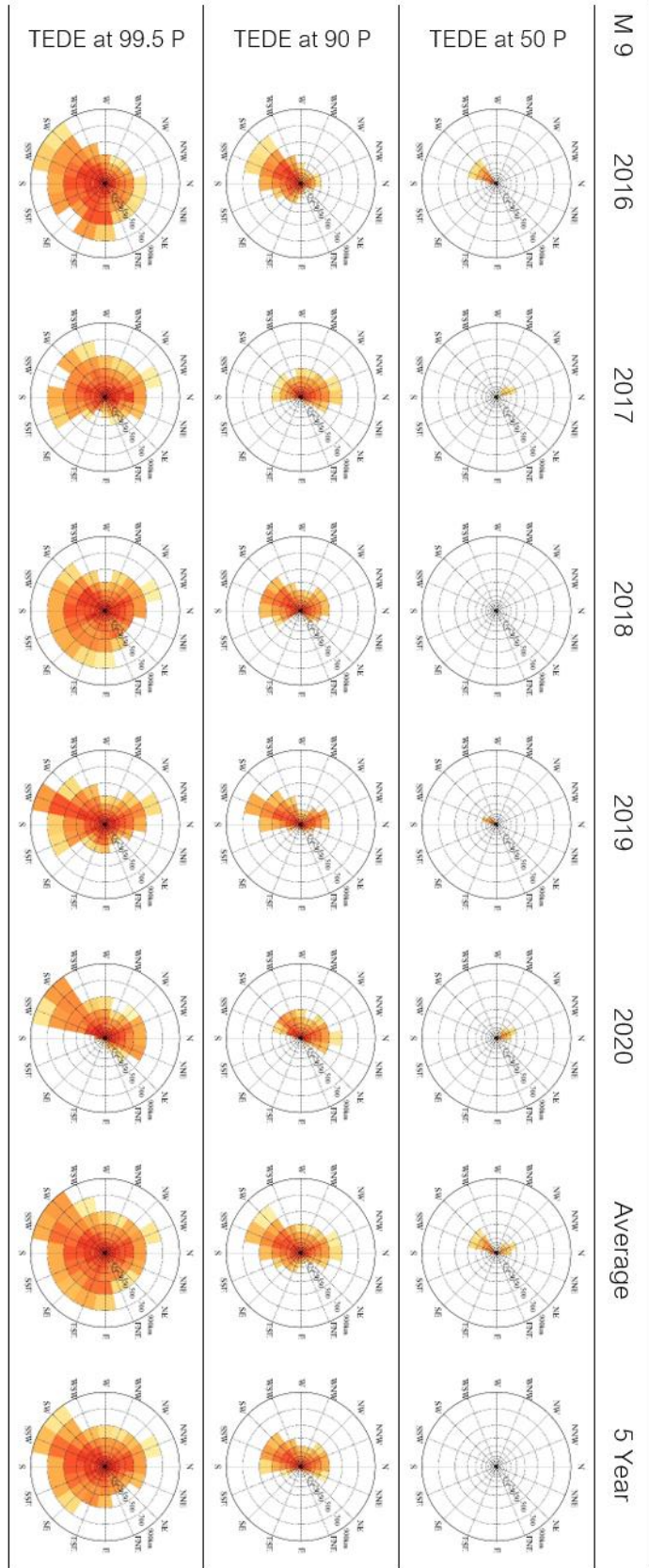


Figure A-14 Dispersion characteristic of TEDE after the accident for 24 hours on 9th month

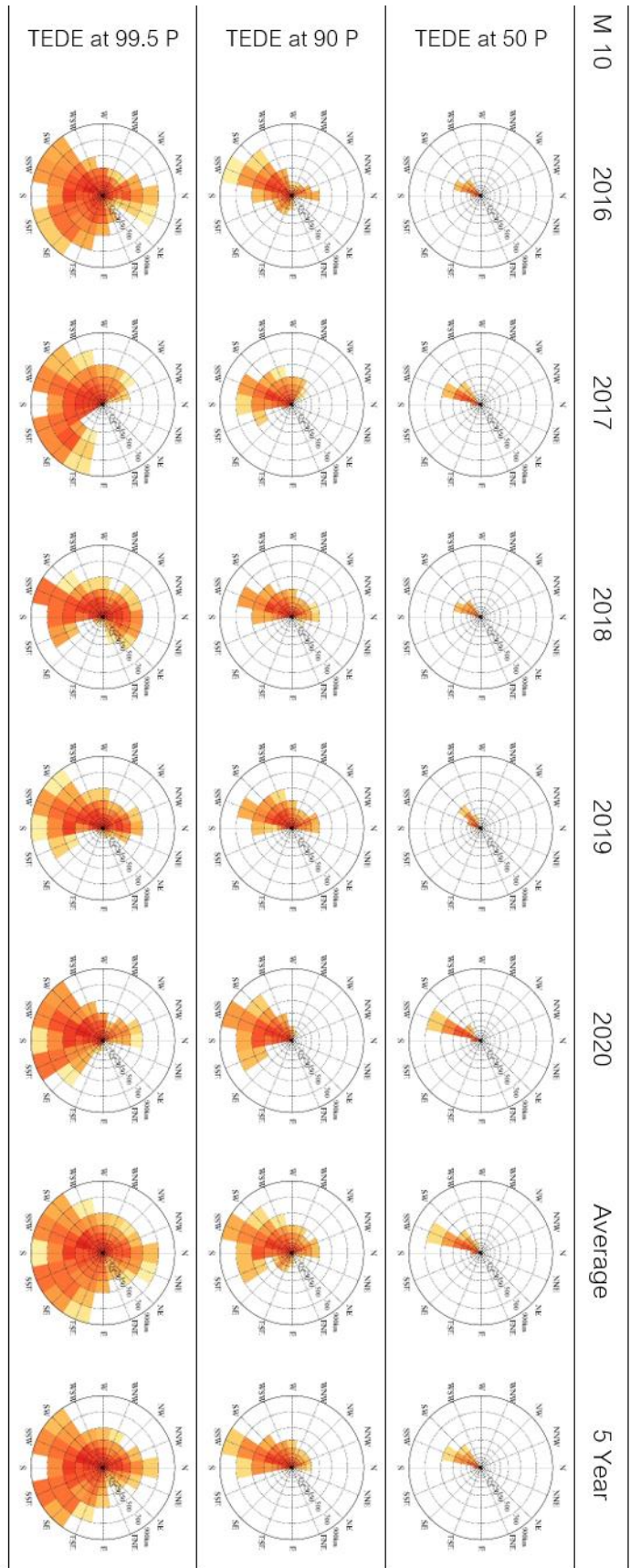


Figure A-15 Dispersion characteristic of TEDE after the accident for 24 hours on 10th month

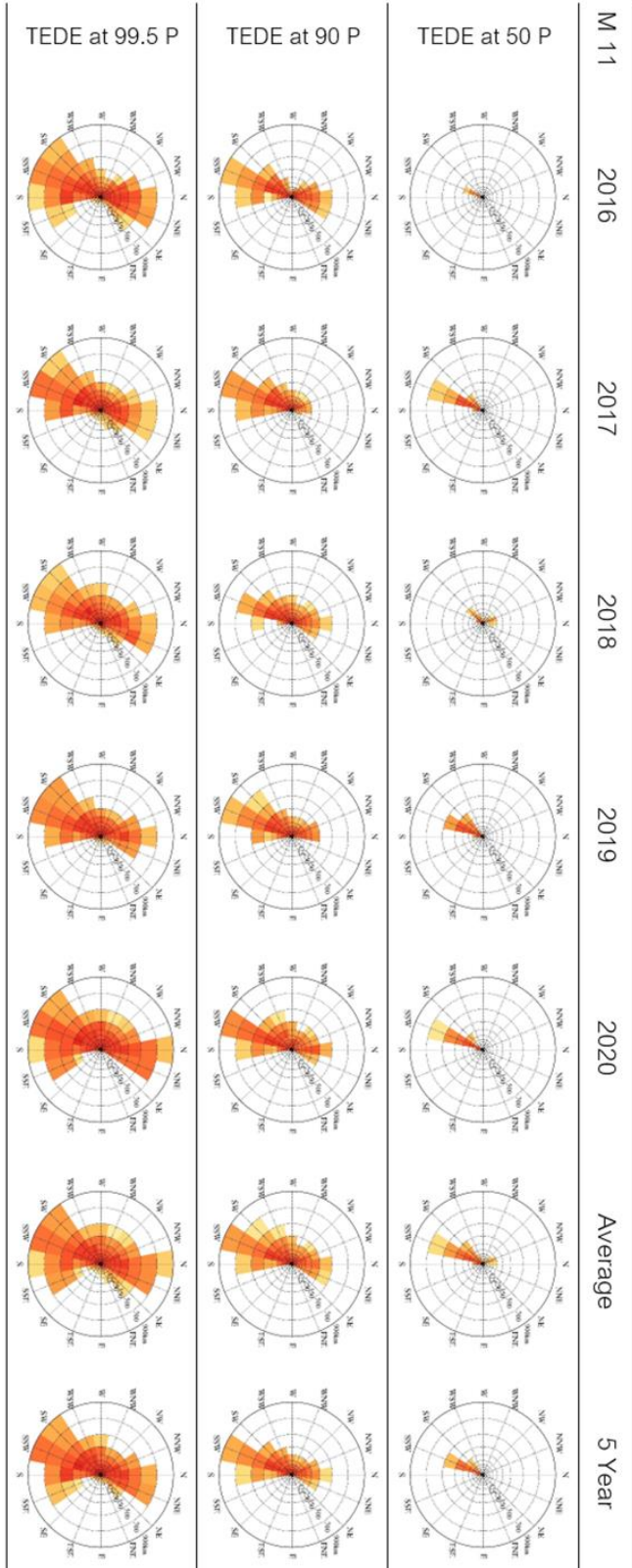


Figure A-16 Dispersion characteristic of TEDE after the accident for 24 hours on 11th month

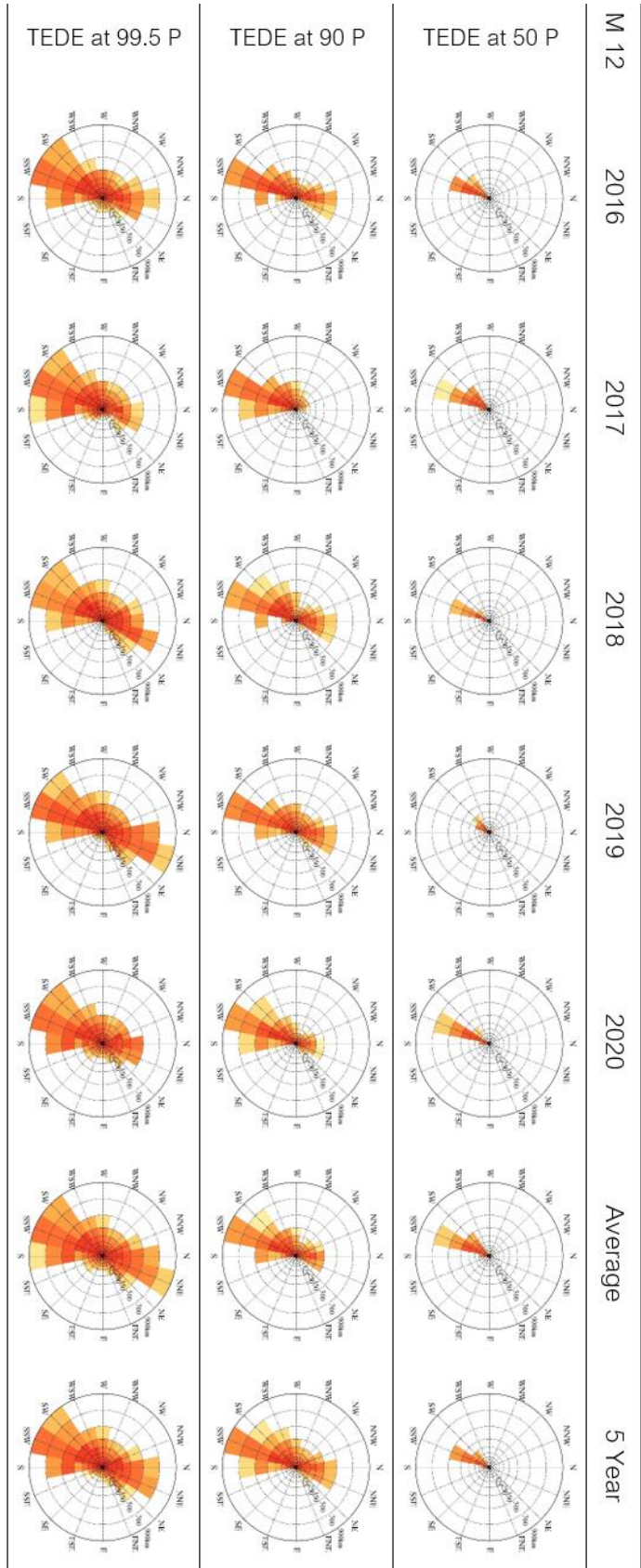


Figure A-17 Dispersion characteristic of TEDE after the accident for 24 hours on 12th month

A6. Frequency distribution of wind direction and average wind speed of ten layers between 2016-2020

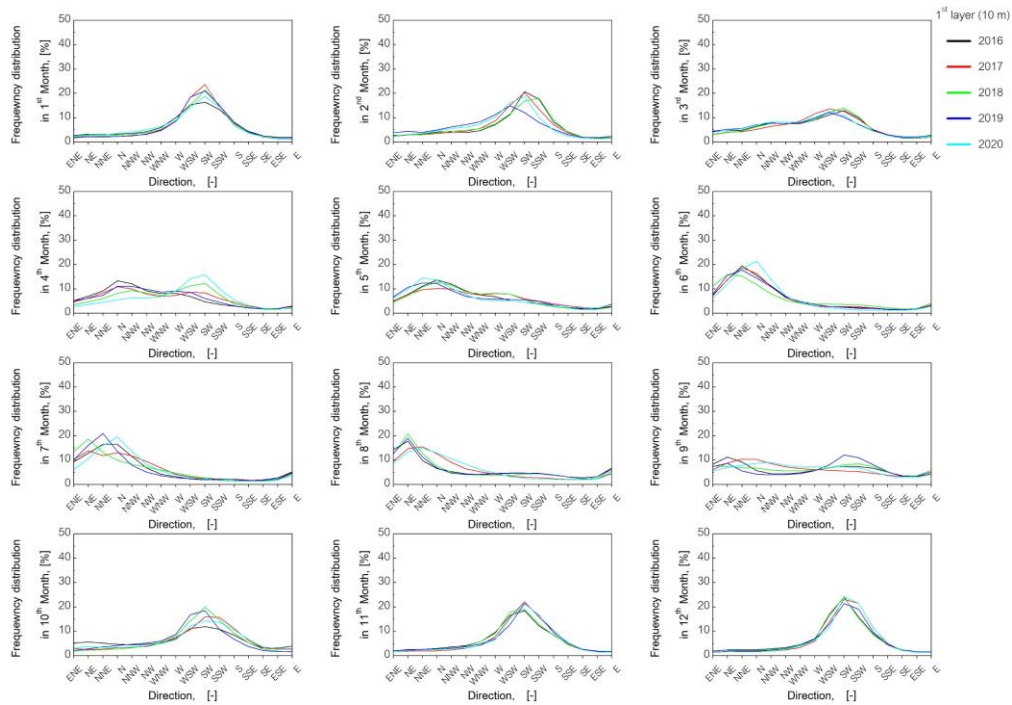


Figure A-17 Frequency distribution of wind direction at 1st layer (10m)

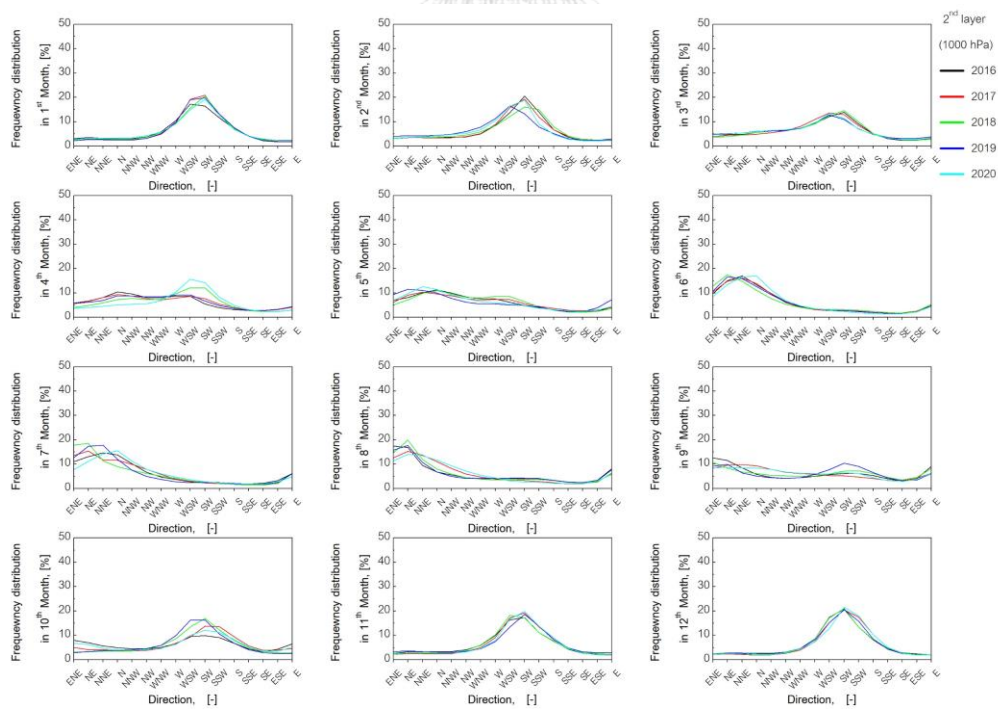


Figure A-18 Frequency distribution of wind direction at 2nd layer (1000 hPa)

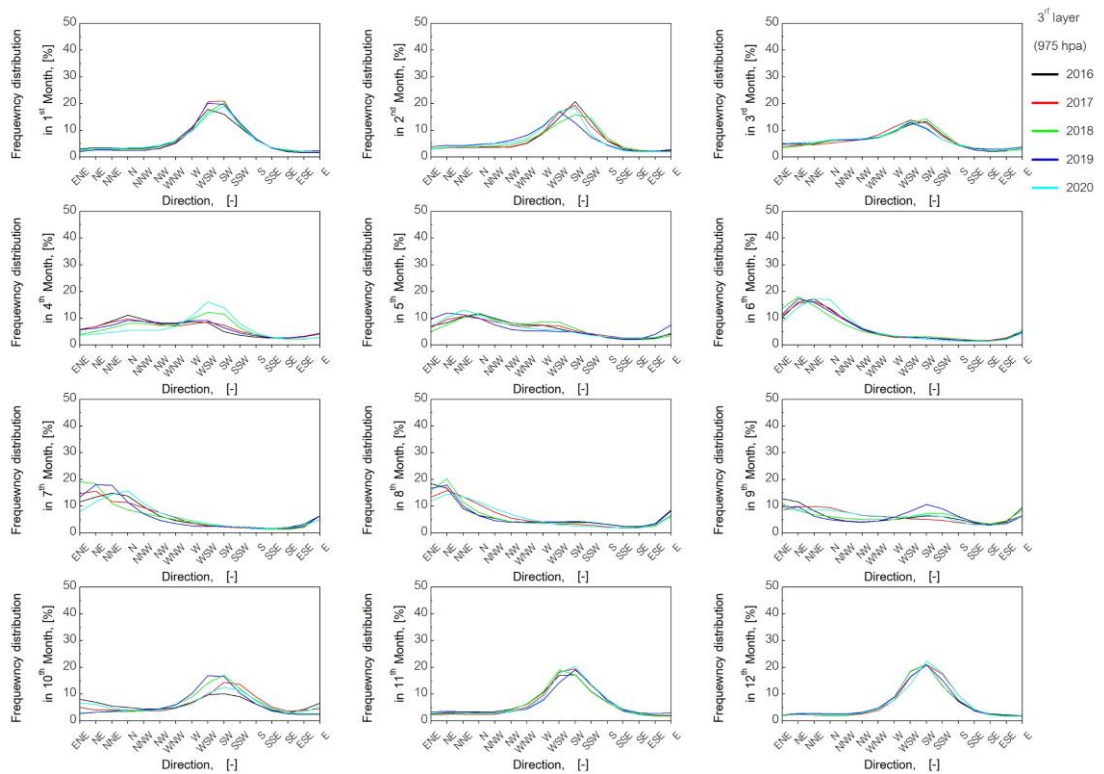


Figure A-19 Frequency distribution of wind direction at 3rd layer (975 hPa)

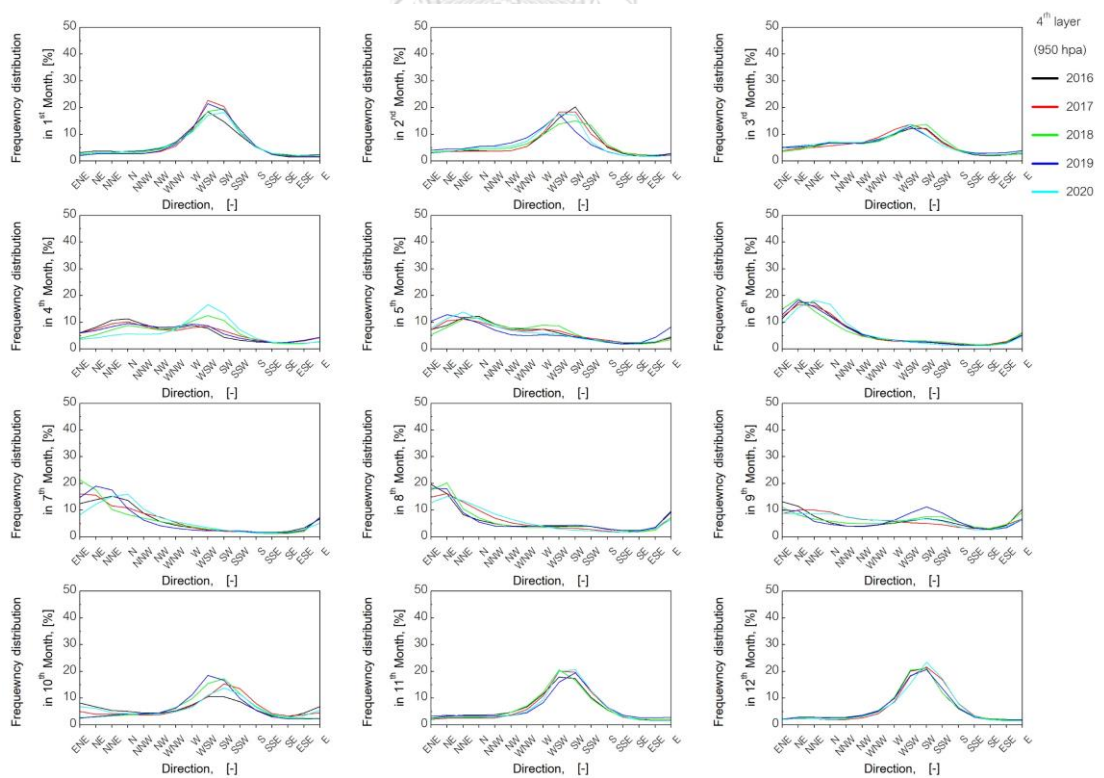


Figure A-20 Frequency distribution of wind direction at 4th layer (950 hPa)

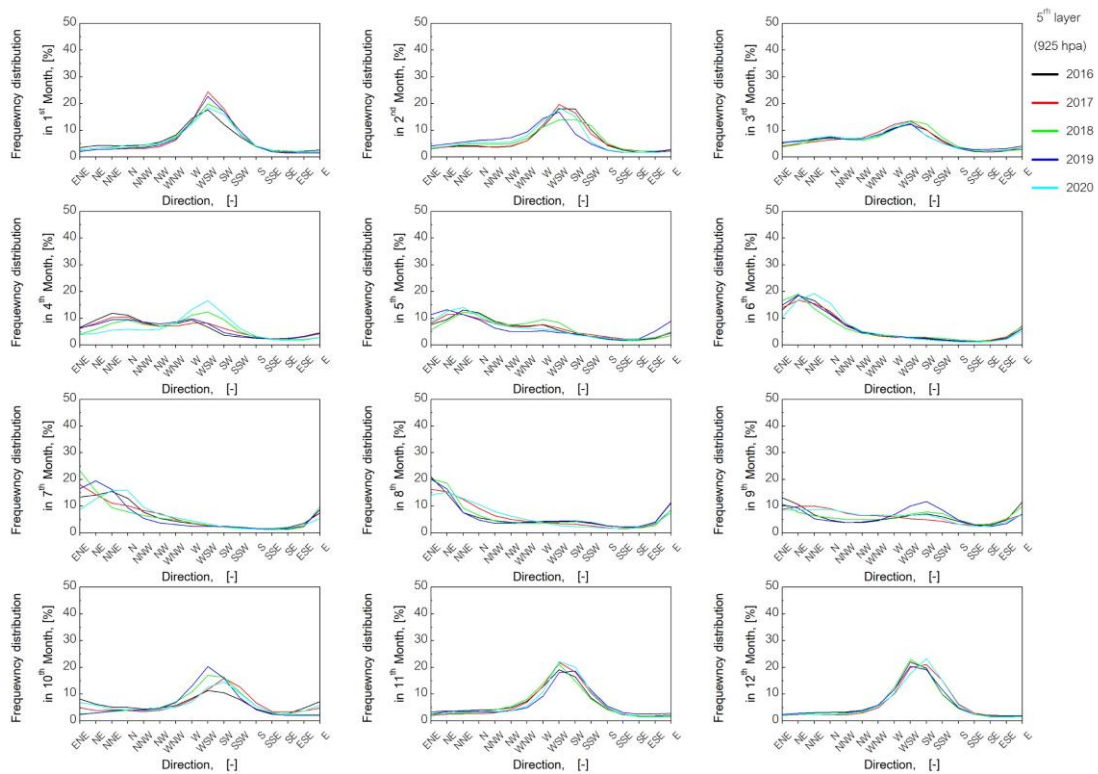


Figure A-21 Frequency distribution of wind direction at 5th layer (925 hPa)

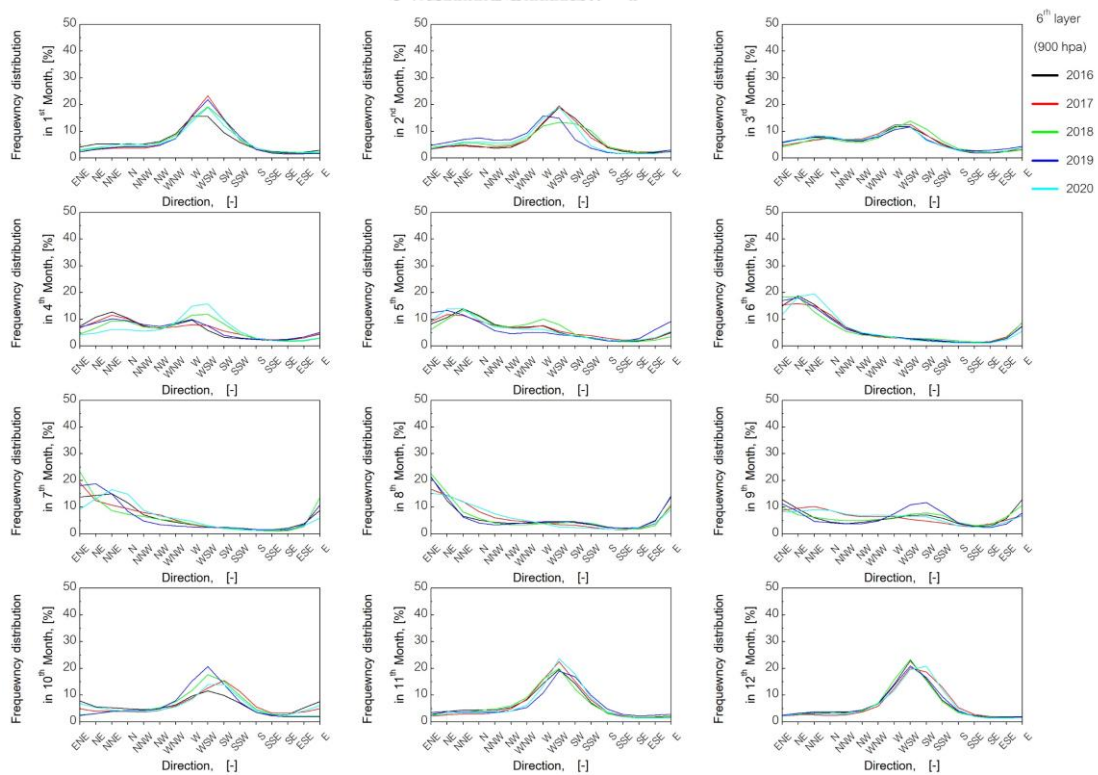


Figure A-22 Frequency distribution of wind direction at 6th layer (900 hPa)

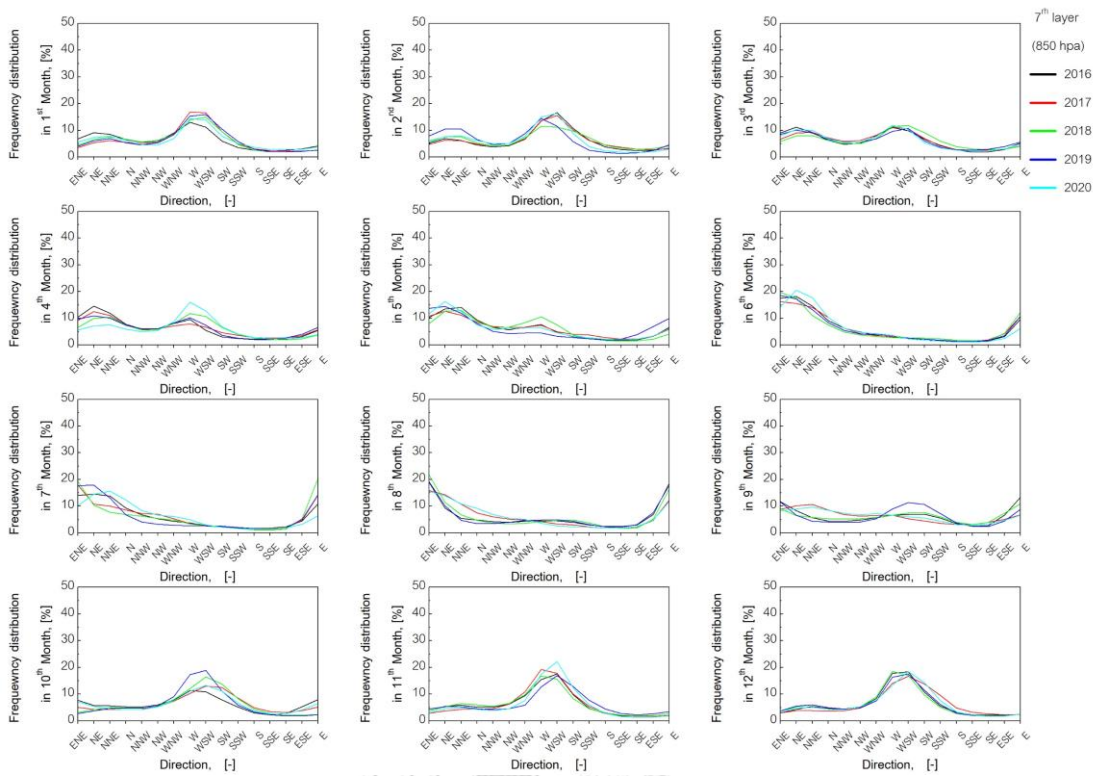


Figure A-23 Frequency distribution of wind direction at 7th layer (850 hPa)

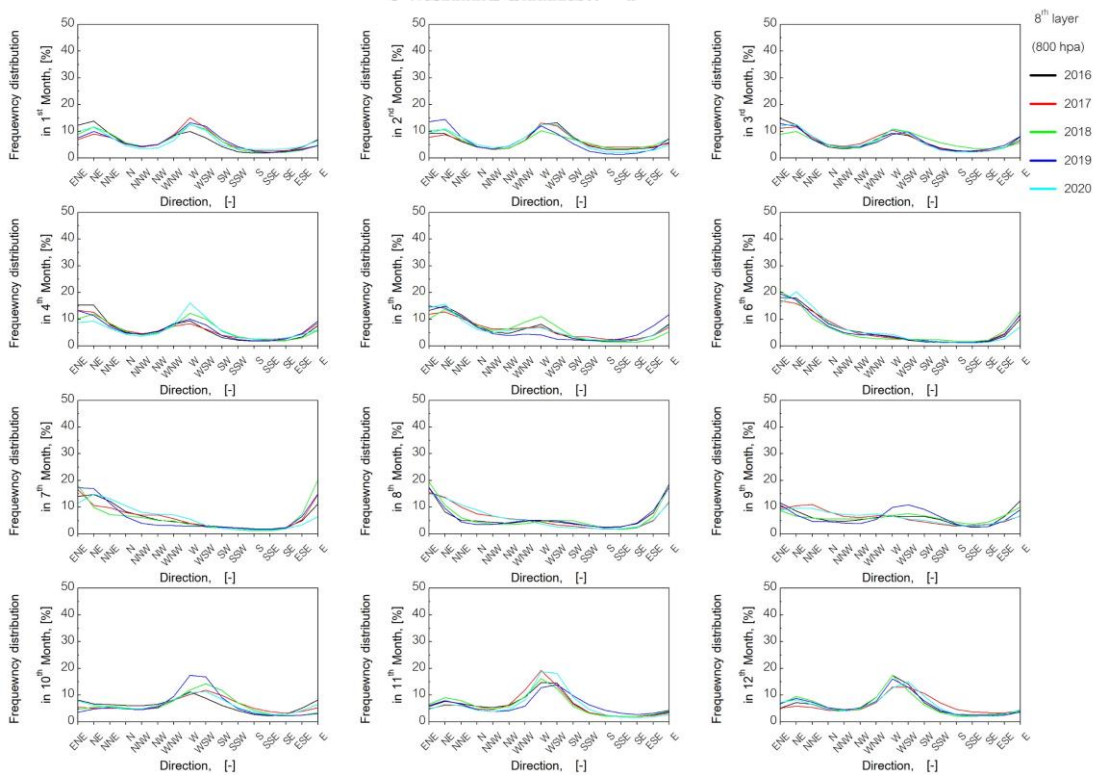


Figure A-24 Frequency distribution of wind direction at 8th layer (800 hPa)

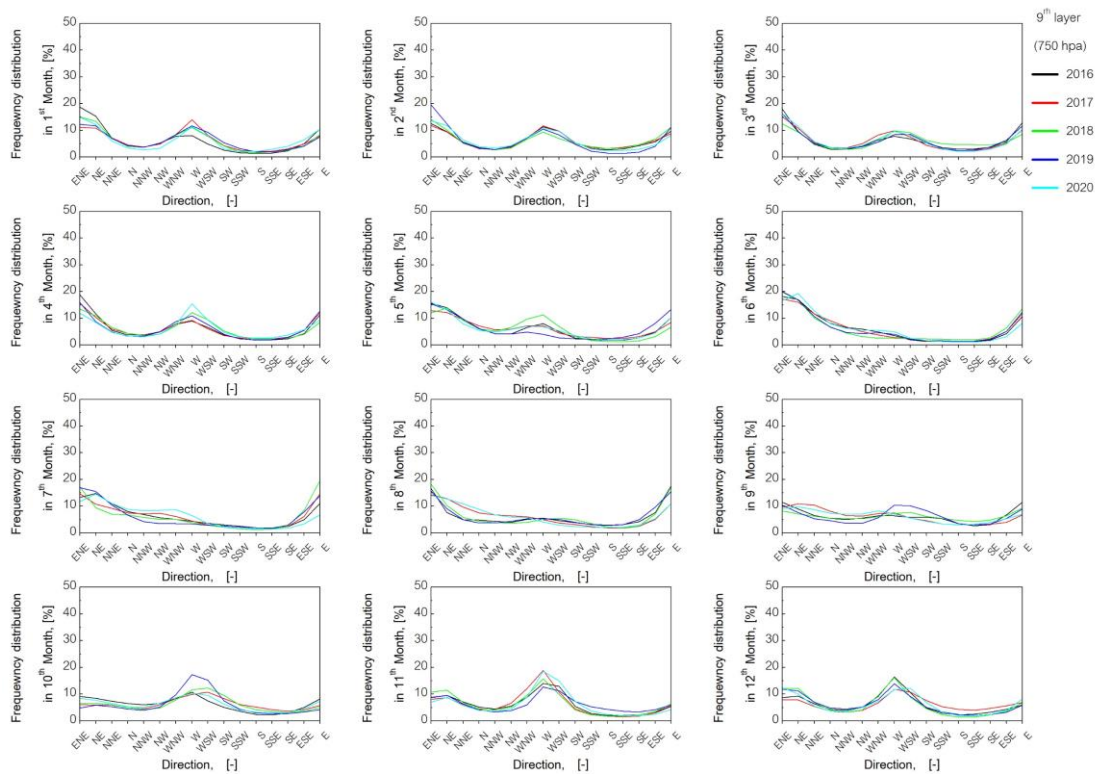


Figure A-25 Frequency distribution of wind direction at 9th layer (750 hPa)

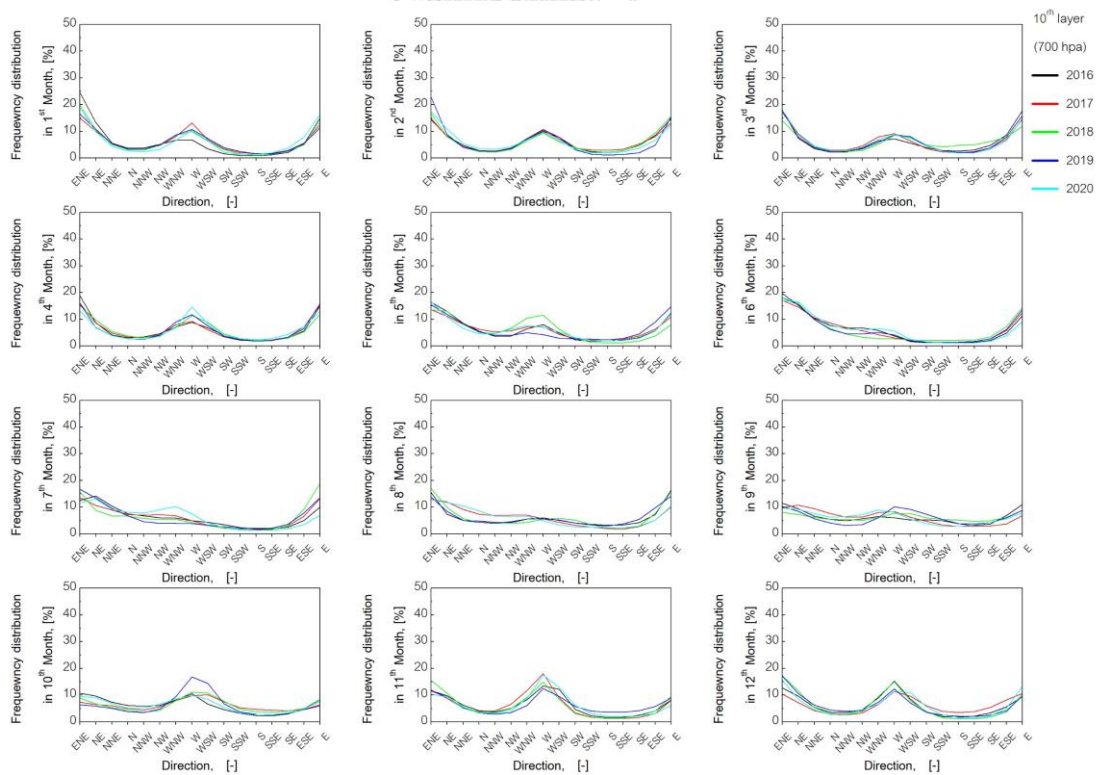


Figure A-26 Frequency distribution of wind direction at 10th layer (700 hPa)

A7. Activity concentrations in dominant dispersion direction of annual average dispersion characteristic.

Air concentration values of Cs-137

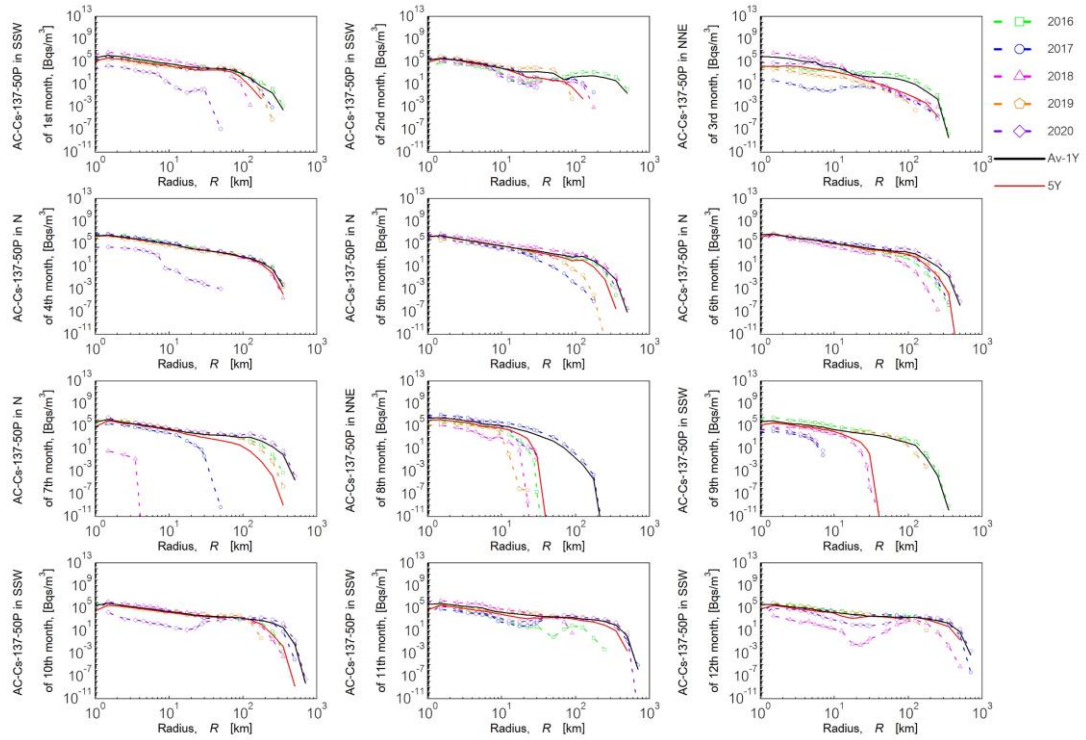
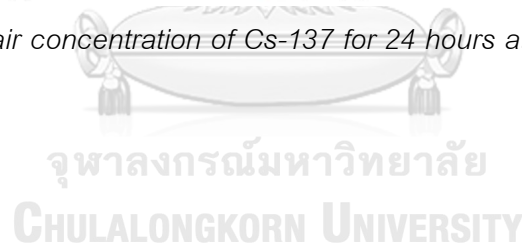


Figure A-28 Total air concentration of Cs-137 for 24 hours at 50th percentile



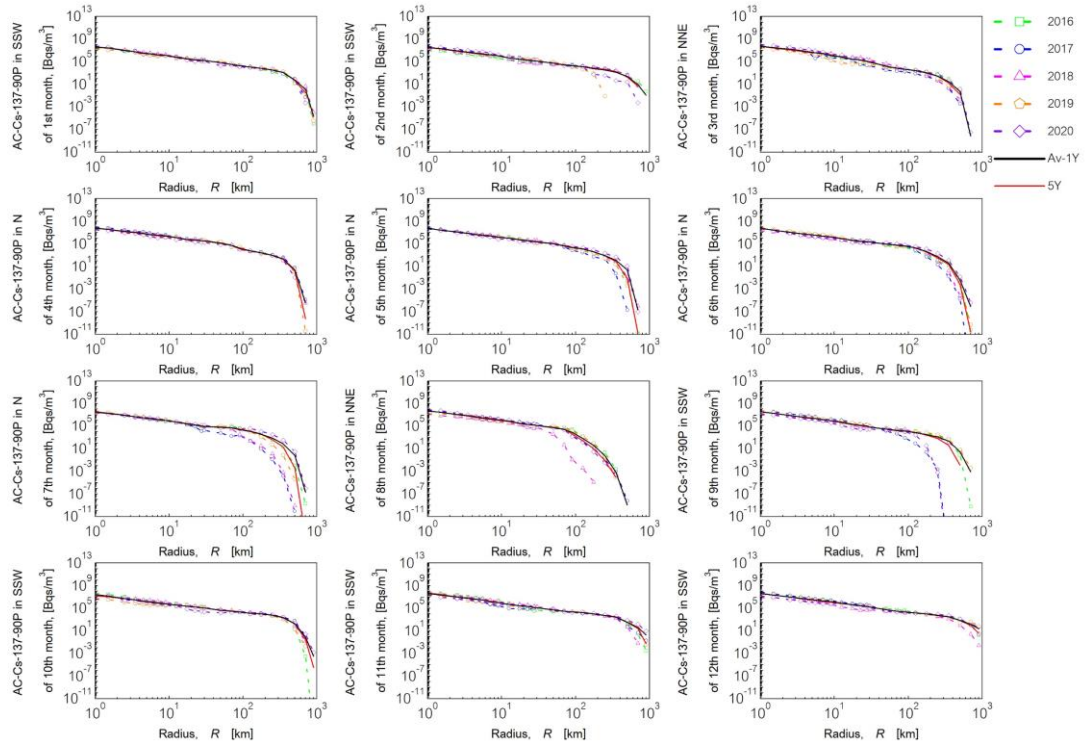


Figure A-29 Total air concentration of Cs-137 for 24 hours at 90th percentile

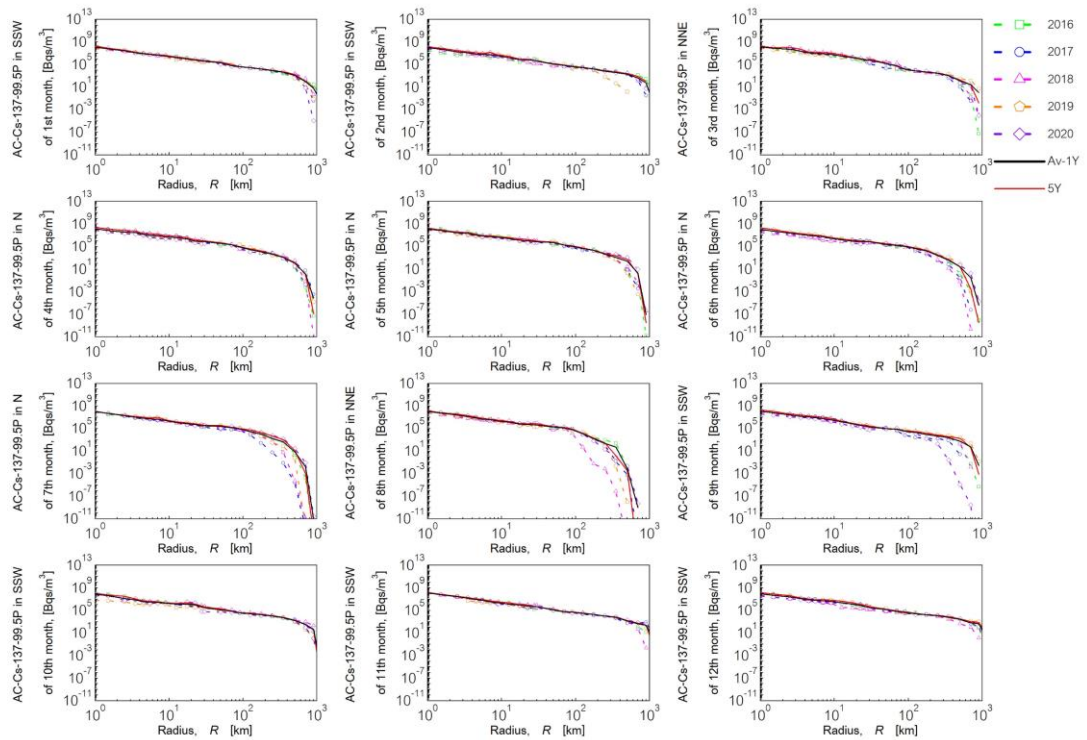
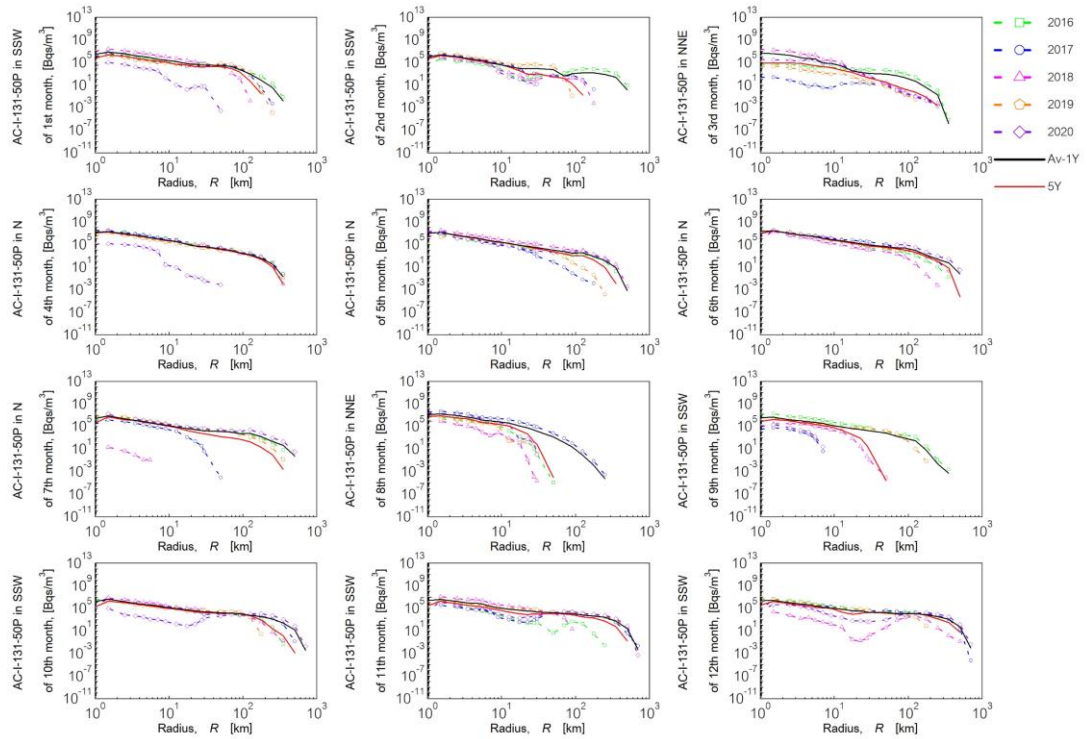
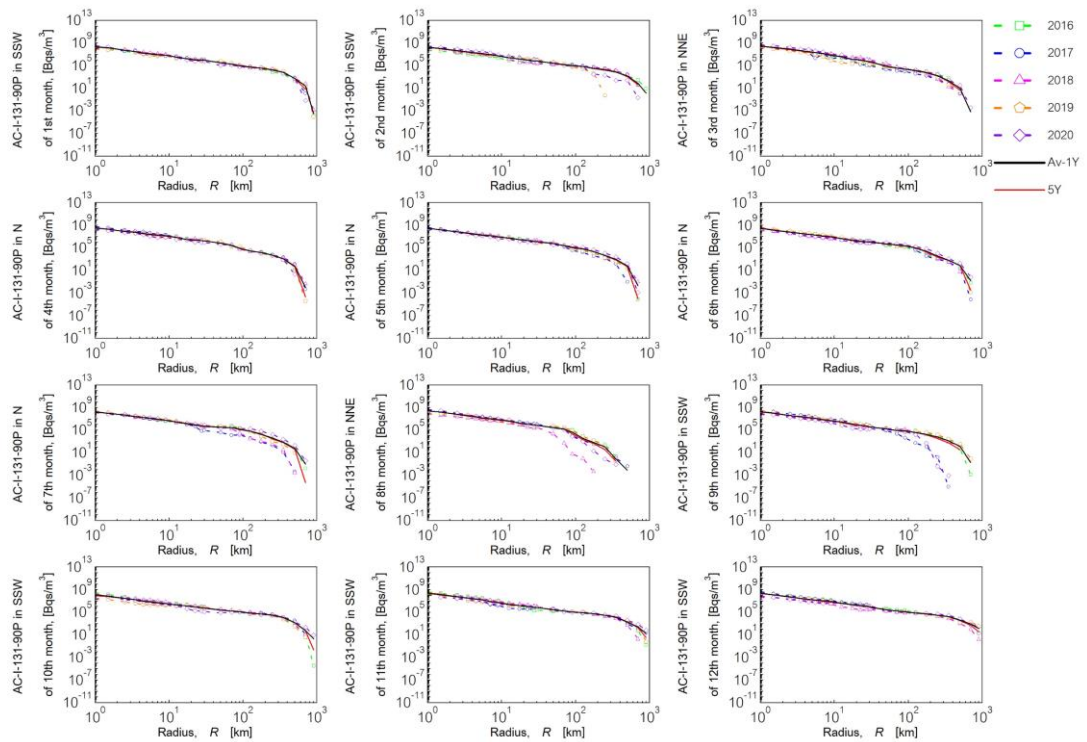


Figure A-30 Total air concentration of Cs-137 for 24 hours at 99.5th percentile

Air concentration values of I-131

Figure A-31 Total air concentration of I-131 for 24 hours at 50th percentileFigure A-32 Total air concentration of I-131 for 24 hours at 90th percentile

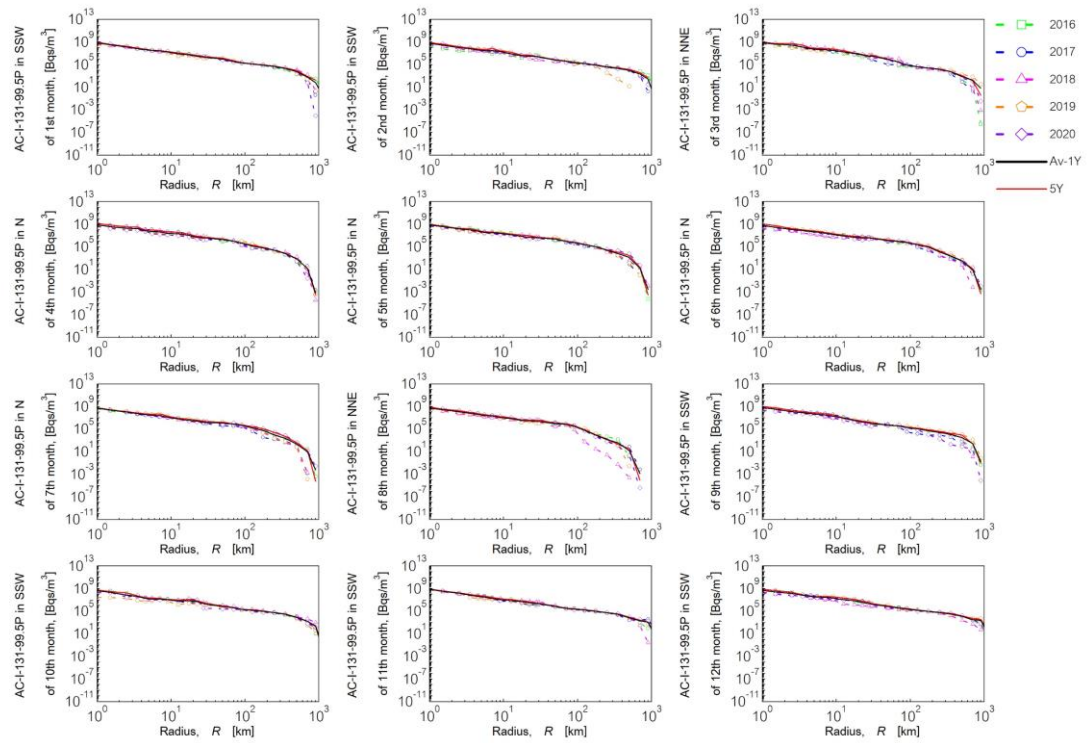


Figure A-33 Total air concentration of I-131 for 24 hours at 99.5th percentile



Ground concentration values of Cs-137

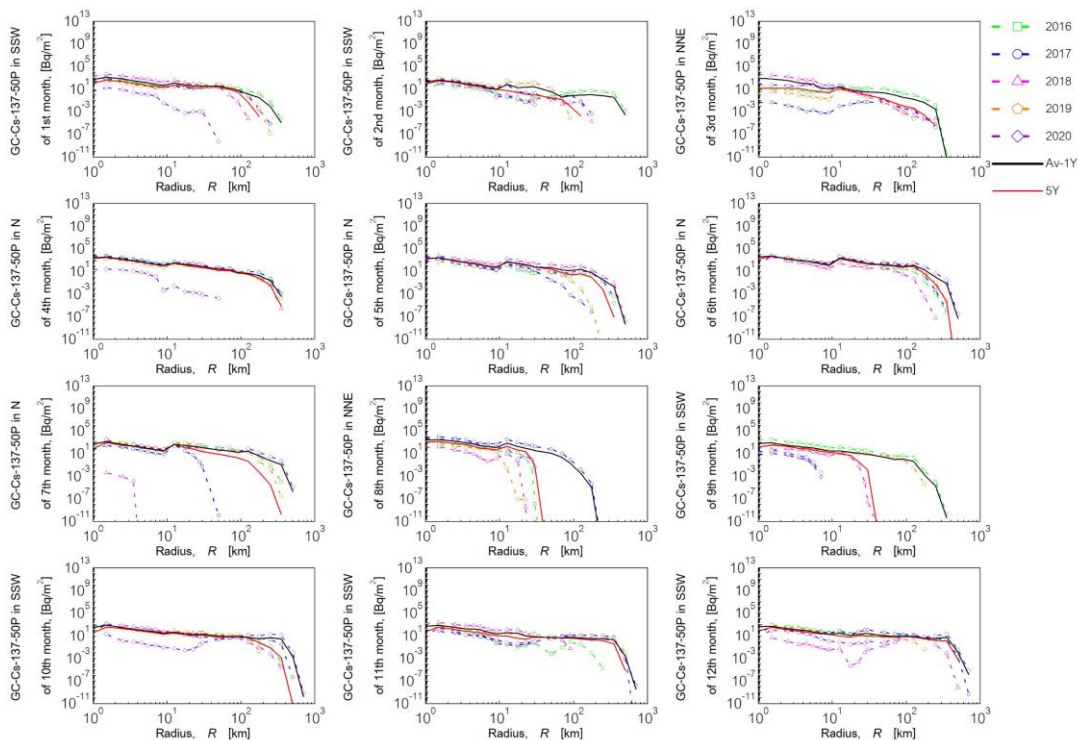


Figure A-34 Total ground concentration of Cs-137 for 24 hours at 50th percentile

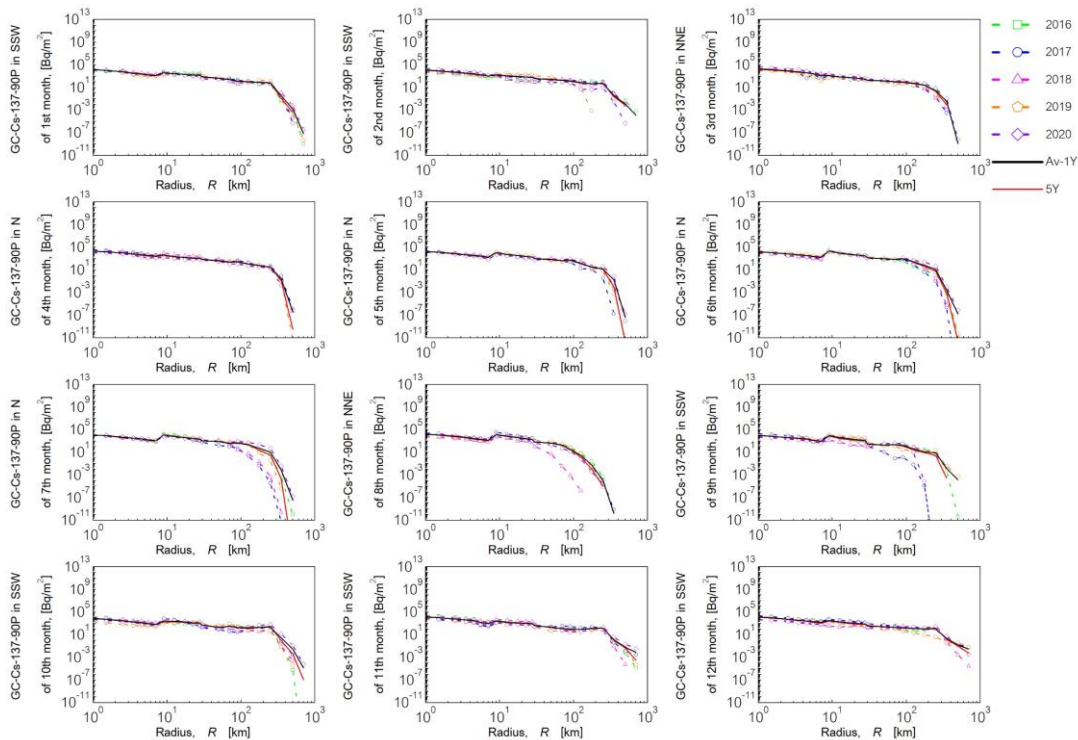


Figure A-35 Total ground concentration of Cs-137 for 24 hours at 90th percentile

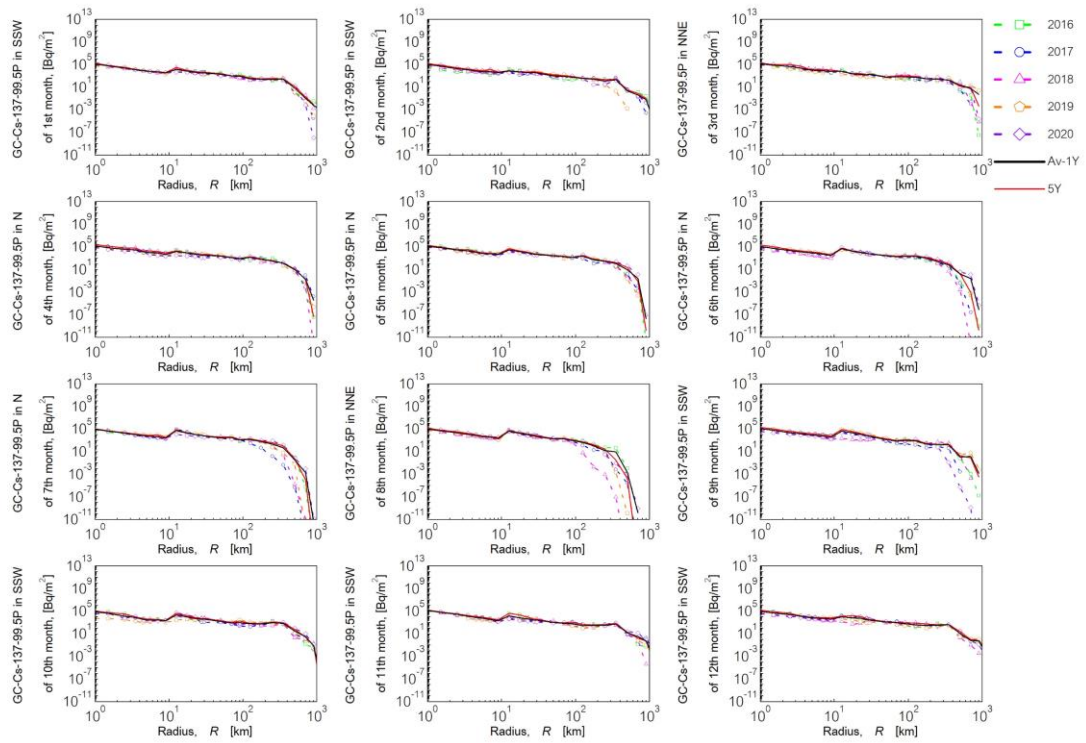


Figure A-36 Total ground concentration of Cs-137 for 24 hours at 99.5th percentile



Ground concentration values of I-131

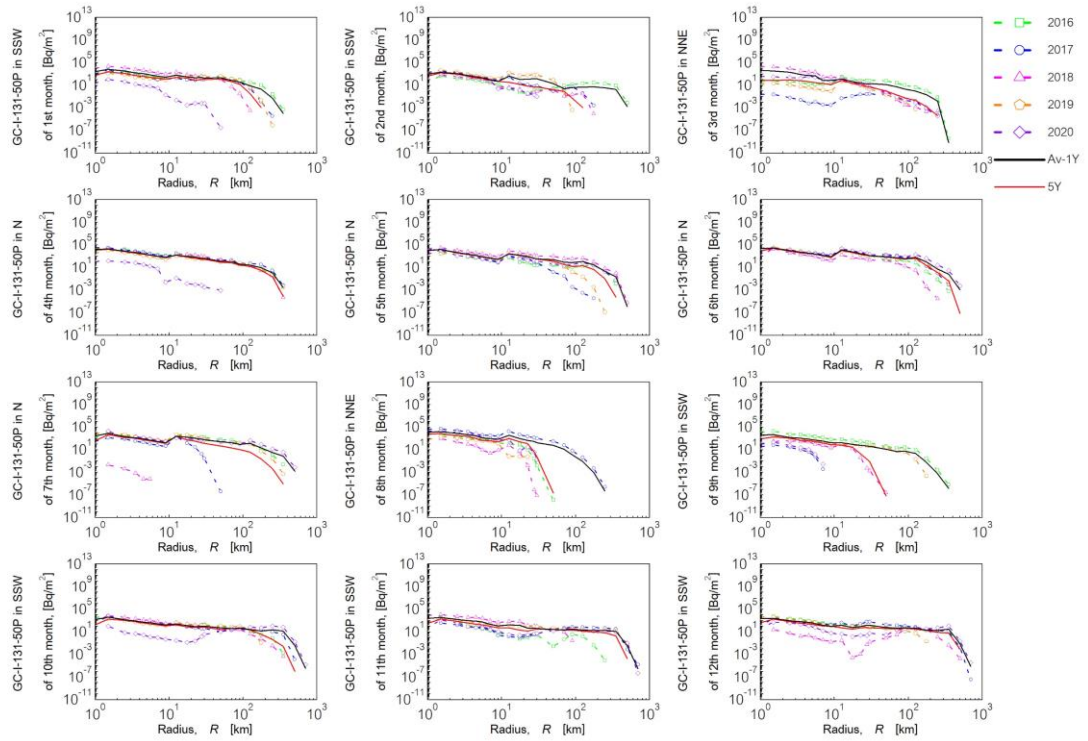


Figure A-37 Total ground concentration of I-131 for 24 hours at 50th percentile

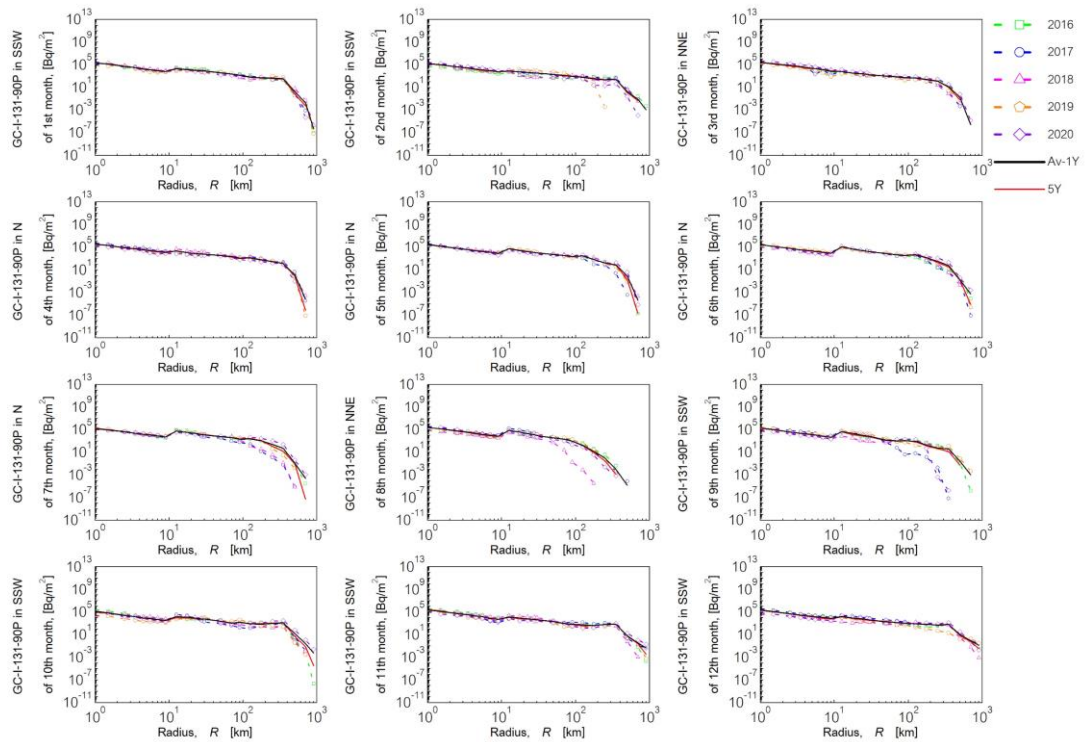


Figure A-38 Total ground concentration of I-131 for 24 hours at 90th percentile

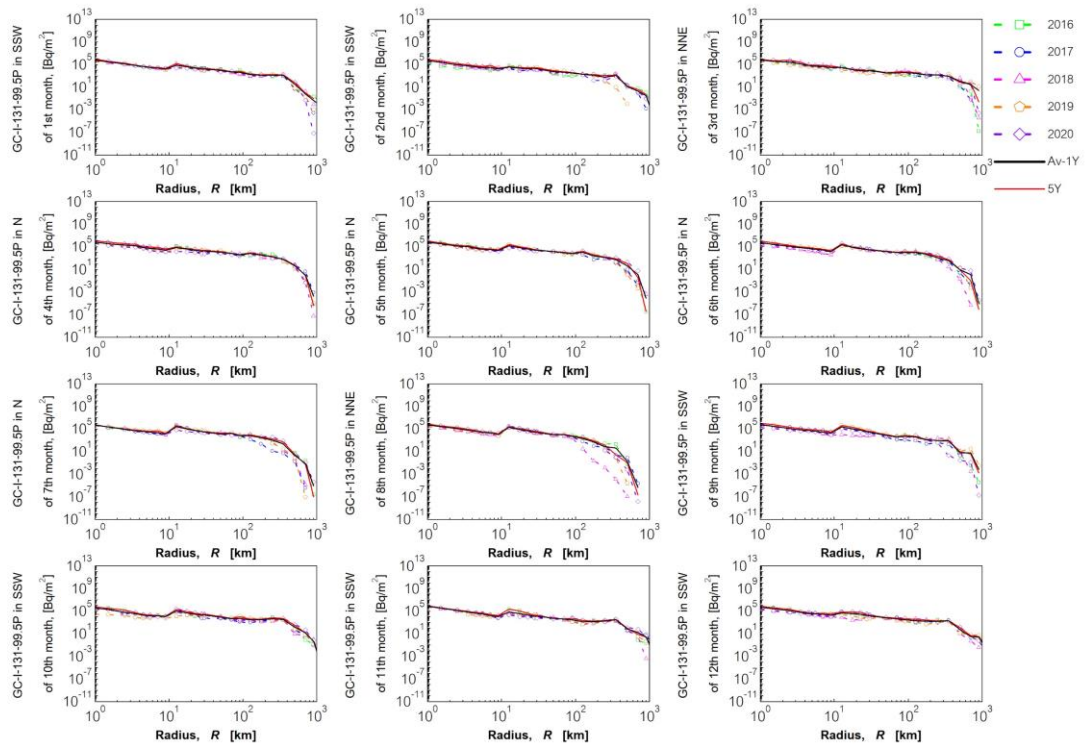


Figure A-39 Total ground concentration of I-131 for 24 hours at 99.5th percentile



Total effective dose equivalence (TEDE)

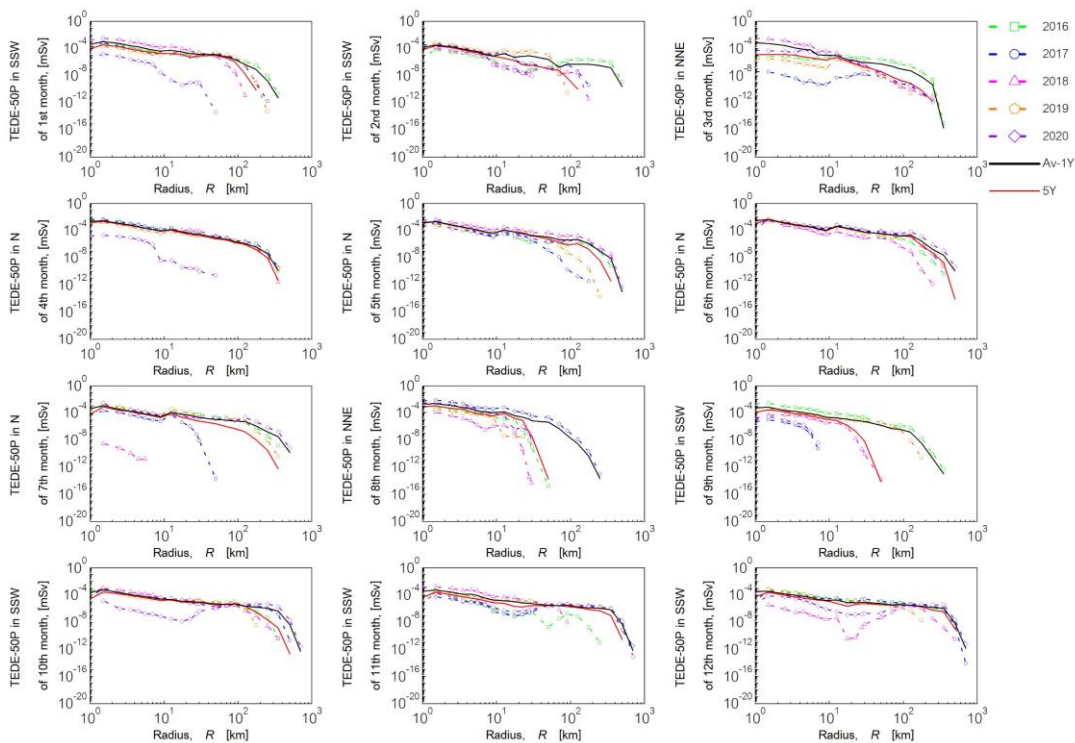


Figure A-40 TEDE for 24 hours at 50th percentile

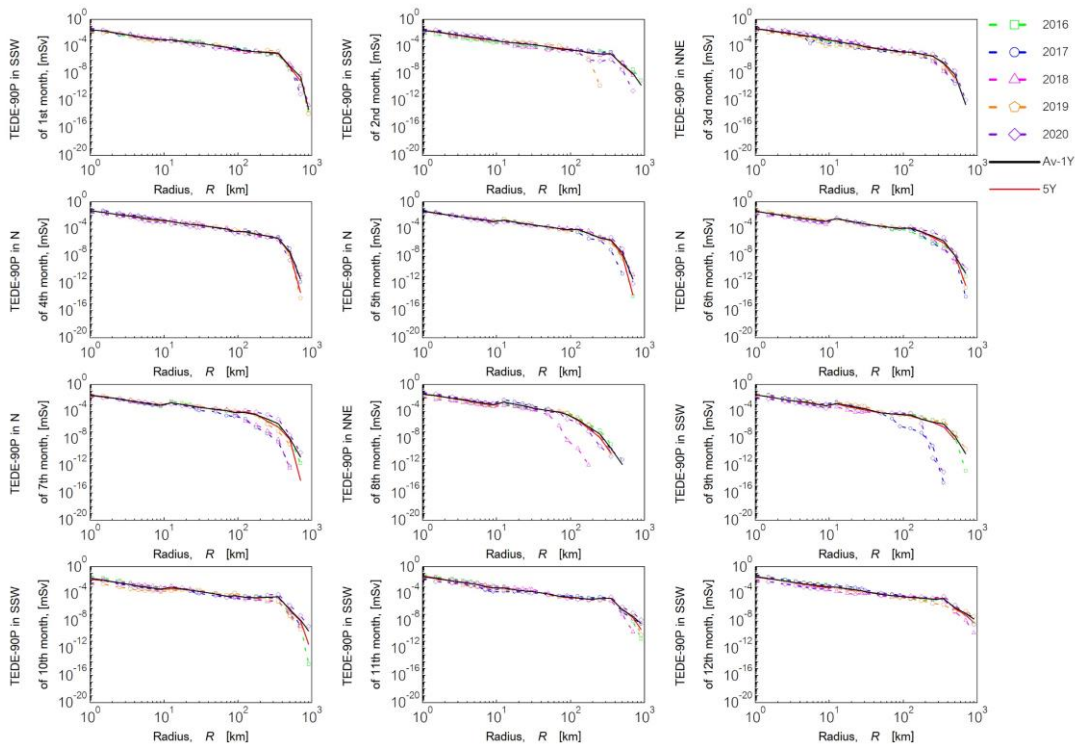


Figure A-41 TEDE for 24 hours at 90th percentile

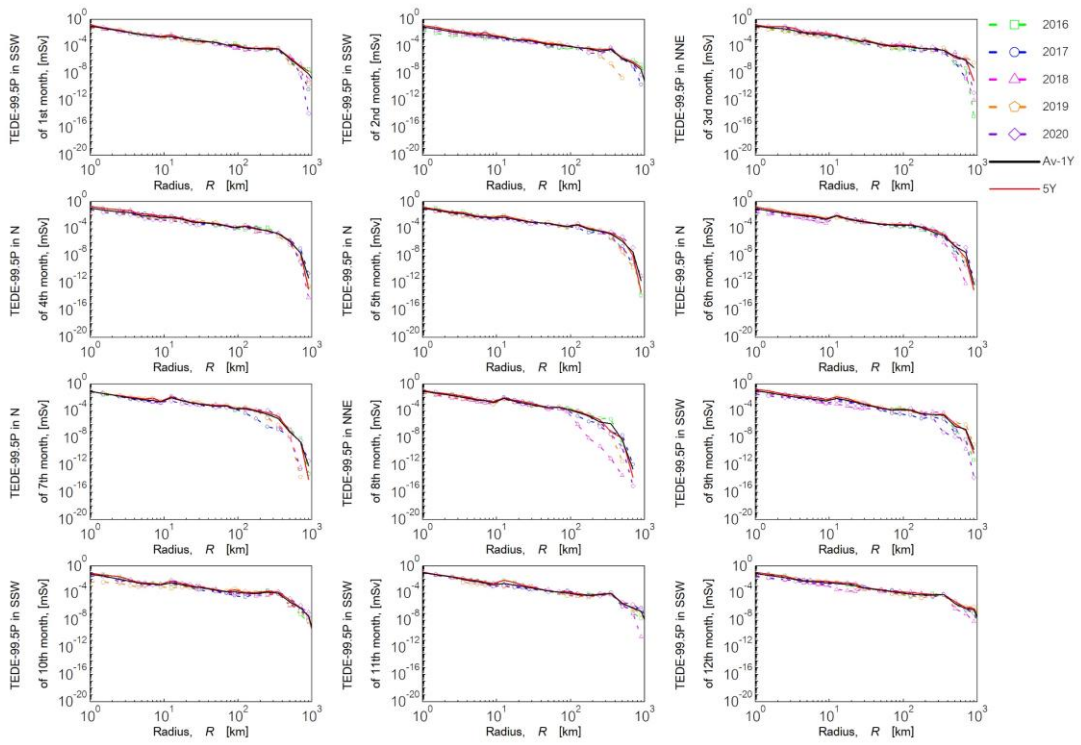


Figure A-42 TEDE for 24 hours at 99.5th percentile



A8. Statistical values of AMBE, RMBE, and CC to investigate the difference in predicted results between a single year and an average over five years.

AMBE 1 year VS Average

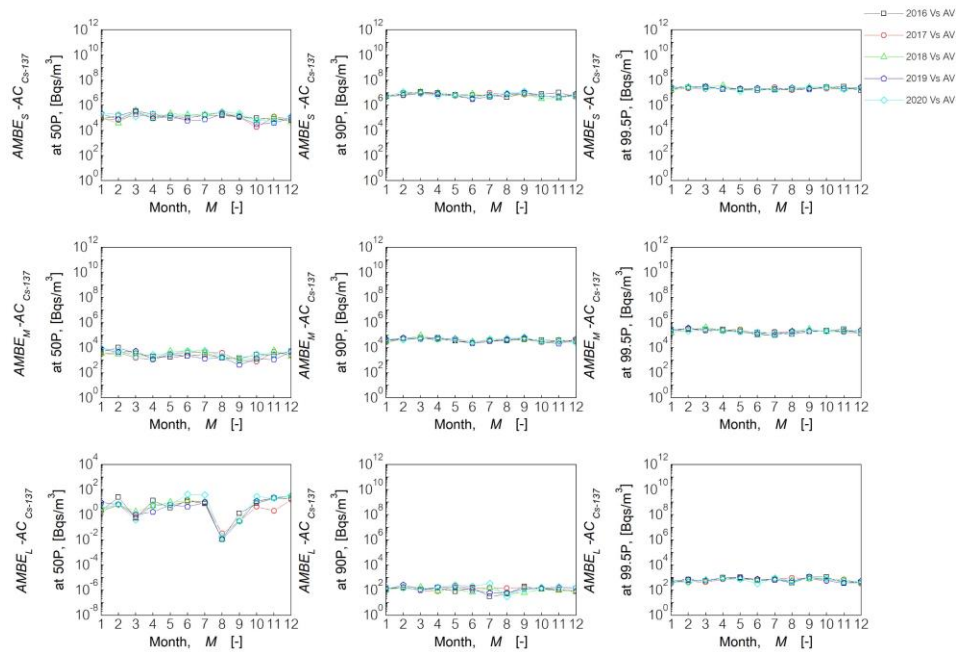


Figure A-43 AMBE value in each single year of air concentration of Cs-137 at 50th, 90th, and 99.5th percentile compared with average value over five years

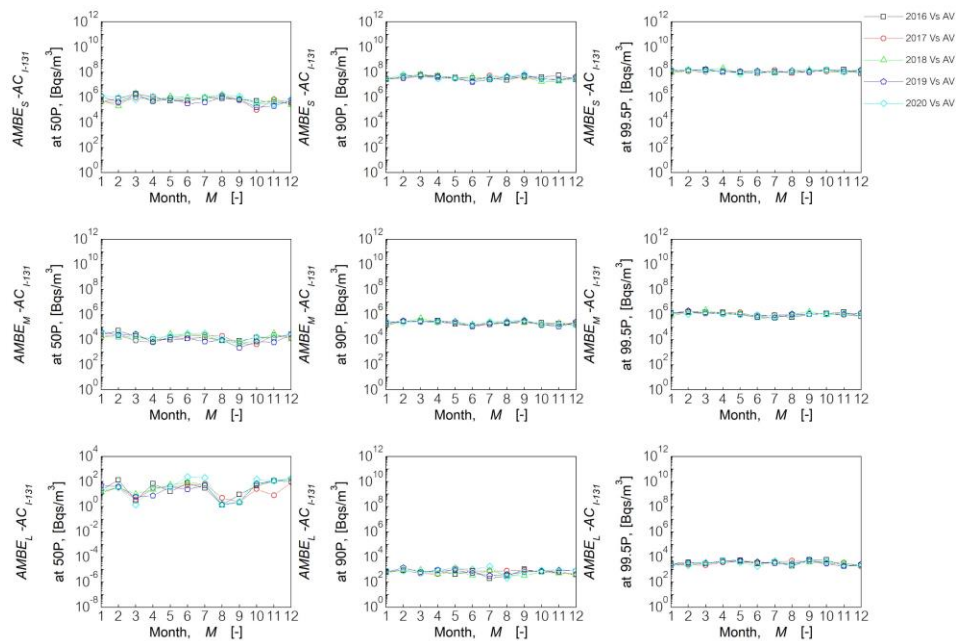


Figure A-44 AMBE value in each single year of air concentration of I-131 at 50th, 90th, and 99.5th percentile compared with average value over five years

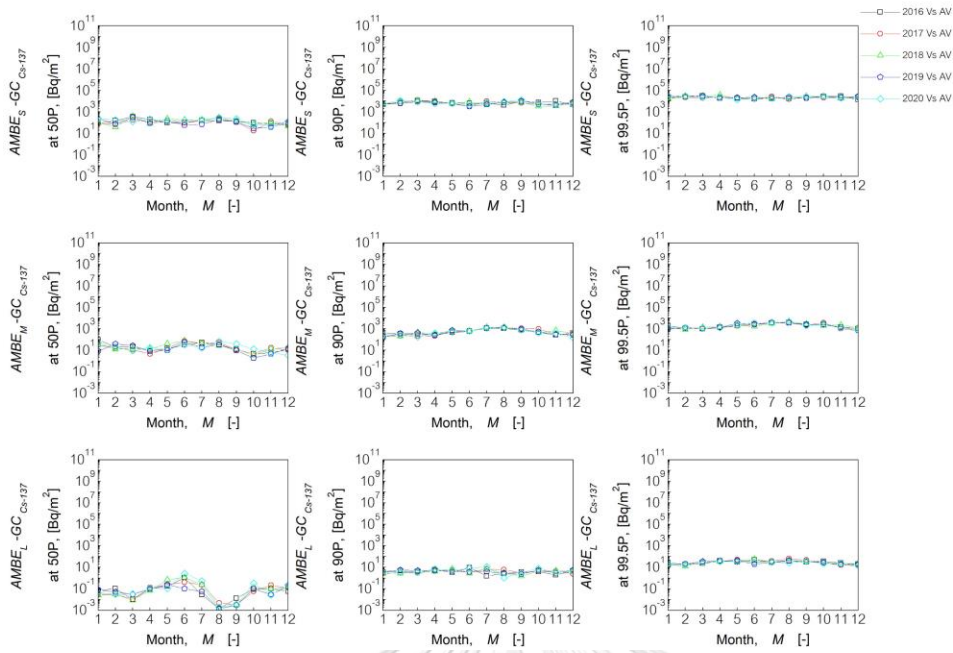


Figure A-45 AMBE value in each single year of ground concentration of Cs-137 at 50th, 90th, and 99.5th percentile compared with average value over five years

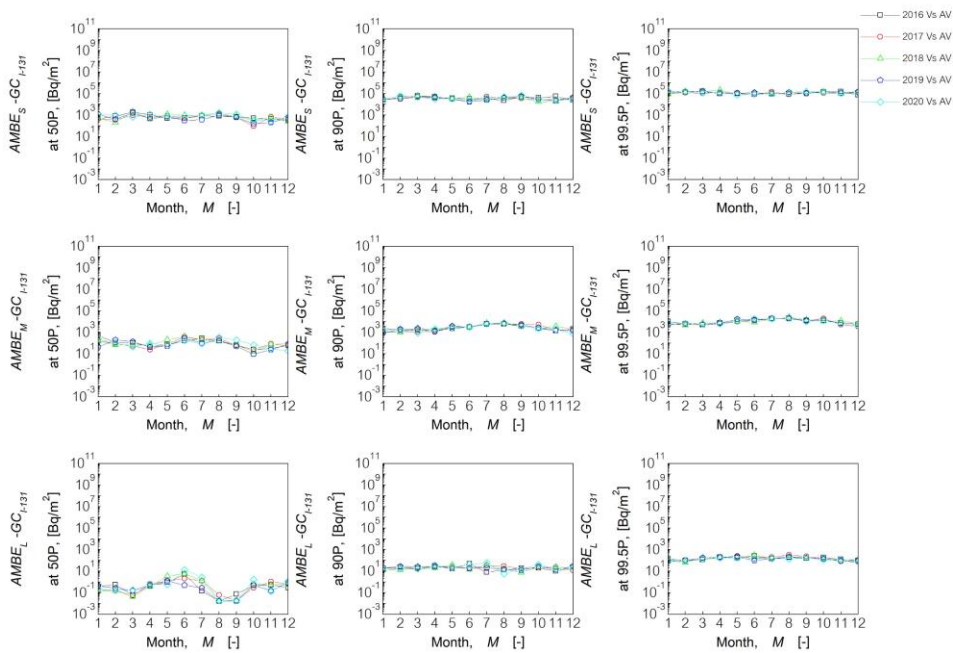


Figure A-46 AMBE value in each single year of ground concentration of I-131 at 50th, 90th, and 99.5th percentile compared with average value over five years

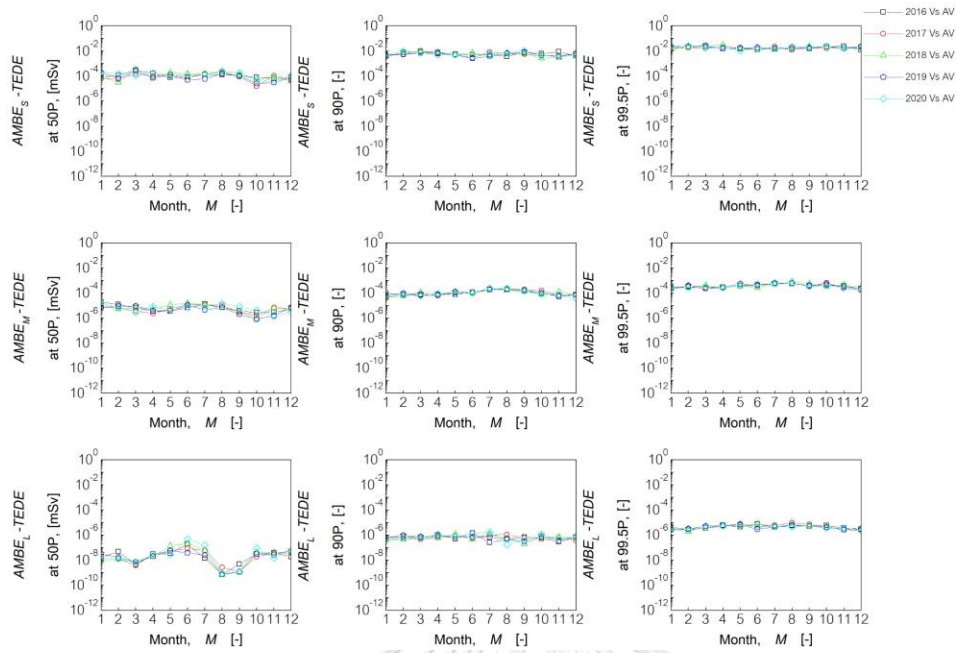


Figure A-47 AMBE value in each single year of TEDE at 50th, 90th, and 99.5th percentile compared with average value over five years

RMSE 1 year VS Average

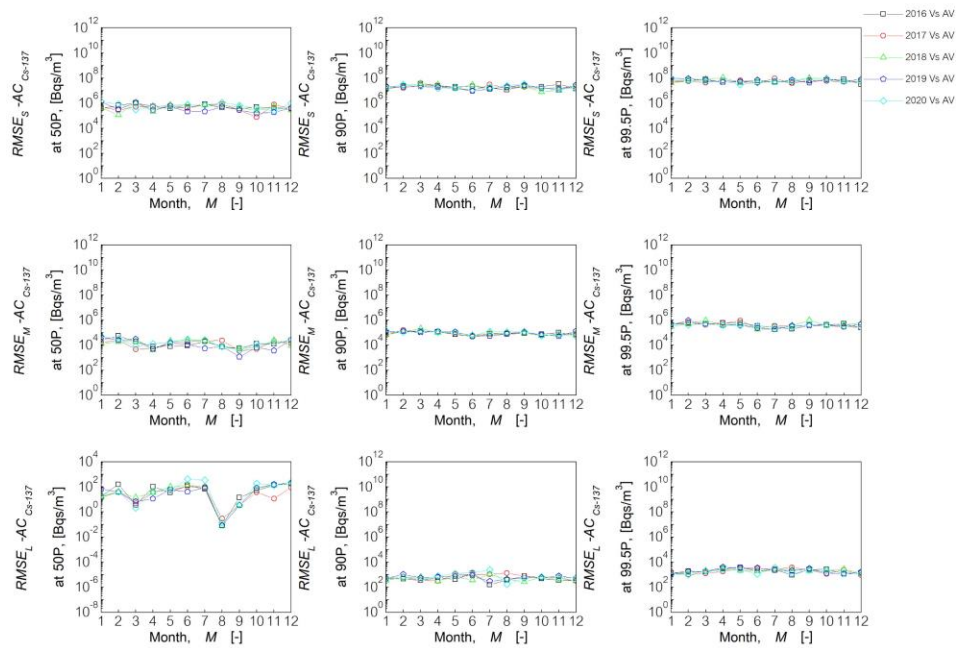


Figure A-48 RMSE value in each single year of air concentration of Cs-137 at 50th, 90th, and 99.5th percentile compared with average value over five years

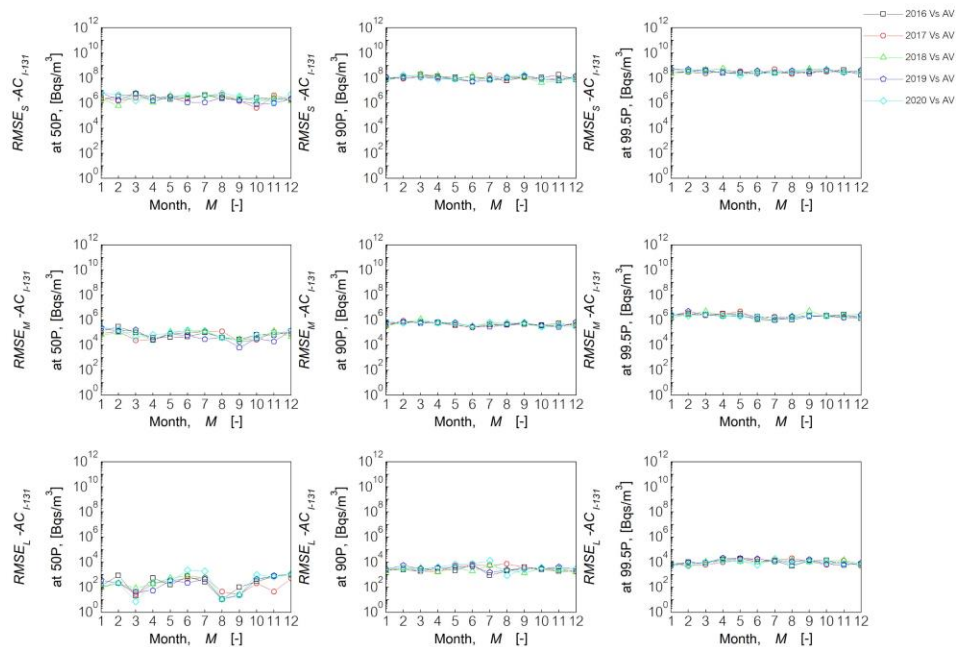


Figure A-49 RMSE value in each single year of air concentration of I-131 at 50th, 90th, and 99.5th percentile compared with average value over five years

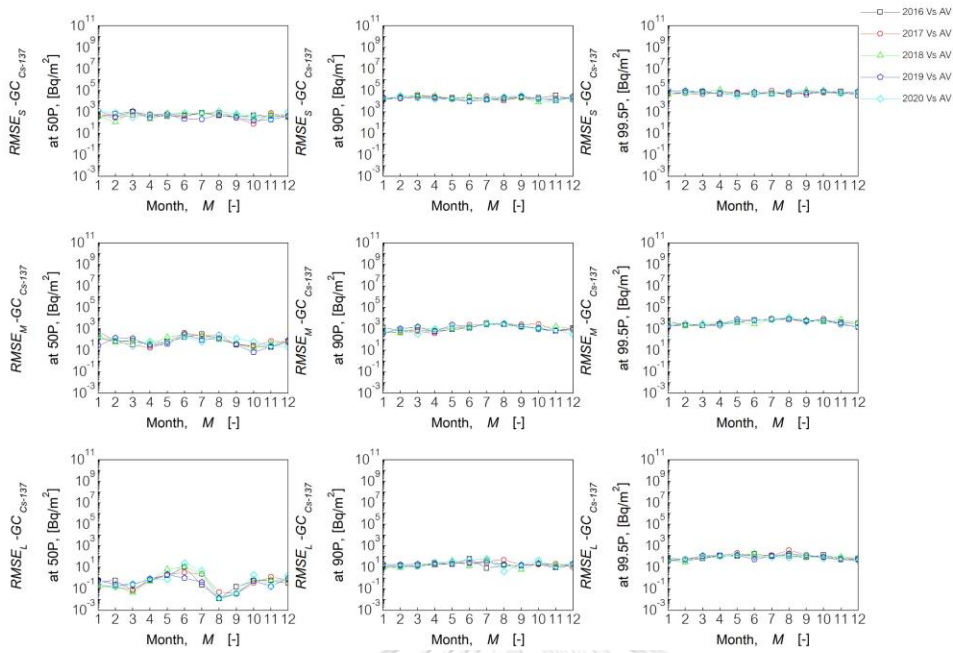


Figure A-50 RMSE value in each single year of ground concentration of Cs-137 at 50th, 90th, and 99.5th percentile compared with average value over five years

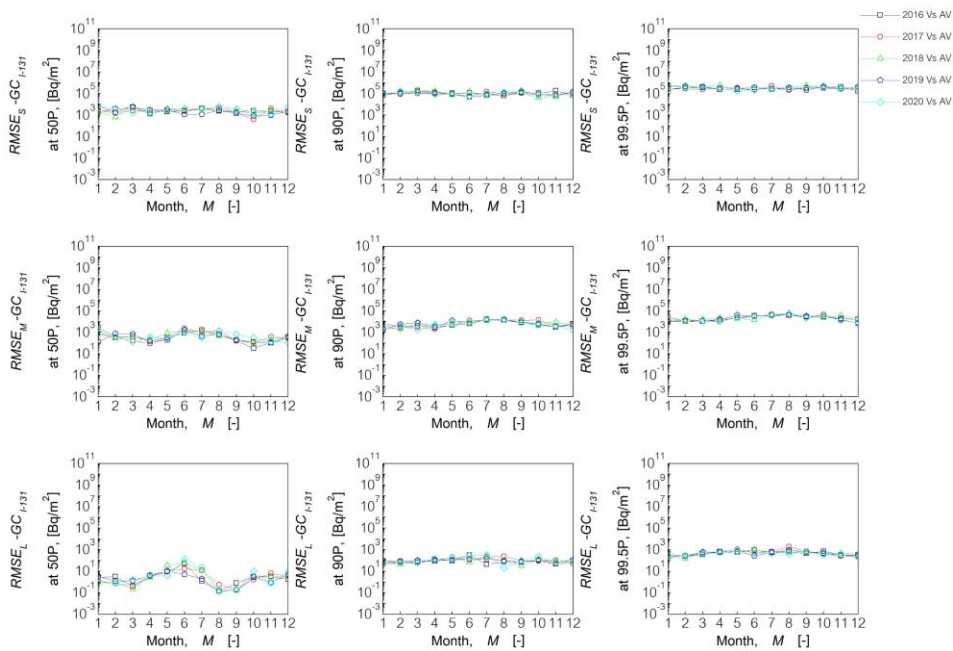


Figure A-51 RMSE value in each single year of ground concentration of I-131 at 50th, 90th, and 99.5th percentile compared with average value over five years

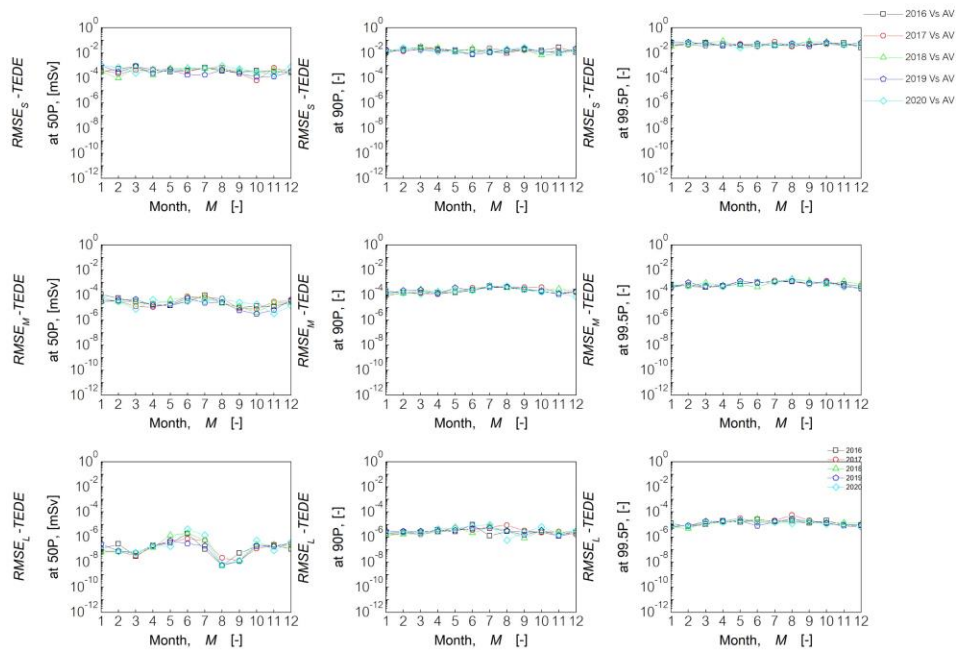


Figure A-52 RMSE value in each single year of TEDE at 50th, 90th, and 99.5th percentile compared with average of those values over five years

CC 1 year VS Average

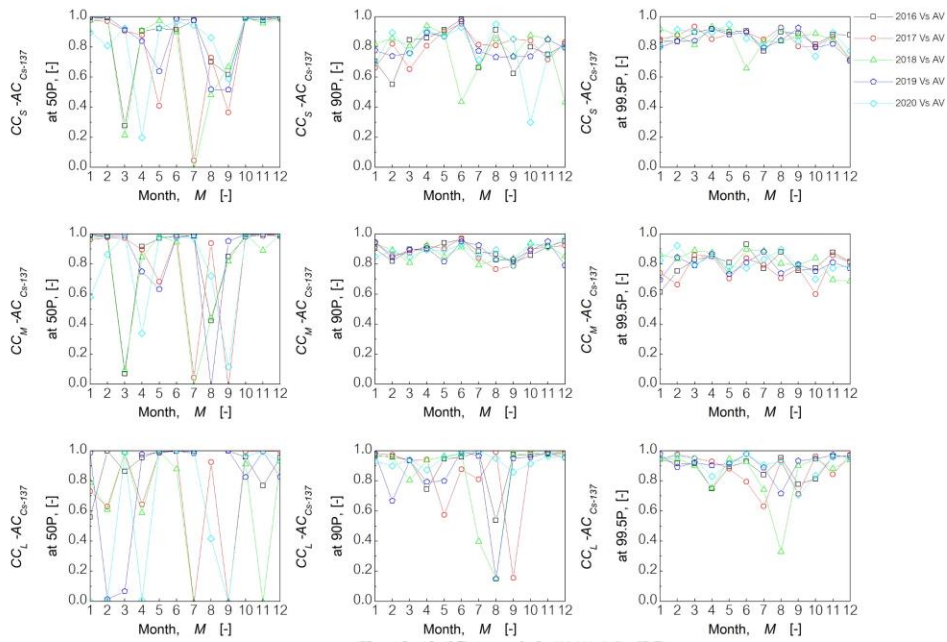


Figure A-53 CC value in each single year of air concentration of Cs-137 at 50th, 90th, and 99.5th percentile compared with average value over five years

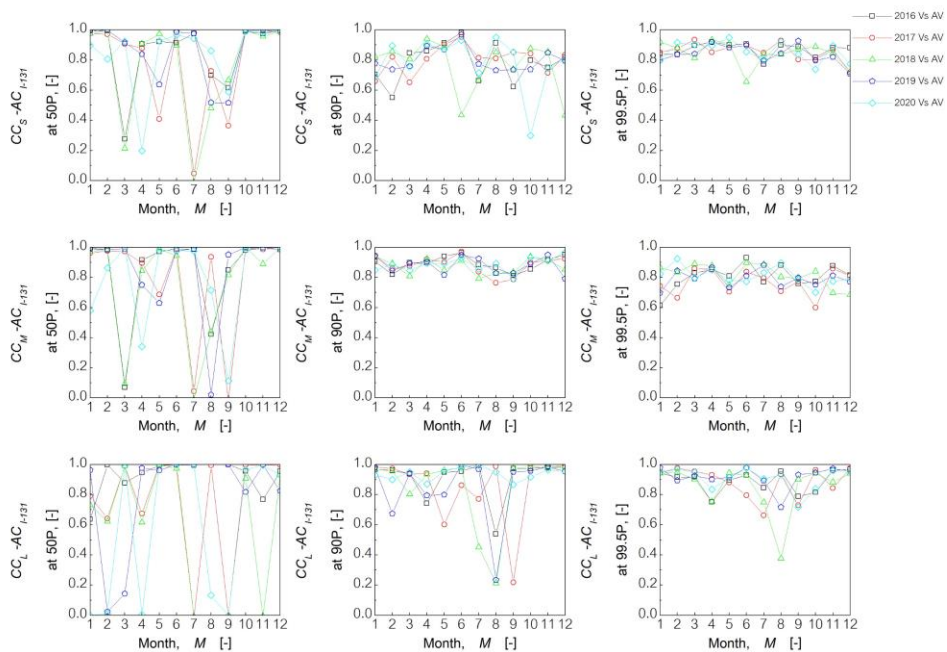


Figure A-54 CC value in each single year of air concentration of I-131 at 50th, 90th, and 99.5th percentile compared with average value over five years

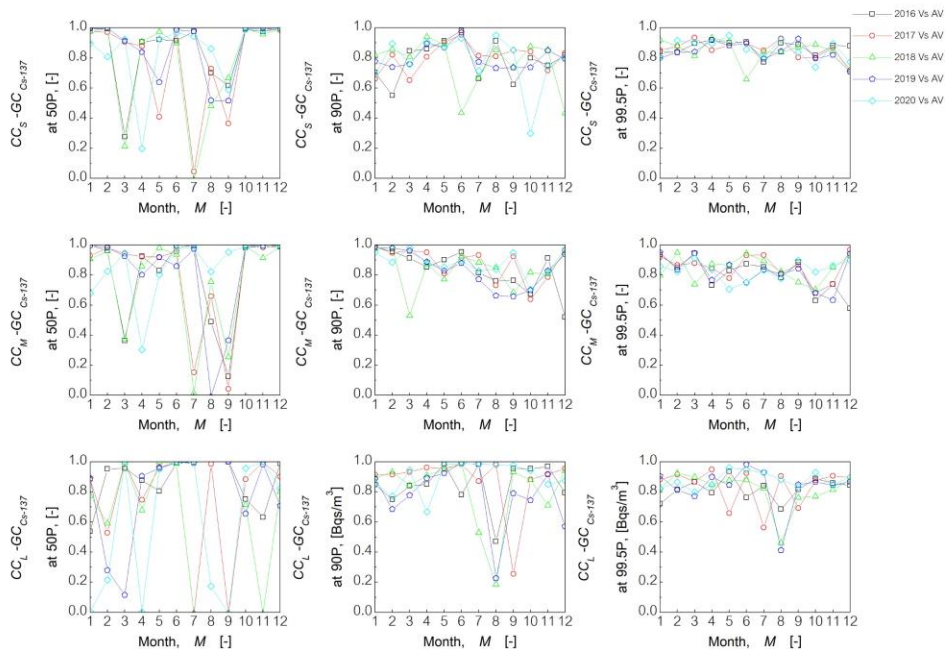


Figure A-55 CC value in each single year of ground concentration of Cs-137 at 50th, 90th, and 99.5th percentile compared with average value over five years

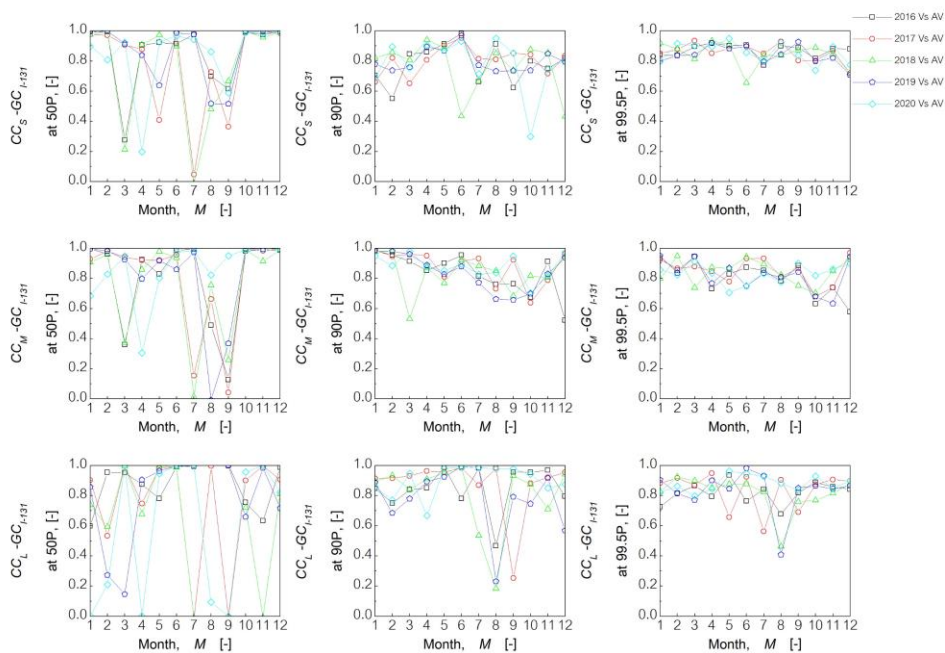


Figure A-56 CC value in each single year of ground concentration of I-131 at 50th, 90th, and 99.5th percentile compared with average value over five years.

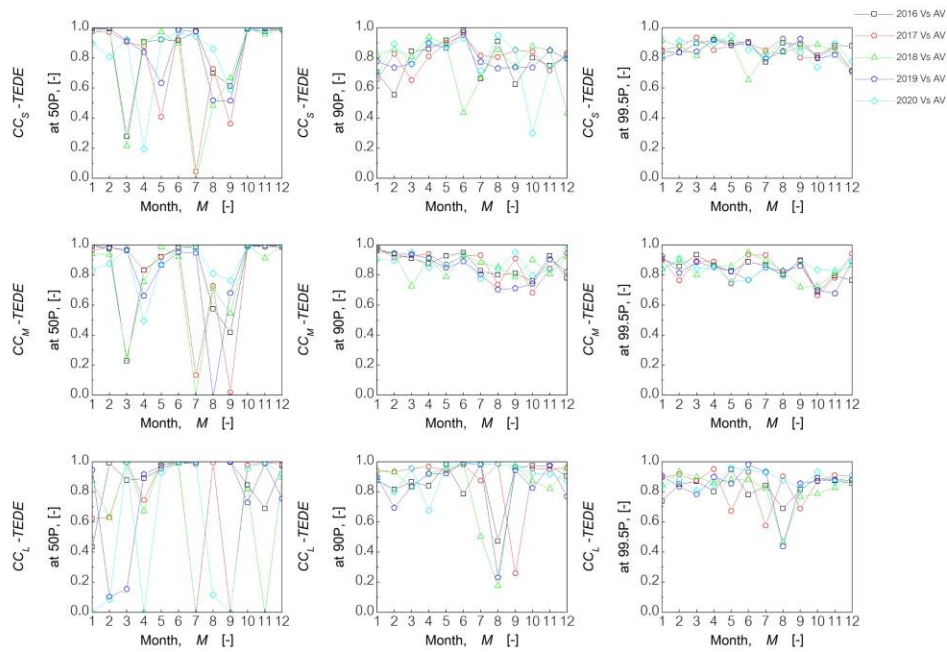


Figure A-57 CC value in each single year of TEDE at 50th, 90th, and 99.5th percentile compared with average value over five years

A9. Statistical values of AMBE, RMBE, and CC to investigate the difference in predicted results between a single year and five years.

AMBE 1 year VS 5 years

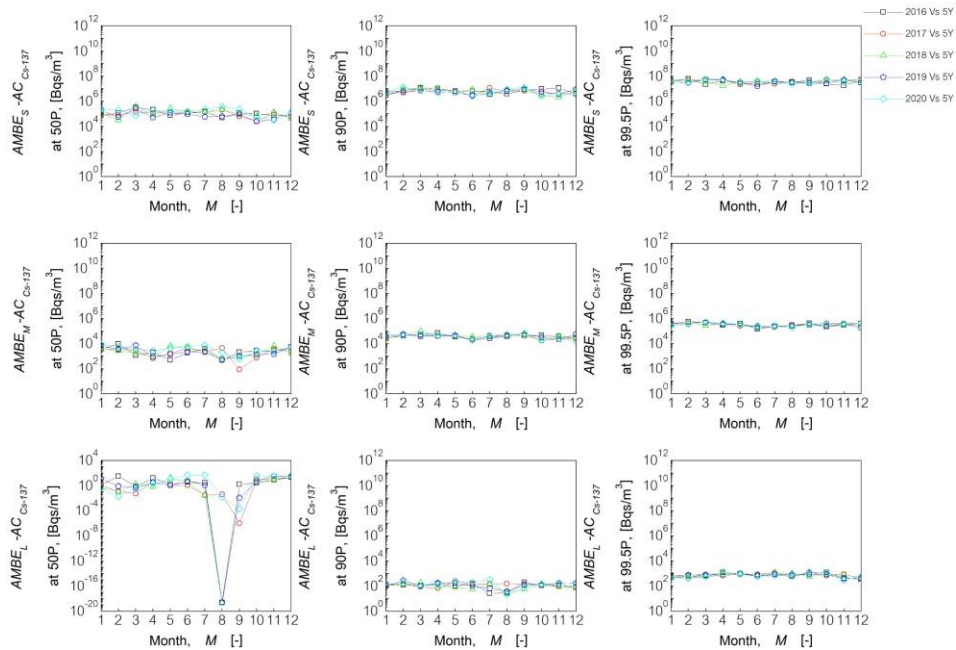


Figure A-58 AMBE value in each single year of air concentration of Cs-137 at 50th, 90th, and 99.5th percentile compared with five years

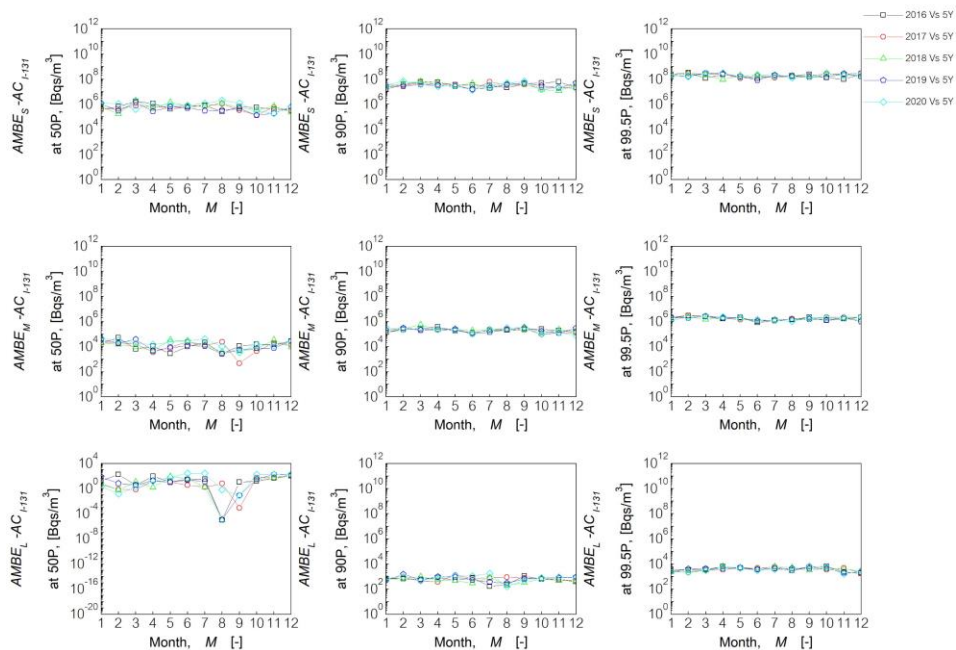


Figure A-59 AMBE value in each single year of air concentration of I-131 at 50th, 90th, and 99.5th percentile compared with five years

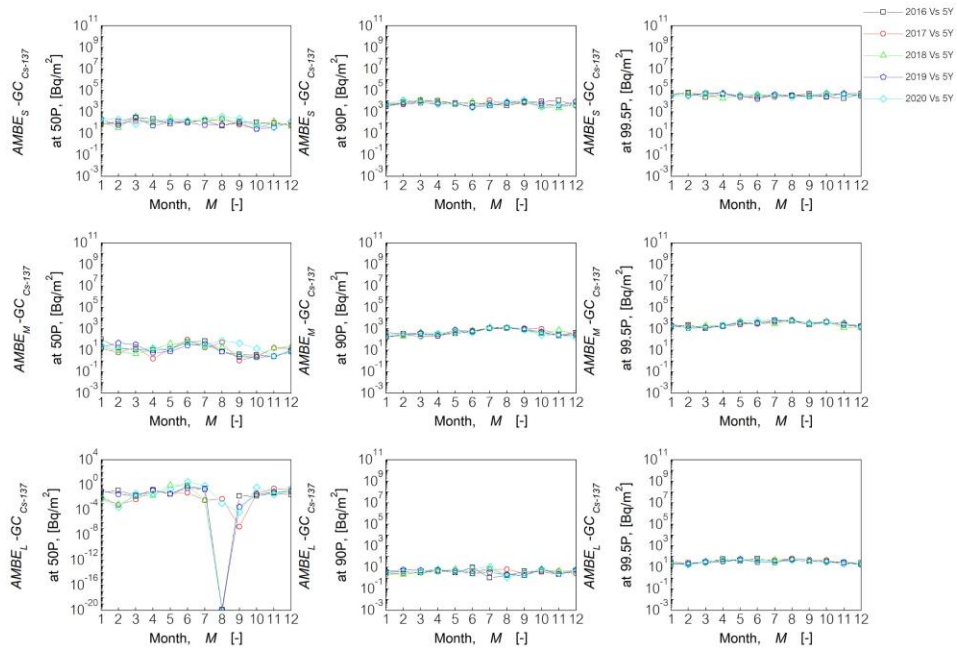


Figure A-60 AMBE value in each single year of ground concentration of Cs-137 at 50th, 90th, and 99.5th percentile compared with five years

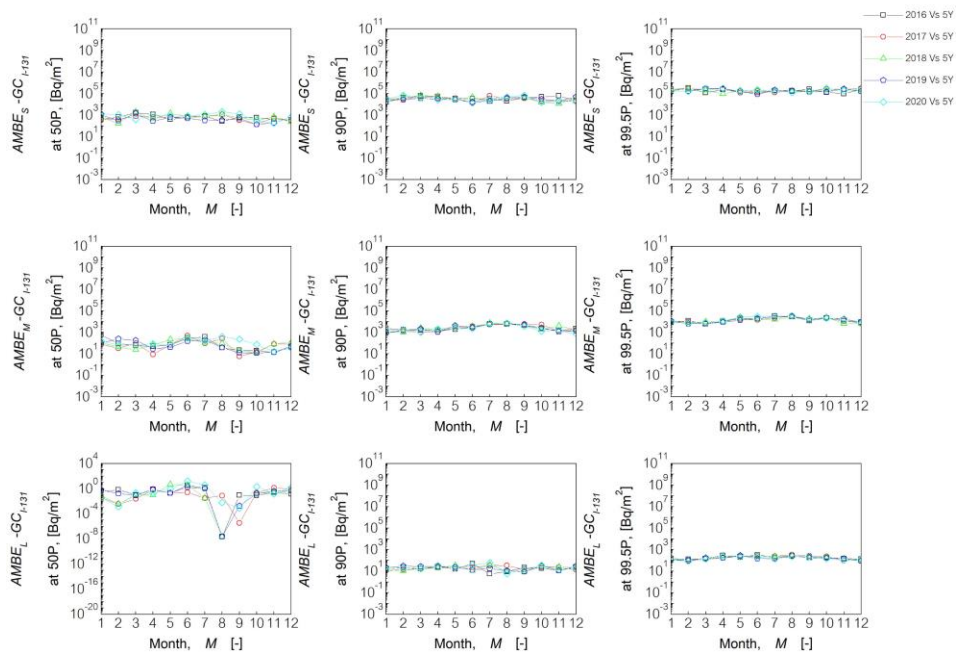


Figure A-61 AMBE value in each single year of ground concentration of I-131 at 50th, 90th, and 99.5th percentile compared with five years

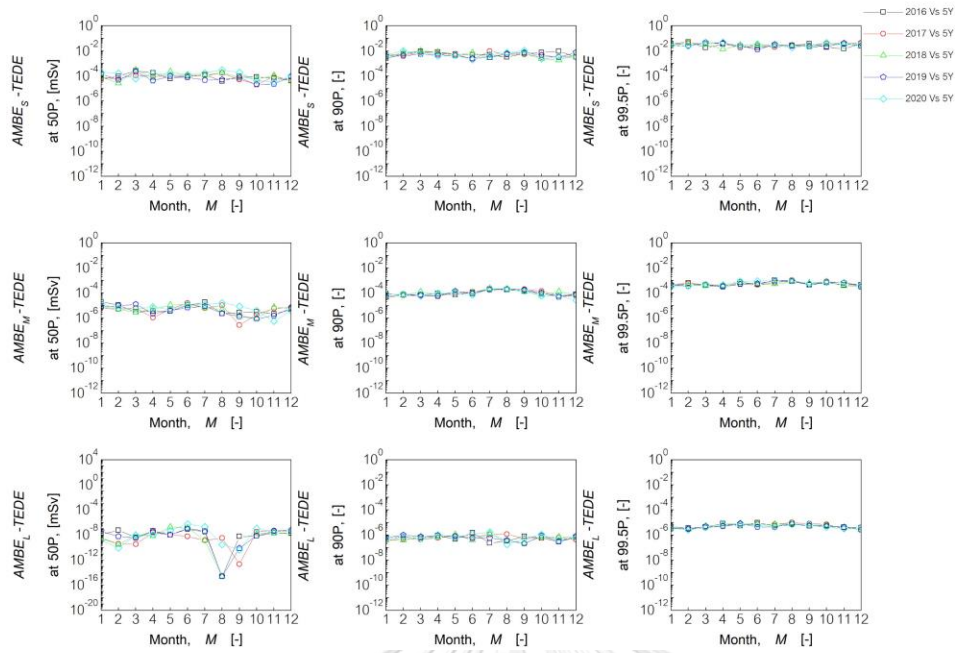


Figure A-62 AMBE value in each single year of TEDE at 50th, 90th, and 99.5th percentile compared with five years



RMSE 1 year VS 5 years

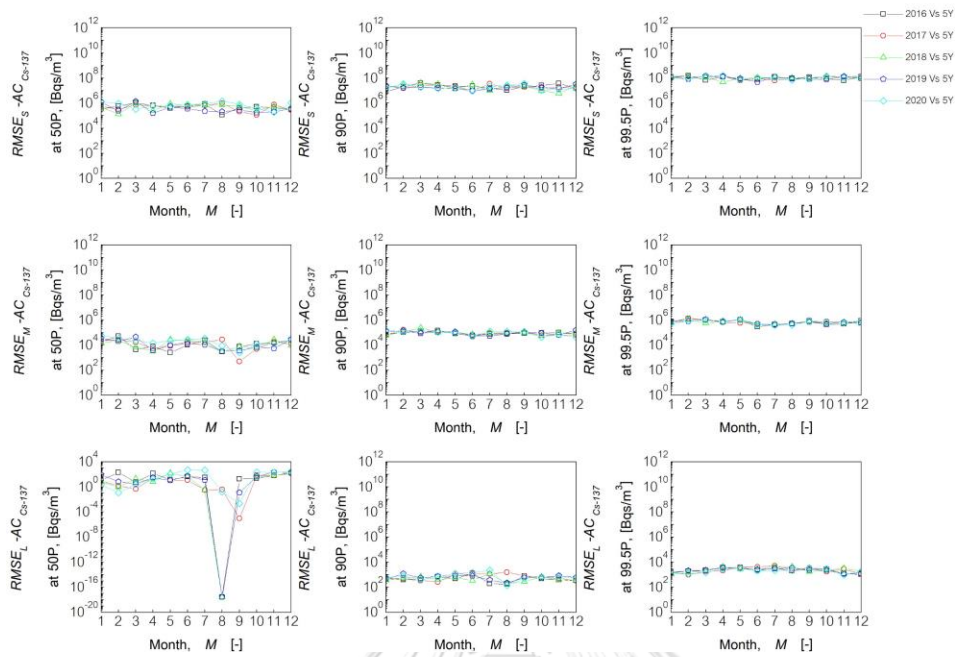


Figure A-63 RMSE value in each single year of air concentration of Cs-137 at 50th, 90th, and 99.5th percentile compared with five years

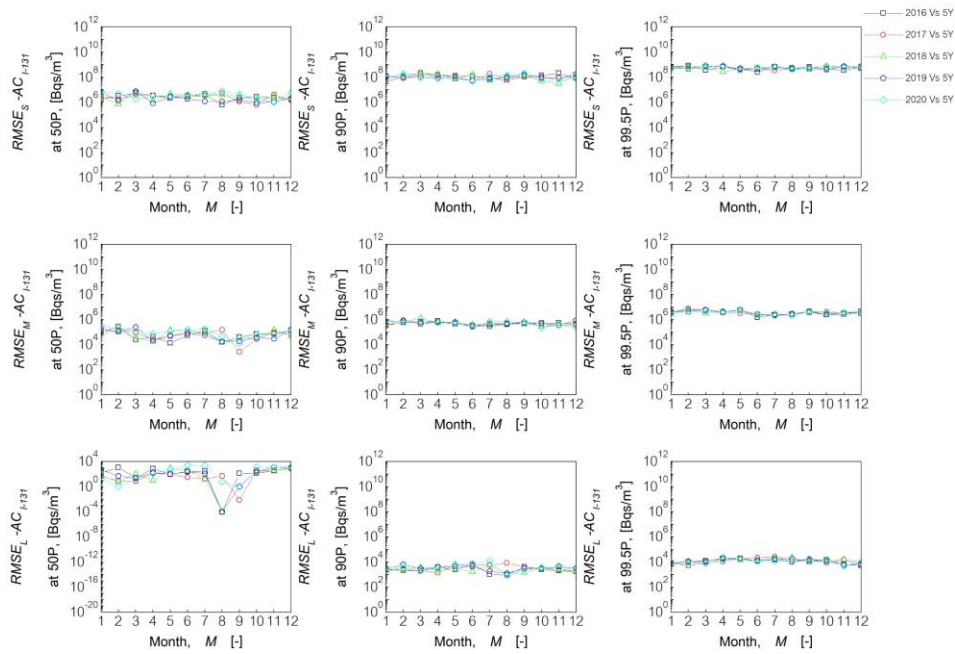


Figure A-64 RMSE value in each single year of air concentration of I-131 at 50th, 90th, and 99.5th percentile compared with five years

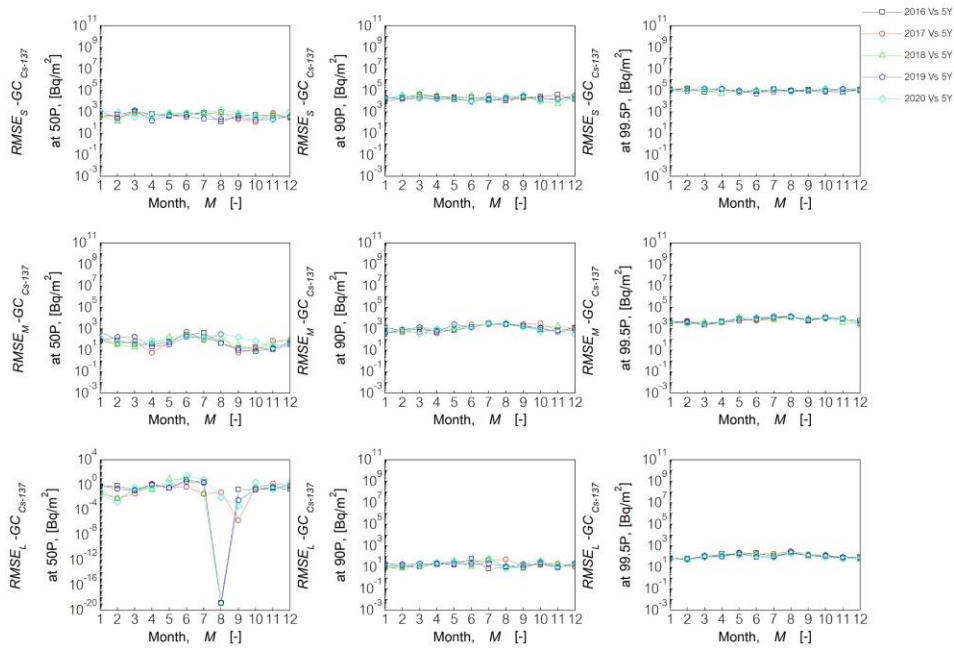


Figure A-65 RMSE value in each single year of ground concentration of Cs-137 at 50th, 90th, and 99.5th percentile compared with five years

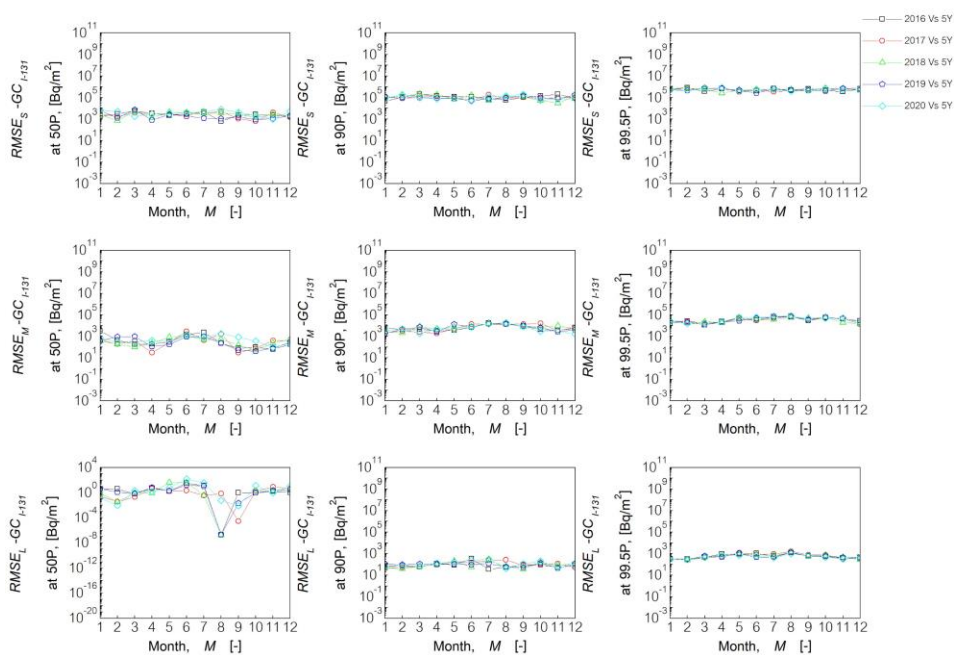


Figure A-66 RMSE value in each single year of ground concentration of I-131 at 50th, 90th, and 99.5th percentile compared with five years

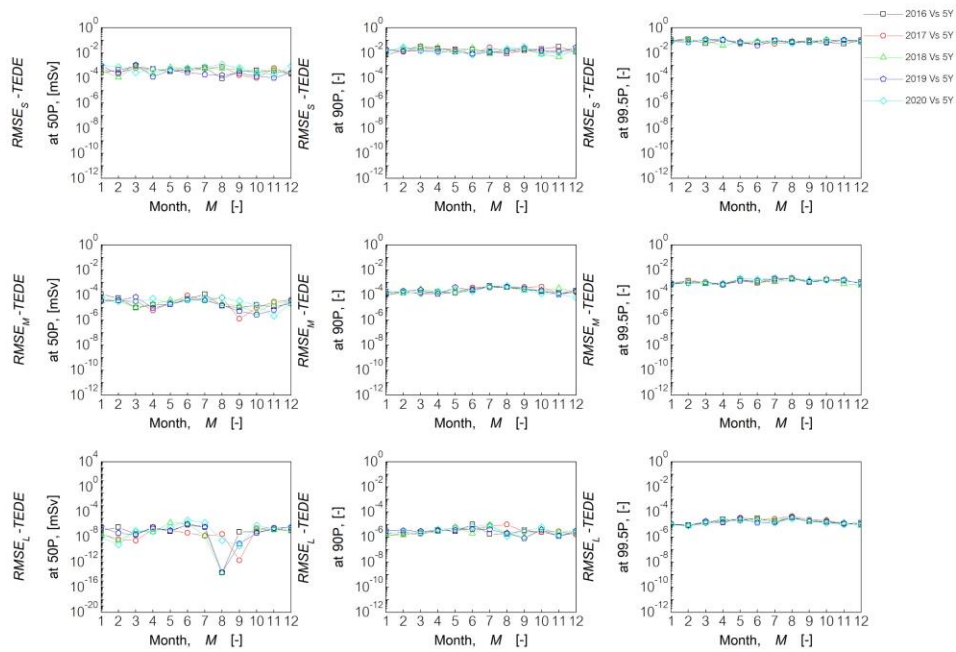


Figure A-67 RMSE value in each single year of TEDE at 50th, 90th, and 99.5th percentile compared with five years

CC 1 year VS 5 years

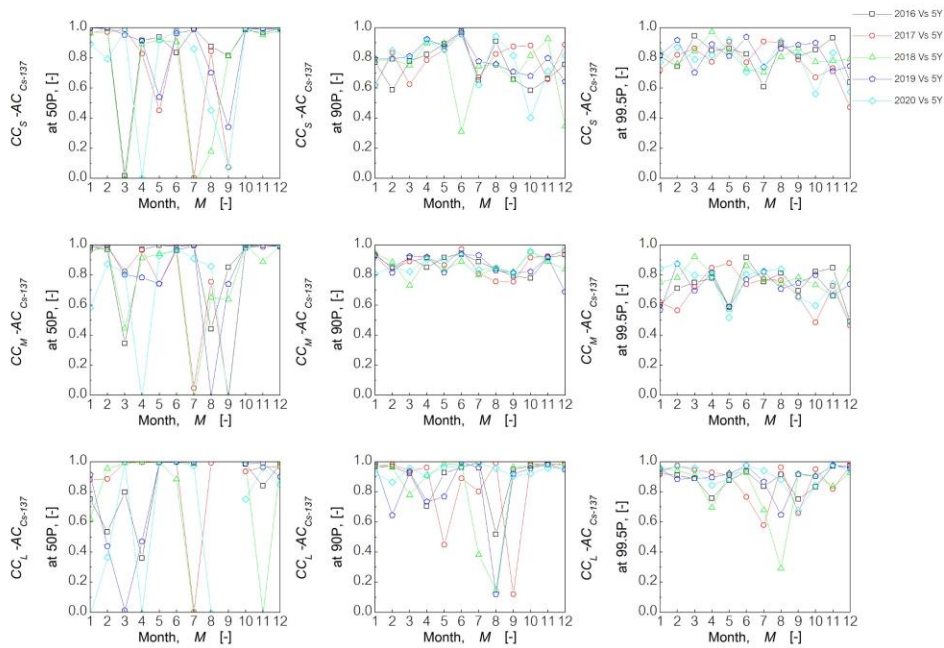


Figure A-68 CC value in each single year of air concentration of Cs-137 at 50th, 90th, and 99.5th percentile compared with five years

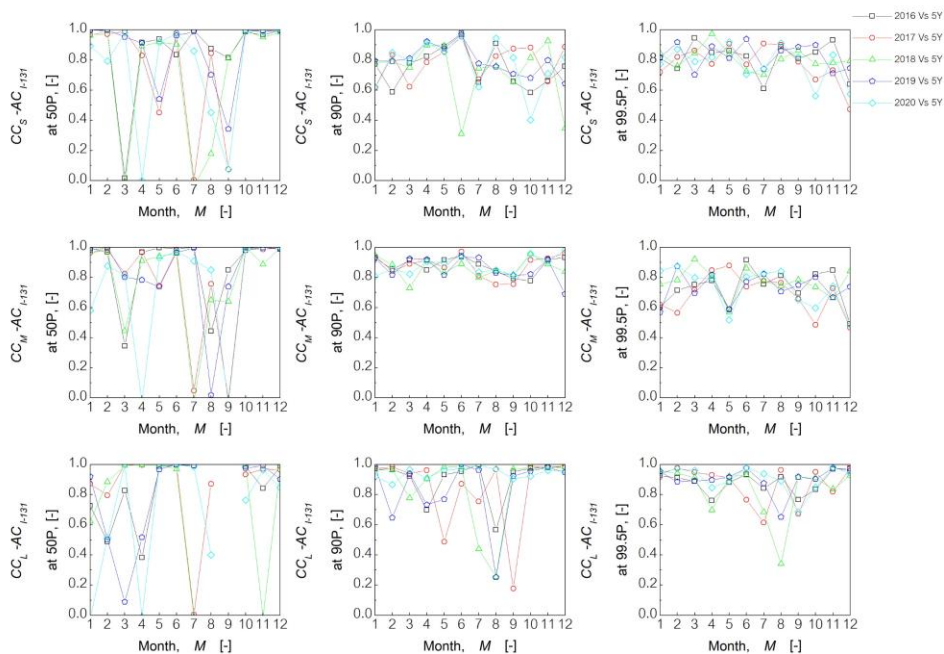


Figure A-69 CC value in each single year of air concentration of I-131 at 50th, 90th, and 99.5th percentile compared with five years

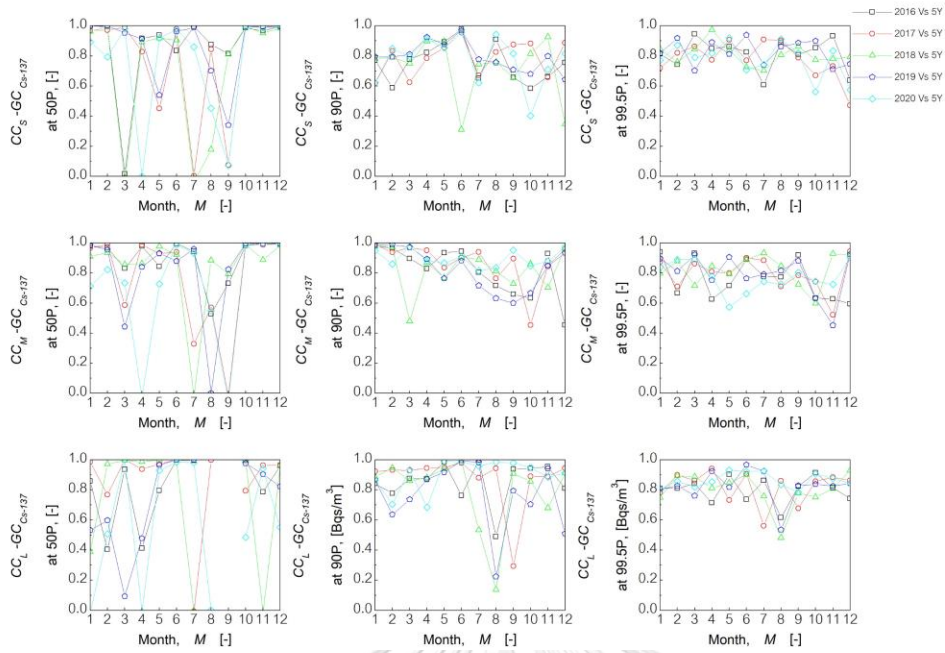


Figure A-70 CC value in each single year of ground concentration of Cs-137 at 50th, 90th, and 99.5th percentile compared with five years

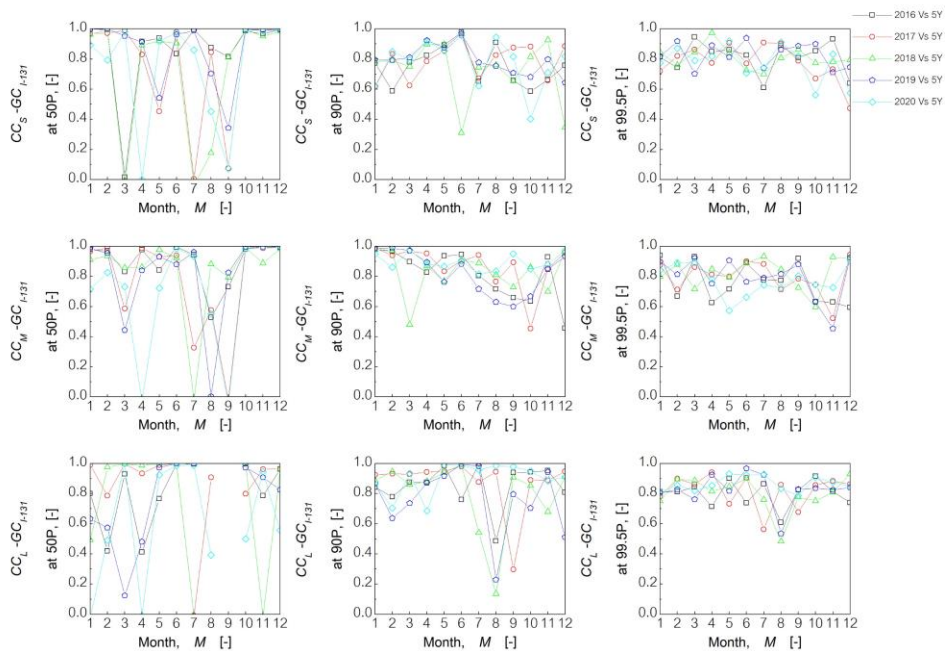


Figure A-71 CC value in each single year of ground concentration of I-131 at 50th, 90th, and 99.5th percentile compared with five years

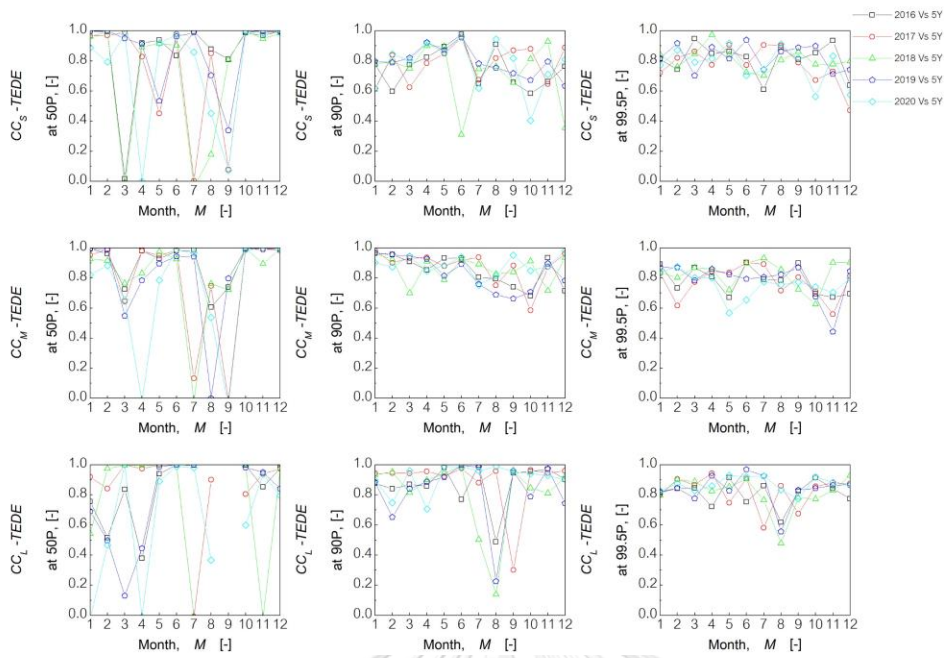
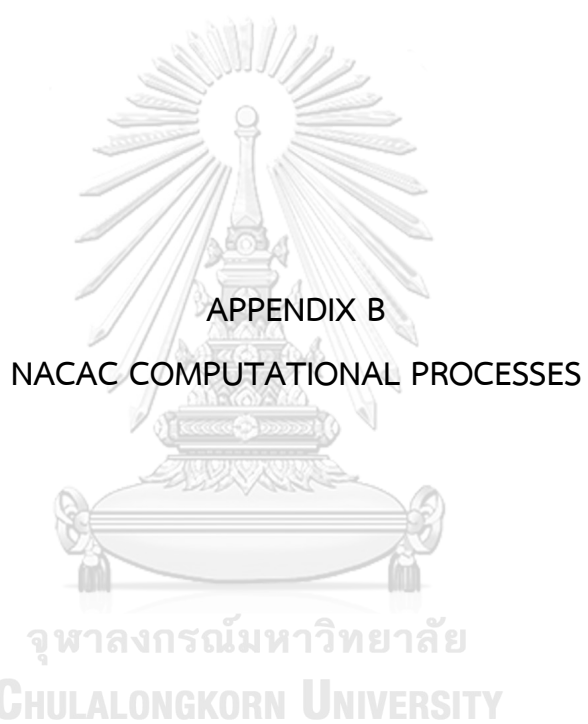


Figure A-72 CC value in each single year of TEDE at 50th, 90th, and 99.5th percentile compared with five years





APPENDIX B

NACAC COMPUTATIONAL PROCESSES

จุฬาลงกรณ์มหาวิทยาลัย

CHULALONGKORN UNIVERSITY

B1. Preparing meteorological data

- The wind components in Y and X directions, rain intensity (total precipitation), total cloud cover, geopotential height, and solar elevation are downloaded from the NCEP with a resolution of $55.5 \times 55.5 \text{ km}^2$, as shown in Figure B-1.

NCEP Climate Forecast System Version 2 (CFSv2) 6-hourly Products
ds094.0 | DOI: 10.5065/D61C1TFX

DESCRIPTION DATA ACCESS CITATION DOCUMENTATION SOFTWARE METRICS

Get a Subset

Refine Your Selections:

INPUT DATA FORMAT: WMO_Grib2

OUTPUT FORMAT: Same as input Converted to netCDF Converted to CSV

VALID DATE RANGE: 2020-01-01 00:00 TO 2020-01-01 06:00

MORE DATE/TIME OPTIONS

PARAMETER(S): All available
u-component of wind

VERTICAL LEVEL(S): All available
Specified height above ground: 10 m

GRIDDED PRODUCT: All available
1-hour Forecast
2-hour Forecast
3-hour Forecast

GRID: 0.5° x 0.5° from 0E to 359.5E and 90N to 90S (720 x 360 Longitude/Latitude)

SPATIAL SELECTION: Data within a bounding box

Map Satellite

INTERACTIVE MAP INSTRUCTIONS:

- Use the 'PAN MAP' option to drag and center the map on your area of interest.
- Use the 'DRAW BOX' option to drag a box around your area of interest. You can also manually enter bounding latitudes and longitudes in the text boxes below.

NORTH: 32
WEST: 95 EAST: 122
SOUTH: 6
RESET

† latitudes must be specified in whole degrees

Figure B-1 Download wind component in x direction at 10 m.

(<https://rda.ucar.edu/datasets/ds094.0/dataaccess/>)

- The file download with a grib2 form is extracted to a CSV file by the wgrib2 program with the command of `./wgrib2 name file.tar -undefine out-box 95:122 6:32 -csv name file.csv`, as shown in Figure B-2.

```
Windows 10@DESKTOP-PEPNM6 /home/grib2/wgrib2
$ ./wgrib2 w10m.grb2 -undefine out-box 95:122.5 6:32 -csv w10m.csv
1:0:d=2020010100:UGRD:10 m above ground:1 hour fcst:
2:3394:d=2020010100:UGRD:10 m above ground:2 hour fcst:
3:6790:d=2020010100:UGRD:10 m above ground:3 hour fcst:
4:10188:d=2020010100:UGRD:10 m above ground:4 hour fcst:
5:13608:d=2020010100:UGRD:10 m above ground:5 hour fcst:
6:17057:d=2020010100:UGRD:10 m above ground:6 hour fcst:
```

Figure B-2 Convert grib2 file to CSV file

(<https://www.cpc.ncep.noaa.gov/products/wesley/wgrib2/>)

- Wind components at 10 m, total cloud cover, and solar radiation are used to evaluate atmospheric stability class by the Pasquill Gifford method as Table B-1 and Table B-2

Table B-1 Condition for evaluation of solar quantity.

| Sky Cover (Opaque or Total) | Solar Elevation Angle > 60° | Solar Elevation | Solar Elevation |
|---|--------------------------------|---------------------------|---------------------------|
| | | Angle < 60° but, > 35° | Angle < 35° but, > 15° |
| 4/8 or less or, Any amount of High Thin Clouds | Strong | Moderate | Slight |
| 5/8 to 7/8 Middle Clouds | Moderate | Slight | Slight |
| 5/8 to 7/8 Low Clouds | Slight | Slight | Slight |

Table B-2 Condition for atmospheric stability classification

| Surface Wind Measured at 10 m (m / sec) | Day | | | Night | |
|--|--------------------------|----------|--------|---------------------|---------------------|
| | Incoming Solar Radiation | | | > 4/8 cloudiness | ≤ 4/8 cloudiness |
| | Strong | Moderate | Slight | | |
| < 2 | A | A-B | B | F | F |
| 2 - 3 | A-B | B | C | E | F |
| 3 - 5 | B | B-C | C | D | E |
| 5 - 6 | C | C-D | D | D | D |
| 6 | C | D | D | D | D |

- Wind components in X and Y directions at 10 m and atmospheric stability class data are formatted in form 2I5,I1 in meso file according to the read format of NACAC, as shown in Figure B-3.

B2.1 Input data

- NACAC uses four input files: condition, meso, synop, and rain. As mentioned above, meso, synop, and rain are meteorological data files. A condition file includes five parts used for simulation.
- The isotope part define release source term data and conditions for concentration calculation, as shown in Figure B-7.

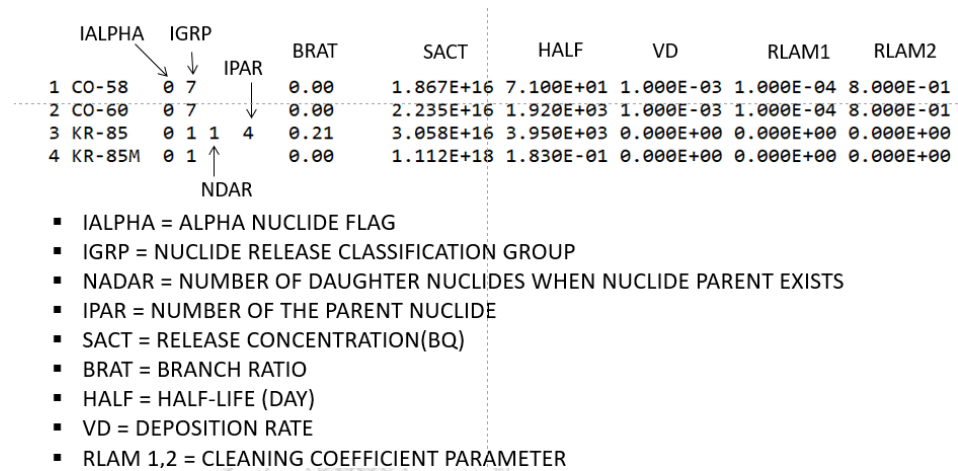


Figure B-7 Isotope part

- The leakage part mainly defines the release period and release high, as shown in Figure B-8.

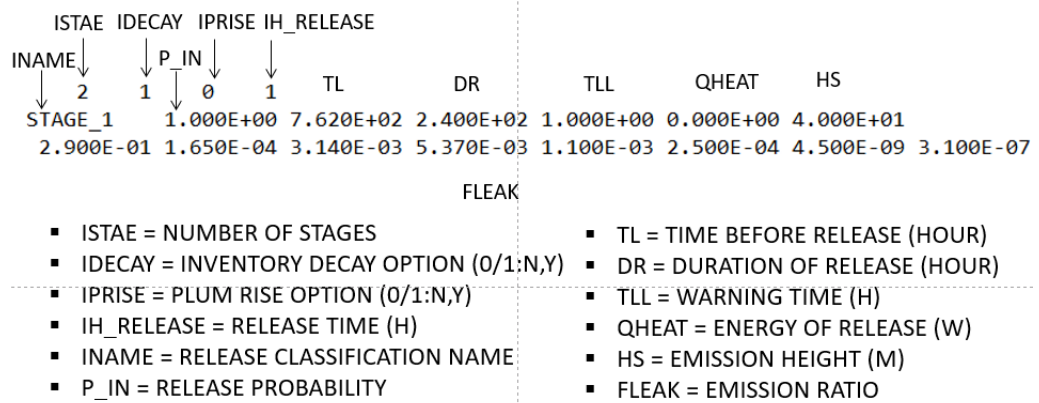


Figure B-8 Leakage part

- The advection part indicates the release location, as shown in Figure B-9.

| ICOLS | JROWS | SLAT | SLON | DELX | IPFCUT | RLIMIT |
|-------|-------|-----------|------------|---------|--------|--------|
| 17 | 20 | 36.453189 | 140.604094 | 152.400 | 0 | 200.0 |

- ICOLS = NUMBER OF WIND GRID COLMUNS
- JROWS = NUMBER OF WIND GRID ROWS
- SLAT = LATITUDE OF REFERENCE POINT (DEGREE)
- SLON = LONGITUDE OF REFERENCE POINT (DEGREE)
- DELX = ADVECTION GRID SIZE (METER)
- RLIMIT = MAXIMUM DISTANCE OF TRAJECTRYING PUFFS(m)

Figure B-9 Advection part

- The receptor part defines receptor locations, as shown in Figure B-10.

| NDIR | NDIST | IPRFG | ICALD | MAXTIM | | | | | |
|-----------|-----------|-----------|-----------|-----------|-----------|-----------|-----------|--|--|
| 32 | 25 | 0 | 0 | 24 | | | | | |
| 5.000E-01 | 1.500E+00 | 2.500E+00 | 3.500E+00 | 4.500E+00 | 5.500E+00 | 7.000E+00 | 9.000E+00 | | |
| 1.250E+01 | 1.750E+01 | 2.250E+01 | 2.750E+01 | 3.000E+01 | 5.000E+01 | 7.000E+01 | 9.000E+01 | | |
| 1.250E+02 | 1.750E+02 | 2.500E+02 | 3.500E+02 | 5.000E+02 | 7.000E+02 | 9.000E+02 | 1.250E+03 | | |
| 1.750E+03 | | | | | | | | | |
| 3.000E+01 | | | | | | | | | |
| RCOUNT | | | | | | | | | |

R {

NDIST = NUMBER OF DISTANCE
 NDIR = NUMBER OF DIRECTION
 IPRFG = OUTPUT CONTROL OF EVALUATION POINT INFORMATION(0/1=NO/OUT)
 ICALD = CLOUDSHINE CALCULATE METHOD (0/1=SUBMERSION/FINITE CLOUD)
 MAXTIM = HOURLY LOOP MAXIMUM CALCULATE TIME
 R = EVALUATION DISTANCE (M)
 RCOUNT = DISTANCE FROM SITE FOR COUNTERMEASURES (M)

Figure B-10 Receptor part

- The weather part defines starting time for simulation and the option for meteorological data selection, as shown in Figure B-11.

| ISTART | ITIME | IDAY | MNST | JIER | IHR | IDA | MON | INSEQ |
|--------|-------|------|------|------|-----|-----|-----|-------|
| 4 | 1 | 1 | 1 | 97 | 6 | 1 | 0 | 100 |

- ISTART = METEOROLOGY SELECTION OPTION (4-6)
- ITIME = STARTING TIME OF THIS SIMULATION
- JIER = STARTING YEAR OF THIS SIMULATION
- MNST = STARTING MONTH OF THIS SIMULATION
- IDAY = STARTING DAY OF THIS SIMULATION

Figure B-11 Weather part

B2.2 Preprocessing process module

Import input data

- A for source term data, a release source term data from isotope part are read and calculated release rate in each advection, as shown in Figure B-12.

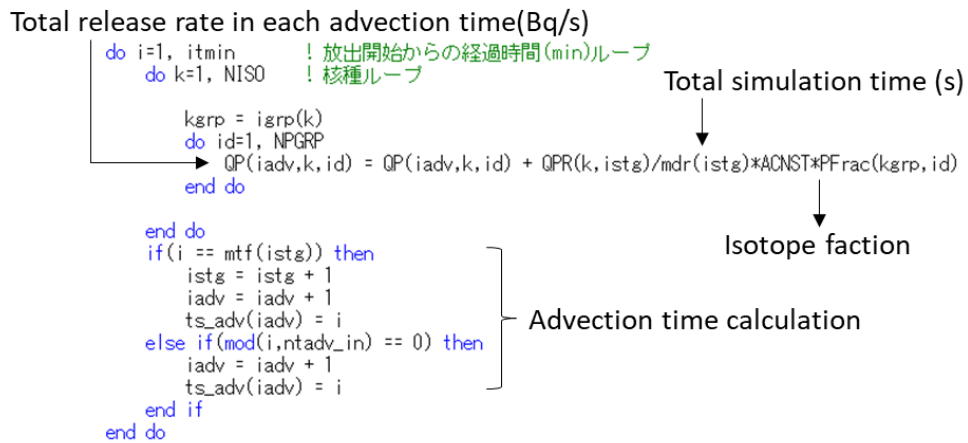


Figure B-12 Release rate calculation

- As for meteorological data, time and each meteorological parameter in the meso, rain, and synop file are read according to the command in Figure B-13. The data from the meso and rain files are imported into the layer at 10 m, while data from the synop file is imported into the remaining nine layers, as shown in Figure B-14.

```

READ(fi_mso,6010,rec=irec) IY,IM, ID, IH
write(*,6010) IY,IM, ID, IH !24-11 h /19/01/2018
!end_vic_ino
WRITE(6,'(a)') '*READ MESO SCALE DATA'
WRITE(6,'(4(a,i2))') ' IY =',IY,' IM =',IM,' ID =',ID,' IH =',IH
DO J=1, NMY
!vic_ino 2002.06.20
READ(12,6020) ( KU(I), KV(I), KS(I), I=1, NMX )
irec = irec + 1
READ(fi_mso,6020,rec=irec) ( KU(I), KV(I), KS(I), I=1, NMX )
READ(fi_mso,6020,rec=irec) ( KU(I), KV(I), KS(I), I=1, NMX )
!end_vic_ino
DO I=1,NMX
    UM(1,J) = KU(I) ← Wind component in X direction
    VM(1,J) = KV(I) ← Wind component in Y direction
    ISTABM(1,J) = KS(I) ← Atmospheric stability class
END DO
END DO
    
```

Read time

(a) Command for meso import data

```

READ RAIN DATA
-----

.ino 2002.12.19
READ(13,5000) IY,IM, ID, IH
irec = irec + 1
READ(fi_ran,5000,rec=irec) IY, IM, ID, IH
do J=1,52
  READ(fi_ran,'(55f5.2)',rec=irec) (FRRAIN(I,J),I=1,55)
END DO
  
```

(b) Command for rain import data

```

WRITE(6,6000) '(2) NEXT SYNOPTIC DATA' read data set 3 (data at
WRITE(6,6200) ' IY =',IY,' IM =',IM,' ID =',ID,' IH =',IH
te(*,*) KFST ! KFST still equal 0

DO J=1, NSY
  DO I=1, NSX
    2002.06.20
    READ(11,5020) ( KU(L), KV(L), KZ(L), L=1, 3 )
    irec = irec + 1 !5725to 8584 read data meteorology data set
    te(*,*) irec ! read each line of data 3 hr
    READ(fi_syn,5020,rec=irec)
      ( KU(L),KV(L),KZ(L), L=1,ilayer )
.ino
    IF( I.EQ.1 .AND. J.EQ.1 ) THEN
      WRITE(6,6100) ' KU =',KU
      WRITE(6,6100) ' KV =',KV
      WRITE(6,6100) ' KZ =',KZ
    ENDIF
    DO L = 1, ilayer
      U2(L,I,J) = KU(L) ← Wind component in X direction
      V2(L,I,J) = KV(L) ← Wind component in Y direction
      Z2(L,I,J) = KZ(L) ← Geopotential high
    END DO
  END DO
END DO
  
```

(c) Command for synop import data

Figure B-13 Command for import data

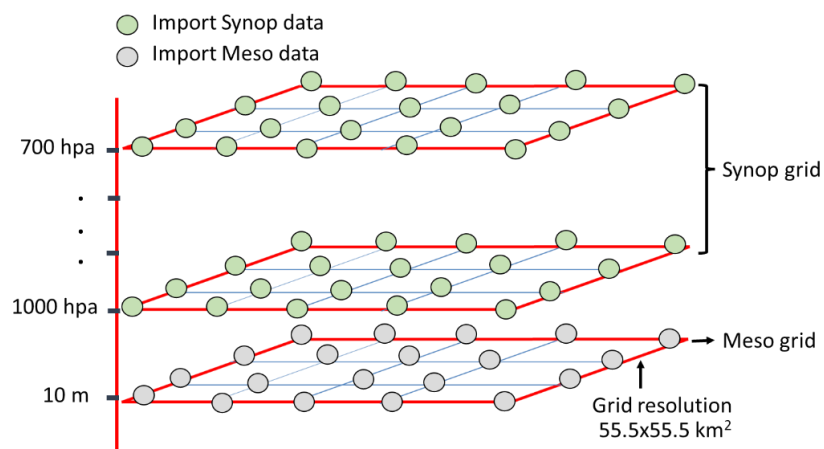


Figure B-14 Meteorological grid system in NACAC

B2.3 Meteorological data selection module

- As for extreme data selection, it is performed with istart 4. The starting time for simulation is defined according to ITIME, IDAY, MNST, and JUER in Figure B-11. As for sequential data selection, it is performed with istart 5. The number of simulation sequent is defined according to the INSEQU parameter, as shown in Figure B-11. The starting time for simulation in the first sequent is defined with ITIME, IDAY, MNST, and JUER parameters. Then, IHR, IDA, and MON set a time interval to select the starting time for the next step simulation. As for the representative data section, it is performed with istart 6. It is conducted with three subroutines: RDMET, BINMET, and RANMIN, as shown in Figure B-15. The RDMET reads meteorological data collected in the area boundary, as mentioned in section 2.7.3. The BINMET classifies meteorological data into several groups. The criteria for classification are evaluated according to the percentile level of the input dataset. The RANMIN selected representative data from all classification groups. The starting time for simulation and the number of simulation sequences are related to the representative data.



```
CALL RDMET  
CALL BINMET  
CALL RANBIN( NSEED, 1, NTOTAL )
```

Figure B-15 subroutines in representative data section module

B2.4. Atmospheric dispersion calculation module

B2.4.1 Depletion

- The release rate calculated in the processing process is calculated depletion by decay, wet and dry deposition, as shown in Figure 16.

```

DO ID=1, NPGRP
  QQ = QDW(K, ID)
  QDW(K, ID) = QDW(K, ID)*EXP(-EXPDC(K)*DELTA*3600.) ← Decay

  IF( PVD(ID).NE.0.0 ) THEN
4.11.17
    DFAC = VD(K)*SIGYSQ*GROUND
    QDW(K) = QDW(K)*EXP(-DFAC*DELTA*3600.)
    DFAC = PVD(ID) * SIGYSQ * GROUND
    QDW(K, ID) = QDW(K, ID)*EXP(-DFAC*DELTA*3600.) ← Dry deposition

4.11.17
    IF( AVRAIN.NE.0. ) THEN
      WFAC = RLAM1(K)*AVRAIN**RLAM2(K)
      QDW(K) = QDW(K)*EXP(-WFAC*DELTA*3600.)
      WFAC = PRLAM1(ID) * AVRAIN**PRLAM2(ID)
      QDW(K, ID) = QDW(K, ID)*EXP(-WFAC*DELTA*3600.) ← Wet deposition
    ENDIF
  ENDIF
  IF( AVRAIN.NE.0. )
    WRITE(6,*) 'DEplete ',K,QQ,DFAC,WFAC,QDW(K)
  ENDIF
END DO

```

Figure B-16 Depletion calculation

B2.4.2 Dispersion

- Meteorological data at four points around the release point is interpolated to calculate meteorological data at the release point. Then, the average wind component in x (u) and y (v) is calculated according to Equation 7 in section 2.6.1. The effective vector of u and v is used to define advection direction and distance, as shown in Figure B-17. The dispersion boundary is calculated according to Equation 8.

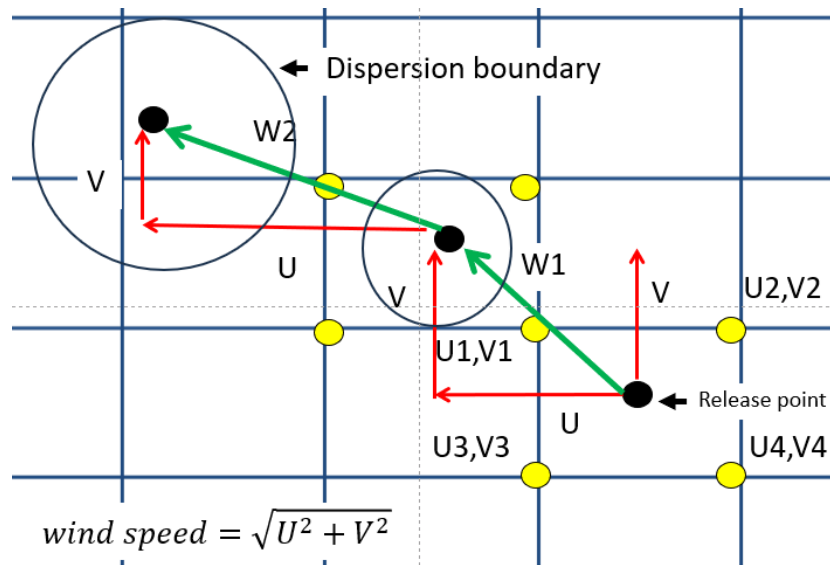


Figure B-17 Advection calculation

B2.4.3 Concentration

- The receptors within the dispersion boundary calculate air concentration by the Gaussian equation. Meanwhile, ground concentration is calculated by multiplying the air concentration with the deposition coefficient, as shown in Figure B-18. The total effective dose equivalence is a summation of ground shine, cloud shine, and inhalation doses, as shown in Figure B-19.

```

DO ID=1, NPGRP
  IF( QP(MLoop,K,ID) /= 0. ) THEN
    !write(*,*)QDW(39,1),QDW(39,2),QDW(39,3)
    AQP = QDW(K, ID) / SIGYSQ
    A = AQP * GAUSSY * ZINV * CNST
    XCON(I,J,K) = XCON(I,J,K) + A*3600. ← Air concentration
    ISUBME(I,J) = ISUBME(I,J) + 1
    CLDWK(K) = CLDWK(K) + A * CLSEM(K)
    IF( PVD(ID) /= 0.0 ) THEN
      AD = PVD(ID)*A ← Ground concentration by dry deposition
      AW = 0.0
      IF( RAIN > 0. ) THEN
        WASH = PRLAM1(ID)*RAIN**PRLAM2(ID)
        AW = WASH*AQP*GAUSSY*CNST ← Ground concentration by wet deposition
      END IF
      XDEP(I,J,K)=XDEP(I,J,K) + (AD+AW)*3600.
      ↓
      Ground concentration by dry and wet depositions
    END IF
  END IF
END DO

```

Figure B-18 Calculation of air and ground concentration

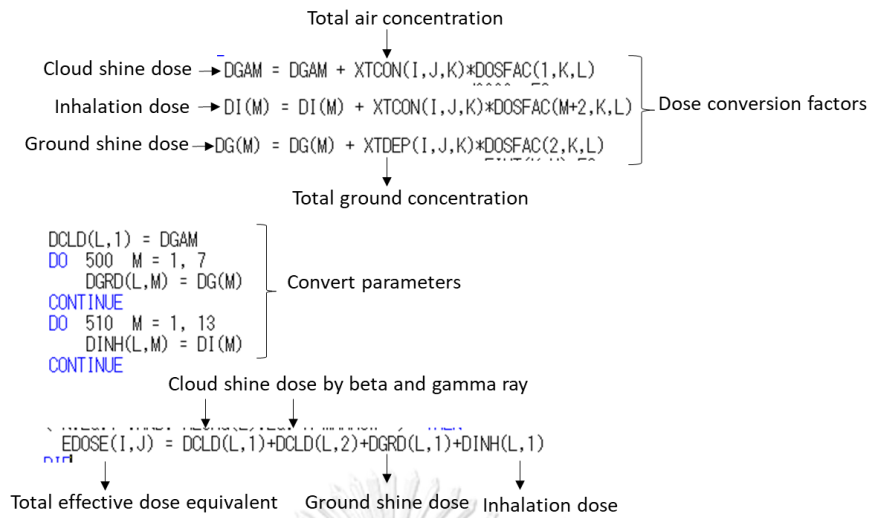


Figure B-19 Calculation of total effective dose equivalence

B2.5 Result display

Predicted results are shown according to receptor location in Figure B-20.

| CHI* T | (SEC*Bq/CUB.METERS) | BY DOWNWIND DISTANCES | ISOTOPE NAME IS | | | | | | | | CS-137 |
|-------------------|---------------------|-----------------------------------|-----------------|----------|----------|----------|----------|----------|----------|--|--------|
| DISTANCE (METERS) | | VALUES TOWARD INDICATED DIRECTION | | | | | | | | | |
| | | S | SSW | SW | WSW | W | WNW | NW | NNW | | |
| 500.0 | 0.00D+00 | 0.00D+00 | 0.00D+00 | 0.00D+00 | 0.00D+00 | 0.00D+00 | 0.00D+00 | 0.00D+00 | 0.00D+00 | | |
| 1500.0 | 5.95D+07 | 2.30D+02 | 0.00D+00 | 0.00D+00 | 0.00D+00 | 0.00D+00 | 0.00D+00 | 0.00D+00 | 0.00D+00 | | |
| 2500.0 | 1.56D+07 | 0.00D+00 | 0.00D+00 | 0.00D+00 | 0.00D+00 | 0.00D+00 | 0.00D+00 | 0.00D+00 | 0.00D+00 | | |
| 3500.0 | 2.04D+06 | 3.97D+01 | 0.00D+00 | 0.00D+00 | 0.00D+00 | 0.00D+00 | 0.00D+00 | 0.00D+00 | 0.00D+00 | | |
| 4500.0 | 3.97D+06 | 6.09D+00 | 0.00D+00 | 0.00D+00 | 0.00D+00 | 0.00D+00 | 0.00D+00 | 0.00D+00 | 0.00D+00 | | |
| 5500.0 | 4.77D+06 | 7.36D+00 | 0.00D+00 | 0.00D+00 | 0.00D+00 | 0.00D+00 | 0.00D+00 | 0.00D+00 | 0.00D+00 | | |
| 7000.0 | 2.72D+06 | 1.63D+00 | 0.00D+00 | 0.00D+00 | 0.00D+00 | 0.00D+00 | 0.00D+00 | 0.00D+00 | 0.00D+00 | | |
| 9000.0 | 1.51D+06 | 6.30D-01 | 0.00D+00 | 0.00D+00 | 0.00D+00 | 0.00D+00 | 0.00D+00 | 0.00D+00 | 0.00D+00 | | |
| 12500.0 | 9.62D+05 | 1.08D-01 | 0.00D+00 | 0.00D+00 | 0.00D+00 | 0.00D+00 | 0.00D+00 | 0.00D+00 | 0.00D+00 | | |
| 17500.0 | 5.99D+05 | 0.00D+00 | 0.00D+00 | 0.00D+00 | 0.00D+00 | 0.00D+00 | 0.00D+00 | 0.00D+00 | 0.00D+00 | | |
| 22500.0 | 5.28D+05 | 0.00D+00 | 0.00D+00 | 0.00D+00 | 0.00D+00 | 0.00D+00 | 0.00D+00 | 0.00D+00 | 0.00D+00 | | |
| 27500.0 | 2.94D+05 | 2.30D-01 | 0.00D+00 | 0.00D+00 | 0.00D+00 | 0.00D+00 | 0.00D+00 | 0.00D+00 | 0.00D+00 | | |
| 30000.0 | 1.95D+05 | 1.11D+00 | 0.00D+00 | 0.00D+00 | 0.00D+00 | 0.00D+00 | 0.00D+00 | 0.00D+00 | 0.00D+00 | | |
| 50000.0 | 8.01D+04 | 4.50D+02 | 0.00D+00 | 0.00D+00 | 0.00D+00 | 0.00D+00 | 0.00D+00 | 0.00D+00 | 0.00D+00 | | |
| 70000.0 | 2.91D+04 | 3.52D+03 | 0.00D+00 | 0.00D+00 | 0.00D+00 | 0.00D+00 | 0.00D+00 | 0.00D+00 | 0.00D+00 | | |
| 90000.0 | 2.90D+03 | 5.83D+03 | 0.00D+00 | 0.00D+00 | 0.00D+00 | 0.00D+00 | 0.00D+00 | 0.00D+00 | 0.00D+00 | | |
| 125000.0 | 2.26D+01 | 3.96D+03 | 1.34D-02 | 0.00D+00 | 0.00D+00 | 0.00D+00 | 0.00D+00 | 0.00D+00 | 0.00D+00 | | |
| 175000.0 | 0.00D+00 | 9.11D+03 | 2.84D+00 | 0.00D+00 | 0.00D+00 | 0.00D+00 | 0.00D+00 | 0.00D+00 | 0.00D+00 | | |
| 250000.0 | 0.00D+00 | 6.26D+03 | 3.10D+01 | 0.00D+00 | 0.00D+00 | 0.00D+00 | 0.00D+00 | 0.00D+00 | 0.00D+00 | | |
| 350000.0 | 0.00D+00 | 1.76D+03 | 2.85D+00 | 0.00D+00 | 0.00D+00 | 0.00D+00 | 0.00D+00 | 0.00D+00 | 0.00D+00 | | |
| 500000.0 | 0.00D+00 | 4.57D+01 | 0.00D+00 | 0.00D+00 | 0.00D+00 | 0.00D+00 | 0.00D+00 | 0.00D+00 | 0.00D+00 | | |
| 700000.0 | 0.00D+00 | 9.36D-01 | 2.98D-04 | 0.00D+00 | 0.00D+00 | 0.00D+00 | 0.00D+00 | 0.00D+00 | 0.00D+00 | | |
| 900000.0 | 0.00D+00 | 2.04D-02 | 7.61D-07 | 0.00D+00 | 0.00D+00 | 0.00D+00 | 0.00D+00 | 0.00D+00 | 0.00D+00 | | |
| 1250000.0 | 0.00D+00 | 0.00D+00 | 0.00D+00 | 0.00D+00 | 0.00D+00 | 0.00D+00 | 0.00D+00 | 0.00D+00 | 0.00D+00 | | |
| 1750000.0 | 0.00D+00 | 0.00D+00 | 0.00D+00 | 0.00D+00 | 0.00D+00 | 0.00D+00 | 0.00D+00 | 0.00D+00 | 0.00D+00 | | |
| DISTANCE (METERS) | | VALUES TOWARD INDICATED DIRECTION | | | | | | | | | |
| | | N | NNE | NE | ENE | E | ESE | SE | SSE | | |
| 500.0 | 0.00D+00 | 0.00D+00 | 0.00D+00 | 0.00D+00 | 0.00D+00 | 0.00D+00 | 0.00D+00 | 0.00D+00 | 0.00D+00 | | |
| 1500.0 | 0.00D+00 | 0.00D+00 | 0.00D+00 | 0.00D+00 | 0.00D+00 | 0.00D+00 | 0.00D+00 | 0.00D+00 | 3.94D+04 | | |
| 2500.0 | 0.00D+00 | 0.00D+00 | 0.00D+00 | 0.00D+00 | 0.00D+00 | 0.00D+00 | 0.00D+00 | 0.00D+00 | 7.97D+03 | | |
| 3500.0 | 0.00D+00 | 0.00D+00 | 0.00D+00 | 0.00D+00 | 0.00D+00 | 0.00D+00 | 0.00D+00 | 0.00D+00 | 2.50D+03 | | |
| 4500.0 | 0.00D+00 | 0.00D+00 | 0.00D+00 | 0.00D+00 | 0.00D+00 | 0.00D+00 | 0.00D+00 | 0.00D+00 | 9.55D+02 | | |
| 5500.0 | 0.00D+00 | 0.00D+00 | 0.00D+00 | 0.00D+00 | 0.00D+00 | 0.00D+00 | 0.00D+00 | 0.00D+00 | 7.62D+02 | | |
| 7000.0 | 0.00D+00 | 0.00D+00 | 0.00D+00 | 0.00D+00 | 0.00D+00 | 0.00D+00 | 0.00D+00 | 0.00D+00 | 3.47D+02 | | |
| 9000.0 | 0.00D+00 | 0.00D+00 | 0.00D+00 | 0.00D+00 | 0.00D+00 | 0.00D+00 | 0.00D+00 | 0.00D+00 | 1.58D+02 | | |
| 12500.0 | 0.00D+00 | 0.00D+00 | 0.00D+00 | 0.00D+00 | 0.00D+00 | 0.00D+00 | 0.00D+00 | 0.00D+00 | 5.72D+01 | | |
| 17500.0 | 0.00D+00 | 0.00D+00 | 0.00D+00 | 0.00D+00 | 0.00D+00 | 0.00D+00 | 0.00D+00 | 0.00D+00 | 2.02D+01 | | |
| 22500.0 | 0.00D+00 | 0.00D+00 | 0.00D+00 | 0.00D+00 | 0.00D+00 | 0.00D+00 | 0.00D+00 | 0.00D+00 | 6.85D+00 | | |
| 27500.0 | 0.00D+00 | 0.00D+00 | 0.00D+00 | 0.00D+00 | 0.00D+00 | 0.00D+00 | 0.00D+00 | 0.00D+00 | 1.23D+00 | | |
| 30000.0 | 0.00D+00 | 0.00D+00 | 0.00D+00 | 0.00D+00 | 0.00D+00 | 0.00D+00 | 0.00D+00 | 0.00D+00 | 2.57D-01 | | |
| 50000.0 | 0.00D+00 | 0.00D+00 | 0.00D+00 | 0.00D+00 | 0.00D+00 | 0.00D+00 | 0.00D+00 | 0.00D+00 | 0.00D+00 | | |
| 70000.0 | 0.00D+00 | 0.00D+00 | 0.00D+00 | 0.00D+00 | 0.00D+00 | 0.00D+00 | 0.00D+00 | 0.00D+00 | 0.00D+00 | | |
| 90000.0 | 0.00D+00 | 0.00D+00 | 0.00D+00 | 0.00D+00 | 0.00D+00 | 0.00D+00 | 0.00D+00 | 0.00D+00 | 0.00D+00 | | |
| 125000.0 | 0.00D+00 | 0.00D+00 | 0.00D+00 | 0.00D+00 | 0.00D+00 | 0.00D+00 | 0.00D+00 | 0.00D+00 | 0.00D+00 | | |
| 175000.0 | 0.00D+00 | 0.00D+00 | 0.00D+00 | 0.00D+00 | 0.00D+00 | 0.00D+00 | 0.00D+00 | 0.00D+00 | 0.00D+00 | | |
| 250000.0 | 0.00D+00 | 0.00D+00 | 0.00D+00 | 0.00D+00 | 0.00D+00 | 0.00D+00 | 0.00D+00 | 0.00D+00 | 0.00D+00 | | |
| 350000.0 | 0.00D+00 | 0.00D+00 | 0.00D+00 | 0.00D+00 | 0.00D+00 | 0.00D+00 | 0.00D+00 | 0.00D+00 | 0.00D+00 | | |
| 500000.0 | 0.00D+00 | 0.00D+00 | 0.00D+00 | 0.00D+00 | 0.00D+00 | 0.00D+00 | 0.00D+00 | 0.00D+00 | 0.00D+00 | | |
| 700000.0 | 0.00D+00 | 0.00D+00 | 0.00D+00 | 0.00D+00 | 0.00D+00 | 0.00D+00 | 0.00D+00 | 0.00D+00 | 0.00D+00 | | |
| 900000.0 | 0.00D+00 | 0.00D+00 | 0.00D+00 | 0.00D+00 | 0.00D+00 | 0.00D+00 | 0.00D+00 | 0.00D+00 | 0.00D+00 | | |
| 1250000.0 | 0.00D+00 | 0.00D+00 | 0.00D+00 | 0.00D+00 | 0.00D+00 | 0.00D+00 | 0.00D+00 | 0.00D+00 | 0.00D+00 | | |
| 1750000.0 | 0.00D+00 | 0.00D+00 | 0.00D+00 | 0.00D+00 | 0.00D+00 | 0.00D+00 | 0.00D+00 | 0.00D+00 | 0.00D+00 | | |

Figure B-19 Predicted result in NACAC

This data is plotted in Python code as follows.

```

import matplotlib.pyplot as plt
import numpy as np
import matplotlib.colors
import matplotlib as mpl
# Define radial of polar coordinate
r,theta =
np.meshgrid([0,0.5,1.5,2.5,3.5,4.5,5.5,7,9,12.5,17.5,22.5,27.5,30,50,70,
90,125,175,250,350,500,700,900]
,np.arange(0,6.47955,0.19635))
z=[]
# Read input file
import glob as gb
aaa=0
windu = gb.glob("./50-1RE/*.csv")
print(windu)
for filenameu in windu:
    aaa+=1
    print(aaa)
    print(filenameu)
    file = open(filenameu)
    for line in file:
        if line.strip() != "":
            x=(float(n) for n in line.split(','))
            z.append(x[0:23])
    file.close()
# Define color bar
boundaries = [-30,-16,-15,-14,-13,-12,-11,-10,-9,-8,-7,-6,-5,-4,-3,-
2,-1,0]#TEDE msv
cmap_reds = plt.cm.get_cmap('YlOrRd', len(boundaries) + 1)
colors = list(cmap_reds(np.arange(len(boundaries))))
colors[0] = "w"
cmap = matplotlib.colors.ListedColormap(colors[:-1], "")
cmap.set_over(colors[-1])
fig, (ax2) = plt.subplots( subplot_kw=dict(projection='polar'))
# Plot graph and save a graph
a=ax2.pcolormesh(theta, r, z, cmap=cmap,norm =
mpl.colors.BoundaryNorm(boundaries, ncolors=len(boundaries)-1,
clip=False))
ax2.set_yticklabels([], color='black')
ax2.tick_params(axis='y', colors='black')
ax2.grid(c='black', ls='--', lw=0.5)
b = fig.colorbar(a, extend="both")
plt.thetagrids([theta * 22.5 for theta in range(16)],
('E', 'ENE', 'NE', 'NNE', 'N', 'NNW', 'NW', 'WNW', 'W', 'WSW',
'SW', 'SSW', 'S', 'SSE', 'SE', 'ESE'), fontsize=13, **csfont)
plt.rgrids(
[0.5,1.5,2.5,3.5,4.5,5.5,7,9,12.5,17.5,22.5,27.5,30,50,70,90,125,175,250
,350,500,700,900],("","","","","","","","","","","","","","","",
"","","","'125',' ',''250',''350',''500',''700 ',''900km'")
, color='black',fontsize=11,**csfont,angle=34.)
plt.savefig(filenameu+'.jpg', dpi=300)
plt.show()
z.clear()
x.clear()

```

VITA

NAME Narakhan Khunsrimek

DATE OF BIRTH October 3,1993

PLACE OF BIRTH Roi-Et

INSTITUTIONS ATTENDED Master of Science (M.S.) Chulalongkorn University

HOME ADDRESS 170 Ratakitkika road, Robmueang. Mueang, Roi-Et, 45000

PUBLICATION Khunsrimek, N., Krisanungkura, P., Vechgama, W., Silva, K., Rassame, S., & Hibiki, T. (2023). Verification of the NACAC atmospheric dispersion calculation using a hypothetical accident in a neighboring nuclear power plant. Progress in Nuclear Energy, 156, 104532.
<https://doi.org/https://doi.org/10.1016/j.pnucene.2022.104532>

Khunsrimek, N., Vechgama, W., Silva, K., Rassame, S., & Hibiki, T. (2023). Simulation using representative data selection for transboundary radiation effect evaluation by Nuclear Accident Consequence Analysis Code (NACAC). Journal of Nuclear Science and Technology, 1-16.
<https://doi.org/10.1080/00223131.2023.2231444>

Khunsrimek N, Krisanungkura P, Vechgama W, Rassame, S., Silva,K,, editors. EFFECTS OF METEOROLOGICAL DATA SET SELECTION ON SIMULATION RESULTS OF ATMOSPHERIC DISPERSION CODE (NACAC). The 47th International Congress on Science,Technology and Technology-based Innovation (STT47); 2021; Kasetsart University, Kamphaeng Saen Campus,Nakhon Pathom, Thailand.